University of Ljubljana
Faculty of Mathematics and Physics
Department of Physics

Rok Dolenec

Time-of-Flight Positron Emission Tomography Using Cherenkov Radiation

Doctoral Thesis

Supervisor: Prof. Dr. Samo Korpar

Ljubljana, 2012

Univerza v Ljubljani
Fakulteta za Matematiko in Fiziko
Oddelek za Fiziko

Rok Dolenec

Uporaba svetlobe Čerenkova za meritev časa preleta pri pozitronski tomografiji

Disertacija

Mentor: Prof. Dr. Samo Korpar

Ljubljana, 2012

Zahvaljujem se vsem z oddelka za eksperimentalno fiziko osnovnih delcev za odlično delovno vzdušje in pomoč pri mojem izobraževanju in delu. To zahvalo moram še posebej posvetiti mentorju Prof. Dr. Samu Korparju, za katerega lahko rečem, da me je naučil skoraj vse, kar vem o eksperimentalni fiziki, ter Prof. Dr. Peteru Križanu, ki s svojim trudom in požrtvovalnostjo omogoča projekte kot je ta doktorat. To delo prav tako ne bi bilo mogoče brez vseh nasvetov in pomoči Dr. Rok Pestotnika ter tehnične podpore Jureta Eržena.

Abstract

The quality of images obtained with positron emission tomography (PET) can be substantially improved by including the measurement of time difference between arrival of the two annihilation gammas (time-of-flight information) in image reconstruction. The resolution of time-of-flight measurements is usually limited by the time response of the scintillators used in PET. This work investigates the possibility of improving the time resolution by detecting Cherenkov photons instead of scintillation light. A simple PET setup using lead fluoride or lead tungstate crystals as Cherenkov radiators and microchannel plate photomultipliers as photon detectors was used to evaluate the performance of such detection method. The effect of excellent time resolution on the reconstructed images was investigated with simulations of a full body PET system.

Keywords: time-of-flight, PET, Cherenkov radiation, microchannel plate photomultipliers, lead fluoride, lead tungstate

Povzetek

Kvaliteta in s tem diagnostična vrednost slik pridobljenih s pozitronsko tomografijo (PET) se izboljša, če vključimo meritev časa preleta. Izboljšanje je odvisno od časovne ločljivosti, s katero lahko zaznamo koincidenčna žarka γ. Glavno omejitev pri ločljivosti meritve časa preleta predstavlja časovni odziv scintilatorjev, ki se uporabljajo za PET. To delo raziskuje možnost izboljšanja časovne ločljivosti z uporabo detektorjev, ki namesto scintilacijske svetlobe zaznavajo svetlobo Čerenkova. Lastnosti takšnih detektorjev so bile raziskane s pomočjo preproste naprave PET, ki je za sevalec svetlobe Čerenkova uporabljala kristale svinčevega fluorida ali svinčevega volframata, za detektorje svetlobe pa mikrokanalne fotopomnoževalke. S pomočjo simulacij je bil ocenjen vpliv odlične časovne ločljivosti na kvaliteto slik, rekonstruiranih v primeru celotne naprave PET.

Ključne besede: čas preleta, pozitronska tomografija, mikrokanalna fotopomnoževalka, svinčev fluorid, svinčev volframat

Contents

1 Introduction **7**
1.1 Objectives of thesis . . . 8
1.2 Conventions . . . 8

2 Positron Emission Tomography **9**
2.1 Radiation materials for PET . . . 9
2.2 Image Reconstruction . . . 10
2.3 Detection of annihilation gammas . . . 14
2.3.1 Scintillators . . . 14
2.3.2 Photomultiplier Tubes . . . 16
2.3.3 PET Scanners . . . 19
2.4 Performance of PET Scanners . . . 20
2.4.1 Position Resolution . . . 20
2.4.2 Sensitivity . . . 23
2.4.3 Fake Events . . . 24
2.4.4 Image Contrast . . . 25
2.4.5 Signal-to-noise Ratio . . . 26
2.5 Time-of-flight PET . . . 27
2.5.1 Performance of TOF PET . . . 29

3 Use of Cherenkov radiation for PET **33**
3.1 Cherenkov radiation . . . 34
3.2 The interaction of gammas with matter . . . 35
3.2.1 Photoelectric Effect . . . 36
3.2.2 Compton Scattering . . . 37
3.2.3 Pair Production . . . 38
3.2.4 Gamma stopping power . . . 39
3.3 The interaction of electrons with matter . . . 39
3.4 Cherenkov radiators for annihilation gammas . . . 40
3.4.1 Requirements . . . 40
3.4.2 Radiator candidates . . . 40
3.5 Estimation of radiator performance . . . 42
3.5.1 Absorption of annihilation gammas . . . 42
3.5.2 Electron production . . . 42
3.5.3 Cherenkov photon production . . . 43
3.5.4 Cherenkov photon detection . . . 45

4 Experimental setup **49**
4.1 Microchannel plate photomultiplier . . . 49
4.2 Cherenkov Radiators . . . 54
4.3 Electronic Readout . . . 55
4.3.1 Readout of MCP PMTs . . . 55

4.3.2 Signal Processing 57
4.3.3 Time-Walk Correction 58
4.4 The 511 keV Gamma Source 61

5 Measurements of MCP PMT intrinsic performance 63
5.1 Charge distributions 63
5.1.1 Maximum charge cut 66
5.2 Time resolution 66
5.3 Coincidence timing resolution 69

6 Coincidence time resolution using Cherenkov light 73
6.1 Initial results 73
6.1.1 Charge distributions 73
6.1.2 Time distributions 74
6.2 Coincidence time resolution with 16 channel readout 77
6.2.1 Charge distributions 79
6.2.2 Time distributions 79
6.3 Coincidence time resolution with 4×4 segmented crystals . . . 85
6.4 Demonstration of position reconstruction 88

7 Cherenkov PET Efficiency 93
7.1 Setup 93
7.2 Reference detector charge distribution 95
7.3 Cherenkov detector event selection 96
7.4 Efficiency estimation 98
7.5 Results 98
7.5.1 Radiator sample 98
7.5.2 Radiator thickness 99
7.5.3 Surface treatment 100
7.5.4 Segmented crystals 100
7.5.5 Effects of MCP PMT 100

8 Measurements Summary 103

9 Simulations 105
9.1 Simulation parameters 105
9.1.1 Physics list 105
9.1.2 Detector construction 106
9.1.3 Material properties 107
9.1.4 The photodetector 110
9.1.5 Generation of primary particles 110
9.2 Simulation results 111
9.2.1 Gamma interactions 111
9.2.2 Electron production 111

9.2.3 Photon production . . . 113
9.2.4 Photon propagation . . . 115
9.2.5 Photon detection . . . 116
9.2.6 Annihilation gamma detection efficiency . . . 118
9.2.7 Intrinsic suppression of scatter events . . . 120
9.2.8 Photon detection timing . . . 122
9.2.9 Coincidence detection timing . . . 124
9.3 Possible improvements of the method . . . 128
9.3.1 Photodetector PDE . . . 130
9.3.2 Cherenkov radiator . . . 131
9.3.3 Extraction of photons . . . 136

10 TOF PET Image Reconstruction 139
10.1 Measurements with virtual PET ring . . . 140
10.2 Simulated PET scanner . . . 145

11 Conclusion 153

12 Povzetek doktorskega dela 155
12.1 Uvod . . . 155
12.2 Pozitronska tomografija . . . 155
12.3 Fotopomnoževalka . . . 159
12.4 Uporaba svetlobe Čerenkova za PET . . . 160
12.5 Meritve . . . 163
12.5.1 Postavitev poskusa . . . 163
12.5.2 Lastnosti mikrokanalnih fotopomnoževalk . . . 165
12.5.3 Meritev časa preleta . . . 166
12.5.4 Meritev učinkovitosti detektorja . . . 170
12.5.5 Primerjava sevalcev . . . 173
12.6 Simulacije . . . 174
12.6.1 Parametri . . . 174
12.6.2 Rezultati . . . 175
12.6.3 Izboljšave detektorja . . . 179
12.7 Rekonstrukcija . . . 182
12.8 Zaključek . . . 186

13 Bibliography 187

Appendices 191

A Time-walk correction with coincidence data 191

B Detection of gammas with the MCP PMT **195**
B.1 Effects of the window 196
B.2 Effects of the MCP 196

1 Introduction

Positron emission tomography (PET) is a non-invasive method for in-depth and in-vivo imaging of live tissue, which allows to track physiological metabolism of biomolecules, which have been marked with a radioactive, positron emitting isotope. The substance distribution in tissue is determined by detecting pairs of the annihilation γ rays with position sensitive detectors, which are usually forming rings around the patient. The two points of detection determine a straight line passing close to the nucleus, which emitted the positron. By detecting a large number of γ ray pairs in such a way, it is possible to reconstruct the three dimensional distribution of sources in the tissue.

Detectors of γ rays consist of a scintillating crystal, in which 511 keV photons produce scintillation light, and a photon detector, which converts this light into electric pulses. Scintillators and photon detectors represent the highest fraction of total PET device cost and also determine its performance. Most PET devices use a combination of BGO ($Bi_4Ge_3O_{12}$) crystal as a scintillator and photomultiplier tube (PMT) as a photon detector. Development of photon detectors with excellent timing resolution enabled an improvement in PET image reconstruction, by measuring the time difference between the arrivals of the two γ rays. Such time-of-flight (TOF) measurement provides additional information of where on the line between the two detectors the decay occurred. This can significantly improve the quality of reconstructed images.

PET detectors optimized for timing can achieve a time resolution of about 300 ps [1, 2], which means that the position of decay can be determined with a position resolution of $\delta x = \delta t \cdot c_0/2 \approx 4.5$ cm. Such resolution includes a contribution from the photomultiplier tubes, which can achive a time resolution of $100 - 200$ ps [3]. Some of the newer photon detectors provide a significantly better time resolution, for instance the microchannel plate photomultipliers (MCP PMTs) provide an excellent resolution with $\sigma < 30$ ps (70 ps FWHM) [4, 5]. By using such light detectors the time-of-flight resolution becomes limited by the time constant of the scintillators, which can be of the order of 10 - 100 ns.

Time-of-flight resolution with fast photon detectors could be improved, if instead of scintillation light we would detect Cherenkov photons, which are produced promptly by a passage of charged particles, such as electrons, through a suitable radiator material. To produce Cherenkov photons from 511 keV annihilation gammas we must first convert these into electrons. Photons with energy of 511 keV interact with matter either through the photoelectric effect or by Compton scattering. Here the former is preferred, since all of the photons energy is deposited in one interaction, which results in a photoelectron with the maximum kinetic energy possible. The material

used as a Cherenkov radiator should have a high index of refraction, i.e. a low Cherenkov threshold, so that many electrons are produced above the Cherenkov threshold. It should also have a high stopping power for 511 keV gammas. All this suggests a high density and high-Z material. Also, the material must have good transmission for light in the blue to near UV region, where most of the Cherenkov photons are produced. Most promising candidates are crystals with high lead content, such as the lead fluoride (PbF_2) and lead tungstate ($PbWO_4$).

Even though the Cherenkov photons are produced promptly, a significant contribution to the timing resolution comes from the Cherenkov photon travel time spread in the crystal, which is expected to contribute a spread of about $\sigma_t \approx 20$ ps. This, combined with the photodetector time resolution of $\sigma_t \approx 20$ ps, results in a total coincidence time resolution of $\sigma_t \approx 40$ ps (approximately 100 ps FWHM), or position resolution of $\sigma_x \approx 6$ mm (approximately 15 mm FWHM). Such good resolution suggests that considerable benefits and improvements of PET image quality may be obtained by detecting annihilation gammas via the prompt Cherenkov photons they produce in suitable radiators.

1.1 Objectives of thesis

The recent availability of very fast MCP PMTs makes possible to experimentally verify the feasibility of TOF PET measurements using Cherenkov photons. This work will study a simple PET device, constructed to perform such measurements. In this device, the PbF_2 and $PbWO_4$ crystals of different thicknesses and with different surface treatments will be tested as Cherenkov radiators. Two main parameters, the time resolution and detection efficiency, will be obtained for different parameters of the detector. The findings of the measurements will be supported with simulation results. Images, reconstucted from measured and simulated data, will be presented and used to evaluate the improvements due to the inclusion of TOF information.

1.2 Conventions

In this work, the time and position resolution will mostly be expressed in terms of full width half maximum (FWHM). Sometimes the resolution will be also expressed the σ parameter of a Gaussian function, which is connected to FWHM by the relation FWHM $\approx 2.35 \cdot \sigma$. In such cases, the use of σ resolution will be clearly marked in order to avoid confusion.

2 Positron Emission Tomography

Positron emission tomography is a class of nuclear medicine imaging, used for observation of a range of biological processes in the body. It provides valuable diagnostic information, such as location of cancerous growth, distribution of brain activity or the time evolution of heart activity. A PET study involves injecting a patient with a radiopharmaceutical, a biologically active compound which is labeled with a positron emitting radionuclide. A choice of radiopharmaceuticals, targeted at different biological processes is available. The body accumulates the radiopharmaceutical mostly in the tissue of interest, where the radionuclides then decay with time. This radioactive decays result in positrons, which annihilate with electrons in the tissue, producing pairs of annihilation gamma pairs. The energy of annihilation gammas is 511 keV, enough that a significant portion of them exits the body without being scattered or absorbed. The fact that the two annihilation gammas are emitted in almost exactly opposite direction is exploited by the PET scanner, which in principle is a position sensitive gamma camera surrounding the patient. The detector is typically composed of a large number of scintillating crystals, in which gammas are absorbed and their energy is converted into scintillation light, and photodetectors, which convert the scintillation light pulses into measurable electric signals. A position of one annihilation, marking the approximate position of originating radiopharmaceutical molecule, is determined, when the two gammas are detected on opposite sides of the PET scanner simultaneously. By accumulating a large number of such events, an image depicting the distribution of the radiopharmaceutical in the body can be formed by the image reconstruction algorithms. Images can also be obtained for specific time intervals, enabling studies of the time evolution of biological processes. PET images are especially valuable, when obtained in combination with other medical imaging modalities, which provide anatomic images, such as magnetic resonance imaging (MRI) or x-ray computed tomography (CT).

2.1 Radiation materials for PET

A nucleus with an excess of protons can decay via the β^+ decay (Figure 2.1). One of the protons decays into a neutron, releasing a positron (β^+ particle) and a neutrino. The positron interacts with the surrounding material, losing its kinetic energy and, when slow enough, annihilates with an electron. The distance which the positron travels before it annihilates depends on the material in which it travels and the initial positron energy. The average distances traveled before annihilation in water (an approximation for tissue) are listed for most common radionuclides in Table 2.1, together with other radionuclide properties. Annihilation of the positron results in two annihilation gammas

with an energy of 511 keV, emitted in almost exactly the opposite directions. The angle between the two gammas differs from exactly 180° by approximately 0.25°, due to the fact that the positron has some kinetic energy left when it annihilates.

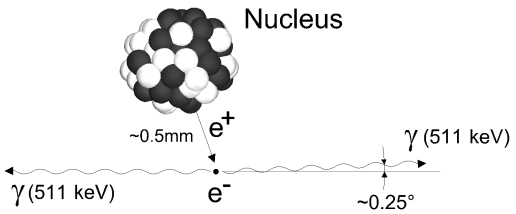

Figure 2.1: An illustration of the β^+ decay.

Isotope	$t_{1/2}$	E_{max} (MeV)	d_{max} (mm)	$\overline{d}$ (mm)
^{11}C	20.4 min	0.97	3.8	0.85
^{13}N	10 min	1.20	5.0	1.15
^{15}O	2 min	1.74	8.0	1.80
^{18}F	110 min	0.64	2.2	0.46
^{68}Ga	68 min	1.90	9.0	2.15
^{82}Rb	75 sec	3.35	15.5	4.10

Table 2.1: Properties of some of the positron emitting radionuclides most commonly used for PET imaging: radioactive decay half time ($t_{1/2}$), maximum energy of emitted positrons (E_{max}), maximum and average range of emitted positron in water (d_{max} and $\overline{d}$) [6].

PET radiopharmaceuticals are based on compounds, which are the analogs of molecules, important in various biological processes. For example, the ^{18}F-Fluorodeoxyglucose is an analogue of glucose used in cellular metabolism. Another example is the ^{18}F-Fluorothymidine. It is treated by the body as thymidine, which is incorporated into the DNA. The ^{18}F-Fluorothymidine can therefore provide a measure of cell proliferation. The positron emitting radionuclides have very short lifetimes (Table 2.1), meaning they must be produced near the site of PET examination. For this reason, the most preferred radiopharmaceuticals are the ones using ^{18}F, with a relatively long half-life ($t_{1/2}$ =110 min). Table 2.2 lists most commonly used radiopharmaceuticals and their uses, illustrating the wide range of diagnostic uses of PET and biological processes, which can be studied with it.

2.2 Image Reconstruction

The PET scanner consists of a large number of position sensitive gamma detectors surrounding the patient, typically arranged in multiple rings. When

Radiopharmaceutical	Uses
^{18}F-Fluorodeoxyglucose	Study of metabolism in the brain and heart, detection of epilepsy and tumors
^{18}F-Fluorothymidine	In-vivo diagnosis and characterization of tumors
^{18}F-Sodium Fluoride	Bone scintigraphy
6-^{18}F-L-Fluorodopa	Assessment of presynaptic dopaminergic function in the brain
^{15}O-Water	Studies of myocardial and cerebral perfusion
n-^{15}O-Butanol	Blood flow measurement in brain and other organs
^{13}N-Ammonia	Studies of myocardial and cerebral perfusion
^{11}C-Sodium Acetate	Measurement of oxygen consumption in the heart
^{11}C-Flumazenil	Neuroreceptor characterization
^{11}C-Methylspiperone	Measurement of dopamine-2 receptor density in patients with neurological disorders
^{11}C-L-Methionine	Detection of different types of malignancies, reflecting amino acid utilization
^{11}C-Raclopride	Detection of various neurological and psychiatric disorders (Parkinsons disease, schizophrenia, etc.)
^{82}Rb-Rubidium Chloride	Studies of myocardial perfusion

Table 2.2: Common radiopharmaceuticals and their uses in PET imaging [6].

two gammas with energy close to 511 keV are registered with two gamma detectors nearly simultaneously (when both hits are inside a narrow coincidence time window, typically about 10 ns), it is presumed that the two gammas originate from the same β^+ decay. The position of annihilation is thus determined to be somewhere on the line between the two gamma detectors, called the line of response (LOR).

Each LOR can be described by the distance of the LOR from the center of PET scanner (r) and angle of orientation (ϕ), shown in Figure 2.2. During the PET examination, the data is accumulated in the $r - \phi$ space in a form of a 2-D histogram, called a sinogram (Figure 2.3). Each bin of the sinogram represents one possible LOR, while each row represents a projection profile of the activity distribution over a single projection angle. When the data acquisition is finished, the bins of the sinogram hold the number of coincidences, detected by the corresponding gamma detector pairs. The image of activity distribution is then reconstructed in real $(x - y)$ space using mathematical algorithms.

The most basic form of image reconstruction is known as simple backprojection (SBP). The image is reconstructed on a 2-D matrix of discrete pixels, where the matrix size is usually chosen to be a power of 2 (e.g. 128×128 pixels). The counts recored for each LOR (i.e. the value of the corresponding sinogram bin) are distributed amongst the pixels that this LOR intersects (Figure 2.4a). Pixels, where a larger number of LORs intersect will

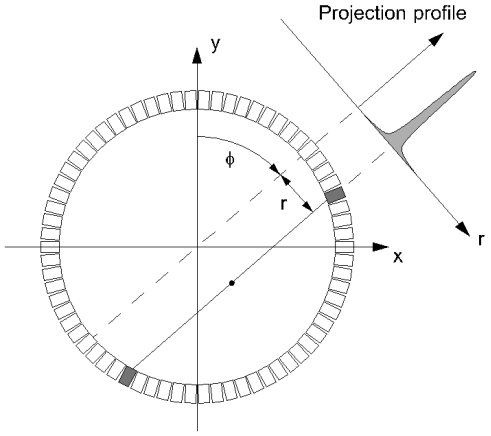

Figure 2.2: The x−y and $r - \phi$ coordinate pairs shown in relation to PET ring.

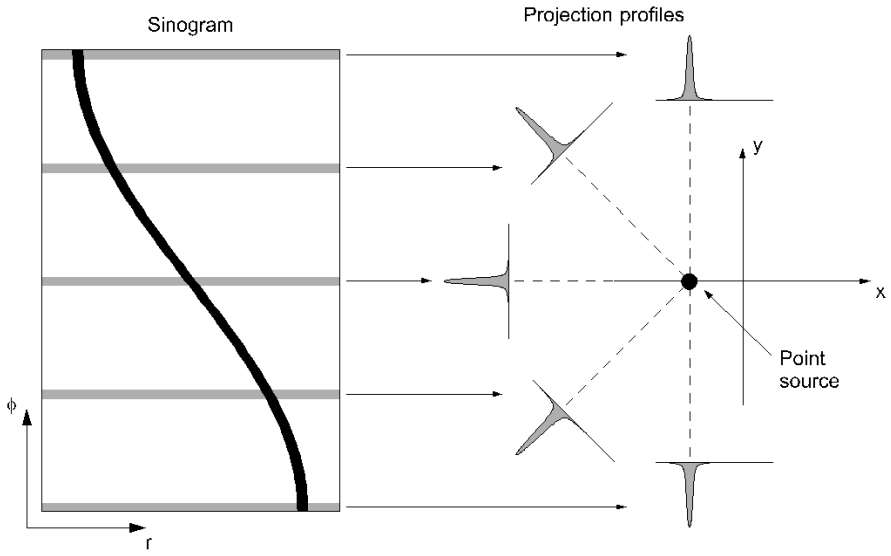

Figure 2.3: Sinogram is a 2-D matrix of counts recorded by different pairs of detectors. Each row corresponds to an individual projection profile in the radial direction.

accumulate a larger count which leads to the image of activity distribution (Figure 2.4c).

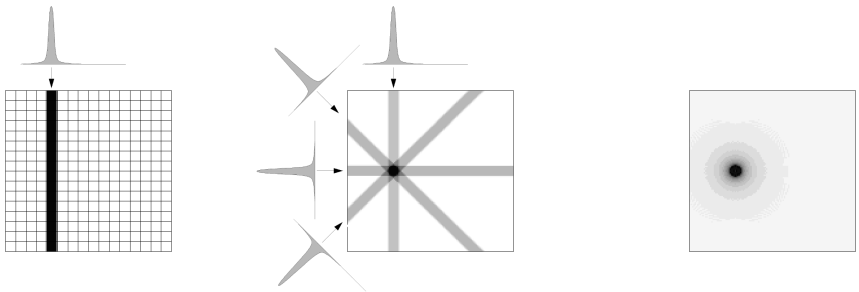

(a) 1 angle (b) 4 angles (c) 64 angles

Figure 2.4: The formation of SBP image, as projection profiles belonging to more and more projection angles are included in the reconstruction of the image.

Images reconstructed using SBP algorithm suffer from a blurring effect, caused by a spillover of counts from other image pixels to the observed pixel. Since the location of event is limited only to the LOR, not only the value of the pixel from which the event originated is increased, but the value of all pixels laying along the LOR is increased by the same amount. In the accumulated image the contribution from one pixel to the others decreases as a $1/r$ function, where r is the distance between the originating and observed pixel. This means that the blurring can be removed by deconvoluting the reconstructed image with the $1/r$ function.

An image reconstruction algorithm that avoids the $1/r$ blurring effect is the filtered backprojection (FBP). Here, the 1-D projection slices (sinogram rows) are Fourier transformed into k-space. Deconvolution with the $1/r$ function is effectively achieved by applying the so called ramp filter (described by $F(k_r) = |k_r|$) to each transformed profile. An inverse Fourier transform is then performed for each slice. After performing a backprojection of the so obtained sinogram the final image is obtained without the $1/r$ blurring [7]. However, such an approach also amplifies high frequency noise, so the ramp filter is usually modified to include some form of a high frequency suppression filter. This re-introduces some blurring, but the amount of blurring can be controlled by the selection of filter to produce the best images possible.

Another possible approach to image reconstruction are the iterative reconstruction algorithms. Reconstruction starts with a simple estimate of activity distribution. This is then forward projected (transformed from real space to $r - \phi$ space) to form a sinogram, which is compared to the measured sinogram data and a better estimate is generated based on the differences. The process is repeated for some number of iterations, until the differences

between the estimated and the measured sinograms fall a below certain level. Iterative methods are more computationally intensive than backprojection methods, but can produce better images.

The reconstruction algorithms described apply to 2-D images and are usually performed on 2-D slices along the axial direction of PET scanner. So obtained 2-D images can then be combined to form 3-D images of activity distribution. The 3-D data can also be rebined to produce images of slices other than that perpendicular to the scanner axis.

2.3 Detection of annihilation gammas

Annihilation gamma detectors used for PET consist of a scintillating crystal and a photodetector, most commonly a photomultiplier tube (Figure 2.5). The incident gamma ray interacts with the scintillating crystal, depositing all or a part of its energy, which is transformed by the scintillator into light. The scintillator is usually wrapped in a reflecting material, so that as many scintillation photons as possible are collected by the PMT that is coupled to the exit face of the scintillator. The PMT then transforms this light into electric signals, which are proportional to the intensity of the scintillation light pulse. The coincidences are formed from signals, arriving within the coincidence time window from two different detectors, and are stored for processing.

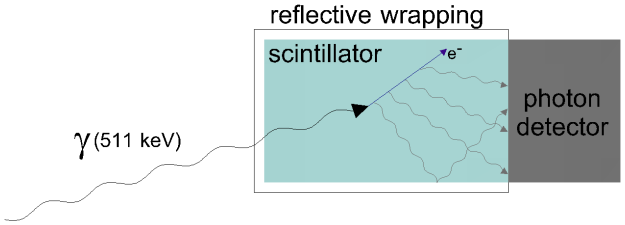

Figure 2.5: Annihilation gamma detector arrangement, typicaly used in PET: a scintillating crystal is wrapped in reflecting material and coupled to a photomultiplier tube.

2.3.1 Scintillators

Scintillators are materials which emit photons of visible or UV light, as a result of interactions with ionizing radiation. Scintillators can be organic, which are usually in liquid form or mixed into plastic material, or inorganic crystals. As the ionizing radiation, for example a gamma ray, interacts with

the scintillator material, it transmits some of its energy to one or more electrons. This electrons than lose their energy by scattering on other electrons in the material, raising them to excited energy states. The excited electrons return to their ground states, emitting scintillation light on transitions between certain atomic or crystalline electron states. In organic scintillators, the emission of scintillation light happens for transitions between delocalised π electron states of the Benzene molecule. In inorganic scintillators the scintillation light is emitted when excited electrons return from the conduction to the valence band. Inorganic scintillators require a small concentration of dopant, which provides additional energy levels between the conduction and valence band. Transition between this states will result in emission of photons with energy smaller than the band gap. This allows the scintillation photons to leave the crystal without being reabsorbed.

Scintillators used in PET have to absorb annihilation gammas and convert their energy into scintillation light with the highest possible efficiency. Due to the depth-of-interaction effect (Section 2.4.1), crystals with small thickness are preferred, meaning that their density must be as high as possible in order to stop 511 keV gammas. For this reason, organic plastic or liquid scintillators are not used in PET. Only the inorganic scintillators in crystalline form are dense enough.

Additional requirements are a large light yield (number of scintillation photons produced per energy unit of the incident gamma) and a short decay time constant of scintillations. The number of produced scintillation photons is proportional to the energy deposited in the crystal by incident gamma, which enables the measurement of event energy. The energy resolution of the measurement is related to the number of detected photons (N):

$$\frac{\Delta E}{E} = \frac{1}{\sqrt{N}}. \tag{2.1}$$

A short decay time constant of scintillations increases the number of photons, which can be collected in an event, reduces problems associated with high count rates (e.g. event pileup) and can enable time-of-flight measurements (Section 2.5).

Another important scintillator material property is the fraction of events, produced by photoeffect. Gammas, which are absorbed by the photoeffect, leave all of their energy in the crystal, while scattered gammas can exit the crystal, carrying away a portion of their energy. To suppress unwanted background due to scattering, gammas detected with energy below a certain level are usually rejected in PET measurements. A crystal with a low fraction of photoeffect will therefore have a lower overall efficiency, and scintillators with higher density and effective atomic number, which lead to a higher fraction of photoeffect, are preferred.

Properties of some of the most important scintillators for PET are sum-

	NaI(Tl)	BGO	BaF_2	LSO	$LaBr_3$(Ce)
ρ (g/cm^3)	3.7	7.1	4.9	7.4	5.1
μ_{511keV} (cm^{-1})	0.35	0.96	0.44	0.87	0.43
τ (ns)	230	300	0.6	40	17
LY (photons/MeV)	38000	6000	2000	29000	58000
Peak emission (nm)	415	480	220	420	356
Refractive index	1.85	2.15	1.52	1.82	1.88

Table 2.3: Properties of some of the most important scintillators: scintillation decay time (τ), density (ρ), 511 keV photon attenuation length (μ_{511keV}), light yield (LY), peak scintillation emission wavelength and refractive index ([6, 8, 9, 10]).

marized in Table 2.3. The thallium doped sodium iodide, NaI(Tl), is not used in PET due to its low density and 511 keV gamma stopping power. However it is often used for other applications, including nuclear medicine studies using gammas with lower energies due to its excellent light yield. The bismuth germanate, $Bi_4Ge_3O_{12}$ (BGO), is the most common scintillator used in PET due to its excellent gamma stopping power ($\mu_{511keV} = 0.96$ cm^{-1}). Barium fluoride, BaF_2 crystals were used in early TOF PET systems due to their extremely short decay time (0.6 ns) but did not prove to be very successful because they have a poor gamma stopping power and the fact that the fast component of their scintillation light is emitted in the UV region, requiring more expensive photodetectors. The Ce-doped Lutetium oxyorthosilicate, Lu_2SiO_5(Ce) (LSO), and lanthanum bromide, $LaBr_3$(Ce), are examples of recently developed scintillators. Their scintillation properties strongly depend on the dopant concentration. Both scintillators have a very high light yield and relatively short decay times. The $LaBr_3$(Ce) has especially impressive light output (58000 photons/MeV with decay time of 17 ns), however its lower density requires thicker crystals to reach the efficiency of more dense scintillators.

2.3.2 Photomultiplier Tubes

The photomultiplier tube is an electronic vacuum tube device, used to convert photons of light into measurable electric signals. Figure 2.6 shows the basic construction and illustrates the principles of operation of a photomultiplier tube. It consists of a photocathode, followed by an electron focusing system, an electron multiplier section (usually a chain of dynodes) and an anode, where the signal is collected. All the parts are enclosed in an evacuated glass tube.

The photocathode is deposited as a thin layer on the inner surface of the entry window. Incident photons of light are converted by the photocathode into electrons (called photoelectrons) via the photoelectric effect. The

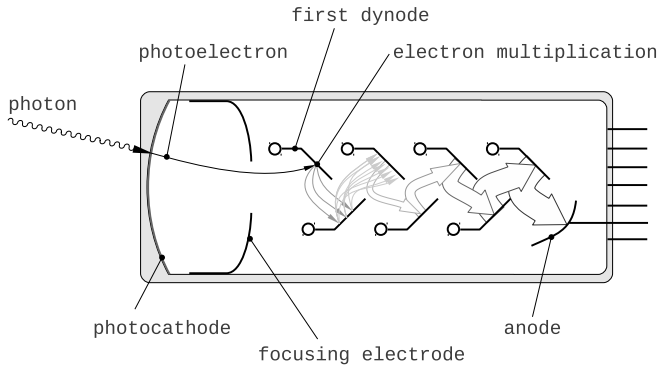

Figure 2.6: A diagram of the photomultiplier tube.

maximum kinetic energy (T) of photoelectrons, exiting the photocathode, is

$$T = E - E_w, \tag{2.2}$$

where E is the energy of incident photon and E_w the work function. The work function depends on the photocathode material and represents the low energy limit for detectable photons: only photons with energy higher than E_w (wavelength shorter than $2\pi\hbar c_0/E_w$) have a chance of leaving the photocathode. The photocathode material is usually a semiconductor, typically a compound of antimony and one or more alkali metals. For scintillation counting the most commonly used photocathode material is the so called Bialkali (Sb-Rb-Cs, Sb-K-Cs), sensitive up to wavelengths of about 700 nm.

The high energy (low wavelength) limit for detectable photons is determined by the transmittance of the entry window material. Figure 2.7 shows

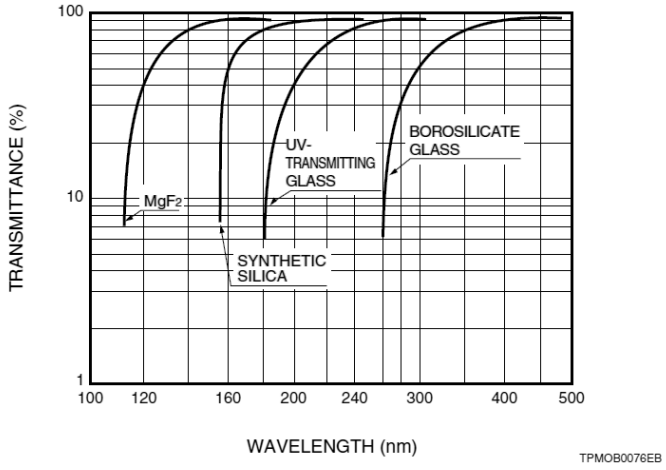

Figure 2.7: Wavelength dependence of transmission for various PMT window materials [11].

the wavelength dependence of transmittance for various window materials.

The most commonly used borosilicate glass has good transmission down to wavelengths of about 300 nm.

The probability of photoelectron emission for incident photons of wavelength λ is defined as the quantum efficiency (QE):

$$\mathrm{QE}(\lambda) = \frac{\text{number of photoelectrons released}}{\text{number of incident photons}(\lambda)}, \tag{2.3}$$

The QE for various photocathode materials is shown in Figure 2.8. The QE

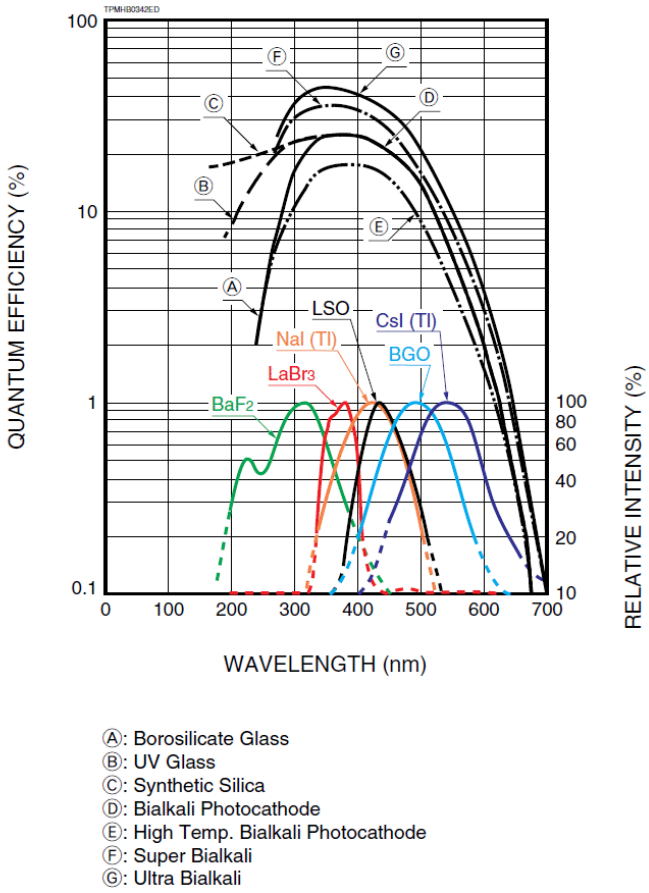

Figure 2.8: Quantum efficiency for various photocathode materials. Also shown are the emission spectra of common scintillators [12].

of bialkali photocathode has a peak of about 20% near emission wavelengths of commonly used scintillators.

After leaving the photocathode, the photoelectrons enter the electron focusing system, consisting of one or more focusing electrodes. These create an electric field which accelerates and guides the photoelectrons towards the electron multiplier section. Not all photoelectrons can be properly directed to the first multiplication stage, resulting in additional efficiency loss. The

fraction of photoelectrons, emitted from the photocathode, which can be multiplied effectively is called the collection efficiency (α) and is typically about 80%. The collection efficiency is important when considering the total photon detection efficiency (PDE) of a photodetector. For photomultiplier tubes, the photon detection efficiency is

$$\mathrm{PDE} = \mathrm{QE} \cdot \alpha. \tag{2.4}$$

The electron multiplier section is usually a chain of secondary emission electrodes (dynodes) with electric field applied between them. The photoelectron striking the first dynode causes an emission of secondary electrons. The average number of secondary electrons emitted per incident electron is called the secondary emission factor (δ) and depends on the energy of the incident electron. Typically $\delta = 3 - 6$ and the number of dynodes in the photomultiplier is $n = 10 - 14$, resulting in a total gain $G = \delta^n \approx 10^6 - 10^7$.

The charge produced in the multiplier section is finally collected by the anode and used for the output signal of the photomultiplier tube. In case of a pulsed light source, i.e. flashes from a scintillator, the charge of the output signal is proportional to the number of photoelectrons, produced by the light pulse. This means that a photomultiplier tube coupled to a scintillator provides a measurement of the energy of the particle, absorbed in the scintillator.

Another important parameter of photomultiplier performance is the time resolution. The main contribution to the time resolution comes from the variation in photoelectron travel time from the photocathode to the first dynode. The photoelectrons are collected from the whole photocathode surface and have to travel different distances before reaching the first dynode, depending on the geometry of the system. The electron focusing system can be optimized, so that photoelectrons produced at more distant points on the photocathode are traveling through higher electric field and are accelerated faster. However there are also variations in travel time caused by the differences in photoelectron emission energy and direction. This effect is called the transit time spread and can only be reduced by increasing the electric field between the photocathode and the multiplier section. Photomultiplier tubes, optimized for timing can reach timing resolutions of 100−200 ps [3].

2.3.3 PET Scanners

PET scanners are composed of a large number of position sensitive gamma detectors that surround the patient. In order to achieve a good position resolution, the scintillator crystals are cut in small pieces with a width of 3 to 5 mm. The thickness of the crystals is about 25 mm, so that a large fraction of coincident gammas are stopped. Individual crystals are rarely coupled to their own photodetector, instead a so called block detector is

used (Figure 2.9). In a block detector, many (usually four) larger PMTs are coupled to a large block of scintillator, which is finely segmented by cuts, not running through the whole thickness of the crystal. The depth of the cuts changes along the crystal side and allows the scintillation light produced in any of the crystal segments to spread across the four PMTs. The exact segment from which the light originates can than be determined by analyzing the ratios of light intensities, detected by the PMTs. With such arrangement a fine position resolution is achievable while using a smaller number of large PMTs, which is less expensive than using an appropriate number of smaller PMTs.

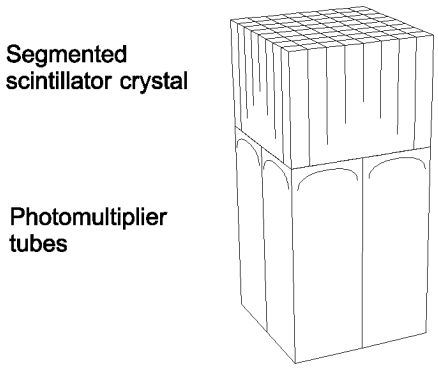

Figure 2.9: A schematic view of a block detector, in which four PMTs are coupled to a scintillator block segmented into 8×8 elements.

In a PET scanner, block detectors are typically arranged in rings. There are 18 to 32 rings in parallel, with an inner diameter of about 80 cm. Coincidences can be acquired only between detectors belonging to the same ring (called 2D acquisition) or between all detectors (3D acquisition). Acquisition in 3D mode has an advantage of much larger geometric efficiency, however it also introduces more background due to fake events. For the 2D acquisition lead shielding can be added between rings to reduce detection of such unwanted events.

2.4 Performance of PET Scanners

2.4.1 Position Resolution

The position resolution can be defined as the smallest distance between two points that can still be distinguished in the reconstructed image. A detector parameter, determining the position resolution is the size of the smallest position sensitive elements (scintillator crystal segments). For elements of width d, the position resolution (FWHM) in the middle of a detector pair is:

$$R_{det} = d/2. \tag{2.5}$$

As the source approaches either one of the detectors, the resolution degrades, reaching a resolution of d at the face of a detector.

Scintillator thickness also degrades the position resolution for events, not originating from the center of the scanner. In order to stop and detect as many 511 keV annihilation gammas as possible, the detector needs to have a certain thickness of the sensitive material. The information at which depth the gamma was absorbed is usually not available, leading to the so called depth-of-interaction (DOI) effect. For elements of width d and thickness x, the position resolution outside the ring center degrades to

$$d' = d \cdot cos\theta + x \cdot sin\theta, \tag{2.6}$$

where θ is the angle indicated in Figure 2.10. The position resolution is thus

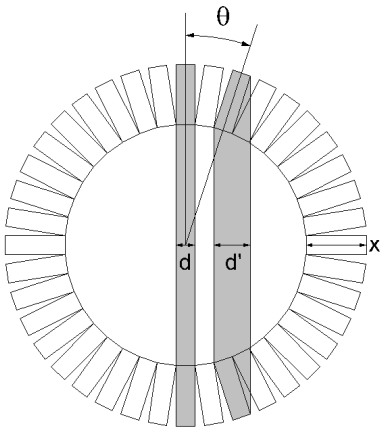

Figure 2.10: The depth-of-interaction effect, illustrated for a ring of gamma detectors.

degraded to

$$R'_{det} = d'/2 = (d/2)[cos\theta + (x/d)sin\theta]. \tag{2.7}$$

The position resolution also has intrinsic limitations, arising from β^+ decay and positron annihilation physics: the range traveled by the positron before annihilation and the non-collinearity of the resulting annihilation gammas.

The PET image is reconstructed from the positions of positron annihilations, which are not precisely the same as the positions of radionuclides, from which the positrons are emitted. Positrons are emitted in the β^+ decay with a continuous spectrum of energies, and lose energy over a highly unpredictable path, undergoing multiple large angle deflections. The distances traveled before stopping and annihilating thus have large variations. The positron range contribution to position resolution is best described by the

root mean square (r.m.s.) effective range, shown in Figure 2.11 in dependence of the maximum positron energy. For the ^{18}F positron source, the r.m.s. effective range is about 0.2 mm in water.

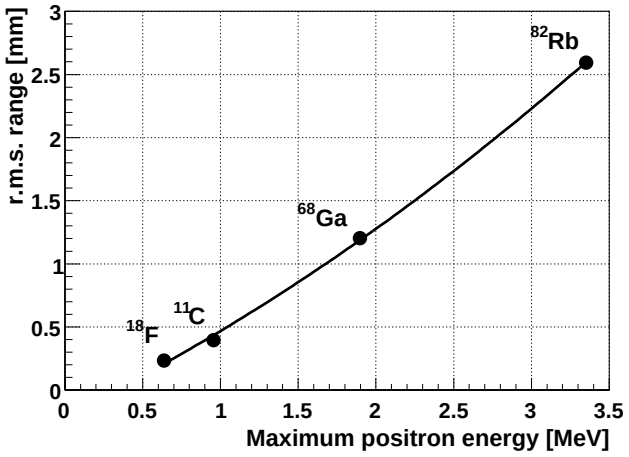

Figure 2.11: Maximum positron energy dependence of r.m.s. effective range for positrons in water. Adapted from [7].

The two annihilation gammas, which result from positron annihilation, are not emitted under an angle of precisely 180°, due to the residual kinetic energy carried by the positron into the annihilation process. The difference from perfect colinearity has an angular distribution with FWHM $\approx 0.5°$. This effect is called non-collinearity and degrades the PET position resolution with a contribution of [7]:

$$R_{180°} = 0.0022 \cdot D, \tag{2.8}$$

where D is the separation between detector elements (the diameter of PET ring).

The total position resolution of a PET system is obtained by combining the individual contributions:

$$R_{PET} \approx \sqrt{R_{det}^2 + R_{range}^2 + R_{180°}^2}, \tag{2.9}$$

where R_{range} is the r.m.s. effective range of positrons. For a typical PET scanner (d = 6 mm, D = 800 mm), using the ^{18}F positron source ($R_{range} \approx 0.2$ mm), the position resolution in the center of the scanner is

$$R_{PET} \approx \sqrt{(6/2)^2 + 0.2^2 + (0.0022 \cdot 800)^2}\ mm \approx 3.5 \text{ mm}.$$

The position resolution is degraded further by image reconstruction and noise reduction algorithms. This degradation depends on the number of counts recorded and the type of study conducted, but is usually a factor of 1.2 to 1.5 [6].

2.4.2 Sensitivity

The sensitivity of a PET system is defined as the fraction of coincidence annihilation gamma pairs emitted by the source ($N_{emitted}$), which is detected (N_{det}):

$$\eta = \frac{N_{det}}{N_{emitted}} = \epsilon^2 g_{PET} T_{body}. \tag{2.10}$$

Here, ϵ is the intrinsic efficiency of each gamma detector

$$\epsilon = \frac{\text{no. of detected gammas}}{\text{no. of gammas striking detector}}, \tag{2.11}$$

g_{PET} is the geometric efficiency of the PET system and T_{body} the fraction of source radiation, not attenuated in the body (object of PET study), determined by the linear attenuation coefficient (μ_B) and the thickness (D_B) of the body:

$$T_{body} = e^{-\mu_B D_B}. \tag{2.12}$$

The geometric efficiency is mainly determined by the fraction of solid angle, covered by the sensitive surfaces of gamma detectors. For a pair of gamma detectors with surface A_{det}, separated by a distance D, this is

$$\frac{\Omega}{4\pi} \approx \frac{A_{det}}{\pi D^2}. \tag{2.13}$$

Additional factors of 2 and 1/3 need to be included, accounting for the fact that a pair detectors is being used and that the geometric efficiency is not constant if the source is moved perpendicularly to the LOR [7]. This results in a two detector (back-to-back) geometric efficiency of

$$g_{BtB} \approx \frac{2A_{det}}{3\pi D^2}. \tag{2.14}$$

A complete ring of detectors, with diameter D and axial dimension h has a geometric efficiency of [7]:

$$g_{Ring} \approx \frac{h}{D}. \tag{2.15}$$

The intrinsic efficiency of gamma detectors is mainly determined by the efficiency of 511 keV gamma absorption and can be expressed as

$$\epsilon = f \cdot \left(1 - e^{-\mu_{511keV} \cdot x}\right), \tag{2.16}$$

where μ_{511keV} is the linear attenuation coefficient and x the thickness of the detector material. Factor f represents the fraction of events, where absorption of gamma results in a useful output signals from the detector. For a typical scintillation detectors, f is limited by the fraction of events, where incident gamma is fully absorbed in the scintillator and the detector energy

resolution, which determines the fraction of events, falling inside the window of accepted energies. Energy discrimination is often used for rejection of scattered events (Section 2.4.3).

The overall sensitivities of PET scanners range from 0.2%−0.5% for single ring systems and 2%−10% for multi-ring systems, allowing coincidences between rings.

2.4.3 Fake Events

So far, it has been presumed that all detected coincidences originate from the same β^+ decay and reach the detectors without any previous interactions (Figure 2.12a). Such events are called true coincidences and are the source of wanted information (signal) in the obtained images. In a real PET system, two other kinds of events happen, introducing an unwanted background: random and scatter coincidences, together called fake events.

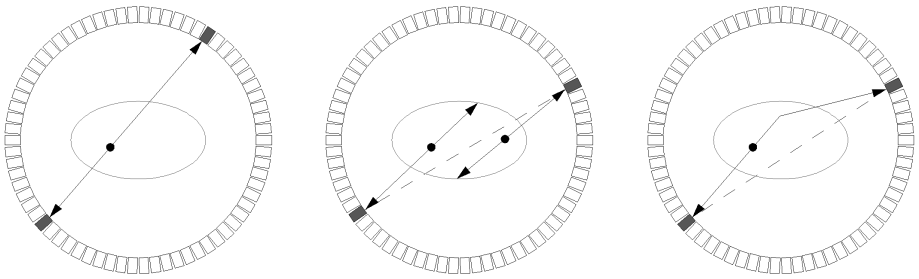

(a) True coincidence (b) Random coincidence (c) Scatter coincidence

Figure 2.12: Different types of events, contributing to PET measurements.

Random coincidences occur, when gammas from two different decays are detected within the coincidence time window and recorded as a single coincidence event. This leads to a LOR, which is not related to the true position of any β^+ decay (Figure 2.12b). Such coincidences can not be distinguished from true coincidences and result in image background. The rate of random coincidences is proportional to the coincidence time window (Δt_{coinc}) and the square of the total counting rate with an individual gamma detector (R_{single}):

$$R_{random} = \Delta t_{coinc} \cdot R_{single}^2 \tag{2.17}$$

The rate of random coincidences can be reduced by reducing the coincidence time window, but this has a lower limit imposed by the time resolution of the system and time-of-flight considerations. It also follows, that the rate of random to true coincidences increases with increasing activity of the source used in the study, since the random rate increases as the square of the true rate.

Background is also introduced due to scatter coincidences, which occur when both gammas detected originate from the same decay, but one or both of them are scattered before detection. The scattering can occur in the patient or in a part of the detector and can again significantly dislocate the measured LOR (Figure 2.12c). Since both gammas are produced in the same decay, the rate of scatter coincidences can not be reduced by narrowing of the coincidence time window. Also, the ratio of scatter to true coincidences is independent of the source activity, since the rate of both increases linearly with it. The effect of background due to scatter coincidences can be reduced by estimating the scatter rate from additional transmission scans (a study performed with a high activity source, located outside the patients body) or the reconstructed activity in small volume, laying just outside the patients body (where no source of true coincidences is expected).

The rejection of scatter coincidences is also possible by energy discrimination. The scattering of annihilation gammas happens through the Compton effect, where the gamma transfers some of its energy to an electron in the matter. A scattered gamma therefore has less energy which can be deposited in the detector. The scatter background can be suppressed, if only gammas, detected with an energy very close to 511 keV are accepted. However, not all incident gammas deposit their full energy in the detector, being Compton scattered in the detector itself. This means that also some true coincidences will be suppressed, which leads to a reduction in detection efficiency.

2.4.4 Image Contrast

The final goal of a PET study is an image, depicting the source distribution. It is important for the diagnostic value of the images that small abnormalities, for example a growing cancerous lesion, can be distinguished from normal tissue. A measure of image quality is the image contrast (C), which refers to the differences in intensities between parts of the image. It can be defined as the ratio of count rate change for an object of interest (tissue abnormality) relative to the count rates in the surrounding tissue:

$$C = \frac{\Delta R}{R_t} = \frac{R_o - R_t}{R_t}, \tag{2.18}$$

where R_o is the count rate at the location of the object of interest and R_t the count rate of the surrounding tissue. As can be seen in Figure 2.13, the contrast deteriorates further, when a uniform background counting rate of R_b is added:

$$C = \frac{(R_o + R_b) - (R_t + R_b)}{R_t + Rb} = \frac{\Delta R}{R_t}\left[\frac{1}{1 + (R_b/R_t)}\right]. \tag{2.19}$$

The tissue count rate R_t depends on the differences in levels of radiophar-

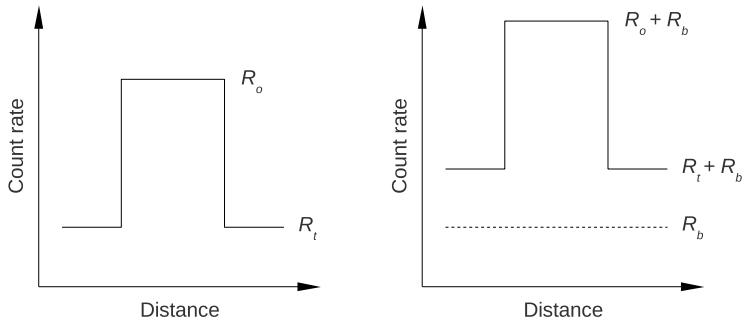

(a) (b)

Figure 2.13: An illustration of the effect a uniform background count rate has on image contrast [7].

maceutical uptake by different types of tissue and so depends on the specific radiopharmacutical, required for selected study. The background rate R_b is a result of fake events and artifacts introduced by the reconstruction algorithm.

Another important quantity is the contrast-to-noise ratio (CNR), which is defined as

$$\mathrm{CNR} = \frac{C_o}{C_b} = C_o\sqrt{N_b}, \tag{2.20}$$

where C_o is the contrast of the object of interest and C_b is the background noise contrast, which is related to the number of events recorded in the same area as the object of interest (N_b) as

$$C_b = \sigma_{N_b}/N_b = \sqrt{N_b}/N_b = 1/\sqrt{N_b}. \tag{2.21}$$

It has been shown that in order to be detectable, an objects CNR must be greater than 3−5 [7].

2.4.5 Signal-to-noise Ratio

Since the events forming the images obtained in nuclear medicine are a result of radioactive decay, which is a random process, the statistical variation of events in one image element (pixel) is a square root of number of recorded events per pixel (N_{pixel}):

$$\sigma_{pixel} = \sqrt{N_{pixel}}. \tag{2.22}$$

The signal-to-noise ratio (SNR) is then related to N_{pixel} as

$$\mathrm{SNR}_{pixel} = \frac{N_{pixel}}{\sigma_{pixel}} = \sqrt{N_{pixel}}. \tag{2.23}$$

This however, is not true in case of PET imaging, because of the reconstruction algorithms used to obtain the images. The SNR in reconstructed PET images can be expressed as [1]:

$$\mathrm{SNR}_{pixel} = k(N_{pixel})^{1/2}(n_{pixels})^{-1/4}, \tag{2.24}$$

where n_{pixels} is the total number of pixels in the reconstructed image and k is a factor connected to the reconstruction algorithm with a value of approximately 1.

To see how the SNR affects the detectability of an object, it has to be related to the CNR. For an object of interest occupying n_o pixels in the reconstructed image, the relation between SNR and CNR is [7]:

$$\mathrm{CNR}_o \approx C_o \cdot \sqrt{n_o} \cdot \overline{\mathrm{SNR}_{pixel}}, \tag{2.25}$$

where the SNR is averaged over pixels in the object.

2.5 Time-of-flight PET

In a time-of-flight PET system, additional information − the difference in arrival times of the two annihilation gammas − is recorded for each coincidence. Hypothetically, if a perfect TOF information were available, the location of the decay could be exactly determined as the point on the LOR, calculated from the measured TOF difference, and the reconstruction of the image would not be necessary. For a difference in arrival times Δt the distance from the source to the center of LOR is

$$\Delta x = \frac{c_0 \cdot \Delta t}{2}, \tag{2.26}$$

where c_0 is the speed of light. The same relation holds between the TOF measurement resolution δt and the position resolution δx, achieved from the TOF information:

$$\delta x = \frac{c_0 \cdot \delta t}{2}, \tag{2.27}$$

According to this equation, to achieve 1 cm resolution along LOR, a time resolution of about 66 ps would be required. In practice, the best timing resolutions achieved with PET systems are about 300 ps under ideal conditions [1, 2], limiting the position resolution to 4.5 cm. Clearly, such resolution is not precise enough and image reconstruction is still required. However, even such imperfect TOF information can still be used to improve the reconstructed image, by at least approximately localizing the coincidence.

In conventional PET reconstruction without TOF information, the source position is only limited to the LOR. Basically, the image is formed by incrementing each pixel value by an amount, proportional to the number of LORs

intersecting this pixel. This means that one event will contribute activity to all pixels along its LOR, not just the pixel, from which it originates. The mean contribution from other pixels can be removed by filtering, however the statistical fluctuations (noise) remain.

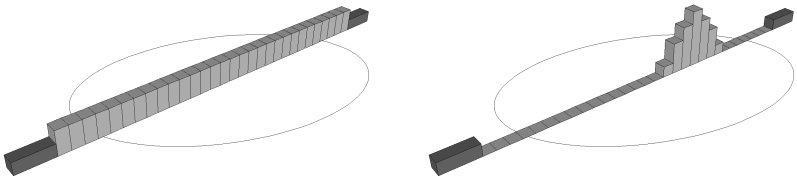

(a) non-TOF (b) TOF

Figure 2.14: An illustration demonstrating, why TOF information leads to reduction of noise: with TOF information only pixels, located near the correct location along the LOR are incremented.

With TOF information available, the coincidence can be localized near the correct pixel, according to the time resolution (Figure 2.14). One event therefore only contributes noise to a few neighboring pixels along the LOR, leading to an overall improvement in the SNR of the image.

The SNR improvement can be calculated by considering Equation (2.24), which states that SNR depends on the number of image pixels, and noting that TOF PET effectively reduces the number of pixels to n_{TOF}:

$$n_{TOF} \approx \pi \left(\frac{\delta x/2}{d} \right)^2 . \tag{2.28}$$

Here the area of TOF uncertainty is presumed to be a circular area of diameter δx, defined by the TOF resolution (Equation (2.26)), and d is the image resolution (pixel size). This leads to a TOF SNR of

$$\mathrm{SNR}_{TOF} = k(N_{pixel})^{1/2} \left(\pi \left(\frac{\delta x}{2d} \right)^2 \right)^{-1/4} . \tag{2.29}$$

If TOF resolution corresponding to the dimension of the object being imaged (D) is considered, Equation (2.29) becomes the SNR of non-TOF system:

$$\mathrm{SNR}_{non-TOF} = k(N_{pixel})^{1/2} \left(\pi \left(\frac{D}{2d} \right)^2 \right)^{-1/4} . \tag{2.30}$$

Therefore, the SNR improvement of TOF system compared to non-TOF system is

$$\frac{\mathrm{SNR}_{TOF}}{\mathrm{SNR}_{non-TOF}} = \sqrt{\frac{D}{\delta x}} = \sqrt{\frac{2D}{c_0 \delta t}}. \tag{2.31}$$

The gain in SNR translates to gain in contrast (Equation (2.25)) and therefore improves detectability of objects in reconstructed images.

Another important quantity describing the TOF PET improvement is the gain in relative sensitivity G_{TOF}:

$$\eta_{TOF} = G_{TOF} \cdot \eta_{non-TOF}, \tag{2.32}$$

where non-TOF PET sensitivity $\eta_{non-TOF}$ is defined in Equation (2.10). By noting that the SNR is proportional to the square root of number of events, the gain can be expressed as:

$$G_{TOF} = \frac{2D}{c_0 \delta t}. \tag{2.33}$$

The gain in sensitivity is a useful quantity, since it measures the reduction in the time of examination or injected dose of the radioactive compound, required to obtain images with the same diagnostic value. TOF PET provides the largest gains in sensitivity for larger parts of the body (i.e. a study of an organ inside the body, compared to a study of the brain) and heavier patients. Table 2.4 shows the calculated sensitivity gains for different TOF PET timing resolutions and three effective patient diameters (D), which can be used to represent patients weighing from 40 to 100 kg [13]. It can be seen

D [cm]	δt [ps]		
	300	600	1000
20	4.4	2.2	1.3
27	6.0	3.0	1.8
35	7.8	3.9	2.3

Table 2.4: Calculated sensitivity gains, for TOF PET with time resolution δt and different effective patient diameters (D).

that even a timing resolution of 1 ns can improve the sensitivity, especially in heavier patients.

The reduction in required statistics needed to reconstruct an image of the same quality is not the only benefit of TOF PET. Another improvement due to a good TOF information is that it also leads to faster and more stable convergence in the case of iterative reconstruction algorithms [13]. This is important in actual clinical practice, where the image should be available shortly after the examination.

2.5.1 Performance of TOF PET

As can be seen in Equation (2.33), the improvement achieved with TOF measurement depends on the TOF measurement resolution δt. However,

this information alone is not enough to compare the performance of scintillators with different gamma stopping powers. By considering the TOF PET sensitivity (Equation (2.32)), expressed as

$$\eta_{TOF} = G_{TOF} \cdot \epsilon^2 g_{PET} T_{body}, \tag{2.34}$$

the contributions from the scintillator can be summarized in a figure of merit (FOM):

$$\text{FOM} = \frac{\epsilon^2}{\delta t}. \tag{2.35}$$

The FOM summarizes the two most important quantities: the 511 keV gamma stopping power and the TOF resolution. Another factor influencing the FOM is the fraction of events, registered with full energy of the incident gamma (i.e. events, where gamma is not scattered outside the crystal, carrying away a portion of the initial 511 keV energy). This contribution is included as a factor f in Equation (2.16) and is approximately 0.5 to 0.8 for the scintillator materials considered here. It will be neglected in the following calculations of FOM.

Historically, the TOF resolution has been limited by the decay constant of the available scintillators. In this case, the TOF resolution can be expressed as [9, 3]

$$\delta t \propto \sqrt{\frac{\tau}{N_{phe}}}, \tag{2.36}$$

where N_{phe} is the number of photoelectrons produced in the PMT (i.e. the number of detected photons). This relation is no longer accurate for some of the recently developed scintillators, which feature a very short decay time and large light yield. For such scintillators the rise time of the scintillations [14] and the fluctuations of the photon transit time from the emission point to the photodetector [15, 16] become important factors limiting the time resolution. However, Equation (2.36) can be used to obtain the lower limit of the TOF resolution.

Scintillator	μ_{511keV} (cm^{-1})	τ (ns)	photons/MeV	ϵ^2	FOM (a.u.)
NaI(Tl)	0.35	230	38000	0.34	4.4
BGO	0.96	300	6000	0.83	3.7
BaF_2	0.44	0.6	2000	0.45	25.7
LSO	0.87	40	29000	0.79	21.1
$LaBr_3$(Ce)	0.43	17	58000	0.43	25.3

Table 2.5: TOF figure of merit for some scintillators. The coincidence detection efficiency (ϵ^2) is calculated for 25 mm thick scintillators.

Table 2.5 contains the FOM values, calculated from scintillator parameters in Table 2.3. The importance of gamma stopping power can be seen, by

considering FOM for $LaBr_3$ and LSO scintillators. Despite a shorter decay time and a higher light yield, $LaBr_3$ has approximately the same FOM as LSO, due to the difference in gamma attenuation length. On the other hand, the very fast decay time of the BaF_2 scintillator results in approximately the same FOM despite the poor gamma stopping power.

3 Use of Cherenkov radiation for PET

In traditional PET the 511 keV annihilation gammas are detected after some of their energy is transformed into photons of visible or near UV light in a scintillating material. Scintillators which produce as many photons per inbound annihilation gamma as possible are preferred, since higher photon statistics enables better energy resolution and therefore better separation of true events from scattered events. The time response of the scintillation process is a fundamental limiting factor for the time resolution of TOF PET measurement.

Another process which can be used to obtain photons of light from annihilation gammas is the Cherenkov radiation, which may be preferred for TOF PET measurements since Cherenkov photons are produced promptly, without delay due to the decay process. Cherenkov photons are produced by a moving charged particle, such as electrons produced by annihilation gamma interactions with a suitable radiator material, which would replace the scintillating crystal in PET gamma detector. However, not many Cherenkov photons are produced by 511 keV gamma interactions. Unlike in traditional PET, where hundreds or even thousands of scintillation photons are available for detection, only a few Cherenkov photons may reach the photodetector. This means that the efficiency of the method may be low and that there is no event energy information, which is available in the usual PET measurement.

The use of Cherenkov photons for TOF PET has already been investigated in [17], where silica aerogel was considered as a Cherenkov radiator. Aerogel can be produced with a unique refractive index range from 1.001 up to 1.2. A detector employing Cherenkov radiator with refractive index of about 1.2 would have the benefit of inherent rejection of scatter events, by only being sensitive to photeffect of 511 keV gammas, while the energy of electrons produced by Compton scattering would be below the Cherenkov threshold. However, despite a possibility of lead doping of aerogel, the density of aerogel and therefore detection efficiency is very low. The use of lead glass and crystals as Cherenkov radiators has been explored in [18]. A timing resolution of 170 ps FWHM was achieved in a basic experiment, and despite a low efficiency an improvement in the SNR of reconstructed images was achieved in simulation studies. In [16], the use of Cherenkov photons for TOF measurements was explored for non scintillating (undoped) and scintillating (Ce-doped) LuAG (lutetium aluminum garnet) crystals. A coincidence time resolution of 250 ps FWHM was achieved using a pair of small undoped crystals.

In this chapter all of the physical processes, important for production of Cherenkov photons from 511 keV gammas, are discussed. The requirements for a good Cherenkov radiator and some candidate materials are presented. Finally, the performance parameters of some Cherenkov radiators are calcu-

lated from simple estimations.

3.1 Cherenkov radiation

A charged particle emits a characteristic light, called the Cherenkov radiation, when it travels through a dielectric medium with a speed greater than the speed of light in that medium:

$$v > c_0/n, \tag{3.1}$$

where n is the refractive index of the medium. The velocity above which the charged particle emits Cherenkov radiation is called Cherenkov threshold velocity

$$v_{Thr} = c_0/n. \tag{3.2}$$

The charged particle locally polarizes the medium, producing electric dipoles along its path. The oscillations of dipoles result in the emission of electromagnetic radiation. In case of a particle velocity lower than c_0/n the contributions from all dipoles destructively interfere and no photons are emitted. When the particle velocity is greater than c_0/n, the dipoles remain trailing the particle in a way that results in constructive interference, or electromagnetic shock wave [19]. This shock wave is analogous to a sonic shock wave, created by a supersonic aircraft. Figure 3.1 illustrates the distribution of dipoles for the cases when the charged particle has velocity lower and grater than c_0/n. As can be seen in Figure 3.2, the electromagnetic shock wave trav-

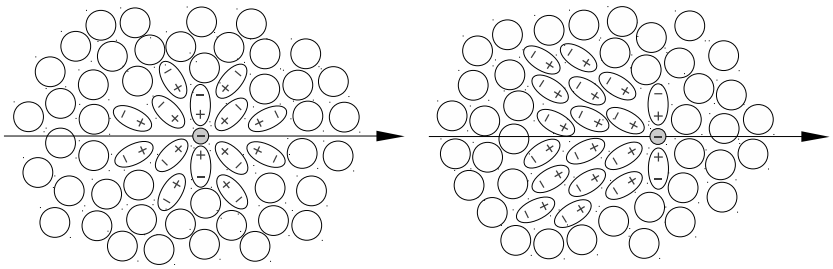

(a) $v < c_0/n$ (b) $v > c_0/n$

Figure 3.1: An illustration of Cherenkov radiation production mechanism.

els over a distance $c_0 t/n$ in the same time as the particle moves by $vt = \beta c_0 t$, where $\beta = v/c_0$. As a consequence, the Cherenkov photon emission angle relative to the particle direction (θ) is given by

$$cos\theta = \frac{1}{n\beta}. \tag{3.3}$$

The spectrum of Cherenkov radiation can be obtained from the Frank-Tamm relation [19]:

$$\frac{d^2N}{dEdl} = \left(\frac{z^2 e_0^2}{4\pi\varepsilon_0 \hbar^2 c_0^2}\right) sin^2\theta. \tag{3.4}$$

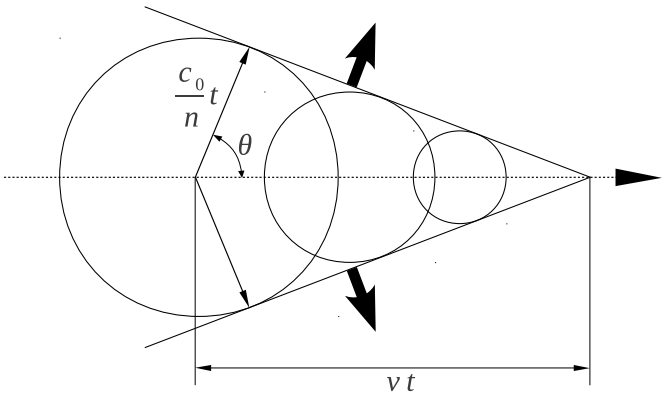

Figure 3.2: An electromagnetic shockwave, resulting from Cherenkov radiation.

Here dN is the number of Cherenkov photons produced in the energy interval between E and $E + dE$, as the particle travels a path of length dl in the medium and ze_0 is the charge of the moving particle. Combining this equation with Equation (3.3) gives the spectral dependence

$$\frac{d^2N}{dEdl} = \left(\frac{z^2\alpha}{\hbar c_0}\right)\left[1 - \left(\frac{1}{n(E)\beta}\right)^2\right], \tag{3.5}$$

where $\alpha = \frac{e_0^2}{4\pi\varepsilon_0\hbar c_0} \approx \frac{1}{137}$ is the fine structure constant. For particles with unit charge, Equation (3.5) can be written as

$$\frac{d^2N}{dEdl} \approx \left(\frac{370}{eV\,cm}\right)\left[1 - \left(\frac{1}{n(E)\beta}\right)^2\right]. \tag{3.6}$$

It follows from Equations (3.5) and (3.6) that at a certain refractive index, the number of Cherenkov photons is uniform over the photon energies, i.e. $dN/dE = \text{const}$. This means that in the wavelength scale the Cherenkov photons are distributed as

$$\frac{dN}{d\lambda} \propto \frac{1}{\lambda^2} \tag{3.7}$$

and are produced in largest numbers in the wavelength range of blue and UV light.

3.2 The interaction of gammas with matter

Gammas interact with matter in three main processes:

- photoelectric effect,

- compton scattering,
- pair production.

Which interaction will be dominant depends on the atomic number of absorbing material Z and gamma energy E_γ (Figure 3.3).

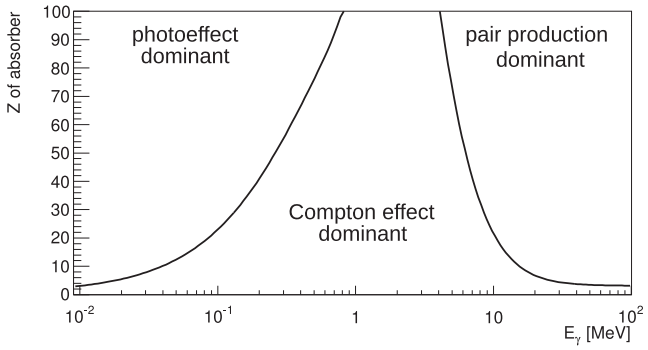

Figure 3.3: Modes of gamma interactions with matter: photoeffect, Compton scattering and pair production. Solid lines represent the borders, where the probabilities for two neighboring modes are equal [20].

3.2.1 Photoelectric Effect

The main mode of interaction at lower energies is the photoelectric absorption (photoeffect). Here a gamma strikes one of the electrons in the absorber, transfers its energy to this electron and is absorbed in the process. The photoelectric effect needs to occur on bound electrons, so that the atomic nucleus absorbs the recoil momentum and thus satisfies the momentum conservation. The energy dependence of the cross section for photoeffect is quite complicated for gamma energies comparable to the binding energies of the electrons, as can be seen in Figure 3.4 in case of the lead absorber. For gamma energies above the highest electron binding energy, the cross section is proportional to

$$Z^n / {E_\gamma}^3, \tag{3.8}$$

where $n \approx 4 - 5$ [22]. The energy of the ejected electron T is

$$T = E_\gamma - E_B, \tag{3.9}$$

where E_B is the binding energy of the electron. In case of lead, the K shell electron binding energy is 88.005 keV [23].

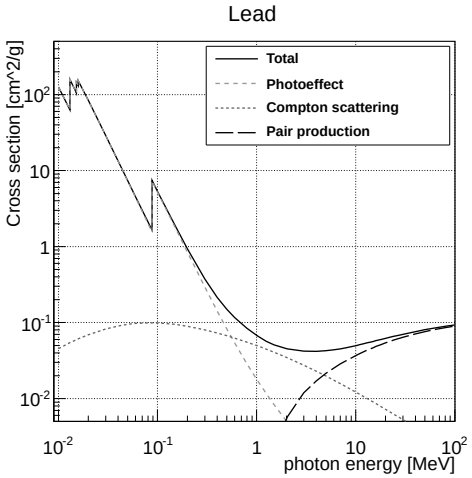

Figure 3.4: Total, photoeffect, Compton scattering and pair production gamma absorption cross sections for lead [21]. Visible is the K-edge at 88 keV and L-edges at lower energies.

3.2.2 Compton Scattering

For intermediate photon energies the dominant mode is the Compton scattering, where the gamma loses only part of its energy by scattering on an electron. The incident gamma is not absorbed but continues its path with reduced energy under certain scattering angle. The cross section is proportional to

$$Z/E_\gamma. \tag{3.10}$$

The Compton scattering process is illustrated in Figure 3.5. The gamma

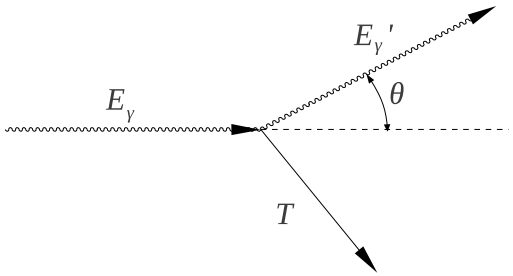

Figure 3.5: Kinematics of Compton scattering.

energy after scattering E'_γ and the scattering angle θ are related to the initial gamma energy:

$$E'_\gamma = \frac{E_\gamma}{1 + \frac{E_\gamma}{m_e c_0^2}(1 - cos\theta)}. \tag{3.11}$$

The energy carried away by the electron is

$$T = E_\gamma - E'_\gamma = E_\gamma \left(\frac{\frac{E_\gamma}{m_e c_0^2}(1 - cos\theta)}{1 + \frac{E_\gamma}{m_e c_0^2}(1 - cos\theta)} \right). \tag{3.12}$$

It follows from Equation (3.12) that the maximum possible energy of the Compton scattered electrons (Compton edge) is

$$T = E_\gamma \left(\frac{2\frac{E_\gamma}{m_e c_0^2}}{1 + 2\frac{E_\gamma}{m_e c_0^2}} \right) \tag{3.13}$$

in the case of backscattered electrons ($\theta = 180°$).

The energy distribution of scattered electrons is given by [22]:

$$\frac{d\sigma}{dT} = \frac{\pi r_e^2}{m_e c_0^2} \frac{1}{g^2} \left[2 + \frac{s^2}{g^2(1-s)^2} + \frac{s}{1-s} \left(s - \frac{2}{g} \right) \right], \tag{3.14}$$

where $g = E_\gamma / m_e c_0^2$ and $s = T/E_\gamma$. Shown in Figure 3.6 are the energy distributions for three incident gamma energies.

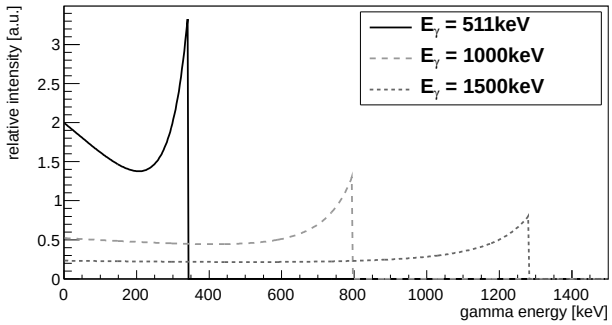

Figure 3.6: Energy distributions of electrons, produced by the Compton scattering of gammas with three different initial energies.

3.2.3 Pair Production

If the energy of incident gamma is higher than 1.022 MeV (double the rest mass of an electron), it can produce an e^+e^- pair near the atomic nucleus. For gamma energies below the threshold this process is not possible, as is the case for 511 keV annihilation gammas.

3.2.4 Gamma stopping power

The gamma stopping power of a material can be expressed as the linear attenuation coefficient μ_l of the material. It can be calculated from the total cross section per atom

$$\sigma = \sigma_{photoeffect} + Z\sigma_{Compton} + \sigma_{Pairproduction} \tag{3.15}$$

multiplied by the density ρ or the density of atoms, depending on units of the cross section:

$$\mu_l = \rho\sigma \left[\frac{\mathrm{cm}^2}{\mathrm{g}}\right] = \left(\frac{N_a\rho}{A}\right)\sigma \left[\frac{\mathrm{barn}}{\mathrm{atom}}\right]. \tag{3.16}$$

Here N_a is the Avogadro's number and A the atomic weight of absorber. The total cross section per atom in case of lead absorber is shown in Figure 3.4, together with individual contributions. With the linear attenuation coefficient, the fraction of gammas absorbed in an absorber of thickness x can be calculated from

$$1 - \frac{I(x)}{I_0} = 1 - e^{-\mu_l x}, \tag{3.17}$$

where I_0 is the incident and $I(x)$ the surviving gamma beam intensity.

3.3 The interaction of electrons with matter

Unlike heavier particles, electrons with high enough energy lose most of their energy through Bremsstrahlung - the emission of electromagnetic radiation arising from scattering in the electric field of a nucleus. In lead, Bremsstrahlung becomes the dominant mode of energy loss for electrons with energies above approximately 10 MeV [22].

At energies below 1 MeV Bremsstrahlung can be neglected and the main mode of energy loss become the inelastic collisions with the atomic electrons (ionization loss). The energy loss can be calculated from the Bethe-Bloch formula, modified for electrons [22]:

$$-\frac{dE}{dx} = 2\pi N_a r_e^2 m_e c_0^2 \rho \frac{Z}{A}\frac{1}{\beta^2}\left[ln\frac{\tau^2(\tau+2)}{2(I/m_e c_0^2)^2} + F(\tau) - \delta - 2\frac{C}{Z}\right], \tag{3.18}$$

where:

- $2\pi N_a r_e^2 m_e c_0^2 = 0.1535$ MeV cm^2/g,
- ρ, Z, A are the density, atomic number and atomic weight of the absorbing material,
- $\tau = E/m_e c_0^2$,

- I is the mean excitation potential,
- $F(\tau) = 1 - \beta^2 + \frac{\tau^2/8 - (2\tau+1)ln2}{(\tau+1)^2}$,
- δ and C are the density and shell corrections.

Besides inelastic collisions electrons also undergo repeated elastic Coulomb scatterings. The path of the electron is therefore very unpredictable and is hard to treat theoretically. However Monte-Carlo simulations can be used to obtain a statistical prediction concerning the electron scattering.

3.4 Cherenkov radiators for annihilation gammas

3.4.1 Requirements

To detect 511 kev annihilation gammas through Cherenkov photons, the gammas must first transfer their energy to electrons in a suitable radiator material. The electrons should be produced with the highest energy possible, so that as they lose their energy through multiple scatterings in the radiator they remain above the Cherenkov threshold velocity for as long as possible. This will increase the number of Cherenkov photons produced. Photoelectric effect of the 511 keV gammas is preferred since the electron receives more energy than it does in the case of Compton scattering. The cross section for photoeffect increases with the atomic number of the material (Figure 3.3), so radiators with high Z are preferred. High Z is also beneficial in terms of the gamma stopping power. However, higher Z of the material also results in a smaller range of electrons. This shortcoming is most likely outweighed by all the benefits of high Z.

Cherenkov radiator must also have good optical properties. Its refractive index should be high, so that the Cherenkov threshold is low. It also has to have good optical transmission for Cherenkov photons, which are produced in the range of visible and near-UV wavelengths, so that the photons can be propagated from the radiator to the photon detector.

In short, the most important requirements for a good Cherenkov radiator for detection of gammas are:

- high atomic number (density),
- high enough index of refraction,
- good optical transmission for visible to near-UV light.

3.4.2 Radiator candidates

Most obvious candidates for Cherenkov radiators would be optically transparent materials with high lead content, such as lead glass. Glasses with

high lead content are used where radiation shielding is required, for example in a room containing a medical X-ray device. Another option are Cherenkov radiators, developed for experiments in high energy physics, such as lead fluoride (PbF_2) and lead tungstate ($PbWO_4$).

Properties of lead glass with two different concentrations of lead, PbF_2 and $PbWO_4$ are summarized in Table 3.1, where the optical transmission cutoff wavelength (λ_{cutoff}) is defined as the lowest wavelength at which the material is still transparent. The wavelength dependences of refractive index

	Glass(57% Pb)	Glass(72% Pb)	PbF_2	$PbWO_4$
n	1.7	1.8	1.8	2.3
ρ (g/cm^3)	4.07	5.2	7.77	8.28
T_{Thr} (keV)	121	104	104	56
λ_{cutoff} (nm)	370	380	250	350
Scintillation L.Y. (ph./MeV)	-	-	-	200
Scintillation τ (ns)	-	-	-	6/30
Scintillation λ_{max} (nm)	-	-	-	440/530

Table 3.1: Properties of Cherenkov radiator candidates: index of refraction (n), density (ρ), Cherenkov threshold for electrons expressed as their kinetic energy (T_{Thr}), optical transmission cutoff wavelength (λ_{cutoff}) and scintillation properties - scintillation light yield, decay time (τ) and emission peaks (λ_{max}) (only $PbWO_4$ has notable scintillations) [18, 24, 25, 26, 27, 28, 29].

and optical transmission for lead fluoride and for lead tungstate are shown in Figure 3.7, where the refractive index was calculated by using the Sellmeier law:

$$n^2 - 1 = \sum_i \frac{n_{s_i}^2}{1 - \frac{\lambda_{s_i}^2}{\lambda^2}}. \tag{3.19}$$

The values for parameters n_{s_i} and λ_{s_i} can be found in the literature [30].

The Equation (3.19) fits to measured values ([26, 29]) sufficiently well if only the first two terms ($i = 0, 1$) are used. The parameters of the first two terms for PbF_2 and $PbWO_4$ are listed in Table 3.2.

	n_{s_0}	λ_{s_0} [nm]	n_{s_1}	λ_{s_1} [nm]
PbF_2 refractive index	0.8183	0	1.144	171.4
$PbWO_4$ ordinary index	1.5914	0	1.092	270.3
$PbWO_4$ extraordinary index	1.6683	0	0.859	266.6

Table 3.2: Parameters for the first two terms of Sellmeier law for PbF_2 and $PbWO_4$ [30, 31].

The lead tungstate crystal appears as the most promising candidate in terms of density and index of refraction. However, lead fluoride has a much lower optical transmission cutoff and is scintillation free. Its price is also lower

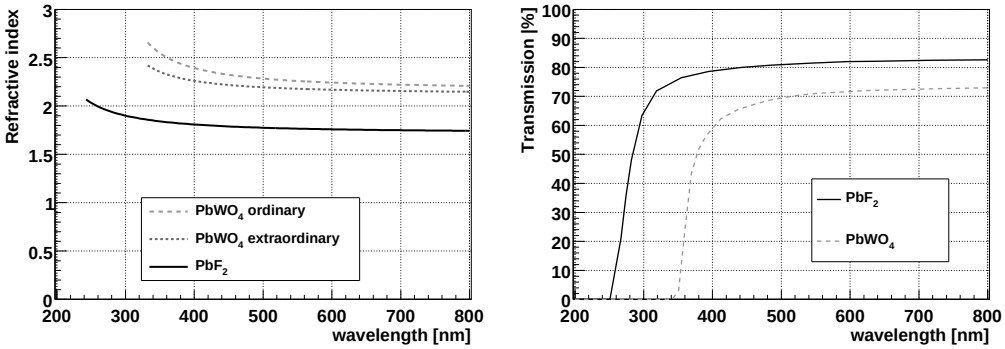

(a) Refractive index (b) Optical transmission

Figure 3.7: Wavelength dependence of refractive index and optical transmission of PbF_2 and $PbWO_4$. The optical transmission was measured for 185 mm thick sample of PbF_2 [25] and 220 mm thick sample of $PbWO_4$ [28]. It includes reflective losses at the two crystal/air boundaries.

than that of lead tungstate and of the scintillators commonly used for PET. Lead glass is a viable Cherenkov radiator, as demonstrated in [18]. However this work concentrates on studies with the PbF_2 and $PbWO_4$ crystals, since they are more appropriate for this application and are both commercially available.

3.5 Estimation of radiator performance

3.5.1 Absorption of annihilation gammas

In PET systems the first function of the Cherenkov radiator is to stop annihilation gammas and convert them to electrons. If we take the total cross section for 511 keV gammas to be 0.136 cm^2/g in PbF_2 and 0.130 cm^2/g in $PbWO_4$ [21], the attenuation coefficients can be calculated from Equation (3.16) to be $\mu_l = 1.06\ cm^{-1}$ for PbF_2 and $\mu_l = 1.08\ cm^{-1}$ for $PbWO_4$. For comparison, in lead the attenuation coefficient is $\mu_l = 1.7\ cm^{-1}$. Table 3.3 lists the fraction of absorbed gammas, obtained from Equation (3.17) for different thicknesses of the PbF_2 radiator. The values for $PbWO_4$ are almost identical. It can be seen that a PbF_2 crystal of 15 mm thickness already absorbs most (about 80%) of incident annihilation gammas and is a slightly better absorber than BGO, the most commonly used scintillator in PET.

3.5.2 Electron production

Once the annihilation gamma interacts with the radiator material, an electron is produced either via photoeffect of by Compton scattering. Electrons

d [mm]	Absorption [%]	
	PbF_2	BGO
5	41.1	38.1
7.5	54.8	51.3
10	65.4	61.7
15	79.6	76.3
20	88.0	85.3
25	92.9	90.9
30	95.8	94.4

Table 3.3: The fraction of absorbed 511 keV gammas for different thicknesses of PbF_2 Cherenkov radiator and BGO scintillator.

produced via photoeffect in PbF_2 will have an initial energy of 423 keV (Equation (3.9)), while electrons produced via Compton scattering will have a continuous energy distribution with an upper cut (Compton edge) at 341 keV (Figure 3.6 and Equation 3.13). This means that some Compton electrons will travel a fraction of their path with energy above the threshold of Cherenkov photon production (104 keV in PbF_2), but because this path will be shorter, they will produce less Cherenkov photons than electrons produced via photoeffect. As can be seen in Figure 3.8, the Compton scattering cross section for 511 keV gammas is only slightly larger than the cross section for photoeffect, in both PbF_2 and $PbWO_4$.

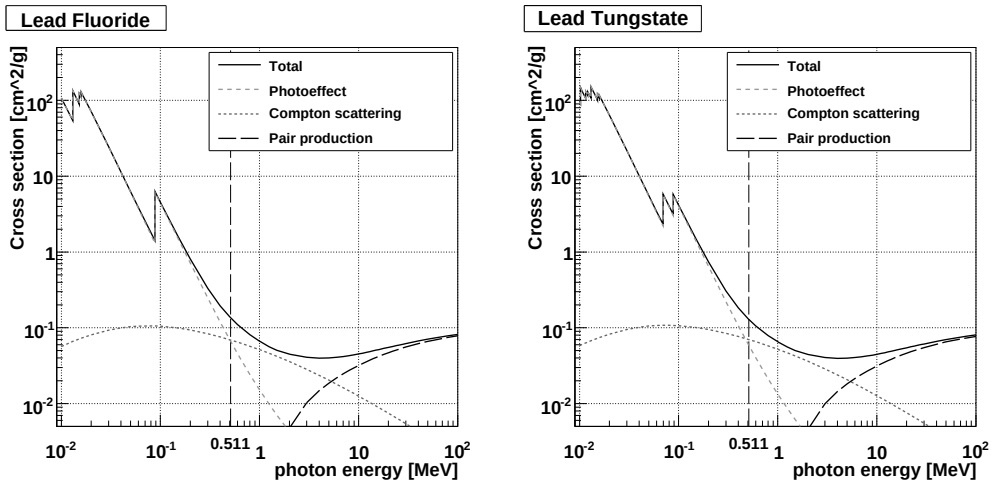

Figure 3.8: Gamma absorption cross sections for PbF_2 (left) and $PbWO_4$ (right) [21].

3.5.3 Cherenkov photon production

The electron will scatter unpredictably as it slows down in the radiator material, however for the number of Cherenkov photons produced, only

the range of electron is important. This can be estimated from Equation (3.18). The energy loss for electrons with energy of 423 keV (the maximum initial electron energy available from annihilation gammas) in Pb is $-dE/dx = 12.6$ MeV/cm. This number is obtained with the following values of parameters in Equation (3.18) [22]:

- $\rho = 11.4$ g/cm^3, $Z = 82$ and $A = 207.2$,
- $I = 823$ keV,
- $\delta = 0$ and $C = -6.2$.

Assuming a constant energy loss

$$E(l) = E_0 - \left(\frac{dE}{dx}\right) l, \tag{3.20}$$

the electron will stop after traveling approximately 0.3 mm. This simple estimate obtained for lead is in good agreement with a value for electron range in PbF_2 of 0.32 mm for 423 keV gammas, obtained from [32].

Again assuming a constant energy loss, the electron will fall below the Cherenkov threshold for PbF_2 after traveling approximately 0.25 mm.

The number of produced Cherenkov photons can than be roughly estimated (Equation (3.6)), by assuming constant electron velocity and no dispersion:

$$N \approx \left(\frac{370}{eVcm}\right) \Delta E L \left[1 - \left(\frac{1}{n\beta}\right)^2\right],$$

where ΔE is the Cherenkov photon energy interval and L the length of electron path, before it falls below the Cherenkov threshold. Photodetectors are typically sensitive in the 250−800 nm (1.55−4.96 eV) range, meaning $\Delta E \approx 3.4$ eV. The estimated number of detectable Cherenkov photons produced by an electron with the initial energy of 423 keV in PbF_2 is then

$$N \approx \frac{370}{eVcm} 3.4\ eV \cdot 0.25\ mm \left[1 - \left(\frac{1}{1.8 \cdot 0.84}\right)^2\right] = 17.7.$$

A more precise calculation, taking into account the electron deceleration (Equation (3.20)) and optical dispersion (Equation (3.19)) yields $N = 13.7$. This number is of course lower for electrons produced via Compton scattering, which have lower initial energy.

Because of the unpredictable nature of electron scattering, no preferred direction can be expected for the emission of Cherenkov photons. Produce Cherenkov photons will most likely have almost an isotropic angular distribution. It is also worth noting here, that according to Equation (3.20) an electron with an initial energy of 423 keV will fall below the Cherenkov threshold for PbF_2 in about 1 ps. This means that after the gamma interaction, the Cherenkov photon production will be practically instantaneous.

3.5.4 Cherenkov photon detection

Despite nearly instantaneous production of Cherenkov photons, their detection time will fluctuate due to the variations in path length between photon production location in the radiator and the photodetector. This variations are made worse by the large refractive index of the dense Cherenkov radiators considered here (photons in the radiator are slowed to a velocity c_0/n).

The simplest estimate of Cherenkov photon travel time variations can be obtained, if two extreme cases are considered. In the first case, the annihilation gamma interacts with the radiator as soon as it enters, meaning that the Cherenkov photon , produced by the interaction, needs to travel the whole thickness of the radiator before it reaches the exit surface, coupled to the photodetector (Figure 3.9a). In the second case, the annihilation gamma interacts at the end of the crystal and the Cherenkov photon exits the crystal almost immediately (Figure 3.9b). If the radiator used is the PbF_2 crystal

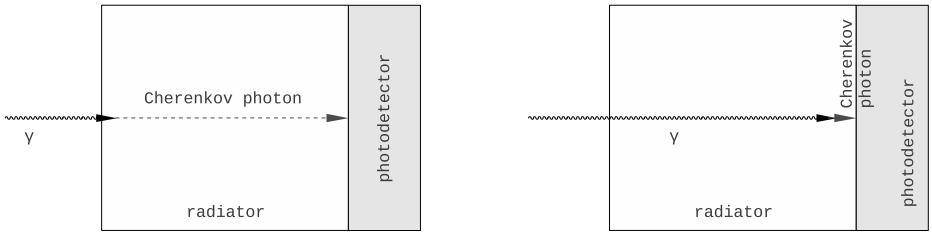

(a) (b)

Figure 3.9: Two cases of Cherenkov photon production events, resulting in a large difference in detection times.

of 15 mm thickness, the Cherenkov photon in the first case reaches the exit surface after

$$t_1 = \frac{d}{c_0/n} = \frac{15 \text{ mm}}{c_0/1.8} = 90 \text{ ps},$$

and in the second case in

$$t_2 = \frac{d}{c_0} = \frac{15 \text{ mm}}{c_0} = 50 \text{ ps}.$$

This means that the difference in detection time can be $\Delta t = 40$ ps, even in this simple case, which does not consider:

- photons traveling to the exit surface under an angle, which increases their path length,
- photons, reaching the exit surface after one or more total internal reflections from the other surfaces of the radiator, which can have the path length a couple of times longer that the one considered,

- the case of reflective wrapping of the radiator, where the photons which leave the crystal can reflect back inside from the wrapping, possibly reaching the photodetector after many reflections,
- photons emitted under certain angles, which can even become trapped inside the radiator, totally internally reflecting until they are scattered on an imperfection and possibly detected with a very large time delay.

It is evident that for the best timing resolution, the radiator dimensions need to be small. It is also beneficial if reflections are suppressed, by not using reflective wrapping and by reducing total internal reflections. This could be achieved by covering the radiator with a material, which has a high index of refraction and absorbs the photons that refract out of the radiator. All of this will of course reduce the total number of Cherenkov photons reaching the photodetector.

The number of Cherenkov photons available for detection is further limited by the total internal reflections on the exit surface of the radiator. The only photons that can exit the radiator in the direction of the photodetector are the ones reaching the exit surface under an angle, relative to the surface normal smaller than the critical angle of total internal reflection

$$\theta_0 = arcsin\left(\frac{n_o}{n}\right), \tag{3.21}$$

where n is the refractive index of the radiator and n_o the refractive index of the material outside of it. If we assume that N Cherenkov photons are produced with an isotropic angular distribution, the number of photons exiting the crystal without reflections (N_{exit}) will be determined by the solid angle, defined by θ_0:

$$\frac{N_{exit}}{N} = \frac{\int_0^{2\pi} d\phi \int_0^{\theta_0} sin\theta d\theta}{4\pi} = \frac{1}{2}\left(1 - cos\theta_0\right). \tag{3.22}$$

Typically the entrance window of the photodetector has a refractive index of about 1.5, and a silicon compound with a similar refractive index is used to couple the crystal and the photodetector. For PbF_2 (n=1.8) and for $PbWO_4$ (n=2.3) this means

$$\theta_0 = \begin{cases} 56.4^\circ & PbF_2 \\ 40.7^\circ & PbWO_4 \end{cases} \quad \text{and} \quad \frac{N_{exit}}{N} = \begin{cases} 0.22 & PbF_2 \\ 0.12 & PbWO_4 \end{cases}.$$

By taking $N = 13.7$ (Section 3.5.3) only

$$N_{exit} = \begin{cases} 3.1 & PbF_2 \\ 1.7 & PbWO_4 \end{cases}$$

direct photons on average exit the radiator and enter the photodetector, where they have a chance of being detected.

The probability of detecting a photon incident on the photodetector is determined by the photon detection efficiency (Equation (2.4)). The typical PDE of photomultipliers, averaged over the energies of available Cherenkov photons, is approximately 5%. Considering this, the number of photons detected will not be a measure of detector quality as is usual in PET with scintillators, but will be a fundamental limit for the efficiency of the whole detector. With only a very small number of Cherenkov photons produced, a trade off will have to be made between the time resolution (only photons, reaching the photodetector without reflections are used) and efficiency (also photons with larger travel time fluctuations are used).

4 Experimental setup

In order to experimentally verify the feasibility of TOF PET based on Cherenkov light, a setup consisting of two gamma detectors, operating on the principles of Cherenkov light detection, was constructed (Figure 4.1 and 4.2). The gamma detectors were based on the microchannel plate photomultipliers with excellent timing. Different Cherenkov radiators were coupled to the MCP PMTs and the performance of such detectors was tested by placing a ^{22}Na β^+ radioactive source between the two detectors. The mechanical support and coupling of the Cherenkov radiators to MCP PMTs was achieved with the use of a plastic frame, which supported the weight of the radiator, while being fully open in the direction of the radioactive source as can be seen in Figure 4.2. The distance between the two detectors was 200 mm, measured from one MCP PMT entry surfaces to the other.

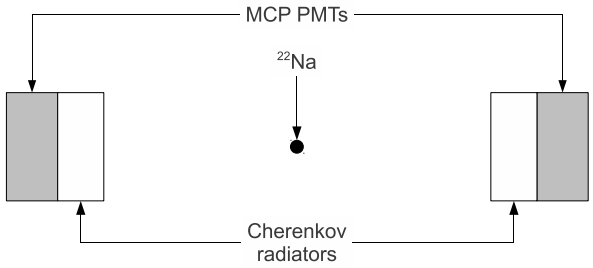

Figure 4.1: Schematic view of the back-to-back setup.

4.1 Microchannel plate photomultiplier

The microchannel plate photomultiplier is different from the usual photomultiplier in the way it achieves the charge amplification. Instead of the usual dynode chain, it uses one or more of the microchannel plates. The microchannel plate is a thin plate of glass (a few 100 μm thick), perforated with a large number of microscopic channels, which are typically 10$-$100 μm in diameter (Figure 4.3). The channels are oriented at a slight angle relative to the plate surface (typically about 15°). Their surfaces are coated with a semiconductor material which functions as the secondary electron emitter, similarly to the dynodes in the usual photomultiplier tubes. The flat surfaces of the microchannel plates are coated with metal, so that a potential difference can be applied along the channels.

The photoelectrons are accelerated from the photocathode towards the microchannel plate, where they may enter one of the channels and strike the channel wall. This results in emission of secondary electrons, which are accelerated by the electric field along the channel. Before hitting the

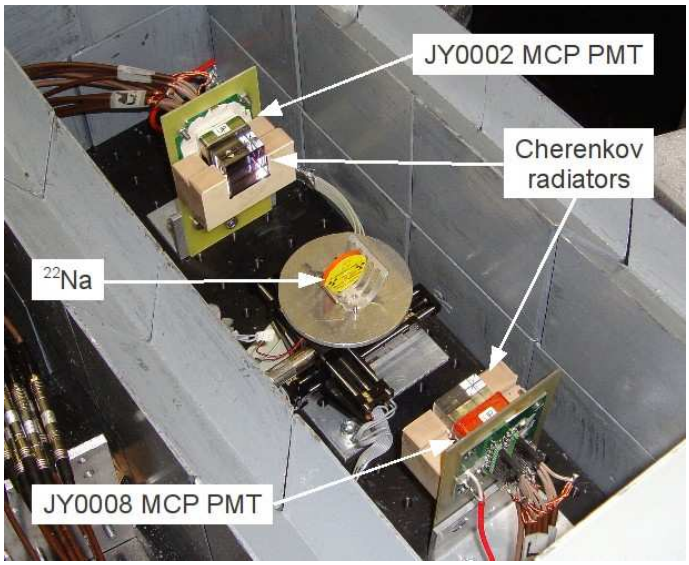

Figure 4.2: The back-to-back setup used in the experiments. The Cherenkov radiators in the picture are bare, 15 mm thick PbF_2 crystals. Also visible is the lead radiation shielding which is surrounding the source and the detectors.

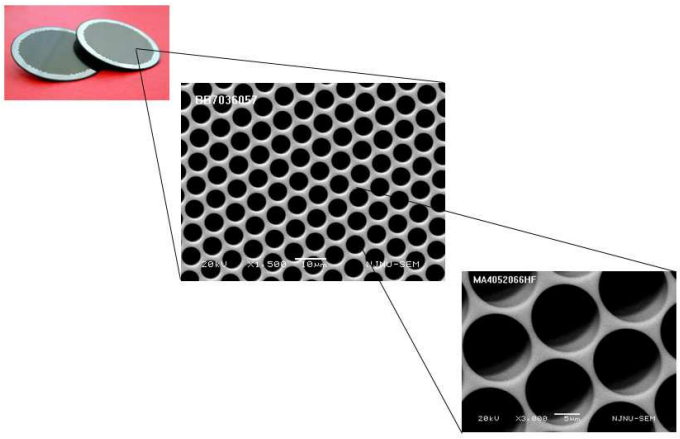

Figure 4.3: A picure of a microchannel plate with magnified views of the microchannel structure [33].

wall again, some of the secondary electrons gain enough energy to cause emission of more than one new electron, thus achieving the next stage of multiplication. A cascade of such secondary electron emissions results in a continuous charge multiplication along the channel.

A single microchannel plate has a multiplication factor of 10^3-10^4. Larger multiplication factors can be achieved by layering two or three plates. One common geometry is the so called chevron configuration, where two plates are cascaded with the channels of the two plates oriented in the opposite direction (Figure 4.4). Such configuration can achieve multiplication factors of 10^5-10^7, comparable to the amplification of the dynode chains used in conventional photomultipliers.

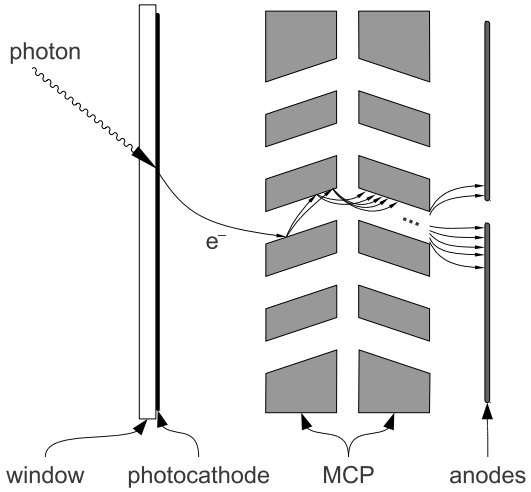

Figure 4.4: Schematic view (not to scale) of the chevron configuration and the operational principles of the microchannel plate photomultipliers. Visible is the charge sharing effect between the two anodes shown.

The main advantage of MCP PMTs is their excellent timing resolution. Since all of the amplification happens over very small distances, the possible variations in the time required for amplification are small. Also helpful is the fact that a planar photocathode geometry, preferred for coupling to the scintillators, will not result in increased transit time spread − photoelectrons produced at all points on the photocathode have the same distance to travel to the flat microchannel plate. The main remaining contribution to the timing resolution are the differences in photoelectron emission energy and direction, which still permit an excellent timing resolution of $\sigma < 30$ ps [4, 5].

However, an additional degradation of timing is caused by a small fraction of events which are detected with significant time delay due to photoelectron backscattering from the MCP surface. A photoelectron, which misses one of

the microchannels and hits the metallic surface of the MCP, can be backscattered. It is than accelerated by the electric field back to the MCP, where it can enter a microchannel and cause the charge amplification as a normal event. Such events are detected with time delays up to about 1 ns [4], causing a tail in the distribution of detection time.

Another drawback of multichannel MCP PMTs, also described in [4], is the crosstalk between the anode pads, resulting in fake signals which are most prominent on the pads neighboring a pad which received a true event. This occurs for two reasons, the first being that when an electron is amplified in a microchannel near the boundary between two pads, a fraction of amplified charge drifts over the boundary and is collected on the neighboring pad (charge sharing effect, illustrated in Figure 4.4). The other reason is the induction between the electrodes of the MCP PMT. The anodes and the second MCP electrode form small capacitors, and when one of them produces a signal due to a true hit, false signals are induced in the neighboring anode pads. The effect can be reduced by making the capacitance of the anodes smaller, by finer anode and second MCP electrode segmentation [5].

Figure 4.5: A Hamamtsu 16 channel MCP PMT.

Available for measurements were three prototype MCP PMTs, based on the devices manufactured by Hamamtsu Photonics for the time-of-propagation counter of the Belle II spectrometer [34]. The three MCP PMTs will be referred to by their labels as JY0002, JY0005 and JY0008. Most of the basic characteristics of the three devices are the same, as is summarized in Table 4.1. One of the MCP PMTs can be seen in Figure 4.5, while Figure 4.6 shows the QEs of the three devices.

The JY0008 is slightly different from the other two MCP PMTs. It has an aluminum protection layer in front of the first MCP, used to stop positively charged ions from reaching the photocathode. The ions are released during the multiplication process in the microchannel plates and are accelerated by the electric field in the direction opposite to that of the electrons. This means that they may hit the photocathode with significant energy and cause

	All MCP PMTs		
Device dimensions	27.5×27.5×15 mm^3		
Effective area	22.5×22.5 mm^2		
Entry window	1.5 mm thick borosilicate glass		
Photocathode material	bialkali		
MCP channel diameter	10 μm		
MCP configuration	2 layers in chevron configuration		
Anode	4×4 segmentation		
Anode pitch	5.575 mm		
	JY0002	JY0005	JY0008
10^6 gain voltage	2400 V	2600 V	3400 V
Al protection layer	No	No	Yes
Collection efficiency	≈60%	≈60%	≈30%
Peak QE	6.4%	20%	24%
PDE integral (1.55−4.96 eV) [%·eV]	1.6	5.9	4.1

Table 4.1: The characteristics of the three MCP PMT samples.

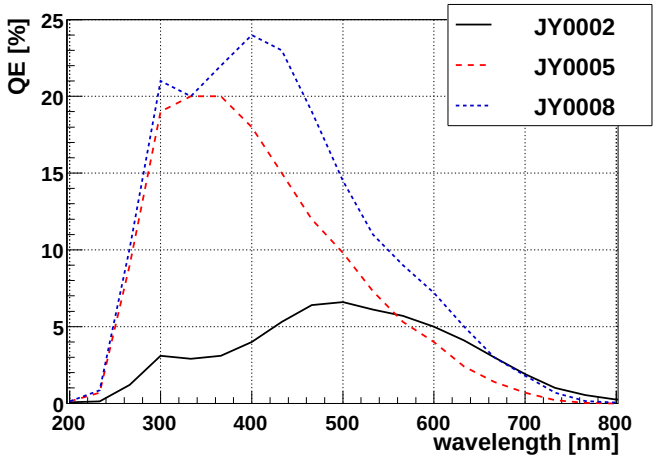

Figure 4.6: The QEs of the three MCP PMT samples, as measured by the producer.

permanent damage. Many such events reduce the QE of the photocathode over time. This effect can be mitigated by the use of an aluminum protection layer, placed in front of the first or second MCP. However, an aluminum protection layer in front of the first MCP has a negative side effect of reducing the collection efficiency from 60% to 30%.

4.2 Cherenkov Radiators

Monolithic PbF_2 and $PbWO_4$ crystals with a cross section of 25×25 mm^2, slightly larger than the 22.5×22.5 mm^2 active area of the MCP PMTs, were used to investigate the effects introduced by different radiator parameters:

- Thickness: crystals with thickness of 5 and 15 mm were used in the tests;
- Surface polish: one of the 25×25 mm^2 large surfaces, which was coupled to the MCP PMT (the exit surface) was always polished, while all other surfaces could be either polished or ground;
- Surface treatment: all but the exit surface were either wrapped in white diffusive reflector (Teflon tape), painted with black paint, or left bare.

Some of the different crystal/surface treatment combinations used are shown in Figure 4.7.

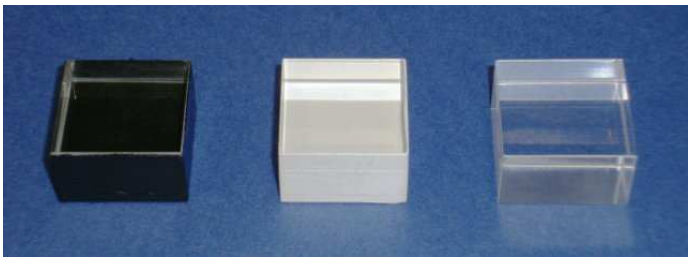

Figure 4.7: Black painted, Teflon wrapped and bare PbF_2 crystals with dimensions of 25×25×15 mm^3.

Measurements were also performed with 4×4 segmented PbF_2 crystal arrays with a thickness of 7.5 mm. The pitch of the crystals in array was ≈ 5.575 mm, matching the pitch of the MCP PMT anode segmentation. All of the surfaces of individual crystals were polished. One pair of arrays had the side surfaces of individual crystals wrapped in white Teflon reflector, while another pair had them painted with black paint. This surface treatment formed a very thin (≈0.1 mm) layer between the crystals. All arrays had the entry and the exit surfaces bare. This enabled an investigation of the effects, different combinations of entry surface/side surface treatments have,

since the treatment of the entry surface could be changed. To enable easier changes of the entry surface treatment, when the effect of black painted entry surface was studied, the entry sufaces were not treated with the usual black paint. Instead an approximation was used: a thin black sheet of plastic was coupled to the entry surface with the silicon coupling grease (refractive index ≈ 1.5). Arrays with different surface treatment combinations are shown in Figure 4.8.

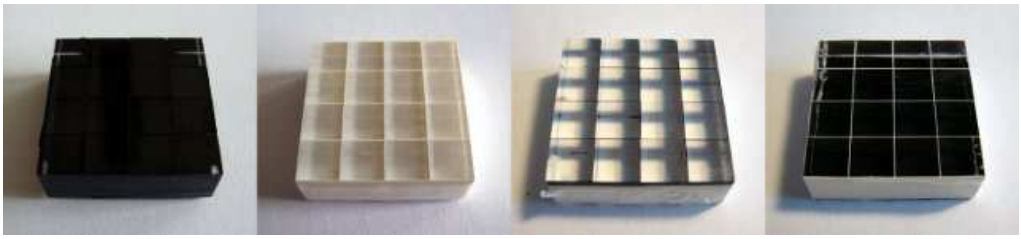

Figure 4.8: 4×4 segmented, 7.5 mm thick arrays of PbF_2 crystals, with entry/side surfaces that are: black painted/black painted, Teflon wrapped/teflon wrappped, Teflon wrapped/black painted and black painted/Teflon wrapped.

All samples were obtained from the Shanghai Institute of Ceramics and Chinese Academy of Sciences (SICCAS) [24].

4.3 Electronic Readout

4.3.1 Readout of MCP PMTs

The MCP PMTs were connected to socket assembly boards, which provided electric connections to individual anodes and contained the voltage distribution circuit for the MCP PMT. The readout of all 32 anode channels (2× 16 anodes per MCP PMT) was complicated by the lack of high precision electronic readout modules, and was limited to 16 channels for time and 32 channels for charge measurements. This meant that not all anode outputs could be readout individually. The following readout schemes were used at different stages:

- Channels were summed into groups of 4, resulting in 4 readout channels per MCP PMT (Figure 4.10a). The summing was achieved by connecting one readout line to 4 anode outputs at the earliest possible stage−at the board output pins. This configuration was used, when coverage of the whole device, but not the best timing information, was required;

- Two of the central channels per MCP PMT were connected individually, while the other 14 anode channels per MCP PMT were summed

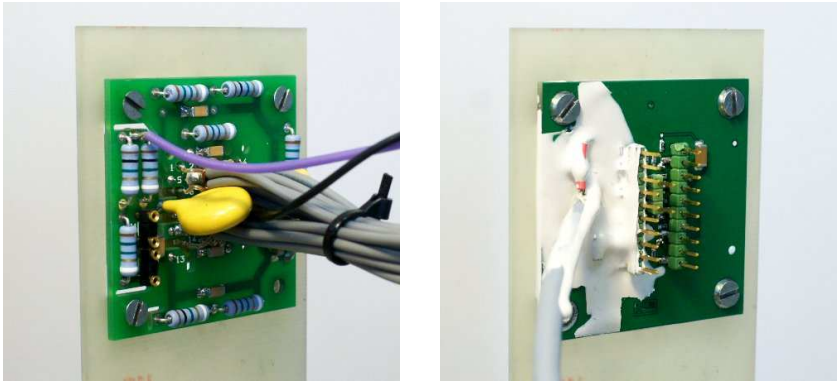

Figure 4.9: Two types of readout boards used in the experiments, viewed from the back side: the board provided by MCP PMT manufacturer (left) and a new board, developed in-house (right).

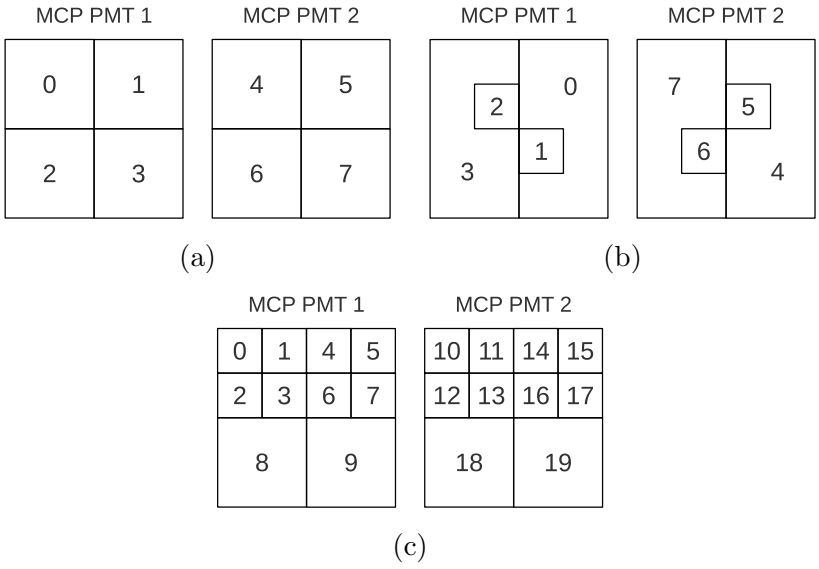

Figure 4.10: Different readout configurations of MCP PMT anode channels used at different stages of measurements, as viewed from the front of the two MCP PMTs.

into two readout channels per device in a symmetric configuration (Figure 4.10b). The two individually connected channels per MCP PMT provided the best possible timing resolution. Only the individually connected channels were used in coincidence logic (Figure 4.12);

- Half of the anode channels per MCP PMT were connected individually, and readout both by their time and charge. The other half of the anode channels was summed into two readout channels, and only readout by their charge (Figure 4.10c). This configuration provided the best approximation for the performance of the whole device readout. Only the individually connected channels were used in the coincidence logic (Figure 4.12).

4.3.2 Signal Processing

The readout channels were instrumented, as shown in Figure 4.11: a readout signal was lead to a charge amplifier then split into two by a passive signal splitter. One line was fed into a leading edge discriminator, which provided logic signals corresponding to the pulse arrival times for the Time to Digital Converter (TDC) and the coincidence logic circuit (Figure 4.12). The other line was fed into Charge to Digital Converter (QDC). The lines going to the TDC and QDC were delayed by 80 ns, to accommodate the processing time required by the coincidence logic circuit. In case of readout configurations shown in Figures 4.10a and 4.10b, the channels which were composed as a sum of multiple anode outputs were lead directly from the amplifier to the QDC, bypassing the signal splitter. The coincidence logic circuit, shown in Figure 4.12, provided the trigger logic signal, marking the measurement start time for the TDC and QDC.

The details of the electronic modules, shown in Figure 4.11 and Figure 4.12, are provided in the following list:

- Amplifier: EG&G ORTEC FTA820 Fast Timing Amplifier (200× amplitude amplification, 350 MHz bandwidth);
- Discriminator: Phillips Scientific Model 708 Octal 300 MHz Discriminator (leading edge);
- TDC: Kaizu Works KC3781A Octal TDC (25 ps least significant bit);
- QDC: CAEN Model V965 16 Ch. Dual Range QDC (measurement range 0−800 pC with 200 fC resolution or 0−100 pC with 25 fC resolution);
- High voltage supply: CAEN Model N471 2 Fold H.V. Power Supply;
- Coincidence logic circuit:

– EG&G ORTEC/ESN LF4000 Quad Logic Fan In/Fan Out (used for OR function);
– EG&G ORTEC/ESN CO4010 4-Fold 4-Input Logic Unit (used for AND function);
– Phillips Scientific Model 752 Quad Two-Fold Logic Unit (used for setting the width of the trigger logic pulse);

The different electronic readout modules were housed in NIM, CAMAC and VME modular system standard crates. A VME-PC module enabled the communication with a computer, which was used to control the data acquisition and store the measurements. The measurement control software was written in LabWindows/CVI environment, while the data analysis was performed in ROOT framework [35]. A veto signal, used in the logic circuit, was enabled by the PC while the acquisition of event was taking place.

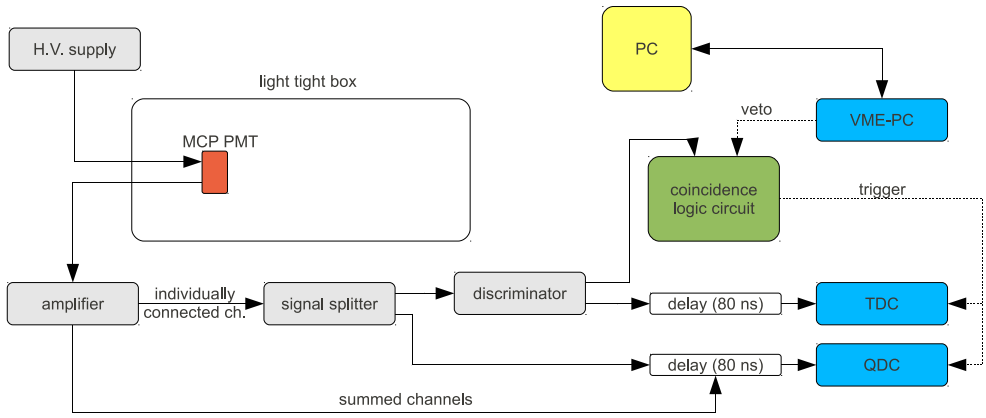

Figure 4.11: The instrumentation of MCP PMT readout lines and the data acquisition system.

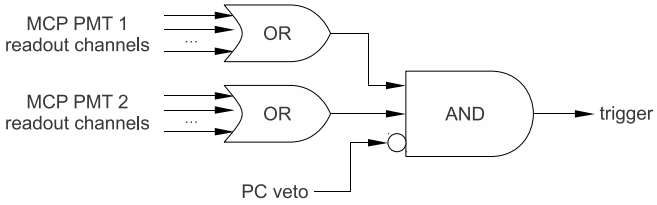

Figure 4.12: The coincidence logic circuit used for most of the measurements.

4.3.3 Time-Walk Correction

The arrival time of MCP PMT pulses was defined by the start of the logic signal, produced by the leading edge (LE) discriminator. The output of the LE

discriminator switches on, when the input pulse amplitude exceeds a preset threshold voltage. This has an important implication for precision of timing – pulses arriving at exactly the same time but with different amplitudes or risetimes will be detected at slightly different times. Of two pulses with same shape but with different amplitudes, the pulse with the larger amplitude will reach the threshold voltage and trigger the discriminator before the smaller pulse. This effect is illustrated in Figure 4.13 and is called time-walk.

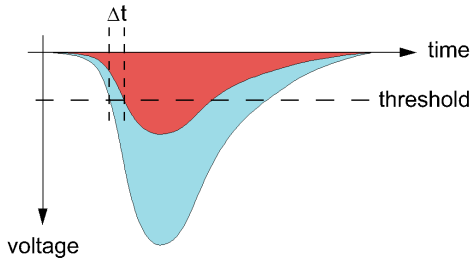

Figure 4.13: The source of time-walk effect: two concurrent signals of the same shape, but with different amplitudes, cross the threshold at slightly different times.

Due to the statistical nature of charge multiplication, the MCP PMT output pulses resulting from single photoelectrons have a large amplitude fluctuations. With multianode devices, additional variation comes from the charge sharing effect. A typical MCP PMT single photoelectron charge distribution (Figure 5.2) is very wide, compared to the location of the pedestal (the measured charge of background noise). This means that a significant time-walk effect is unavoidable when detecting single photon pulses with the use of a leading edge discriminator.

However, a time-walk correction can be applied after the data is taken. This requires both the measurement of time and charge. A histogram of the measured time (y-axis) vs. the measured charge (x-axis) for a large number of events is shown in Figure 4.14. The time-walk effect is clearly visible and is less pronounced for pulses with a larger amplitude (events to the right side of the plot), while the smallest amplitude pulses (events to the left side of the plot) are detected with as much as 500 ps delay. The shape of the distribution is determined by the pulse shape and details of discriminator operation. This means that for certain hardware configuration the detection delay caused by time-walk can be determined for each individual pulse just by knowing its charge.

The time-walk correction was performed by fitting the time vs. charge distribution with the following function:

$$f(x) = p_0 + \frac{p_1}{\sqrt{x - p_2}}, \tag{4.1}$$

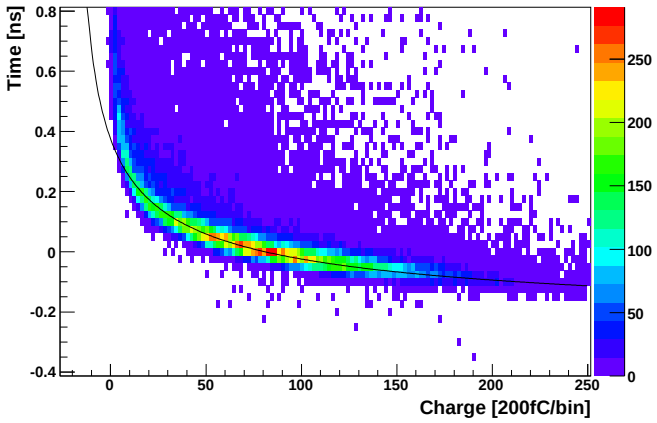

Figure 4.14: Plot of event count vs. the event time and charge. Also shown is the fit fuction from Equation (4.1).

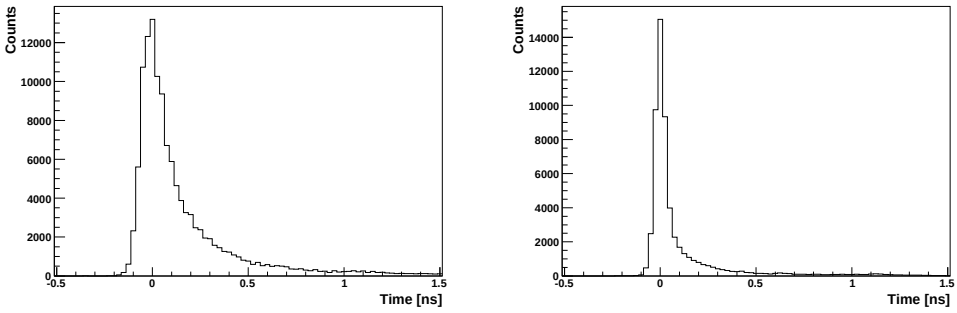

(a) Before (b) After

Figure 4.15: Time distributions before and after the time-walk correction.

where x represents the charge and $f(x)$ the time-walk shift of pulses, while p_0, p_1 and p_2 are the parameters, determined by the fit. The fit function form follows from the presumption that initially the pulse shape is quadratically dependent of time. As can be observed in Figure 4.14, this function does not follow the distribution perfectly at lower charges. However, this had very little effect on the final results. The corrected time can than be determined for each pulse by subtracting from the measured time the time-walk shift, calculated by inserting the measured charge in Equation (4.1). Figure 4.15 shows examples of the measured pulse arrival time distributions before and after the time-walk correction. Clearly a significant improvement in resolution is achieved by the correction.

4.4 The 511 keV Gamma Source

As the source of 511 keV annihilation gammas, a β^+ emitting ^{22}Na point source was used. The source was in a shape of a very small sphere with a diameter of ≈ 0.3 mm, contained in a plastic disc, in which the positrons annihilate. Besides β^+ particles, ^{22}Na also emits gamma rays with an energy of 1275 keV.

The ^{22}Na decay occurs by two mechanisms:

- β^+ decay, which has two branches:

$$^{22}\mathrm{Na} \rightarrow {}^{22}\mathrm{Ne(ground\ state)} + \mathrm{e}^+ + \nu \quad (0.06\%\ \text{of all decays})$$
$$^{22}\mathrm{Na} \rightarrow {}^{22}\mathrm{Ne^*(1275\ keV)} + \mathrm{e}^+ + \nu \quad (90.3\%\ \text{of all decays})$$

- Electron capture:

$$^{22}\mathrm{Na} + \mathrm{e}^- \rightarrow {}^{22}\mathrm{Ne^*(1275\ keV)} + \nu \quad (9.64\%\ \text{of all decays})$$

The first excited state of ^{22}Ne at 1275 keV decays with a lifetime of approximately 5 ps [36],

$$^{22}\mathrm{Ne^*(1275\ keV)} \rightarrow {}^{22}\mathrm{Ne(ground\ state)} + \gamma(1275\ \mathrm{keV}).$$

In total about 90.4% of decays produce 511 keV annihilation gamma pairs and 99.94% of decays produce a 1275 keV gamma.

The 1275 keV gammas will represent a background for annihilation gamma detection. This however should be negligibly small when operating in coincidence mode, since the 1275 keV gammas are emitted in random direction, relative to the direction of possibly accompanying annihilation gamma pair. The probability of detecting one annihilation gamma on one side, while detecting the 1275 keV gamma on the other side of the detector, is proportional to the fraction of solid angle, covered by the detectors. This is very small ($\approx 10^{-4}$) in the back-to-back detector arrangement used in the experimental setup. This is also not a problem in a real PET applications, where pure β^+ emitters, like ^{18}F, are used.

5 Measurements of MCP PMT intrinsic performance

The performance of MCP PMTs used in the experiments was determined by illuminating them with very low intensity laser pulses. Pulses of either red (636 nm) or blue (404 nm) light were produced by a pair of PiLas EIG1000D diode laser systems [37]. The laser output was attenuated by neutral density filters to a very low level, where almost no events resulted from detection of more than one photon per laser pulse. The laser control unit also provided the trigger signal. The attenuated light from the laser was lead into the light-tight box via an optical cable and focused to a narrow spot with a diameter of less than 1 mm. The optical cable and the focusing lenses were mounted on a computer controlled 3D movable stage with a positioning accuracy of the order of 10 μm. The experimental setup described in Section 4 was modified, so that the two MCP PMTs were positioned side by side, facing in the same direction (Figure 5.1). In this configuration, the 3D movable stage was used to accurately position laser illumination on the centers of the pads of both MCP PMTs. The readout scheme with 8 channels per MCP PMT individually connected (Figure 4.10c) was used. The trigger logic was modified, so that instead of the coincidences between the two MCP PMTs, the laser trigger signal was used.

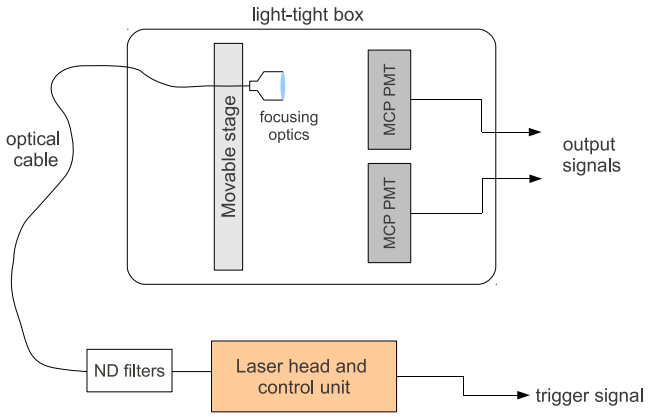

Figure 5.1: Schematic view of setup used for measurements with the laser.

5.1 Charge distributions

The typical charge distribution for very low level illumination, obtained with the described experimental setup, is shown in Figure 5.2. The narrow peak at approximately bin 60 is the pedestal (electronic noise). Events above the pedestal belong to the single photon peak, which is significantly spread due

to the statistical nature of charge multiplication and collection in the MCP PMT.

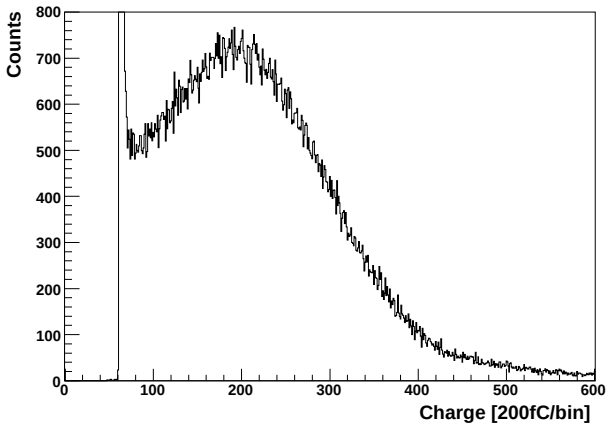

Figure 5.2: A typical MCP PMT charge distribution for a very low level illumination.

Figure 5.3 shows the charge distributions for all readout channels of the JY0002 MCP PMT, obtained when the center of each pad was illuminated by the focused light spot. All the pads were illuminated with the same light intensity, however not all pads collected a comparable count of single photon events. This is seen as a lower number of events in the single photon peak, compared to the number of events in the pedestal. This can be explained by the inhomogeneity of the MCP PMT PDE over the sensitive surface.

The distributions for different pads also have a different position of pedestal, which is a consequence of slight differences between the readout channels of the QDC. Variations between QDC channels also contribute to small differences between amplification of individual channels. Other contributions to differences in amplification are coming from the diferencess between the amplifier channels and amplification of the MCP PMT itself. Different pads of the same MCP PMT could have a slightly different amplification due to accelerating electric field inhomogeneities and variations in MCP structure.

The variation between amplification of different pads is most evident in the lower half of Figure 5.3, which shows the charge distributions for the two readout channels, which are composed as a sum of four anode pads each. The focused light illuminated the centers of four contributing pads, while the summed signal was read out through the same amplifier and QDC channel. The differences in amplification can therefore only be attributed to differences between the MCP PMT pads.

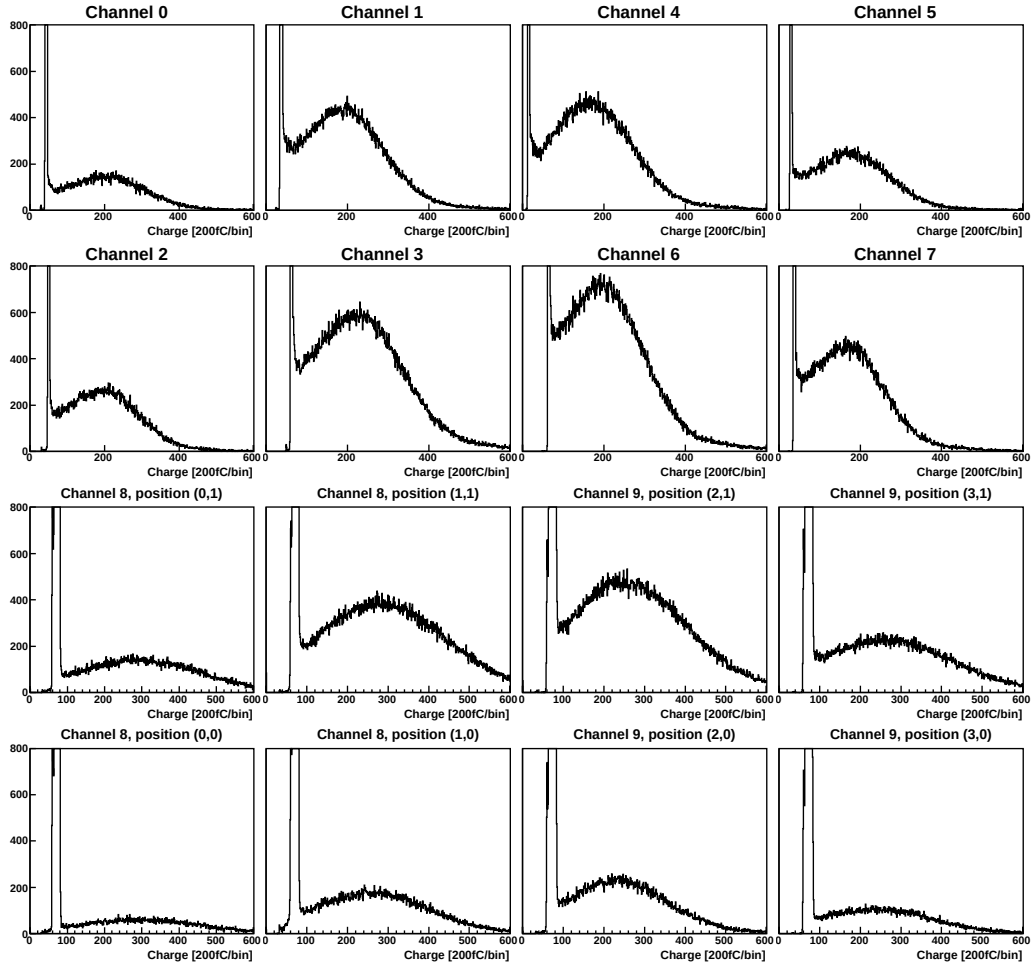

Figure 5.3: The charge distributions for readout channels of JY0002 MCP PMT at very low level illumination. The position of the histograms corresponds to the position of the channels on MCP PMT (Figure 4.10c). In case of readout channels, composed as a sum of four anode pads each, the position of the histograms also corresponds to the center of the illuminated pad.

5.1.1 Maximum charge cut

The charge distributions include not only the true signals produced on the observed pad, but also signals which are a result of crosstalk between anode pads (Section 4.1). Fake crosstalk events have a very small effect in measurements presented in this section, where only the center of one anode pad was illuminated and laser trigger was used. However the number of recorded crosstalk events becomes a significant problem in coincident 511 keV gamma detection, where incident photons are spread over the whole active surface of MCP PMT and the trigger used for measurements is derived from logical OR of more than one anode pad per MCP PMT. To reduce the effect of crosstalk, histograms belonging to individual readout channels had an additional cut applied. Only events, for which the observed channel had the maximum charge of all channels belonging to one MCP PMT were selected for the cut. Before comparing the charges of all the channels, the charge distributions were baseline corrected. Calibration of amplification was attempted, but no significant improvements in results were achieved. The following results were obtained without such calibration.

5.2 Time resolution

The time distribution of events obtained when one of JY0005 MCP PMT pads was illuminated with red laser pulses attenuated to very low intensity is shown in Figure 5.4. The distribution is composed of a narrow peak at time 0 and an approximately 1.5 ns long tail, which is a result of electrons backscattering from the MCP surface (Section 4.1). As can be seen in Figure 5.4, in this case the maximum charge cut removes only a small fraction of events, which are most likely caused by crosstalk and a detected with time delay of 2 ns or more.

After the time-walk correction (Section 4.3.3) is applied, the time distribution from Figure 5.4 becomes a significantly narrower distribution, shown in Figure 5.5(b). Figure 5.5 also shows the time-walk corrected distribution for JY0002 MCP PMT. The distributions are fitted with a sum of two functions: a Gaussian function, accounting for the narrow peak (dashed red curve in Figure 5.5):

$$\mathrm{G\_Const} \cdot e^{-\frac{1}{2}\left(\frac{x-\mathrm{G\_Mean}}{\mathrm{G\_Sigma}}\right)^2},$$

and an exponential function, suppressed at the lower end with an error function, which accounts for the electron backscattering tail (full blue curve):

$$\left[\mathrm{Exp\_p0} \cdot e^{\frac{x}{\mathrm{Exp\_p1}}} + \mathrm{Exp\_p2}\right] \cdot \left[\frac{1}{2} + \frac{1}{2} Erf\left(\frac{x - \mathrm{Erf\_p0}}{\mathrm{Erf\_p1}}\right)\right].$$

Here the parameters are labeled the same as they are in the figures. The FWHM was calculated as the width of fitted function at half height. The time

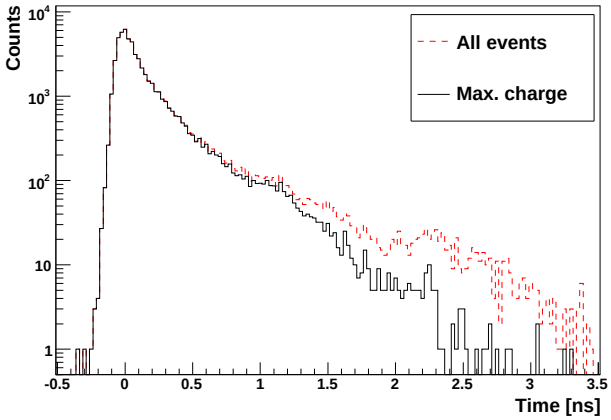

Figure 5.4: The JY0005 MCP PMT time distribution, not corrected for time-walk, with and without the maximum charge cut applied.

resolution is 63.4 ps FWHM (Gaussian $\sigma = 23.0$ ps) for JY0002 and 63.2 ps FWHM ($\sigma = 25.0$ ps) for JY0005 MCP PMT. This includes contributions from the laser ($\approx$ 14 ps r.m.s. for red and 18 ps r.m.s. for blue laser [38]) and electronics ($\approx$ 11 ps r.m.s.). Figure 5.6 shows the time-walk corrected distribution for JY0008 MCP PMT, obtained in the same way. The time resolution with 58.7 ps FWHM ($\sigma = 22.0$ ps) was achieved. This distribution also features the shortest electron backscattering tail, which is a consequence of the aluminum protection foil in front of the MCP. Table 5.1 lists the time resolutions obtained on all instrumented channels of JY0002 and JY0005 MCP PMTs. As can be seen, the time resolution is very consistent over the channels of the same MCP PMT.

				JY0002				
Readout channel	0	1	2	3	4	5	6	7
FWHM [ps]	63.7	66.6	66.6	67.5	66.1	65.9	63.4	62.2
σ [ps]	23.5	24.1	24.9	25.0	24.3	23.9	23.0	23.9
				JY0005				
Readout channel	10	11	12	13	14	15	16	17
FWHM [ps]	64.7	62.7	63.9	73.2	64.9	63.3	63.1	65.0
σ [ps]	25.1	24.1	25.1	27.4	25.1	24.3	25.0	24.8

Table 5.1: The time resolutions (FWHM and Gaussian σ) of all instrumented MCP PMT channels for red (636 nm) light illumination.

The time resolution was slightly degraded, when a blue laser light was used. This can be seen in Figure 5.7, where the same two channels are shown as were in Figure 5.5 in the case of red light. In case of blue light, the time resolution has a 74.8 ps FWHM ($\sigma = 28.7$ ps) for JY0002 and 83.4 ps FWHM

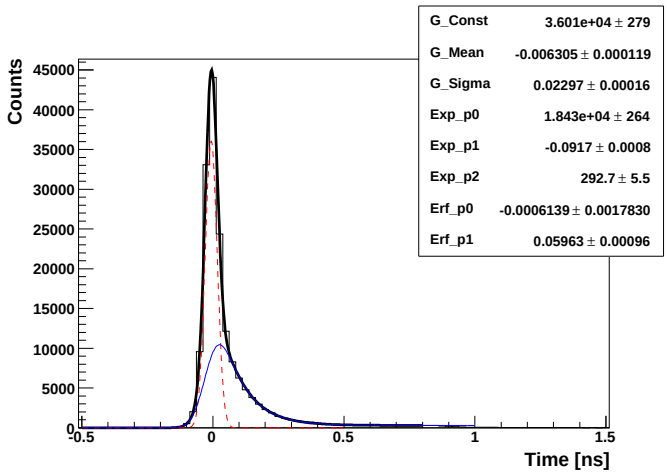

(a) JY0002, Channel 6

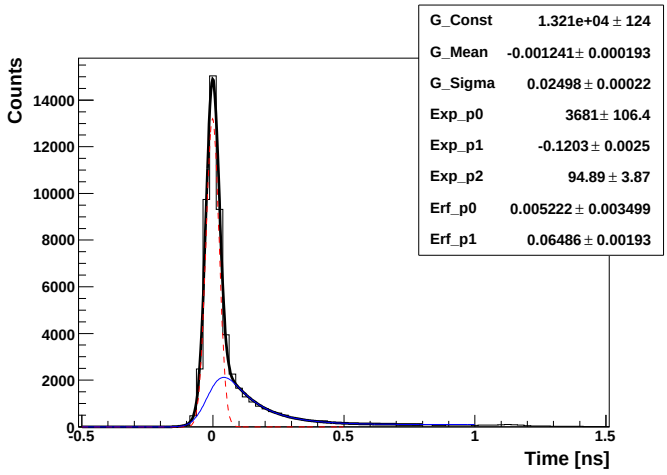

(b) JY0005, Channel 16

Figure 5.5: The MCP PMT time distribution after time walk correction, in case of red (636 nm) light illumination.

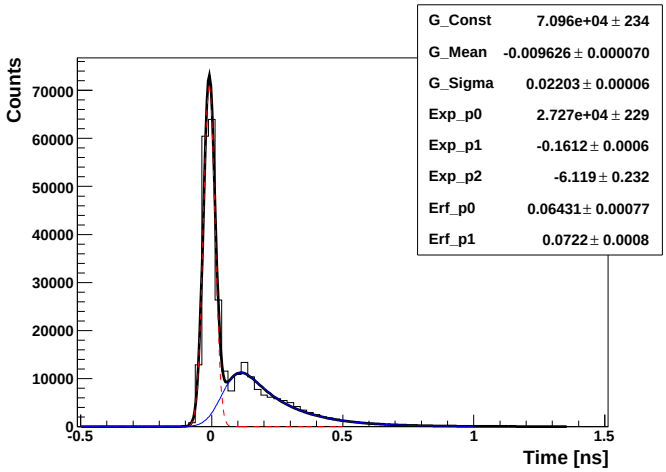

Figure 5.6: Time distribution obtained with channel 6 of JY0008 MCP PMT, in case of red (636 nm) light illumination.

($\sigma = 33.9$ ps) for JY0005 MCP PMT. The degradation of time resolution can be explained by different contributions of the two lasers used and by the fact that blue light has a higher energy (≈ 3.0 eV) than the red light (≈ 1.9 eV). This leaves the photoelectron with a higher kinetic energy after exiting the photocathode, which leads to a larger transit time spread.

5.3 Coincidence timing resolution

The pulses of laser light were also used to estimate the performance when the coincidence logic circuits are used. For this purpose, the laser light was split into two light beams with a 50%:50% light splitting prism. Each beam was attenuated to very low intensity, lead into the light tight box via an optical cable and focused into a spot with diameter less than 1 mm. In this way the centers of two pads, one belonging to each MCP PMT, were illuminated by the same light pulse. Instead of the laser trigger, the coincidence logic between JY0002 and JY0008 MCP PMTs (as described in Section 4.3.2) was used.

The time-walk correction was performed using the parameters obtained when a laser trigger was used (the same time-walk correction parameters as those used to obtain distributions in Figure 5.5 and values in Table 5.1). The coincidence time distributions were obtained by histogramming the difference in event times, recorded for the two illuminated channels. Figure 5.8 shows the coincidence time distributions obtained with red an blue laser illumination, with the maximum charge cut applied. The coincidence time distributions are composed of three main parts: the narrow central peak, which is a convolution of narrow peaks in individual MCP PMT time re-

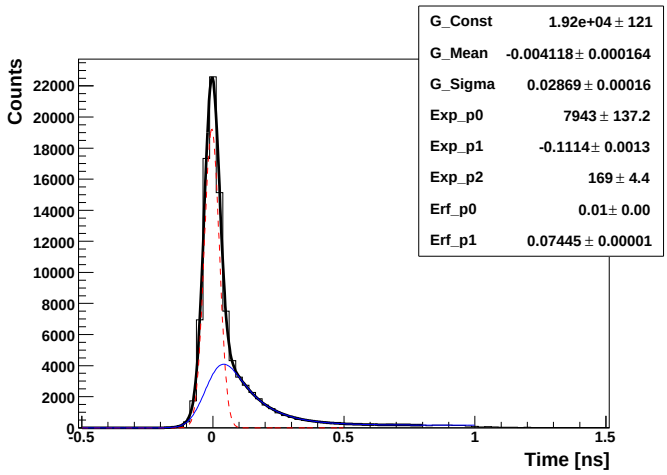

(a) JY0002, Channel 6

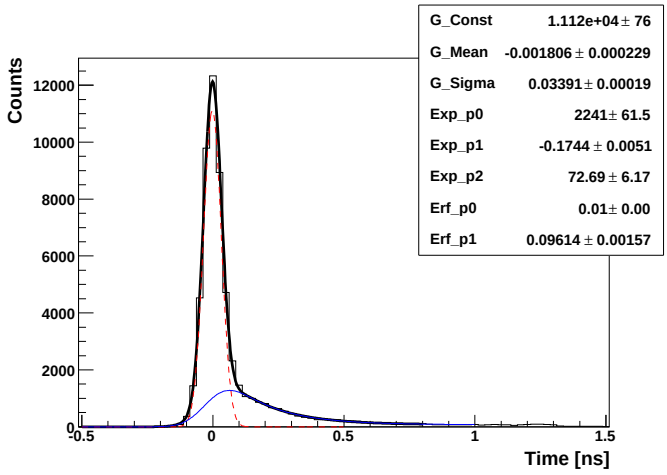

(b) JY0005, Channel 16

Figure 5.7: The MCP PMT time distribution after time walk correction, in case of blue (404 nm) light illumination.

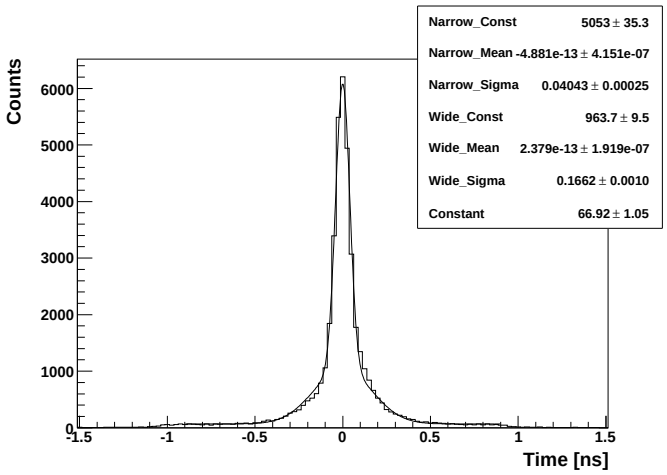

(a) Red light

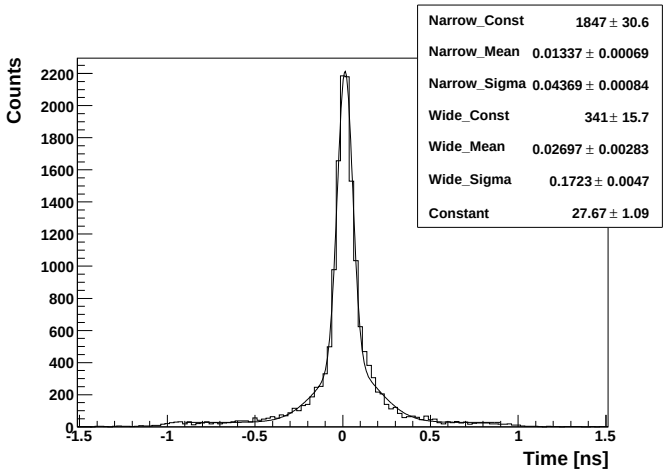

(b) Blue light

Figure 5.8: The coincidence time distributions, in case of blue and red light illumination.

sponses, a wider peak and the approximately 1 ns long tails, both of which are produced by electron backscatter events in individual MCP PMTs. The distributions in Figure 5.8 were fitted with a sum of two Gaussian functions, to account for the narrow and wide central peak, plus a constant, to approximate the offset due to the tails. The distributions in Figure 5.8 have a resolution of 107 ps FWHM ($\sigma = 40.4$ ps) in case of red and 119 ps FWHM ($\sigma = 43.7$ ps) in case of blue light.

If contributions from the measured time responses of the two MCP PMTs are combined, the expected coincidence time resolutions would be 89.5 ps FWHM in case of red and 112 ps FWHM in case of blue light. The measured coincidence time resolutions are worse than expected, since the laser output jitter contribution is doubled ($\sqrt{2}\cdot$ r.m.s.) for the coincidence measurements (one photon needs to be detected by each MCP PMT).

6 Coincidence time resolution using Cherenkov light

The timing resolution of a simple back-to-back system, described in Section 4, was measured for different parameters of Cherenkov detectors. The effects of material, thickness and surface treatment of the Cherenkov radiator were examined when different readout schemes (Section 4.3.1) were employed. Initially, a back-to-back setup with JY0005 and JY0008 MCP PMTs was used. It was observed that during the measurements the JY0008 MCP PMT performance slowly degraded* and it had to be replaced with JY0002, which has a significantly lower PDE but very similar time response.

6.1 Initial results

First measurements with back-to-back setup were performed with JY0005 in coincidence with JY0008 MCP PMT. The devices were plugged into readout and high voltage distribution boards provided by the producer. This readout boards featured a connection cable for each of the 16 anode pad outputs. This complicated the summing of readout lines, which could not be instrumented individually, since this summing could only be achieved after the initial length of the output cable. The readout configuration with 2 individually instrumented channels and 2 channels, composed as a sum of 7 anode pad outputs (Figure 4.10b) was used. A ^{22}Na point source with activity of approximately 25 kBq was used as a source of annihilation gammas.

6.1.1 Charge distributions

The charge distributions obtained for individually connected anode outputs of JY0005 and JY0008 MCP PMTs are shown in Figure 6.1a and 6.1b respectively, when 25×25×15 mm^3 PbF_2 radiators were used. This distributions are very closely resembling the distributions, obtained with very low intensity laser illumination (Figure 5.3). The distributions with the maximum charge cut applied (Section 5.1.1) are almost identical to the ones without the cut, only events in and very near the pedestal are suppressed. This suggest that there is very little crosstalk effect between the two individually connected pads, which are touching only with their corners (Figure 4.10b). Figures 6.1c and 6.1d show the charge distributions for the channels composed as as sum of 7 anode outputs. The shapes of this distributions are very different from the shapes of distributions for individually connected anodes.

*The amplification was decreasing while the current running through the device was increasing. This was attributed to damage caused by occasional discharges between the high voltage pin and two closest anode pins on the MCP PMT. The time resolution of the device however seemed not to be degrading.

The signals are most likely distorted when they are propagating through the joined wires, which perform the summing. Despite this, the information obtained from their registered charge enabled a usefull implementation of the maximum charge cut.

6.1.2 Time distributions

The time information was only available for the four channels, corresponding to the individually connected anodes. The time-walk correction was applied for each channel, using correction parameters obtained in previous measurements with laser illumination. Alternatively, the correction parameters could also be obtained from the coincidence measurements themselves, with no significant difference in the final results (Appendix A). Coincidence time distributions were obtained, by histogramming the difference in time-walk corrected time information between channels belonging to different MCP PMT. The so obtained distributions, for cases with and without the maximum charge cut applied, are shown in Figure 6.2. As can be seen, the maximum charge cut improves the results by filtering mostly the events with larger time delay. However, it does not have the same effect on all channels − channel 1 seems to be much more susceptible to crosstalk than other three channels. What remains after the cut is a narrow peak with about 1 ns long tails on both sides, as expected from the convolution of two MCP PMT time responses. It is also visible that the tails are not of the same shape on both sides, which is expected considering the differences in time responses of JY0005 and JY0008 MCP PMTs (Figures 5.5b and 5.6). All of the following plots and results were obtained with the maximum charge cut applied.

Channels	1−5	1−6	2−5	2−6
FWHM [ps]	93.9	85.2	79.1	74.2
σ [ps]	35.9	33.0	30.9	29.3

Table 6.1: The coincidence time resolution FWHM and narrower Gaussian σ for the four combinations of individually connected anode outputs, in case of 5 mm thick, black painted PbF_2 crystals. The values are obtained from distributions with the maximum charge cut applied.

The coincidence time resolution was obtained by fitting the distributions with a sum of two Gaussian functions, and calculating the FWHM as the width of the fit function at half height. The resolution was also expressed as σ of the narrower Gaussian function. The resolutions for the four combinations of channels when 5 mm thick, black painted PbF_2 crystals were used are listed in Table 6.1. The best timing resolution with 74.2 ps FWHM ($\sigma = 29.3$ ps) is achieved by combination of channels 2 and 6, while the average over the four combinations is 83.1 ps FWHM ($\sigma = 32.3$ ps).

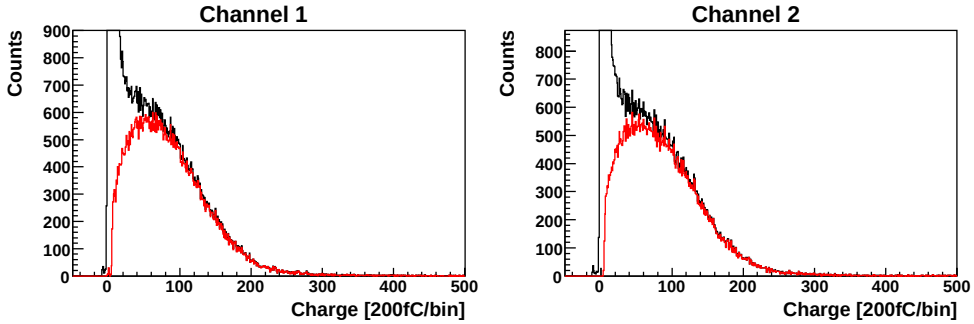

(a) JY0005, individual channels

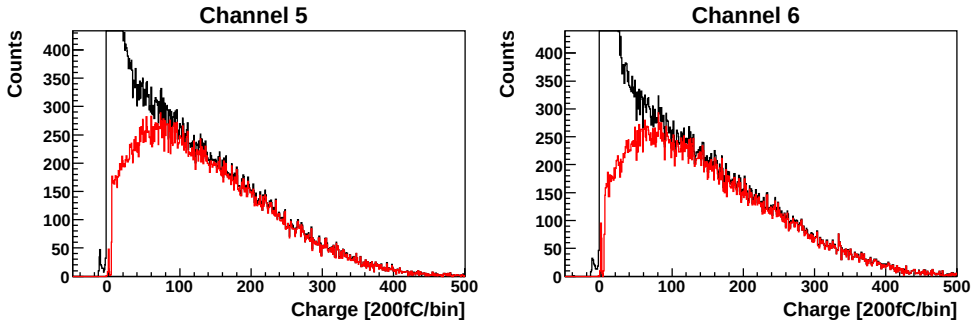

(b) JY0008, individual channels

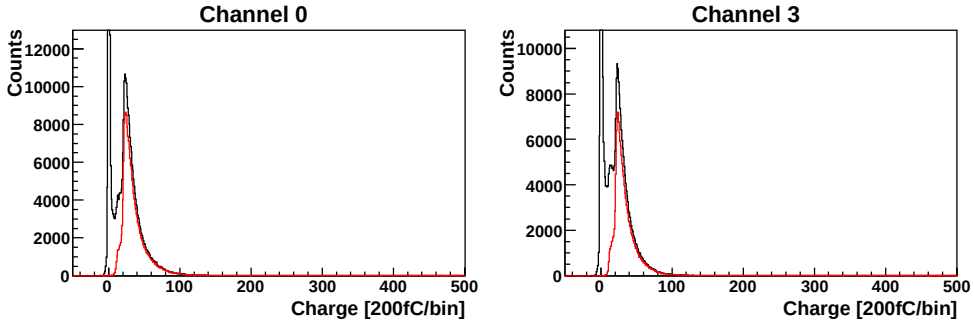

(c) JY0005, summed channels

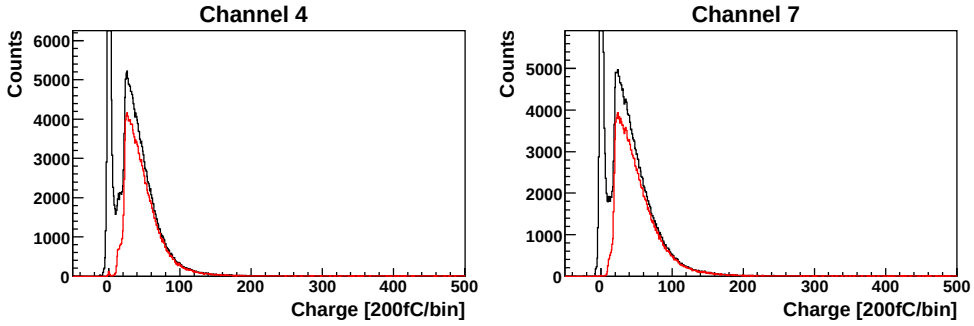

(d) JY0008, summed channels

Figure 6.1: The charge distributions obtained with the back-to-back setup, showing the channels corresponding to the individually connected anode outputs and the channels, composed as as sum of 7 anode pad outputs. The red colored histograms represent the distributions with the maximum charge cut applied.

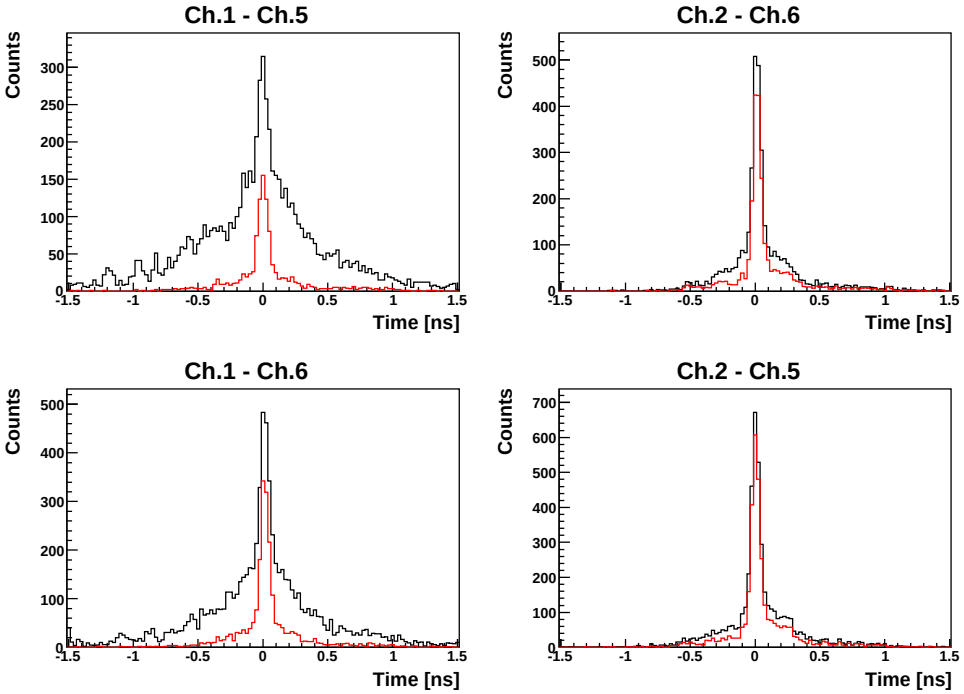

Figure 6.2: Coincidence time distributions, obtained for the four combinations of individually connected anode outputs. Here, 5 mm thick, black painted PbF_2 crystals were used. The red colored histograms represent the distributions with the maximum charge cut applied.

	Cherenkov radiator			Time resolution [ps]	
Material	Polish	Surface	Thickness	FWHM	σ
PbF_2	polished	black paint	5 mm	74.2	29.3
PbF_2	polished	black paint	15 mm	98.0	37.5
PbF_2	ground	black paint	5 mm	76.1	30.2
PbF_2	ground	black paint	15 mm	104	39.0
PbF_2	polished	bare	5 mm	90.1	31.7
PbF_2	polished	bare	15 mm	154	41.9
PbF_2	ground	bare	15 mm	156	42.5
PbF_2	polished	Teflon	15 mm	302	50.4

Table 6.2: The timing resolution of the back-to-back setup for different parameters of the Cherenkov radiator. The results are reported as FWHM (and narrow Gaussian σ) of distributions, obtained as time difference between readout channels 2 and 6.

Table 6.2 lists the timing resolutions between channels 2 and 6, which consistently gave the best results, in case of different Cherenkov radiators. The coincidence time distributions obtained for some of this Cherenkov radiator configurations are shown in Figure 6.3. As expected, the timing resolution decreases as the thickness of the radiator increases. In case of black painted, polished PbF_2 crystals, a thickness of 5 mm resulted in FWHM of 74.2 ps (σ = 29.3 ps), while a thickness of 15 mm lead to a FWHM of 98.0 ps (σ = 37.5 ps). When the surfaces of the radiators were left bare, the time resolution slightly degraded and the contributions from delayed events increased, as more photons were reaching the photodetector after on or more total internal reflections. The delayed events are even more evident when the radiator is wrapped in Teflon reflector, where photons that leave the radiator but are reflected back also contribute. Surprisingly however, the results with ground surfaces are practically identical to results with polished surfaces, both for black painted and bare surfaces. At least a part of the reason for this can be attributed to the readout configuration, where only the anodes at the center of the device are contributing to results. A large fraction of the photons that interact with radiator side surfaces never reach this central pads, making the details of surface interaction less important.

6.2 Coincidence time resolution with 16 channel readout

An improvement of the setup was attempted by designing a different readout and voltage distribution boards for the MCP PMTs. The boards were designed to supply the same voltages to the MCP PMT and provide the same outputs as the boards designed by the producer. The main difference was that the anode outputs were provided as pins on the board itself, making the summing of the channels easier. The summing could now be achieved by connecting the same readout line to multiple anode output pins, with only a few mm variation in line length between all of the summed outputs. Readout configuration with 8 individually connected anode outputs and 2 channels, composed as a sum of 4 outputs per MCP PMT (Figure 4.10c) was used. The detectors in back-to-back configuration were consisting of JY0002 and JY0005 MCP PMTs, and were exposed to gammas originating from a ^{22}Na source with an activity of approximately 3200 kBq. The source position was set about 5.5 mm higher than in previous measurements, so that it was aligned with the centers of areas, corresponding to the individually connected anodes of the two MCP PMTs.

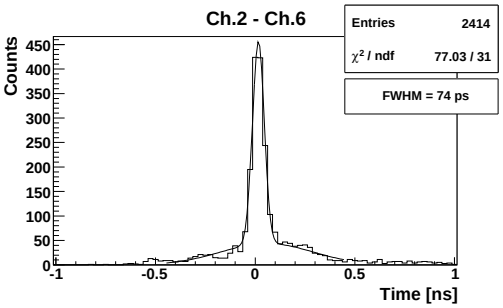

(a) 5 mm (polished, black paim)

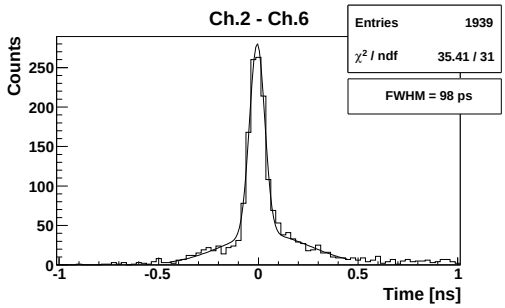

(b) 15 mm (polished, black paint)

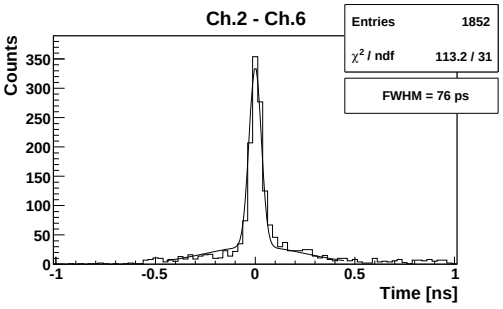

(c) 5 mm (ground, black paint)

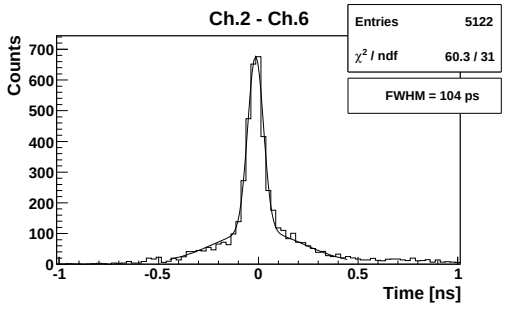

(d) 15 mm (ground, black paint)

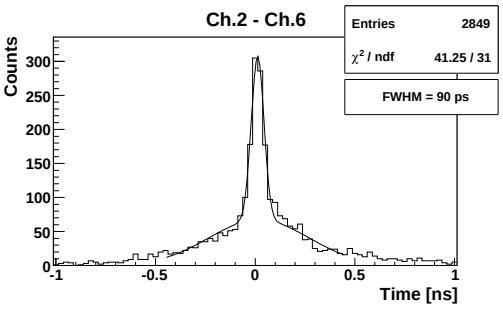

(e) 5 mm (polished, bare surface)

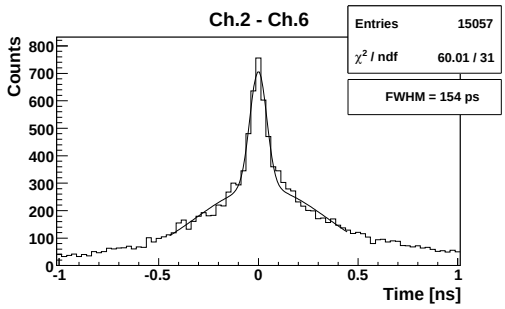

(f) 15 mm (polished, bare surface)

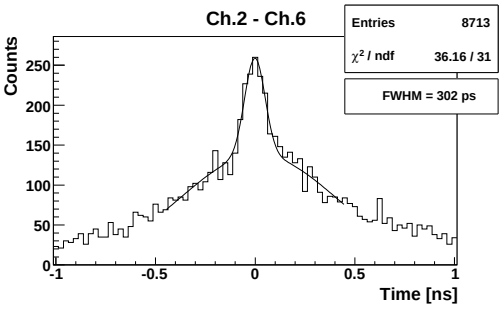

(g) 15 mm (polished, Teflon wrapping)

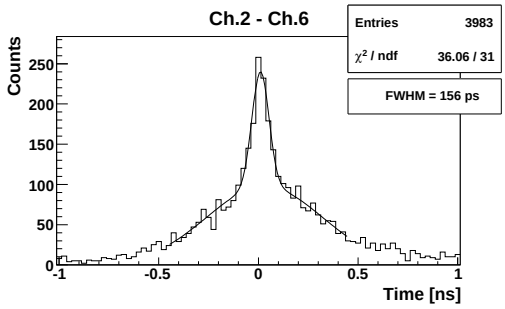

(h) 15 mm (ground, bare surface)

Figure 6.3: The coincidence time distributions between readout channels 2 and 6, in case of different PbF_2 Cherenkov radiators. The distributions are fitted with a sum of two Gaussian functions.

6.2.1 Charge distributions

The charge distributions obtained with the improved setup are shown in Figures 6.4 and 6.5 for all 20 readout channels. The distributions without the cut, shown in black color, are now much less clean than the charge distributions shown in previous chapters. The distributions are dominated by electronic noise, introduced by a discriminator threshold setting lower than that used for previous measurements. The threshold was lowered so that the smallest possible fraction of events was lost, while the noise on individually connected anode outputs and crosstalk were still very effectively removed by the maximum charge cut. Additionally, a detection time cut was applied, where only the events, detected inside a -2 ns $< t < 2$ ns time window were included in the histograms with the cuts (colored red in Figures 6.4 and 6.5). For a TOF PET application such a narrow time window is not unreasonable, considering that it represents a 120 cm wide annihilation gamma travel distance interval, which is larger than internal ring diameter of most PET systems.

6.2.2 Time distributions

The time information was available for 8 channels per MCP PMT, leading to a total of 64 combinations of channels, which could provide TOF information. However, since a stationary point source of annihilation gammas was used, not all of the channel combinations received the same number of events. Figure 6.6 shows the number of coincidences between all channels on one side and two selected channels on the other side of the back-to-back setup, using 5 mm thick, black painted PbF_2 crystals. One of the selected channels lies on the edge of its MCP PMT, while the other is located near the center. Despite the fact that an unsegmented Cherenkov radiator was used, the coincidences are mostly limited to one anode pad, that is in geometric coincidence with the observed channel (their LOR intersects the position of the source). For this study, 8 pairs of channels that were in geometric coincidence and thus accumulated the highest statistics were closely examined. The results for timing resolution would not change significantly if coincidences between other channel combinations were used. As can be seen in Figure 6.6, the timing resolution is very homogeneous for all channel combinations, except for the ones that were far away from the geometric coincidence and had very low statistics.

The coincidence time resolutions for the 8 channel combinations, obtained with 5 mm thick, black painted PbF2, are shown Figure 6.7. As can be seen, the maximum charge cut significantly improves the results. The distributions as before feature a narrow and slightly wider central peak, but now there are also two smaller peaks, registered with delay of approximately 0.6 ns on both sides of the central peak. This peaks are most likely a result of coincidences,

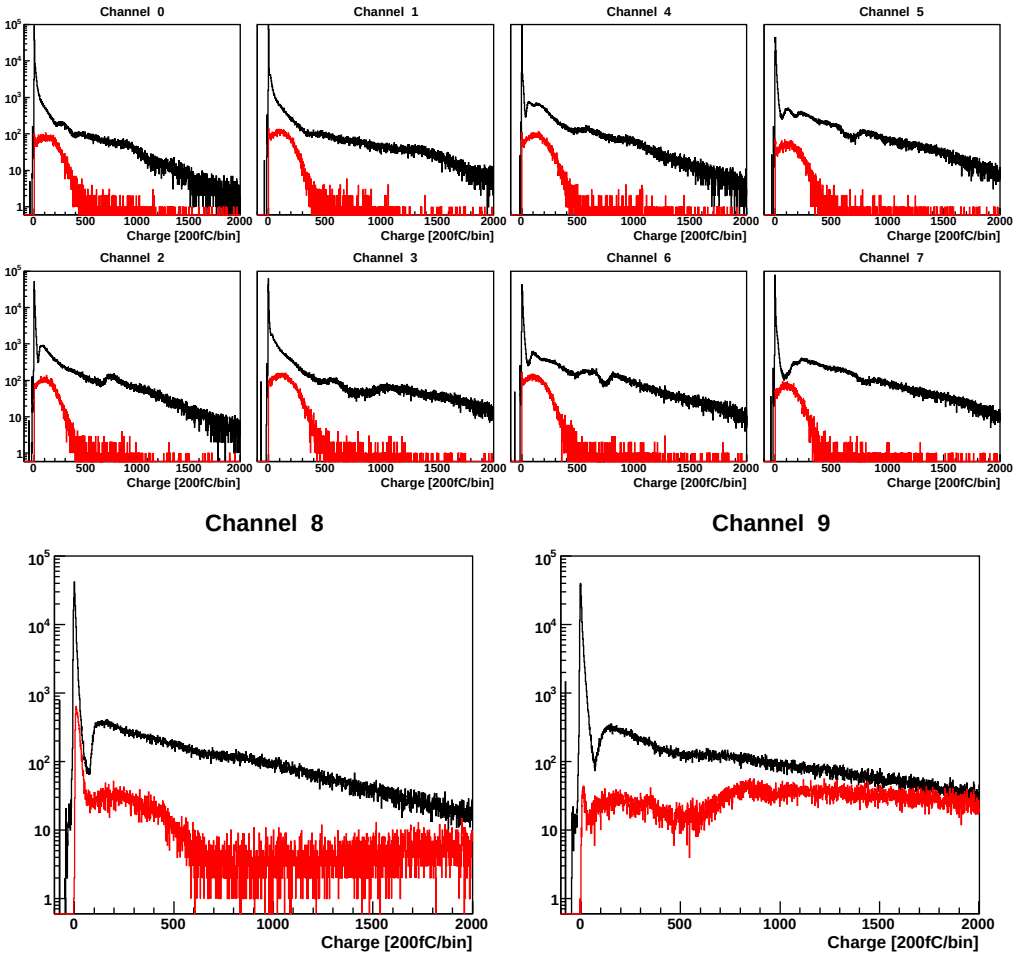

Figure 6.4: The charge distributions showing all channels connected to JY0002 MCP PMT. The position of the histograms corresponds to the position of the channels on MCP PMT (Figure 4.10c). The two bottom histograms belong to the channels, composed as as sum of 4 anode pad outputs. The red colored histograms represent the distributions with both the maximum charge and detection time cuts applied.

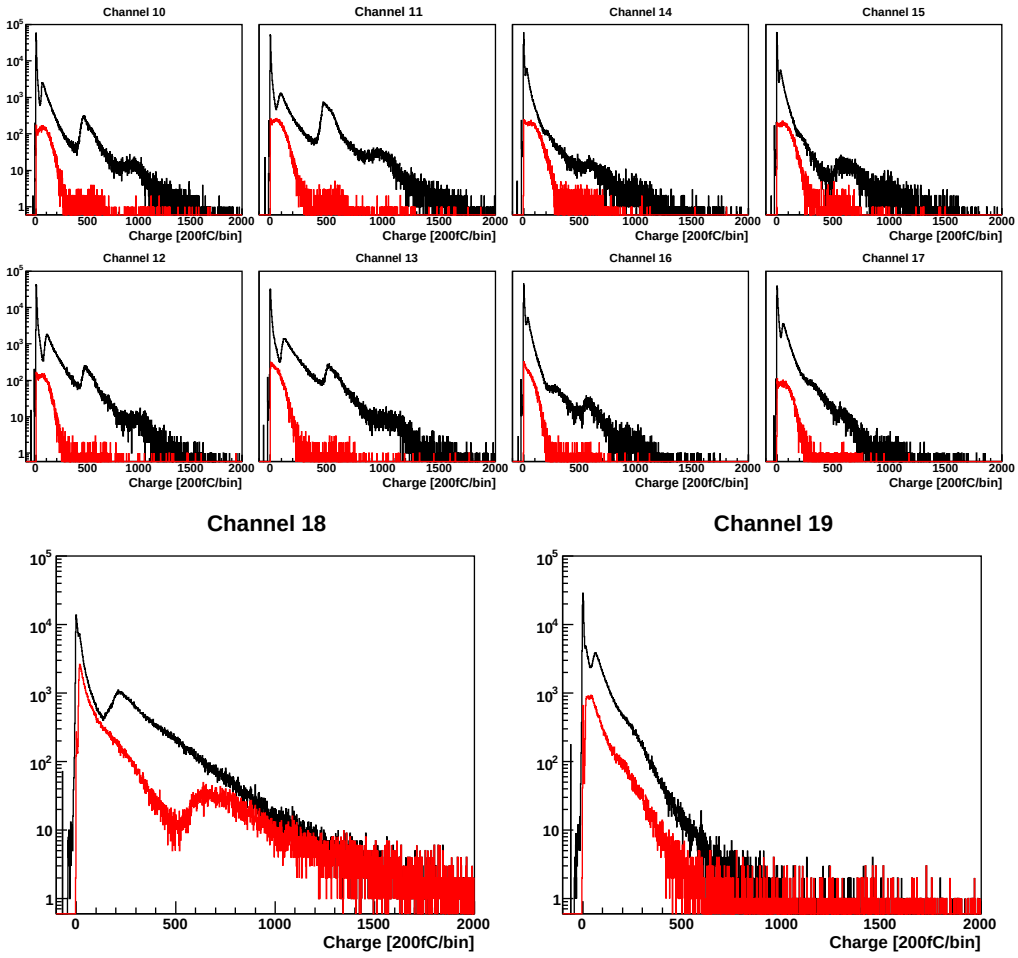

Figure 6.5: The charge distributions showing all channels connected to JY0005 MCP PMT. The position of the histograms corresponds to the position of the channels on MCP PMT (Figure 4.10c). The two bottom histograms belong to the channels, composed as as sum of 4 anode pad outputs. The red colored histograms represent the distributions with both the maximum charge and detection time cuts applied.

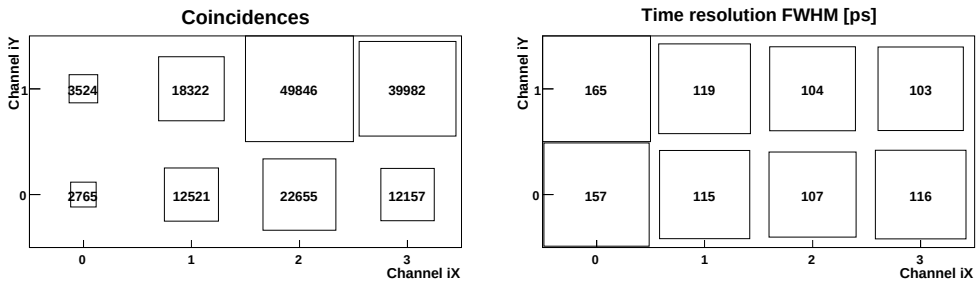

(a) Coincidences with ch.6

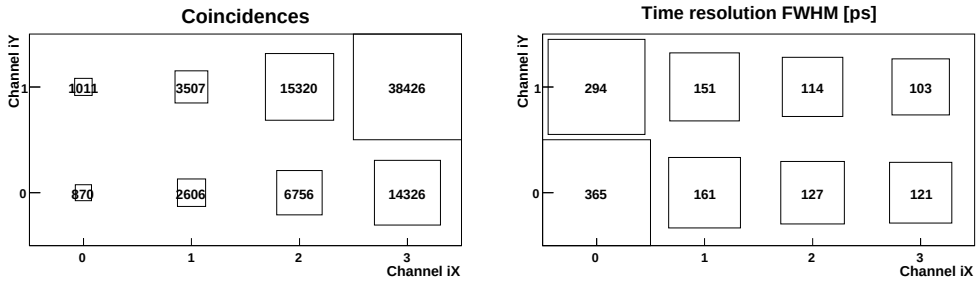

(b) Coincidences with ch.7

Figure 6.6: The number of coincidences (left) and the time resolution (right) between 8 channels of JY0005 MCP PMT and channels 6 (located near the center of device) and 7 (located on the edge of device) of JY0002 MCP PMT. The location of channels in the figures matches the locations of respective anode pads on the device (only upper half is shown). Black painted, 5 mm thick PbF_2 crystals were used.

where one annihilation gamma was converted and detected directly in the MCP of one detector, while the other gamma was detected in the normal way, when the other detector registered a Cherenkov photon produced in the radiator. The fraction of events in delayed peaks can be reduced to negligible levels if thicker radiators or photodetectors with higher QE are used, which leads to a larger number of events in the central peak. The effect of larger photodetector QE was seen in the previous measurements (Section 6.1) where the delayed peaks were not apparent. The peaks are also less pronounced for 15 mm thick than they are for 5 mm thick radiators, as can be seen in Figure 6.8. The effects of gamma detection in MCP are explored in more detail in Appendix B.

All timing resolutions in this chapter were obtained, by fitting the coincidence time distributions with a sum of five Gaussian functions. Two were, as before, used for the narrower and wider contribution in the center. Additional two were needed for the two smaller peaks, offset for $\pm$ 0.6 ns from the center. The fifth Gaussian function accounted for the approximately $\pm$ 1.5 ns wide background contribution, which is due to the electron backscattering in the MCP PMT and the significantly delayed photons, in case of reflective side surfaces or scintillations in $PbWO_4$. Table 6.3 lists the timing resolutions for the 8 channel combinations, in case of 5 mm thick, black painted PbF_2 crystals. There is very little variation in the timing resolutions between this combinations of channels.

Channels	0−12	1−13	2−10	3−11	4−16	5−17	6−14	7−15
FWHM [ps]	95.0	101	104	101	104	109	104	104
σ [ps]	32.9	35.6	36.0	34.9	36.6	34.9	35.3	34.9

Table 6.3: The coincidence time resolution FWHM and narrower Gaussian σ for the eight combinations of individually connected channels, in case of 5 mm thick, black painted PbF_2 crystals.

The time resolutions obtained with different Cherenkov radiators, listed in Table 6.4, are worse than the values obtained with the previous readout configuration (Table 6.2). Part of the reason is the fact that the values reported here are the averages over the 8 combinations of channels, while previously the best values were reported. Another reason is the geometry of previous configuration, which only included the central anode pads, leading to better timing. The biggest contribution to worsening of the FWHM values comes from the increased background. Although the narrow central peak σ only slightly worsened, the increase in background pushed the whole distribution higher, leading to worse FWHM. Figure 6.8 shows the coincidence time distributions between channels 6 and 14, a combination which consistently had a relatively high number of detected coincidences and a good timing resolution, for different parameters of the Cherenkov radiators. Besides the

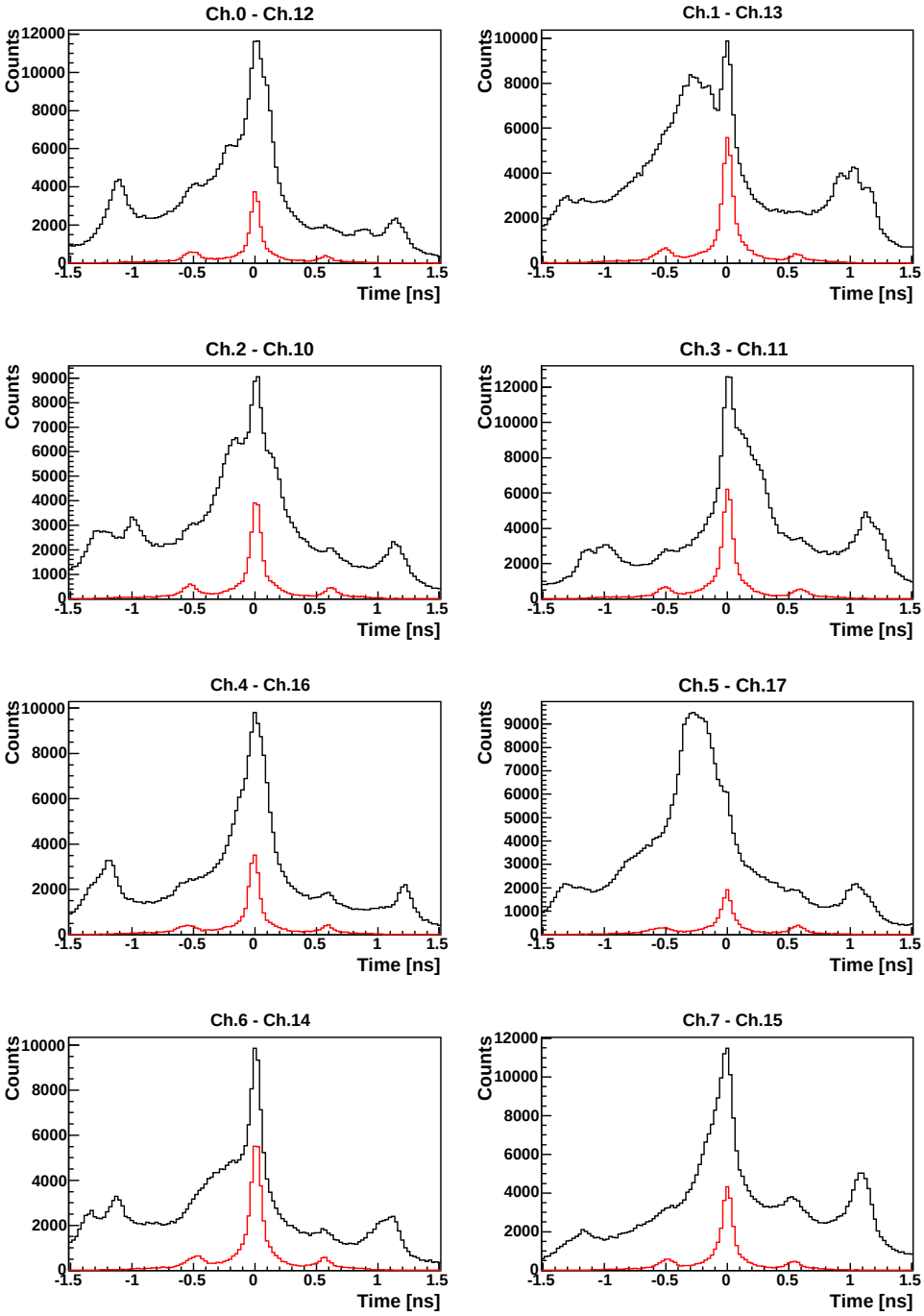

Figure 6.7: Coincidence time distributions, obtained for eight combinations of individually connected anode outputs, which were in geometric coincidence. Here, 5 mm thick, black painted PbF_2 crystals were used. The red colored histograms represent the distributions with the maximum charge cut applied.

additional background, the distributions are much the same as those shown in previous section.

Cherenkov radiator				Time resolution [ps]	
Material	Polish	Surface	Thickness	FWHM	σ
PbF_2	polished	black paint	5 mm	103	35.1
PbF_2	polished	black paint	15 mm	132	45.4
PbF_2	ground	black paint	5 mm	106	35.9
PbF_2	ground	black paint	15 mm	132	44.0
PbF_2	polished	bare	5 mm	125	38.1
PbF_2	polished	bare	15 mm	186	53.3
PbF_2	polished	Teflon	5 mm	162	46.2
PbF_2	polished	Teflon	15 mm	271	66.2
$PbWO_4$	ground	black paint	5 mm	1402	47.2
$PbWO_4$	ground	black paint	15 mm	2067	72.0

Table 6.4: The timing resolution of the back-to-back setup for different types of the Cherenkov radiator. The results are reported as the FWHM and σ of the narrow Gaussian, averaged over the eight pairs of readout channels, which are in geometric coincidence.

Table 6.4 and Figure 6.9 show the results obtained with $PbWO_4$ crystals. Although there is a relatively narrow central peak, which most likely is a consequence of coincidences, defined by Cherenkov photon detection on both sides, the distributions are dominated by a very wide background. This background is a consequence of scintillation photons, which are produced with significant time delays in much larger numbers than Cherenkov photons. Although events are defined by the first detected photon, a Cherenkov photon is not detected for every gamma interacting with the radiator. The timing is then defined by one of the scintillation photons and such events fill the distribution. Even in cases, when the events on both sides are defined by a Cherenkov photon, the timing can be degraded by scintillation photons that reach the photodetector later in the same event. Although the timing is defined by the Cherenkov photon, scintillation photons may still contribute to the charge measurement, which reduces the effectiveness of the time-walk correction. All in all, scintillation photons represent a significant problem and make $PbWO_4$ seem less appropriate for the investigated method of TOF measurements than PbF_2.

6.3 Coincidence time resolution with 4×4 segmented crystals

The measurements presented in Section 6.2 were repeated with 4×4 segmented, 7.5 mm thick PbF_2 crystals, which could have different treatments of entry and side surfaces, as described in Section 4.2. As can be seen in Figure 6.10, the coincidences are slightly more confined to channels in geometric

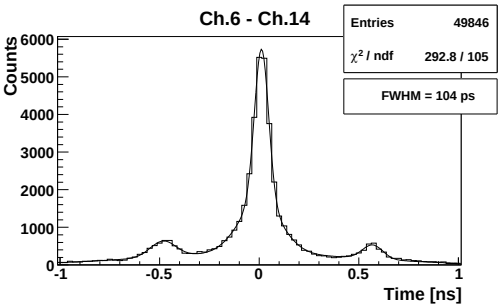

(a) 5 mm (polished, black paint)

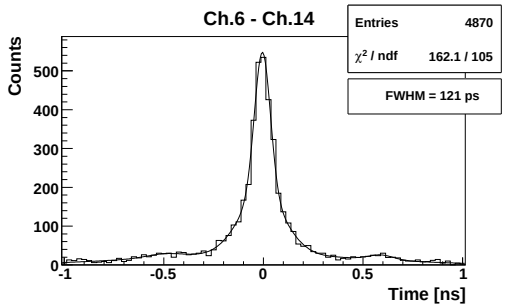

(b) 15 mm (polished, black paint)

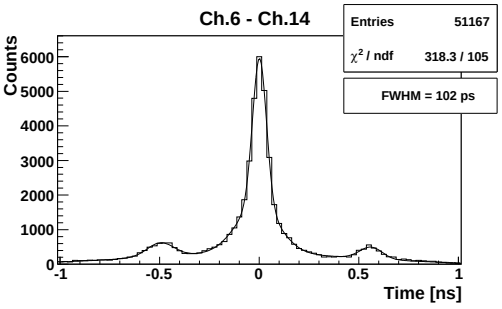

(c) 5 mm (ground, black paint)

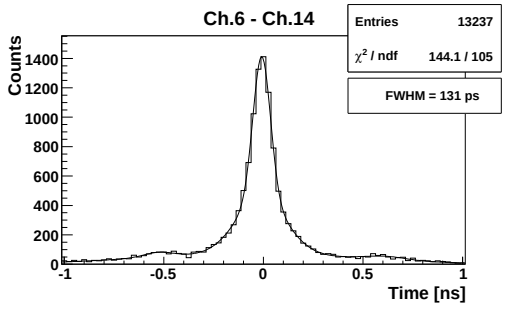

(d) 15 mm (ground, black paint)

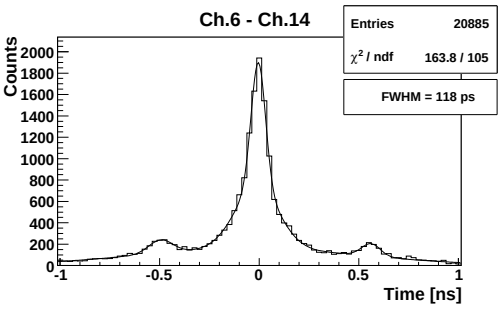

(e) 5 mm (polished, bare surface)

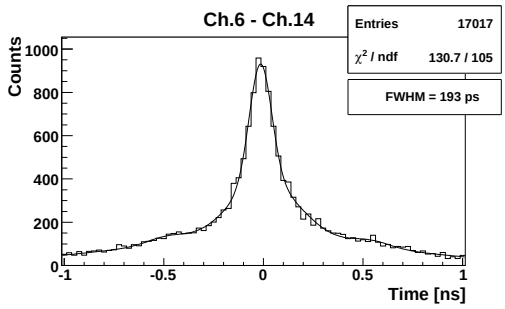

(f) 15 mm (polished, bare surface)

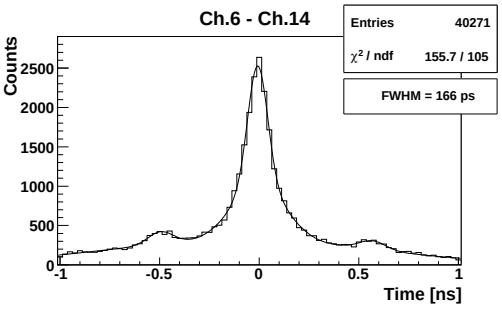

(g) 5 mm (polished, Teflon reflector)

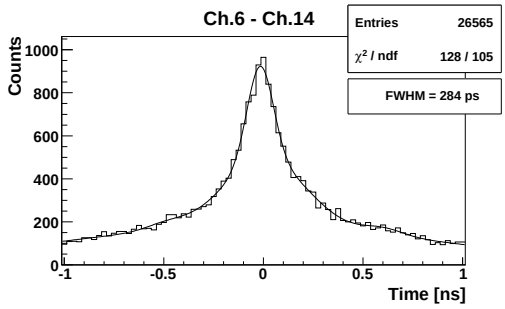

(h) 15 mm (polished, Teflon reflector)

Figure 6.8: The coincidence time distributions between channels 6 an 14, in case of different PbF_2 Cherenkov radiators. The distributions are fitted with a sum of five Gaussian functions.

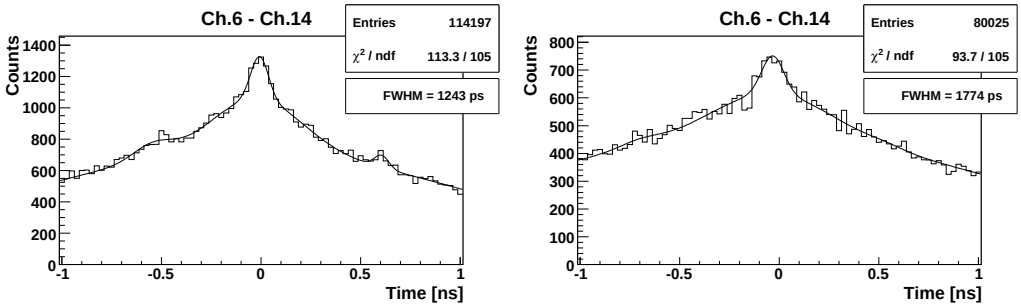

(a) 5 mm (ground, black paint) (b) 15 mm (ground, black paint)

Figure 6.9: The coincidence time distributions between channels 6 an 14, in case of different $PbWO_4$ Cherenkov radiators. The distributions are fitted with a sum of five Gaussian functions.

coincidence with the segmented than they were with the monolithic crystals. There is still some spread of events over neighboring channels, most likely due to Compton scattering, misalignment of crystal arrays to MCP PMTs, propagation of photons through the window and electron propagation effects in the MCP PMT.

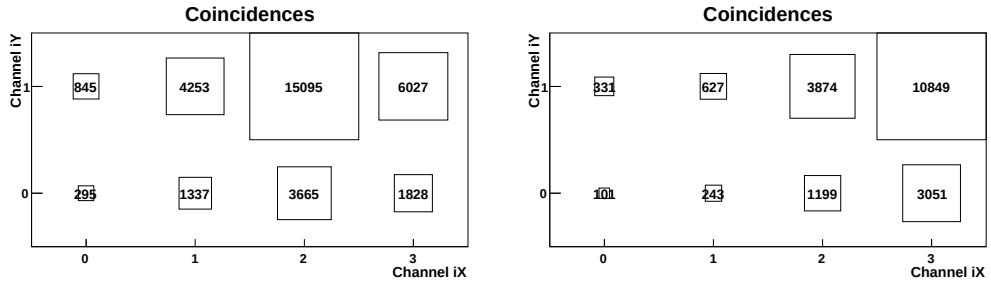

(a) Coincidences with ch.6 (b) Coincidences with ch.7

Figure 6.10: The number of coincidences between 8 channels of JY0005 MCP PMT and channels 6 (located near the center of device) and 7 (located on the edge of device) of JY0002 MCP PMT. The location of channels in the figures matches the locations of respective anode pads on the device (only upper half is shown). 4×4 segmented crystals with entry and side surfaces painted black were used.

The time resolutions obtained for different combinations of surface treatments are listed in Table 6.5. With fully black painted crystals a time resolution with 116 ps FWHM (σ = 39.3 ps) was achieved, which compares well to measurements with monolithic crystals, when the 7.5 mm thickness of segmented crystals is considered. Figure 6.11 shows the coincidence time distributions for different combinations of surface treatments. Very obvious

is an asymmetry in distributions obtained with crystals that had their side surfaces wrapped in Teflon (Figures 6.11d to 6.11f). This asymmetry is not limited to the combination of channels shown, but is present for all pairs of channels. The effect is also visible in the case where the entry surface was left bare, which means that the most likely reason for the asymmetry is caused by differences between the side surfaces of the two Teflon wrapped arrays. Also because of this, in cases with Teflon wrapped side surfaces the FWHM values reported in Table 6.5 are somewhat larger than expected.

Surface treatment		Time resolution [ps]	
entry surface	side surfaces	FWHM	σ
black paint	black paint	116	39.3
bare	black paint	133	41.0
Teflon	black paint	178	49.4
black paint	Teflon	172	44.5
bare	Teflon	245	50.9
Teflon	Teflon	301	63.5

Table 6.5: The timing resolution of the back-to-back setup for different surface treatments of the 4×4 segmented, 7.5 mm thick PbF_2 arrays. The results are reported as the FWHM and σ of the narrow Gaussian, averaged over the eight pairs of readout channels, which are in geometric coincidence.

6.4 Demonstration of position reconstruction

As was demonstrated in previous chapters, an excellent TOF resolution of $\approx$ 100 ps FWHM can be achieved by detecting Cherenkov photons. To demonstrate how such TOF information translates to position resolution, the measurements were performed for different positions of the annihilation gamma source along the LOR. Table 6.6 and Figure 6.12 show the results for five positions of the source, separated by 10 mm, in case of 5 mm thick, black painted PbF_2 crystals. The coincidence time distributions between channels 6 and 14 were fitted with a sum of five Gaussian functions and the position of the source was estimated from the narrow central Gaussian mean position, using Equation (2.26). All of the five estimated source positions are less than 1 mm away from the expected values, and the distributions in Figure 6.12, corresponding to 20 mm shifts, are more than one FWHM away from each other.

The same results, obtained with 15 mm thick, Teflon wrapped PbF_2 crystals, are shown in Table 6.7 and Figure 6.13. Despite much less precise TOF information, the fit resulted in very accurate estimated positions. However, the activity reconstruction might not be so successful if a full TOF PET image reconstruction and a more realistic source distribution were employed. In such a case, a faint signal corresponding to the object of interest (for example

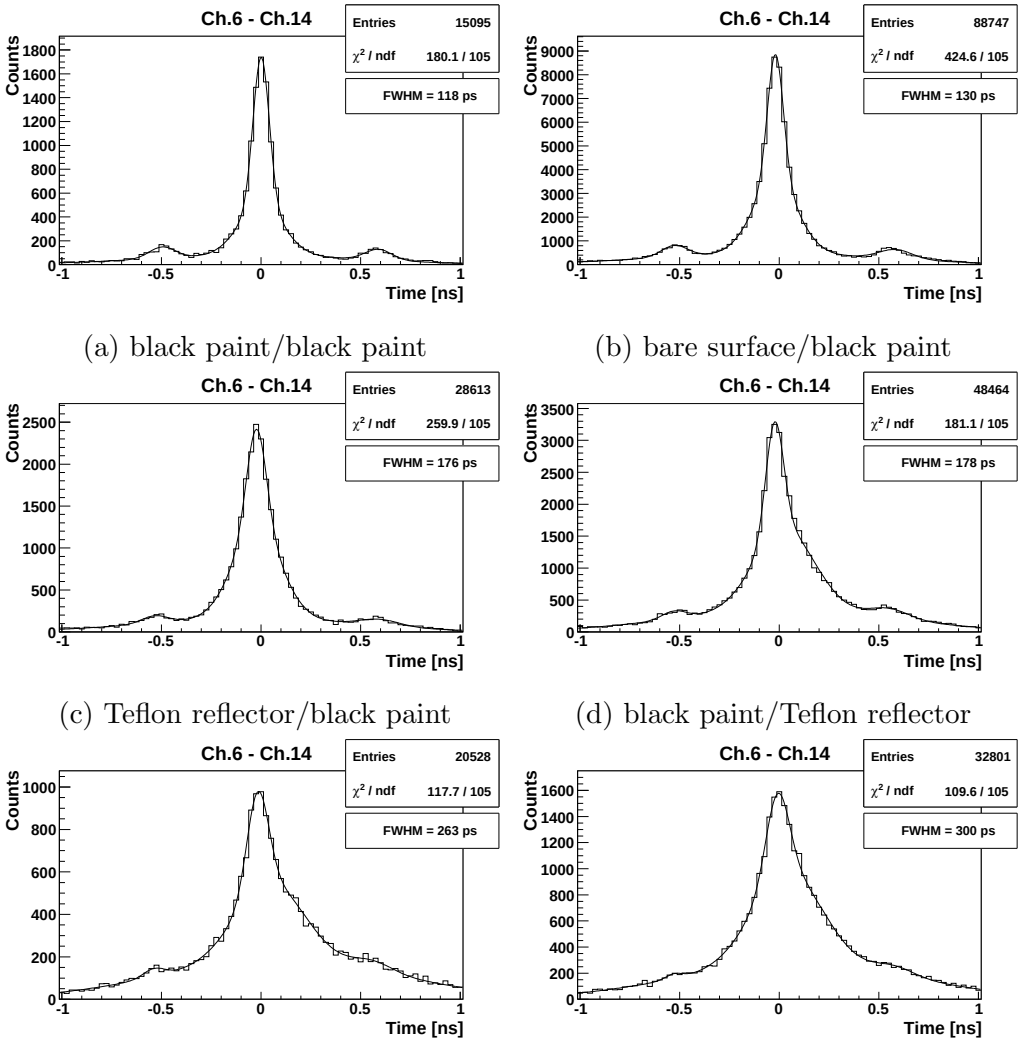

(a) black paint/black paint

(b) bare surface/black paint

(c) Teflon reflector/black paint

(d) black paint/Teflon reflector

(e) bare surface/Teflon reflector

(f) Teflon reflector/Teflon reflector

Figure 6.11: The coincidence time distributions between channels 6 and 14, in case of different surface treatments of the 4×4 segmented, 7.5 mm thick PbF_2 arrays. The distributions are fitted with a sum of five Gaussian functions.

Source position [mm]	FWHM [ps]	σ [ps]	Mean [ps]	Estimated position [mm]
x_0+ 20 mm	98.0	35.3	133.5	20.0
x_0+ 10 mm	99.0	32.1	72.7	10.9
x_0	103	33.6	4.2	0.6
x_0− 10 mm	110	33.6	-60.1	-9.0
x_0− 20 mm	103	34.3	-131.0	-19.6

Table 6.6: The timing resolution FWHM and σ, narrow Gaussian peak mean position and position, estimated from the TOF information, obtained with 5 mm thick, black painted PbF_2 crystals when the source was moved to five positions, displaced by 10 mm.

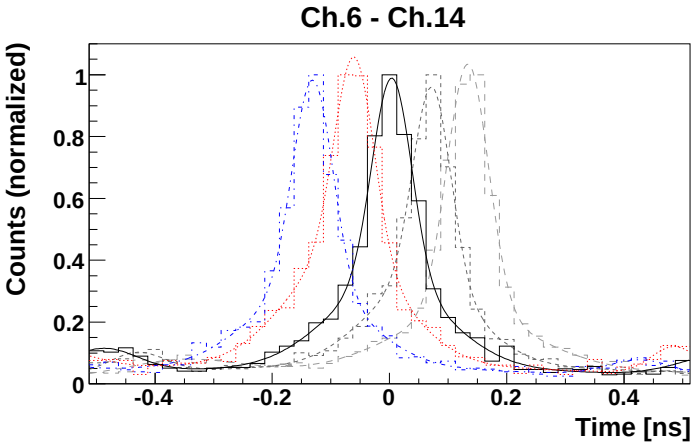

Figure 6.12: The coincidence time distributions between channels 6 and 14, obtained with 5 mm thick, black painted PbF_2 crystals, when the source was moved to five positions, displaced by 10 mm.

a lesion) needs to be distinguished from background noise, which is present due to uncertainties in surrounding tissue activity uptake and image reconstruction artifacts. Although the coincidence time distributions obtained here have a very narrow peak, the tails in the distributions in case of reflective wrapping might present a challenge for the full image reconstruction.

Source position [mm]	FWHM [ps]	σ [ps]	Mean [ps]	Estimated position [mm]
x_0+ 20 mm	312	84.3	133.0	20.0
x_0+ 10 mm	243	63.0	65.8	9.9
x_0	267	61.8	-4.5	-0.7
x_0− 10 mm	289	70.4	-77.8	-11.7
x_0− 20 mm	256	69.5	-148.4	-22.3

Table 6.7: The timing resolution FWHM and σ, narrow Gaussian peak mean position and position, estimated from the TOF information, obtained with 15 mm thick, Teflon wrapped PbF_2 crystals when the source was moved to five positions, displaced by 10 mm.

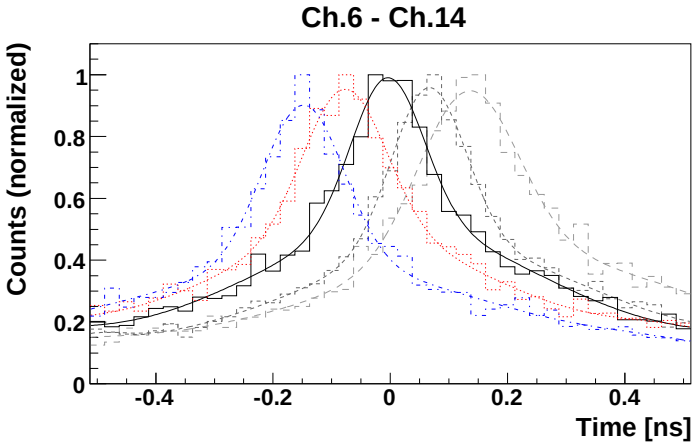

Figure 6.13: The coincidence time distributions between channels 6 and 14, obtained with 15 mm thick, Teflon wrapped PbF_2 crystals, when the source was moved to five positions, displaced by 10 mm.

7 Cherenkov PET Efficiency

A reference gamma detector, consisting of a scintillation crystal and a photomultiplier tube, was used in coincidence with Cherenkov detector in order to estimate the 511 keV gamma detection efficiency of the Cherenkov detector. The reference detector enabled a precise selection of events by providing a measurement of event energy. By selecting only events with measured energy very close to 511 keV on the reference detector, the Cherenkov detector on the other side was hit by the other annihilation gamma with a high degree of confidence. By counting the number of events, detected with Cherenkov detector when annihilation gamma was detected by the reference detector, the efficiency of Cherenkov detector could be estimated.

7.1 Setup

The experimental setup for the efficiency measurements (Figure 7.1) was based on the setup, described in Section 4. One MCP PMT was connected through a readout scheme with MCP PMT channels summed into 4 readout channels (Figure 4.10a). The other MCP PMT was replaced with a reference detector, which consisted of a small BGO scintillation crystal and a photomultiplier tube (Figure 7.2). One of the long sides of the scintillator crystal of dimensions $4.2 \times 4.2 \times 20$ mm^3 was coupled to a Hamamatsu R5900-00-M16 multianode PMT [39], which has a flat, square shaped sensitive surface of 18×18 mm^2. All other surfaces of the scintillator were wrapped in white reflector (Teflon).

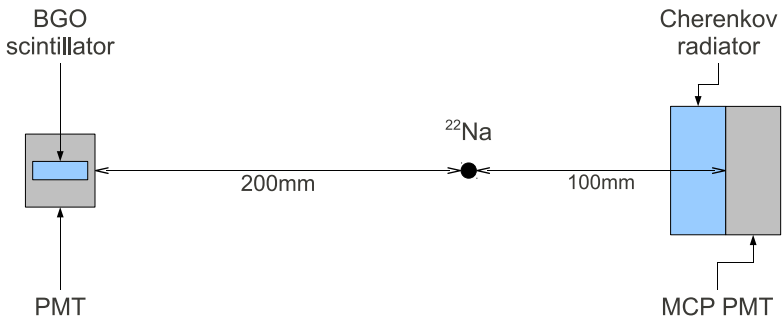

Figure 7.1: Schematic view of the setup used to measure the efficiency of Cherenkov detectors.

Another change to the setup was the distance between the reference detector and the source, which was increased to 200 mm. The small cross section of the reference crystal combined with the large distance from the source ensured a very tight collimation of annihilation gammas on the Cherenkov

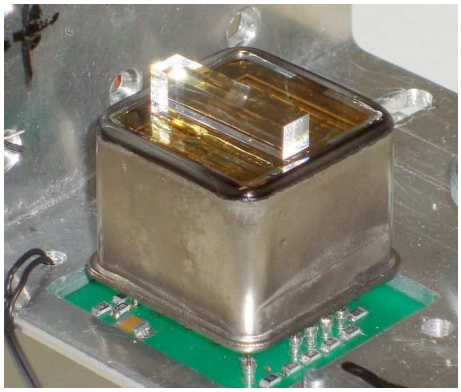

Figure 7.2: The reference detector used to select 511 keV annihilation gammas. The BGO scintillation crystal and the PMT are exposed on the picture, but were covered with white Teflon reflector for the measurements.

radiator. Annihilation gammas which were in coincidence with gammas, detected with the reference detector, were impinging on only $\approx 0.9 \times 0.9$ mm^2 central part of the Cherenkov radiator entry surface. The lead shielding was rearranged, so that the reference detector was located outside the shield. A narrow ($\approx$ 1 cm wide) vertical slit in the shield allowed the reference detector to be exposed to the annihilation gammas in coincidence with the Cherenkov detector, while minimizing the number of events, resulting from Compton scattering of source gammas in the lead shielding (Figure 7.3).

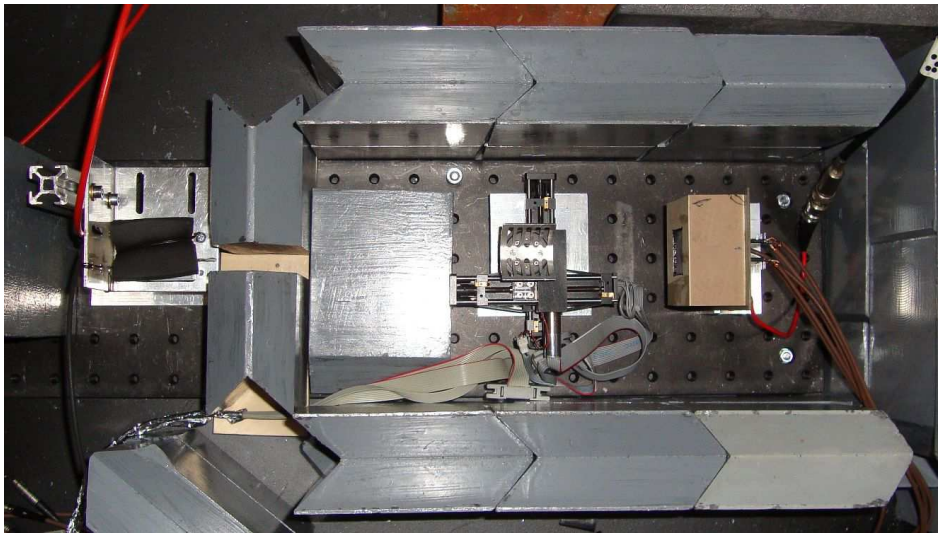

Figure 7.3: The setup used for the efficiency measurements. Visible are the Cherenkov detector (right), the ^{22}Na source holder (middle), the vertical slit in the lead shielding (left) and the reference detector (far left).

The 16 (4×4) PMT anode channels were combined into one readout chan-

nel on the PMT connection and voltage divider board. The PMT readout was slightly different than that of the MCP PMT, due to differences in signal amplitudes. The PMT signal was amplified by a factor of 10x instead of 200x by a Phillips Scientific Model 772 octal bipolar amplifier (300 MHz bandwidth). The amplifier provided two output lines, one of which was lead into a discriminator, from where the readout configuration was the same as for the MCP PMT. The other line led to the QDC through attenuator (Phillips Scientific Model 804), set to attenuation factor of 0.1. The QDC gate for PMT signals was lengthened to 500 ns in order to accommodate the relatively long decay time constant of the scintillator. The measurement was triggered by the PMT.

7.2 Reference detector charge distribution

The charge distribution obtained with the reference detector is shown in Figure 7.4. Since the charge output of the PMT is proportional to the number of photons detected in an event, the obtained charge is a measure of the energy, absorbed in the scintillation crystal. The distribution has all the expected features for a ^{22}Na source: the 511 keV gamma Compton continuum (which is truncated at lower energies due to a relatively high discriminator threshold), the 511 keV gamma photopeak at bin ≈ 500, the 1275 keV gamma Compton continuum and the 1275 keV gamma photopeak. All features are spread by the detector energy resolution of $\sigma_E/E \approx 13\%$.

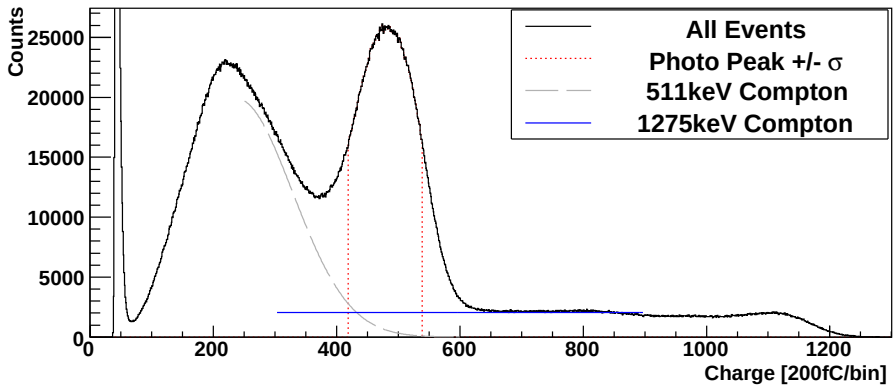

Figure 7.4: The charge distribution as measured by the reference detector. The dotted red lines show the 2 σ_E wide part of the photopeak, which was used for event selection, while the gray dashed and solid blue lines show the 511 keV and 1275 keV gamma Compton continuum contributions respectively.

The role of the reference detector was to select events produced by the 511 keV annihilation gamma. This events are registered in the 511 keV

gamma Compton continuum or photopeak. However some of the Compton continuum events are produced by gammas, which are scattered in the lead shielding used in the experimental setup. The annihilation gammas, which are in coincidence with such scattered events, are most likely not incident on the Cherenkov detector. Events registered in the Compton continuum should therefore not be used, as this would cause uncertainty in efficiency estimation.

The 511 keV photopeak also has a background contribution due to the Compton scattering of 1275 keV gammas, produced by the ^{22}Na source. At the energies of the 511 keV photopeak, the 1275 keV gamma Compton continuum can be approximated by a constant function (Section 3.2.2). The constant can be obtained by fitting (blue line in Figure 7.4) and the number of such events can be estimated.

A 2 σ_E wide interval (marked with dotted red lines in Figure 7.4), centered on the photopeak was chosen as most likely to contain events, produced by 511 keV gamma absorption. As can be seen in Figure 7.4, some Compton scattering events still fall inside this interval. The estimated number of 1275 keV Compton events can be subtracted in efficiency calculation, while the smaller contribution of 511 keV Compton scattered event, falling inside the 2 σ_E interval, contains mostly the wanted events, where the 511 keV gamma was scattered in the reference detector.

7.3 Cherenkov detector event selection

Figure 7.5 shows the charge and time distributions, obtained with the Cherenkov detector composed of JY0005 MCP PMT and a 15 mm thick, black painted PbF_2. The black histograms represent all events detected by the MCP PMT, which includes crosstalk between MCP PMT channels, MCP PMT noise and also detection of random and scatter coincidences. The red histograms were obtained after two cuts on the collected events. The first cut is the maximum charge cut, as described in Section 5.1.1, which suppresses MCP PMT crosstalk, and ensures only one TDC count per event. To improve the comparison between charges of different channels, the charge distributions in Figure 7.5a were baseline corrected. The second cut is the selection of events, where the reference detector registered a hit with energy within 2 σ_E wide interval around the 511 keV photopeak (Figure 7.4), which leaves mostly the events, where a 511 keV gamma was passing through the Cherenkov detector. This second cut excludes many of the wanted events, since it is only 2 σ wide. This however will not effect the estimated efficiency, which will be properly normalized.

The time distributions in Figure 7.5b are not time-walk corrected, and have a very long rise time. This is defined by the scintillation decay of the BGO crystal used in the reference detector that triggers the measurement.

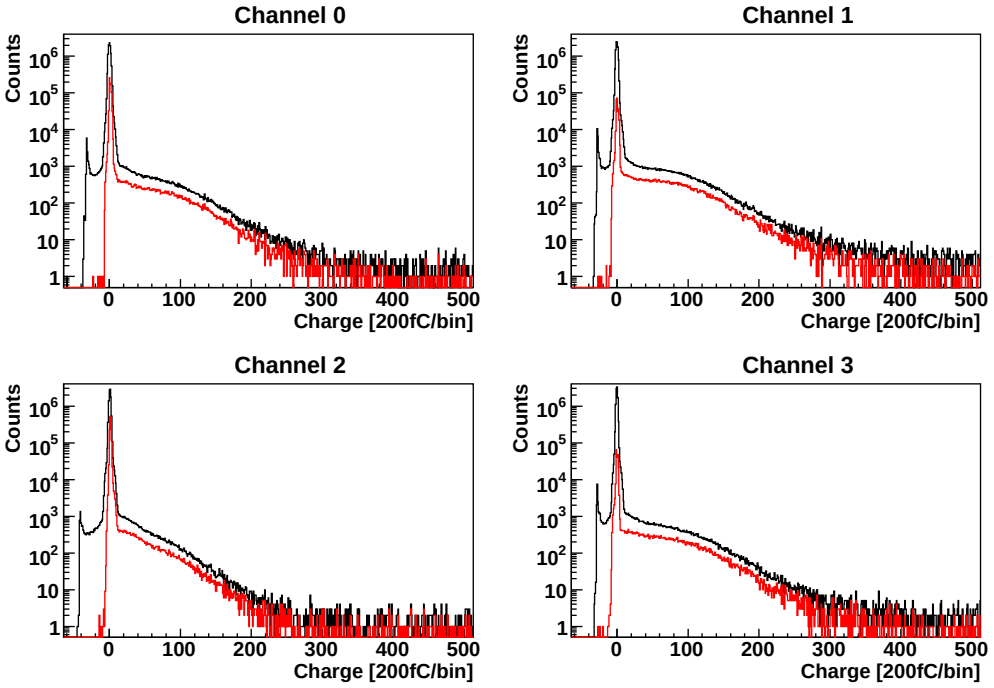

(a) Charge distributions

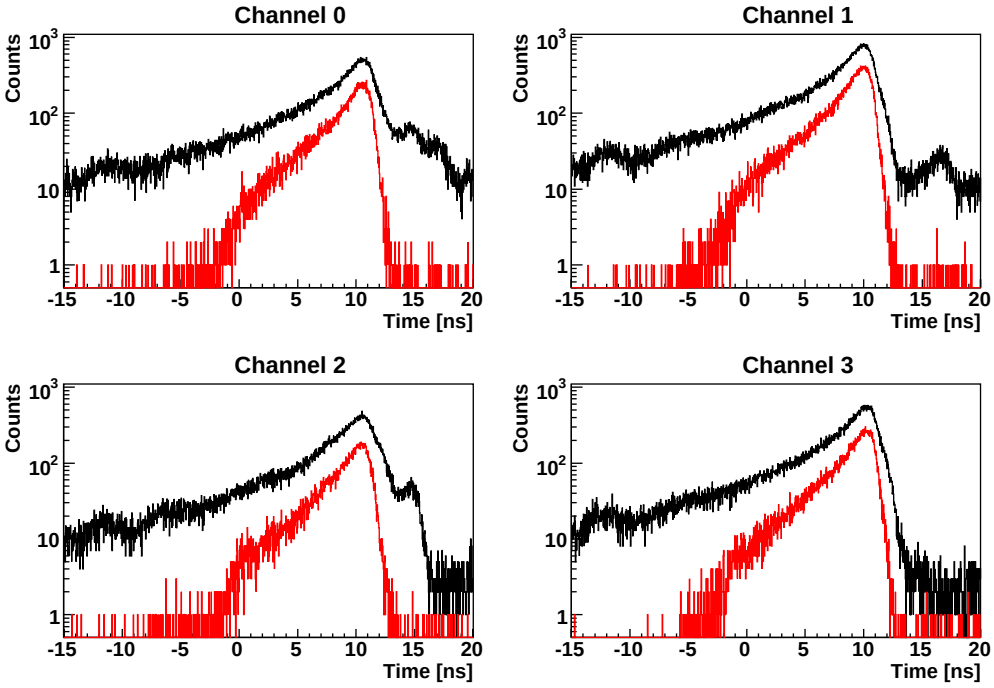

(b) Time distributions

Figure 7.5: The charge and time distributions for the 4 readout channels (each a sum of 4 anode pads) of the MCP PMT. The black histograms include all collected events, while the red histograms have a maximum charge and photopeak cuts applied, as described in the text.

7.4 Efficiency estimation

The 511 keV gamma detection efficiency of the Cherenkov detector can be defined as the number of hits on Cherenkov detector, when the reference detector registered a 511 keV gamma ($N_{MCPPMT/photopeak}$), divided by the number of 511 keV gammas registered on the reference detector ($N_{photopeak}$):

$$\epsilon = \frac{N_{MCPPMT/photopeak}}{N_{photopeak}}. \tag{7.1}$$

The number of hits on Cherenkov detector ($N_{MCPPMT/photopeak}$) was estimated as the number of events, registered by the TDC, after the cuts described in previous section were applied. In other words, $N_{MCPPMT/photopeak}$ is the sum of events in the four red colored TDC histograms in Figure 7.5b. Additional correction was made, by subtracting the number of background events, estimated by fitting the time distributions with cuts in the off-time interval (20−50 ns for distributions in Figure 7.5b). The effect of this correction was negligibly small, the values for efficiency changed by less than 1%.

The number of 511 keV gammas registered on the reference detector was estimated as the number of events inside the 2 σ_E interval in the PMT charge distribution (Figure 7.4), with the Compton scattering background subtracted:

$$N_{photopeak} = N_{2\sigma} - N_{Compton}. \tag{7.2}$$

Here $N_{2\sigma}$ is the total number of events inside 2 σ_E wide interval around the 511 keV photopeak, and $N_{Compton}$ the estimated number events, belonging to the 1275 keV gamma Compton continuum inside the 2 σ_E interval.

An example of efficiency estimation can be made for the measurement with the Cherenkov detector composed of JY0005 MCP PMT and a 15 mm thick, black painted PbF_2, presented in Figures 7.4 and 7.5. From Figure 7.4, the values of $N_{2\sigma} = 2690734$ and $N_{Compton} = 249644$ were obtained. From Figure 7.5b, the number of hits on Cherenkov detector was estimated as $N_{MCPPMT/photopeak} = 146657$. This leads to an efficiency $\epsilon = 6.0\%$.

7.5 Results

Measurements were repeated while changing different parameters of the Cherenkov detector: Cherenkov radiator sample, material, segmentation, thickness and surface treatments. The effects of the MCP PMTs were also investigated.

7.5.1 Radiator sample

Most of Cherenkov radiator crystals were available in two samples, one for each side of the back-to-back setup. The efficiencies for some of the radiator

parameters are gathered in Table 7.1. What can be seen is that the sample to sample variation is very small. This results are also one indication that the re-coupling of the crystal to the MCP PMT, which had to be performed for each change of the radiator parameters, was very consistent and had negligible effect on the results.

Cherenkov radiator					Efficiency [%]	
Material	Polish	Surface	Segmentation	Thickness	Sample 1	Sample 2
PbF_2	polished	black painted	monolithic	15 mm	6.0	6.1
PbF_2	ground	black painted	monolithic	15 mm	6.2	6.1
PbF_2	polished	Teflon wrapped	4×4	7.5 mm	7.3	7.1
PbF_2	polished	black painted	4×4	7.5 mm	5.0	5.1
$PbWO_4$	ground	black painted	monolithic	5 mm	16	16
$PbWO_4$	ground	black painted	monolithic	15 mm	29	29

Table 7.1: The estimated efficiencies of Cherenkov detectors, composed of JY0005 MCP PMT coupled to different Cherenkov radiators. The 4×4 segmented crystals had a bare entry surface.

The estimated efficiency of the $PbWO_4$ Cherenkov radiator is almost a factor of 5 larger than that of the comparable PbF_2. However this value also includes events, produced by scintillations in the $PbWO_4$, which have a significantly worse timing than events produced in Cherenkov process.

7.5.2 Radiator thickness

Table 7.2 lists the efficiencies obtained with Cherenkov radiator of different thicknesses. As expected, the efficiency increases with thickness, however the difference between the thicknesses are not as large as would be expected just by considering the gamma absorption efficiencies (Table 3.3). The propagation of optical photons also needs to be considered. Longer average path in thicker crystal means less Cherenkov photons reach the photodetector due to optical absorption. Additional contribution may come from the photons, which travel near the edge of the crystal and reach the photodetector in the thinner crystal, while they refract out of the crystal through the side surface in the thicker crystal.

Thickness [mm]	Efficiency [%]
5	4.3
10	5.7
15	5.9

Table 7.2: The estimated efficiencies of Cherenkov detectors, composed of JY0005 MCP PMT coupled to PbF_2 crystals with polished, black painted surfaces. The value for thickness of 15 mm is different than the value reported in Table 7.1, because it was obtained in another measurement.

7.5.3 Surface treatment

The results for different treatments of the Cherenkov radiator surfaces are listed in Table 7.3. The crystals wrapped in white Teflon reflector had the largest efficiency, since even photons which leave the crystal have a chance to be reflected back into it and to eventually reach the photodetector. The efficiency for bare crystals can only include direct photons and photons, which reach the photodetector after one or more total internal reflections (inner surfaces of the crystal support mechanism were black, so after a photon exited the crystal it had almost no chance to reflect back and be be detected). The efficiency measured with black painted crystals is even lower than that measured with the bare crystals, which is an indication that the black paint reduces the effective refractive index on the crystal boundary. The solid angle for total internal reflection thus reduces, which leads to a larger fraction of photons which exit the crystal and are absorbed in black paint.

Surface treatment	Efficiency [%]	
	5 mm thick	15 mm thick
black paint	4.3	6.1
bare surface	7.0	12
Teflon reflector	11	18

Table 7.3: The estimated efficiencies of Cherenkov detectors, composed of JY0005 MCP PMT coupled to 5 and 15 mm thick PbF_2 crystals. The surfaces of the crystal were polished and were left bare, painted with black paint or wrapped in white Teflon reflector.

7.5.4 Segmented crystals

In Table 7.4, the efficiencies obtained with all combinations of surface treatments of the segmented crystals are collected. Again the white Teflon reflector wrapping leads to larger efficiencies than bare surfaces, which in turn are better compared to the black painted surfaces. The efficiencies with segmented crystals are smaller than that obtained with unsegmented crystals (Table 7.3) if the effect of radiator thickness is taken into account. The reason is geometrical, as was in the case of different crystal thicknesses (Section 7.5.2): the photons produced near the edge of the crystal under certain angles refract out of the segmented crystals, while the edge would be much farther away in unsegmented crystal, meaning this photons could reach the photodetector.

7.5.5 Effects of MCP PMT

Two measurements with exactly the same Cherenkov radiator (a 15 mm thick black painted PbF_2) but with two different MCP PMTs were performed. The

Surface treatment		Efficiency [%]
entry surface	side surfaces	
black paint	black paint	4.3
bare surface	black paint	5.0
Teflon reflector	black paint	6.3
black paint	Teflon reflector	5.6
bare surface	Teflon reflector	7.3
Teflon reflector	Teflon reflector	8.6

Table 7.4: The estimated efficiencies of Cherenkov detectors, composed of JY0005 MCP PMT coupled to the 4×4 segmented PbF_2 crystals. The surfaces of the crystal were polished and had different treatment applied to the entry and side surfaces.

results for efficiencies, shown in Table 7.5, are in qualitative agreement with expectations, based on the relative PDEs of the two MCP PMTs: the JY0005 MCP PMT has a better efficiency than JY0002. However the difference is much smaller than anticipated. The integral of PDE in the energy range of detectable Cherenkov photons is 3.6 times larger for JY0005 than that for JY0002, while the efficiency is only 1.5 times larger. The most probable explanation for the missing efficiency is the aging effect. The JY0005 MCP PMT has been extensively used for different measurements over many months, while JY0002 was out of use for most of that time. This might have lead to faster degradation of the JY0005 photocathode.

MCP PMT	Efficiency [%]
JY0002	3.9
JY0005	5.9

Table 7.5: The estimated efficiencies of Cherenkov detectors, composed of either JY0002 or JY0005 MCP PMT coupled to 15 mm thick PbF_2 crystals with polished black painted surfaces.

8 Measurements Summary

The performance of Cherenkov detectors for TOF PET can be evaluated by the figure of merit, which includes the effects of both the time resolution and the detection efficiency. Table 8.1 summarizes the experimental results

Radiator	ϵ^2 [%]	FWHM [ps]	FOM [%/ns]
5 mm, black paint	0.18	103	1.8
15 mm, black paint	0.37	132	2.8
5 mm, bare	0.49	125	3.9
15 mm, bare	1.44	186	7.7
5 mm, Teflon	1.21	162	7.5
15 mm, Teflon	3.24	271	12.0
4×4 black/black	0.18	116	1.6
4×4 bare/black	0.25	133	1.9
4×4 Teflon/black	0.40	178	2.2
4×4 black/Teflon	0.31	172	1.8
4×4 bare/Teflon	0.53	245	2.2
4×4 Teflon/Teflon	0.74	301	2.5
Scintillator PET system	10	300	33.3

Table 8.1: The measured values for coincidence detection efficiency (ϵ^2) and time resolution (FWHM) with calculated FOM for different parameters of Cherenkov radiator. For comparison, values for a traditional PET system which uses scintillation light are also included.

and lists the FOM values for different Cherenkov radiators. The FOM was calculated using Equation (2.35), where the FWHM value was used for the TOF resolution. FOM values in Table 8.1 should not be compared to the values in Table 2.5, which were used as a comparison of different scintillation materials and are expressed in different units. The TOF PET performance of Cherenkov radiators can be compared to performance of traditional detector, based on detection of scintillation light, by using values of 10% for coincidence detection efficiency and 300 ps for time resolution. Such values are a bit optimistic if a full PET system is considered, however they are appropriate when a comparison is being made to the simple back-to-back setup, used in experiments with Cherenkov detectors.

The values for FOM in Table 8.1 suggest that the detection efficiency is still more important that the time resolution. Radiators that were not painted black but left bare or wrapped in Teflon have far better FOM. However, for such cases the effects of more pronounced tails in time distributions are not fully included in the FOM value. The performance of bare and Teflon wrapped Cherenkov radiators might be worse than is estimated here, when the full effect of coincidence time distribution shape is introduced into a realistic image reconstruction.

When compared to FOM of a traditional scintillation detector, the per-

formance of black painted Cherenkov radiators is more than a factor of 10 worse. Even the 15 mm thick, Teflon wrapped PbF_2, which is the Cherenkov radiator with the highest FOM, has a factor of 2 worse FOM. However, it should be noted that the detection efficiency was not limited only by the Cherenkov radiators but also by the PDE of photodetectors used.

9 Simulations

Simulations have been performed to better understand the effects, different parameters of the detector have on the results and to investigate the scenarios not possible with the available experimental hardware. The simulations were designed in the GEANT4 toolkit [40]. The basic component of the simulation was a detector, composed of a Cherenkov radiator coupled to a photodetector. All of the parameters which were explored in the experiments, such as the radiator thickness and surface treatment, were included in the simulation. The simulated setup could be composed of a single detector or two detectors in a back-to-back configuration (Figure 9.1). The detectors were then exposed to a simulated source of annihilation gammas. The physical processes, such as gamma absorption and optical photon propagation could then be followed, and results obtained with the simulation could be compared to the experimental results.

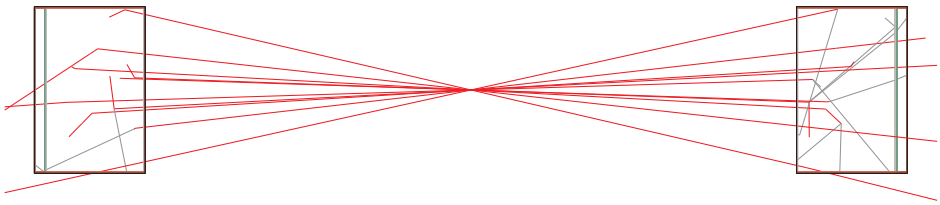

Figure 9.1: The visualization of the GEANT4 simulation, in case of back-to-back detector arrangement. Visible are the detectors, composed of various components (enclosed in black colored boxes), 10 pairs of annihilation gammas (red colored lines) and Cherenkov photons (gray colored lines).

9.1 Simulation parameters

The simulation was performed in version 4.9.2.p02 of GEANT4 toolkit.[†] The construction of the simulation and the parameters used are discussed in the following chapters.

9.1.1 Physics list

A selection of physics modes, relevant for the simulation of Cherenkov PET experiments, was made. The particles included in the simulation and the physics modes connected with them were the following:

[†]This and some later versions of GEANT4 have a bug in the part of the code responsible for propagation of optical photons through optical surfaces, described in [41]. This bug was fixed according to instructions in [41] for the presented simulations.

- **gamma particles:** photoeffect, Compton scattering and gamma conversion;
- **electrons:** multiple scattering, ionization and bremsstrahlung;
- **positrons:** multiple scattering, ionization, bremsstrahlung and annihilation process;
- **optical photons:** absorption and boundary process.

The optical photons were created through the Cherenkov and, where applicable, scintillation processes.

9.1.2 Detector construction

The simulated Cherenkov detector was constructed to closely match the real detectors used in the experiments. The detector was composed of three main parts: Cherenkov radiator, the coupling to the photodetector and the radiator surface.

Cherenkov radiator: A Cherenkov radiator of any dimensions and different compositions could be simulated. The standard size was $25\times25\times15$ mm^3, matching the most commonly used crystal size in the experiments. The radiator could also be segmented, up to a 4×4 segmentation.

Coupling to the photocathode: The exit surface of the Cherenkov radiator was always polished and coupled to the sensitive surface of the photodetector (the photocathode). The simulation included a thin layer (0.2 mm thickness) of optical coupling material and the 1.5 mm thick glass window of the photodetector. The refractive index of both materials was set to n=1.5 for all wavelengths, and a perfect transmission characteristics were presumed. The effect of the window transmission was taken into account in the PDE of the photodetector.

The radiator surface: The radiator entry surface and the four side surfaces were implemented in a way, that enabled the simulation of different surface treatments investigated by experiments. This five surfaces of the radiator were simulated to be in contact with thin (0.1 mm thick) layers of plastic material, used to represent the paint or wrapping of the surfaces. The wrapping/paint was simulated as a diffuse reflector with the specified reflectivity. A thin boundary layer between the surface and the wrapping was included in the simulation. The three surface treatments examined in the experiments could be simulated using this approach in the following ways:

- **Bare surface:** The bare surface was simulated, by setting the refractive index of the boundary layer to n=1.0 and the reflectivity of the paint to R=0. In this way the optical processes on the interface are correctly simulated and the photons are stopped as soon as they leave the radiator.

- **Teflon wrapped surface:** The refractive index of the boundary layer was set to n=1.0, to simulate a thin layer of air between the radiator and the wrapping. The reflectivity was set to R=1.0, in order to best see the effects of the reflective wrapping.

- **Black painted surface:** The refractive index was set to n>1.0, while the reflectivity was set to R=0. Although the exact effect of the black paint used for experiments was not known, a refractive index higher than n=1.0 increases the fraction of optical photons, which are refracted out of the radiator. This in turn reduces the fraction of photons, detected after total internal reflections from radiator sides, which is associated with worsening of the Cherenkov photon detection time resolution. A refractive index of n=1.5 was presumed for the paint material in the simulations.

The optical interfaces on the entry surface and the four side surfaces were defined separately, so that different surface treatments could be applied. For example, a 4×4 segmented radiator array with entry surfaces covered with Teflon tape and the side surfaces painted with black paint could be simulated. All of the optical interfaces were modeled using the GEANT4 "*unified*" optical surface model [42].

9.1.3 Material properties

Most of the required material properties are derived by the GEANT4 itself, based on the definition of material density and elemental composition. The densities used for simulation of PbF_2 and $PbWO_4$ crystals are specified in Table 3.1. However the optical properties of the materials and optical boundaries need to be defined by the user. Cherenkov photons are only produced and the optical photons are only propagated inside the energy range, where the refractive index of enclosing material is defined. The energy interval between 1.55 eV and 6.2 eV (wavelength interval between 200 nm and 800 nm) was used.

The values of refractive indices of the PbF_2 and $PbWO_4$ crystals, used in the simulation, were calculated from the first two terms of the Sellmeier law (Section 3.4.2). For $PbWO_4$, an average of ordinary and extraordinary indices was used. The values used for the simulation are shown in Figure 9.2. The refractive index between 200−240 nm and 200−330 nm for PbF_2 and $PbWO_4$ respectively, was approximated as having a constant value. This has no effect on the results for detected photons, since photons generated in this wavelength range are absorbed before they can exit the Cherenkov radiator.

The values for optical absorption lengths were estimated from the transmission data, shown in Figure 3.7, by taking into account the thickness of

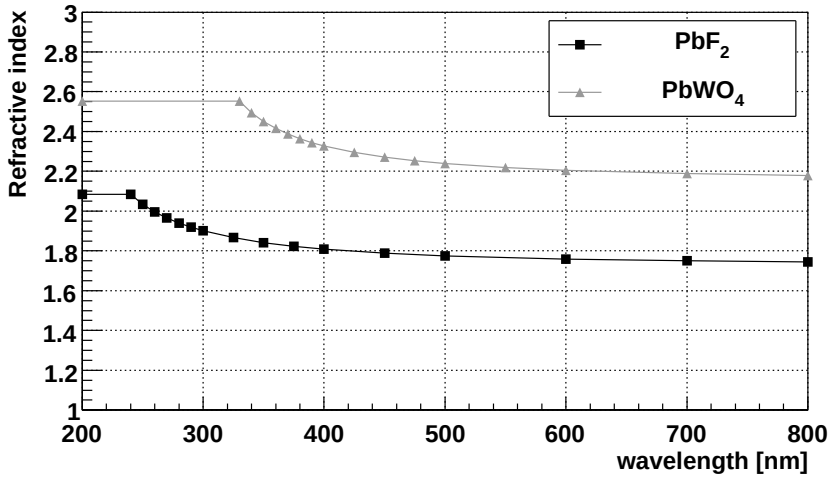

Figure 9.2: The values for refractive index of PbF_2 and $PbWO_4$ crystals, used for the simulation.

the samples and the reflective losses at the two crystal/air boundaries:

$$\mu_{op}(\lambda) = -\frac{d}{ln\left(\frac{T(\lambda)}{T_{max}(\lambda)}\right)}, \tag{9.1}$$

where μ_{op} is the optical absorption length, d the thickness of the sample, T the measured transmission and T_{max} the maximum transmission, limited by perpendicular reflections at the two crystal/air boundaries:

$$T_{max}(\lambda) = 1 - \frac{2R(\lambda)}{1 + R(\lambda)}. \tag{9.2}$$

Here R is the reflection coefficient for a single crystal/air boundary:

$$R(\lambda) = \left|\frac{1 - n(\lambda)}{1 + n(\lambda)}\right|^2. \tag{9.3}$$

The obtained values, used for the simulation, are shown in Figure 9.3.

The scintillation properties of $PbWO_4$, listed in Table 3.1, were included in the simulation. The exact shape of the scintillation emission spectrum was not provided by the producer. An approximation for the spectrum was constructed, consisting of two Gaussian distributions, centered at the producer specified values for scintillation peaks of the two components (440 nm for fast and 530 nm for slow component). The fast/slow component ratio was set to 70/30%, which is consistent with ratios reported in [43, 44]. Figure 9.4 shows the so constructed emission spectrum in comparison to the spectrum measured in [45].

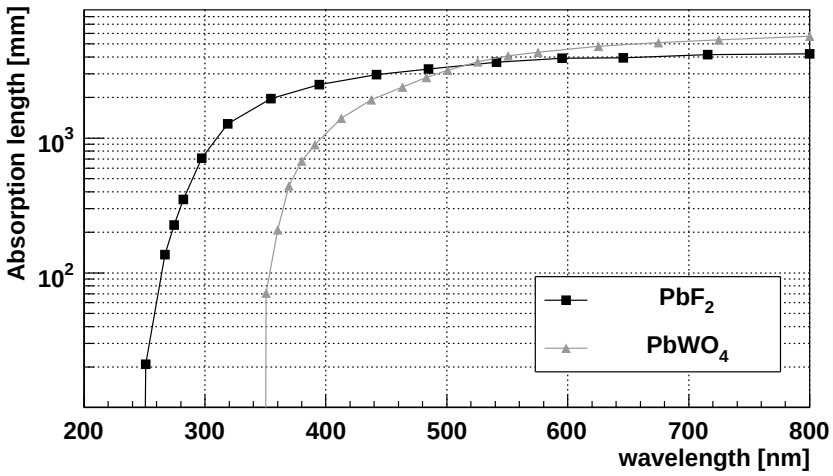

Figure 9.3: The values for optical absorption length of PbF_2 and $PbWO_4$ crystals, used for the simulation.

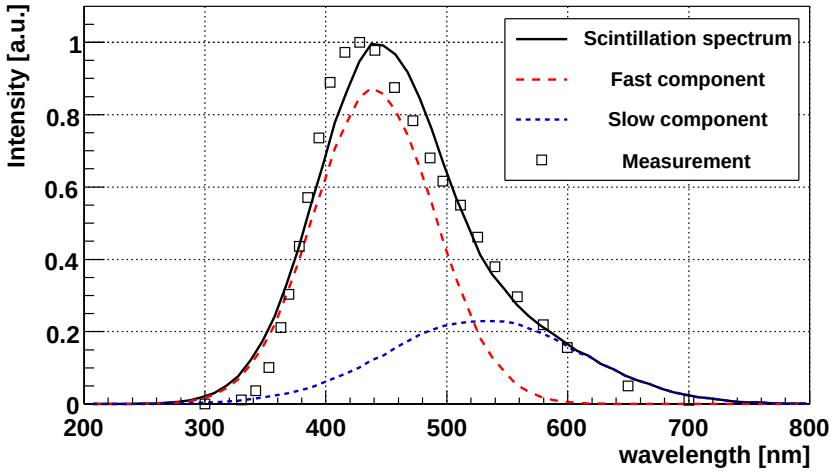

Figure 9.4: The scintillation emission spectrum, used to simulate the $PbWO_4$ crystals (full black line). Also shown are the contributions of the fast (red line) and slow (blue line) components and the scintillation spectrum, as measured in [45].

9.1.4 The photodetector

The photocathode was covering the whole exit surface of the window, which was of the same size as the exit surface of the Cherenkov radiator. This means that for a radiator with 25×25 mm^2 cross section, the sensitive surface of the simulated photodetector was slightly larger than that of the MCP PMTs used in the experiments, which had an area of 22.5×22.5 mm^2. The propagation of the optical photons was stopped as soon as they reached the photocathode.

The PDE of the photodetector was taken into account in the simulation. By default, the PDE of JY0005 MCP PMT (Section 4.1) was used. One way that the PDE could be implemented is to propagate all optical photons, look up the PDE at the wavelength of each photon reaching the photocathode, and only save a randomly selected portion of them, corresponding to the PDE. However, a significant improvement in simulation performance is achieved if the random selection of photons, which are to be detected according to the PDE, is performed at the moment of photon production. In this way the photons, which would anyway be rejected once reaching the photocathode, were not propagated at all. The latter approach was used in the presented simulations.

The time response of the photodetector could also be included, by assigning to each detected photon a time delay, randomly selected according to the experimental time distributions obtained by illuminating the MCP PMTs with laser pulses (Section 5). However, for most of the simulations the effect of the photodetector time response was not taken into account, in order to better expose the effects of the Cherenkov radiator itself.

9.1.5 Generation of primary particles

Different configurations of primary particle source were used in the simulations. For investigations of processes inside a single Cherenkov detector, 511 keV gammas were randomly generated with direction perpendicular to the radiator entry surface and the point of intersection uniformly distributed over the radiator entry surface. When the coincidences between two detectors in back-to-back configuration were simulated, the ^{22}Na source used in the experiments was simulated as a simple point source of perfectly collinear coincident 511 keV gammas. The gammas were randomly generated with isotropic angular distribution and the simulation was only conducted for events, where the two gammas were generated within an angle, which resulted in the two gammas intersecting the entry surfaces of the Cherenkov radiators.

9.2 Simulation results

The simulation enabled a close investigation of every step from gamma absorption to optical photon detection. The following chapters present the simulation results for each step. Results in chapters 9.2.1−9.2.8 were obtained with a simulation of a single Cherenkov detector, exposed to 511 keV gammas uniformly distributed over and perpendicular to the radiator entry surface. Results in chapter 9.2.9 were obtained with a back-to-back setup and a point source of isotropically distributed annihilation gammas.

9.2.1 Gamma interactions

The first step required for the Cherenkov method of 511 keV gamma detection is that the gamma interacts with the radiator material. To estimate the fraction of incident gammas interacting, the gammas which interacted at least once either through photoeffect of Compton scattering were counted. Once divided by the number of generated gammas, the values presented in Table 9.1 were obtained. Although not representing exactly the same quantity, this values are almost exactly the same as the gamma absorption efficiencies listed in Table 3.3. Also the fraction of events, where the first interaction is the photoeffect is consistent with expectations (Section 3.5.2).

d [mm]	Interacting fraction [%]		Photoeffect fraction [%]	
	PbF_2	$PbWO_4$	PbF_2	$PbWO_4$
5	41.6	42.0	49.1	45.7
10	65.6	66.1	48.8	45.4
15	79.7	80.1	48.8	45.4
20	88.0	88.3	48.7	45.3
25	92.9	93.1	48.7	45.3
30	95.8	96.0	48.6	45.3

Table 9.1: The fraction of incident 511 keV gammas interacting with PbF_2 and $PbWO_4$ crystals of different thicknesses and the fraction of events, were the first interaction is the photoeffect.

9.2.2 Electron production

The electrons produced in the radiator either through photoeffect of Compton scattering were counted. Their initial energy is shown in Figure 9.5. Clearly visible are the photopeaks at energies of initial gamma (511 keV) minus the binding energy of K shell electrons (88.005 keV for lead and 69.525 keV for tungsten [23]), the Compton continuum and the Compton edge. It is important to consider that the distributions include multiple interactions: a gamma may undergo one or more Compton scatterings, and may exit the radiator or end its path with a photoeffect. A feature, resembling a reversed

Compton edge at approximately 100 keV, and a continuous distribution of electrons produced via photoeffect, are a result of photoeffect of gammas which initially undergo Compton scattering.

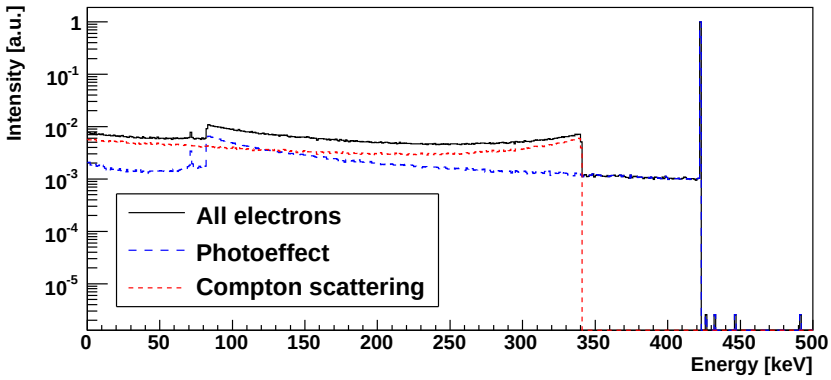

(a) PbF_2

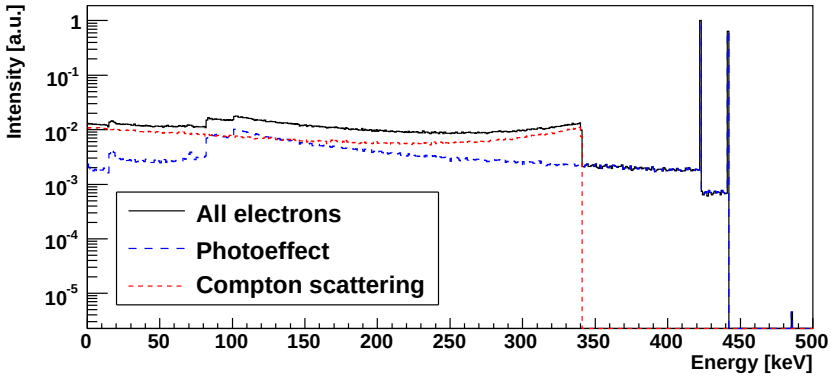

(b) $PbWO_4$

Figure 9.5: Energy distributions of electrons produced by 511 keV gammas in 15 mm thick PbF_2 and $PbWO_4$ crystals. Also shown are the separate contributions from photoeffect and Compton scattering.

Table 9.2 lists some of the electron production statistics, where the values expressed per interacting gamma were obtained by dividing the value per incident gamma with fraction of gammas interacting with the radiator (Table 9.1). According to this results, on average approximately one electron with energy high enough to produce Cherenkov photons is produced for each incident gamma in 15 mm thick PbF_2 and $PbWO_4$ crystals.

	PbF_2	$PbWO_4$
e^-/incident γ	1.22	1.26
e^-/interacting γ	1.53	1.57
fraction of e^- above T_{Thr} [%]	76.6	87.9
Photoeffect fraction [%]	41.6	44.1

Table 9.2: Statistics of electron production in 15 mm thick PbF_2 and $PbWO_4$ crystals: average number of electrons produced per incident and interacting gamma, fraction of electrons above Cherenkov threshold and fraction of electrons produced via photoeffect.

9.2.3 Photon production

Figure 9.6 shows the wavelength distributions of produced optical photons. As can be seen in Figure 9.6a, most of the Cherenkov photons are produced at lower wavelengths, indicating that good radiator optical transmission and photodetector PDE are especially important there. In $PbWO_4$, a dominant contribution to the number of produced optical photons comes from the scintillation photons (Figure 9.6b).

In case of PbF_2, the value for the number of produced Cherenkov photons per interacting gamma, listed in Table 9.3 is in good agreement with the estimated number of 13.7 Cherenkov photons (Section 3.5.3). At this point, $PbWO_4$ still seems to be a better Cherenkov radiator. This will change as the optical absorption is taken into account in the next chapter.

	PbF_2	$PbWO_4$
Ch. photons/interacting γ	15.1	22.2
Ch. photons/e^- above T_{Thr}	12.8	16.0
Scint. photons/interacting γ	-	89.7

Table 9.3: Statistics of photon production in 15 mm thick PbF_2 and $PbWO_4$ crystals: the average number of Cherenkov and scintillation photons produced per interacting gamma and the average number of Cherenkov photons per electron, produced above the Cherenkov threshold.

The simulation was also used to extract the direction of produced Cherenkov photons. Figure 9.7 shows the distribution of the angle between the initial direction of Cherenkov photons and direction of incident gammas (which is perpendicular to the radiator entry surface). As can be seen, the distribution resembles an isotropic angular distribution. However there is a slight preference for the forward direction − only 41.2% of the photons are produced in the backward direction. This can be explained by the contribution from electrons, produced via Compton scattering, which receive more energy when the gamma is scattered at large angles (Equation (3.12)). Although the electron soon scatters under large and unpredictable angle, the

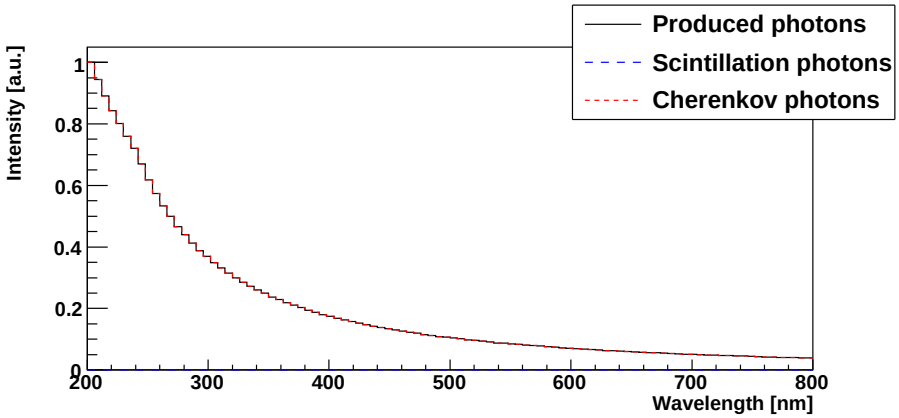

(a) PbF_2

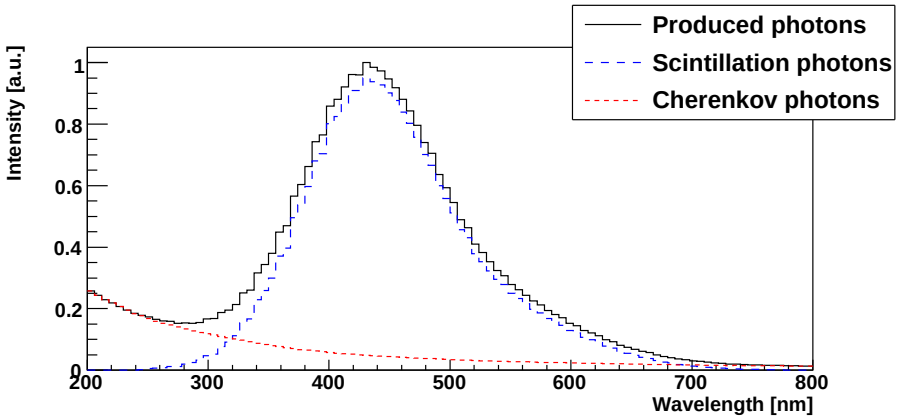

(b) $PbWO_4$

Figure 9.6: Wavelength distributions of photons produced by 511 keV gamma interactions in 15 mm thick PbF_2 and $PbWO_4$ crystals. Also shown are the separate contributions from Cherenkov and scintillation photons.

first Cherenkov photons may still preferentially be produced in the initial direction of the electron.

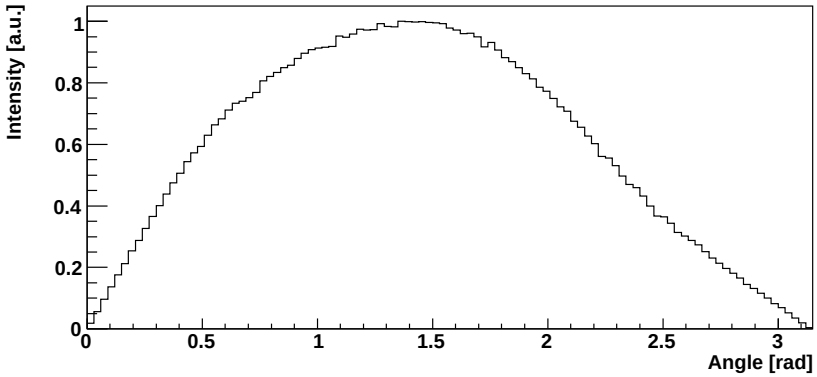

Figure 9.7: The distribution of Cherenkov photon production angle, relative to the incident gamma direction.

It is important to remember that the results presented in this chapter may not be the most accurate, since the refractive index below the optical transmission cutoff wavelength (250 nm for PbF2 and 350 nm for $PbWO_4$) was approximated with a constant value (Figure 9.2).

9.2.4 Photon propagation

Table 9.4 lists the simulation results for optical photons that reach the photocathode. Now the optical absorption of the radiator, the surface treatment of the radiator entry and side surfaces and the optical coupling to the photodetector all contribute to the results. However the photodetector PDE is still not taken into account.

	PbF_2			$PbWO_4$
	Black paint	Bare surface	Teflon	Black paint
All/interacting γ	2.11	3.27	3.68	1.27
Direct/interacting γ	1.51	1.51	1.52	0.87
Reflected/interacting γ	0.59	1.76	2.16	0.40

Table 9.4: Simulation results for the average number of Cherenkov photons reaching the photocathode per interacting gamma, in case of different 15 mm thick radiators and surface treatments. The scintillation photons are not counted in the case of $PbWO_4$.

As can be seen, the number of direct photons (photons reaching the photocathode without reflections at radiator side or entry surfaces) for PbF_2 is now significantly larger than that of $PbWO_4$. The number of photons,

reaching the photocathode after one or more reflections depends on the surface treatment. Black paint, as simulated here, stops most of the reflected photons by decreasing the total internal reflection angle and stopping the photons, once they exit the radiator. Photons are also stopped after exiting the radiator in case of bare surface, however in this case, a larger fraction of photons undergoes total internal reflections, which eventually guide a larger fraction of them to the photocathode. Compared to the bare surfaces the Teflon wrapping only increases the number of photons at the photocathode by a small amount, since most of the photons undergo total internal reflections in both cases.

9.2.5 Photon detection

Figure 9.8 and Table 9.5 show the results obtained, when the PDE of the photodetector was also taken into account. Additionally, only the first photon reaching the photocathode in an event was counted which reflects the fact that experimental setup was triggered by the first pulse from the MCP PMT.

The wavelength distributions of detected photons in Figure 9.8 are basically the distributions of produced photons in Figure 9.6, suppressed by a combination of radiator optical absorption and the photodetector PDE (which in turn is truncated at lower wavelengths by the window optical absorption).

	PbF_2			$PbWO_4$
	Black paint	Bare surface	Teflon	Black paint
Ch. photons/interacting γ	0.14	0.21	0.23	0.072
Scint. photons/interacting γ	-	-	-	0.47

Table 9.5: Simulation results for the average number of photons detected per interacting gamma, in case of different 15 mm thick radiators and surface treatments. The PDE of JY0005 MCP PMT was used.

It can be seen from values in Table 9.5 that very few of the produced Cherenkov photons survive the propagation to the photocathode and the probability for detection (the PDE). There is only a 14% probability that a Cherenkov photon is detected per interacting gamma in black painted, 15 mm thick PbF_2, coupled to a photodetector with JY0005 MCP PMT characteristics.

The effect of the photodetector PDE is illustrated in Figure 9.9 and Table 9.6, where the PDEs of the three MCP PMTs available for the experiments (Figure 4.6 and Table 4.1) were used. As can bee seen, the photodetector PDE has a large effect on the number of detected photons: a factor of 3.4 more photons are detected with the simulated JY0005 compared to JY0002 MCP PMT.

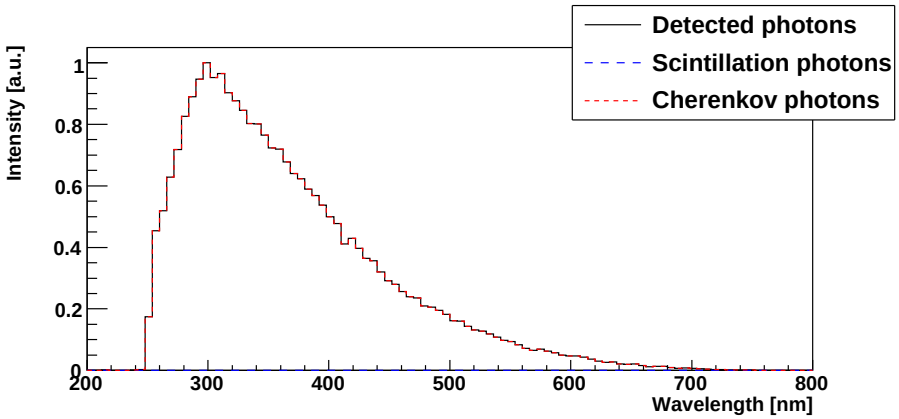

(a) PbF_2

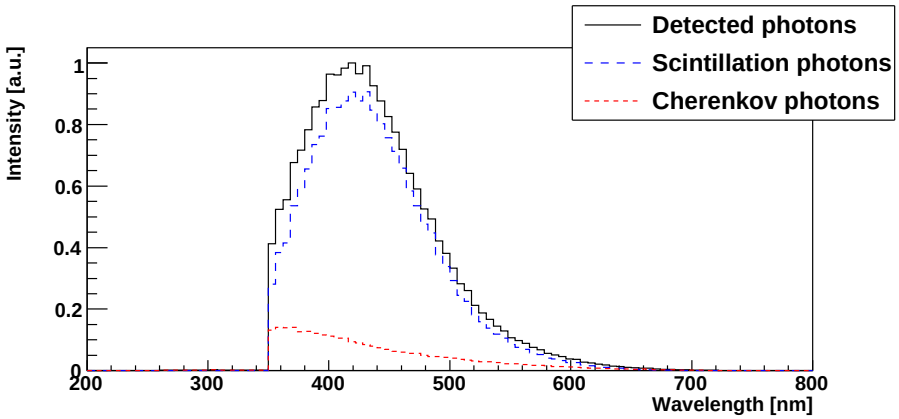

(b) $PbWO_4$

Figure 9.8: Wavelength distributions of photons detected with 15 mm thick PbF_2 and $PbWO_4$ radiators, coupled to a photodetector with PDE of JY0005 MCP PMT. Also shown are the separate contributions from Cherenkov and scintillation photons.

	PDE		
	JY0002	JY0005	JY0008
Ch. photons/interacting γ	0.041	0.14	0.089

Table 9.6: Simulation results for the average number of Cherenkov photons detected per interacting gamma, in case of different photodetector PDEs. The Cherenkov photons were produced in 15 mm thick, black painted PbF_2 crystal.

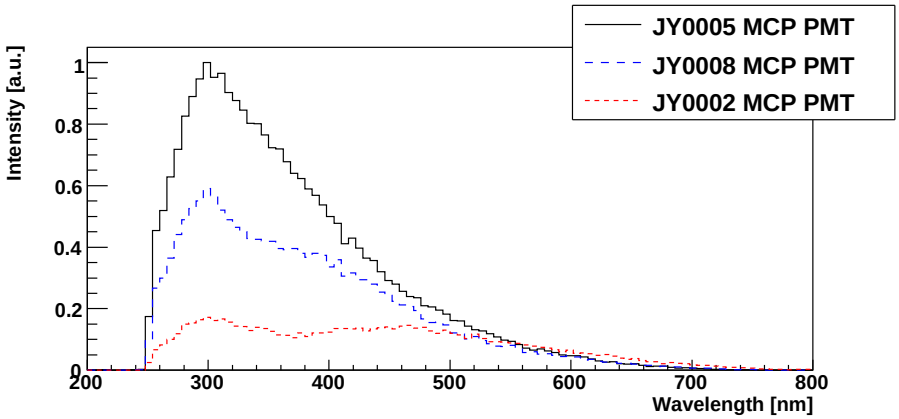

Figure 9.9: Wavelength distributions of Cherenkov photons detected with the PDEs of the three MCP PMTs used in experiments. The Cherenkov photons were produced in 15 mm thick, black painted PbF_2 crystal.

9.2.6 Annihilation gamma detection efficiency

The values in Table 9.5, expressed in terms of incident gamma instead of interacting gamma, represent the 511 keV gamma detection efficiency of a single detector. Table 9.7 lists the detection efficiencies for different Cherenkov radiator thicknesses, where the values for $PbWO_4$ also include the contribution from scintillation photons. Tables 9.8 and 9.9 contain the detection efficiencies for different surface treatments of the monolithic and segmented crystals respectively. The detection efficiencies in case of different photodetector PDEs are collected in Table 9.10.

Thickness [mm]	Efficiency [%]	
	PbF_2	$PbWO_4$
5	6.2	21
10	9.5	35
15	11	43

Table 9.7: The resulting simulated efficiencies of Cherenkov detectors, composed of JY0005 MCP PMT coupled to crystals with polished black painted surfaces. Results for $PbWO_4$ include the contribution from the scintillation photons.

The simulation results for detection efficiencies are within a factor of 2 from the values obtained by the experiments, however the discrepancies are not consistently in the same direction. For example, the simulated efficiency for 15 mm thick, black painted PbF_2 is a factor of 1.8 larger than the measured efficiency, while this factor drops to 1.0 in case of Teflon wrapping of the same crystal. This would mean that too many photons are detected in the simulation with black painted surfaces.

Surface treatment	Efficiency [%]	
	5 mm thick	15 mm thick
black paint	6.2	11
bare surface	8.3	16
Teflon reflector	9.1	18

Table 9.8: The resulting simulated efficiencies of Cherenkov detectors, composed of JY0005 MCP PMT coupled to 5 and 15 mm thick PbF_2 crystals. The surfaces of the crystal were polished and were left bare, painted with black paint or wrapped in white Teflon reflector.

Surface treatment		Efficiency [%]
entry surface	side surfaces	
black paint	black paint	6.7
bare surface	black paint	8.0
Teflon reflector	black paint	9.2
black paint	Teflon reflector	8.2
bare surface	Teflon reflector	11
Teflon reflector	Teflon reflector	12

Table 9.9: The resulting simulated efficiencies of Cherenkov detectors, composed of JY0005 MCP PMT coupled to the 4×4 segmented, 7.5 mm thick PbF_2 arrays. The surfaces of the crystal were polished and had different treatment applied to the entry and side surfaces.

MCP PMT	Efficiency [%]
JY0002	3.3
JY0005	11
JY0008	7.1

Table 9.10: The resulting simulated efficiencies of Cherenkov detectors, composed of either JY0002, JY0005 or JY0008 MCP PMT coupled to 15 mm thick PbF_2 crystals with polished black painted surfaces.

However, let's assume that the PDE of JY0005 MCP PMT used in the experiments was a factor of 2 lower than the PDE values used in the simulation (due to the aging of the photocathode, see Section 7.5.5). This seems reasonable, when comparing the simulated and measured efficiency vales in case of JY0002 MCP PMT, which are very similar. In this case the simulation of black painted surfaces seems to be in good agreement with experimental result. However, now too few photons are detected in the simulations with bare and especially Teflon wrapped surfaces, even though perfect reflectivity of the wrapping was presumed in the simulation. It is also worth noting that the discrepancies increase with the radiator thickness, which indicates that the radiator side surfaces play an important role.

Changing the radiator surface parameters to introduce a less polished surface (using the ground surface with a large fraction of reflections still treated as occurring on a polished surface) did increase the efficiency for all surface treatments, but more so for the bare and Teflon wrapped surfaces than for the black painted surfaces. This made the results of the simulations more consistent for all surface treatments, which might suggest that the crystals used in the experiments were not perfectly polished. Scattering on optical imperfections in the crystal, which was not simulated but is most likely present in real crystals to some extent, could also contribute to this end. Despite this, all of the following simulations were performed with a perfectly polished surfaces, in order to better expose other effects contributing to final results.

9.2.7 Intrinsic suppression of scatter events

In full PET systems, an unwanted background is introduced by the scatter coincidences, which are created when 511 keV annihilation gamma undergoes Compton scattering in the patients body or elements of the PET device. In traditional PET measurements, such events are rejected on the basis of energy discrimination, i.e. only events with the measured energy close enough to 511 keV are accepted. The energy information is obtained from the number of scintillation photons detected. In the investigated method of annihilation gamma detection, at most a few Cherenkov photons are detected per event, which is not enough for any kind of incident gamma energy measurement. This means that coincidences due to scattered gammas cannot be separated from true coincidences and their unwanted contribution to the reconstructed images cannot be removed. However, there is an intrinsic suppression of scattered events, due to a reduced detection efficiency for gammas with lower energy. When undergoing Compton scattering, the gamma looses some of its initial energy, depending on the scattering angle (Equation (3.11)).

Figure 9.10a shows the detection efficiency of 15 mm thick, black painted PbF_2 crystal coupled to a photodetector with JY0005 MCP PMT proper-

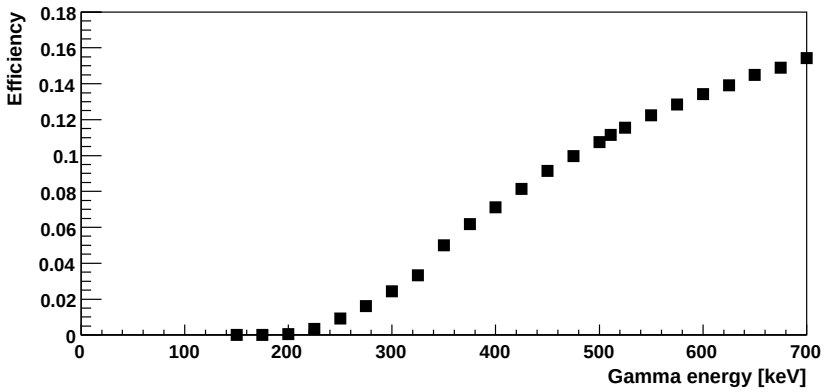

(a)

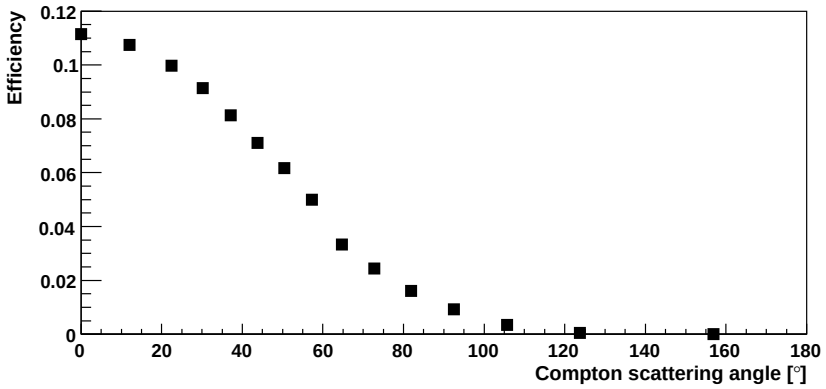

(b)

Figure 9.10: Dependence of detection efficiency as a function of the energy of the incident gamma (a) and as a function of the Compton scattering angle of gammas with initial energy of 511 keV (b).

ties, when exposed to gammas with different initial energies. Figure 9.10b shows the same dependence, expressed in terms of Compton scattering angle for 511 keV gammas. The detection efficiency drops to zero when the gamma energy is below 150 keV. This is expected when considering that the Cherenkov threshold for PbF_2 is a about 104 keV. Even though the gamma energy is still above the threshold, the electrons produced by such low energy gammas are slowed below the threshold before they can emit any Cherenkov photons.

9.2.8 Photon detection timing

The difference between the time of arrival and the primary particle creation time was histogrammed for the first photons, reaching the photocathode. Figure 9.11 shows the results in case of black painted and Teflon wrapped 15 mm thick PbF_2. The offset in the arrival of first photons is a consequence of primary particle travel time from the point of origin (here simulated to be 10 mm from the crystal entry surface) to the point of absorption and the resulting optical photon travel time to the photocathode. The photons that reach the photocathode without reflections from the radiator side surfaces are detected inside a very narrow time window of about 200 ps. The photons that undergo one or more reflections are being detected with significant time delays, up to 2 ns in the case of Teflon wrapping. Even in case of black paint, a small fraction of photons is detected with approximately 0.7 ns delay. Most likely, this are the photons that are internally reflected only once from the side surfaces.

The time distribution of Cherenkov photons reaching the photocathode in case of $PbWO_4$ radiator, shown in Figure 9.12, is very similar to the distributions in case of PbF_2. However the scintillation photons produced in $PbWO_4$ create a very long tail, corresponding to a combination of photons produced with scintillation time decay constants of 6 ns and 30 ns. However, the peak corresponding to prompt Cherenkov photons is clearly seen.

Figure 9.13 shows the effects of radiator dimensions on the photon detection timing. Here, radiators with different geometrical cross sections were simulated as monolithic radiators, coupled to the photodetector with the same cross section. Considering Figure 9.13a, it is very obvious what an important effect the radiator thickness has on the photon travel time spread. The differences in start times are a consequence of longer combined gamma and optical photon travel times through the thicker radiators. However the cross section of the radiator has very little effect on timing, at least in the case of black paint as in Figure 9.13b. This is a consequence of total internal reflections. Photons, which would directly exit and be detected in the larger radiator, but first reach the side surface in the smaller one, are anyway internally reflected and travel a path of equivalent length before reaching the

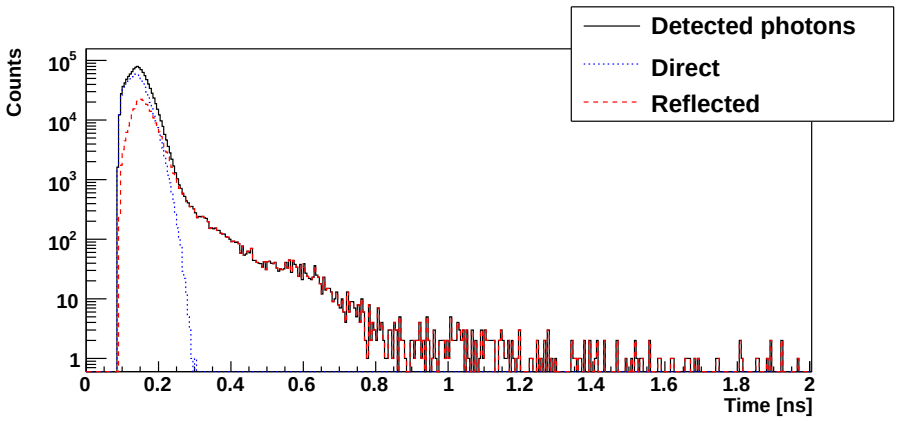

(a) black paint

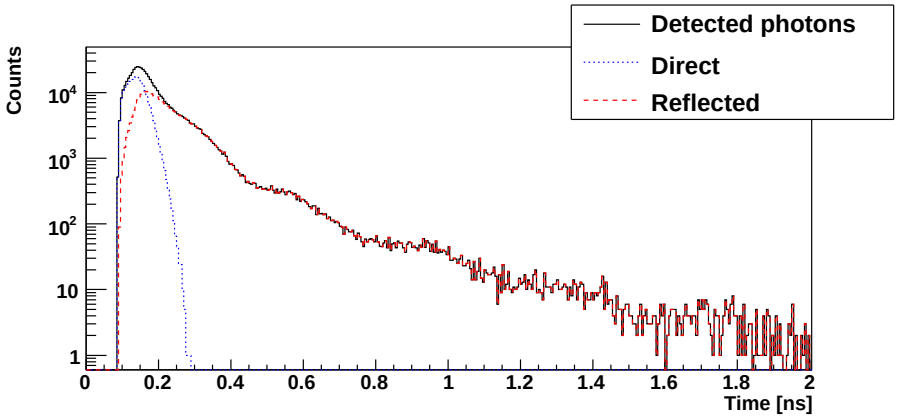

(b) Teflon reflector

Figure 9.11: Time distributions of first photons detected per event, in case of black painted and Teflon wrapped 15 mm thick PbF_2. Also shown are the contributions from photons that reach the photocathode without (direct) and with (reflected) reflections.

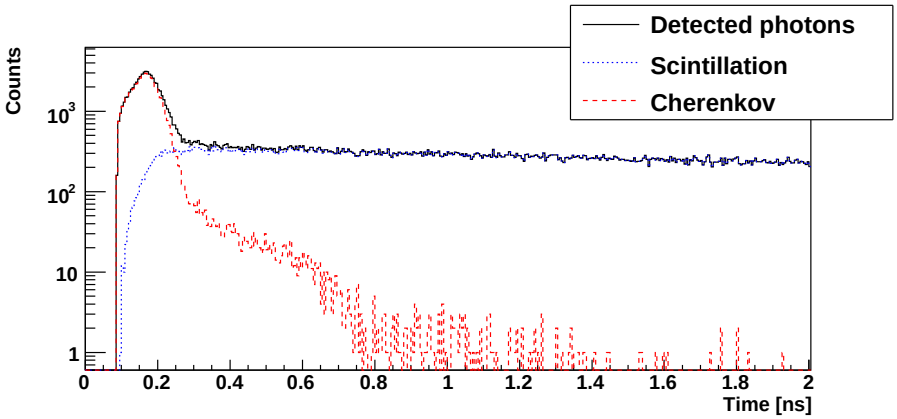

Figure 9.12: Time distributions of first photons detected per event, in case of black painted 15 mm thick $PbWO_4$.

photocathode.

9.2.9 Coincidence detection timing

To obtain the coincidence time distributions, a setup consisting of two identical detectors in back-to-back arrangement was simulated. Each detector was positioned 85 mm from the point source of annihilation gammas. These were generated with isotropic angular distribution, limited to the angular acceptance of the two detectors. The coincidence time distributions obtained with different parameters of PbF_2 radiators are shown in Figure 9.14, while the time resolutions of the obtained distributions are listed in Table 9.11. Again the effect of radiator thickness on the time resolution is obvious: while coincidences between two 5 mm thick, black painted PbF_2 crystals are detected with time resolution of 37.1 ps FWHM, this degrades to 92.8 ps FWHM when 15 mm thick crystals are used. This values do not include the time response of the photodetector and only reflect the contributions due to the Cherenkov radiator. The time resolution deteriorates further in cases of bare and Teflon wrapped radiators, where the time distribution also obtains tails due to reflected photons. Figure 9.14e shows the time distribution obtained, when a slightly ground (70% of reflections were still treated as if occurring on a polished surface) surface is introduced. Compared to fully polished surface, the distribution obtained tails but has only a slightly worse resolution with 96.3 ps FWHM.

Figure 9.15 shows the coincidence time distributions for 5 and 15 mm thick, black painted $PbWO_4$ radiators. The time resolution for events, where Cherenkov photons are detected on both detectors, is worse than in the case of PbF_2 radiators, due to higher refractive index. On this small time scales, the effect of $PbWO_4$ scintillations is an almost constant background of events,

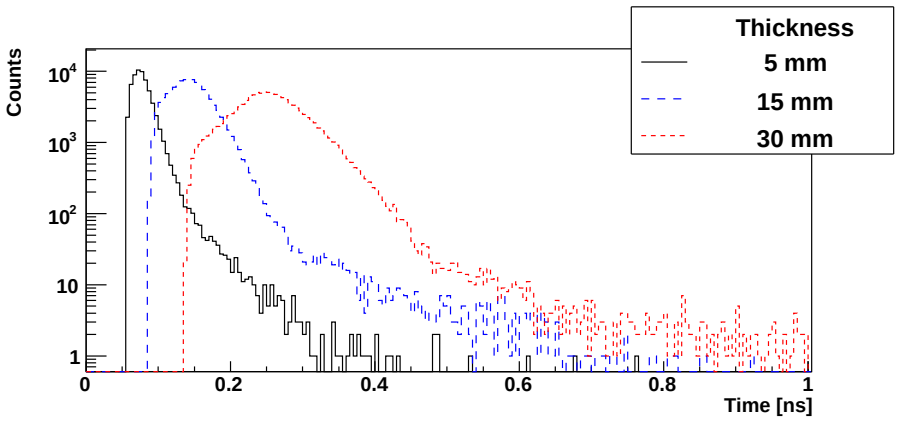

(a) Timing vs. radiator thickness

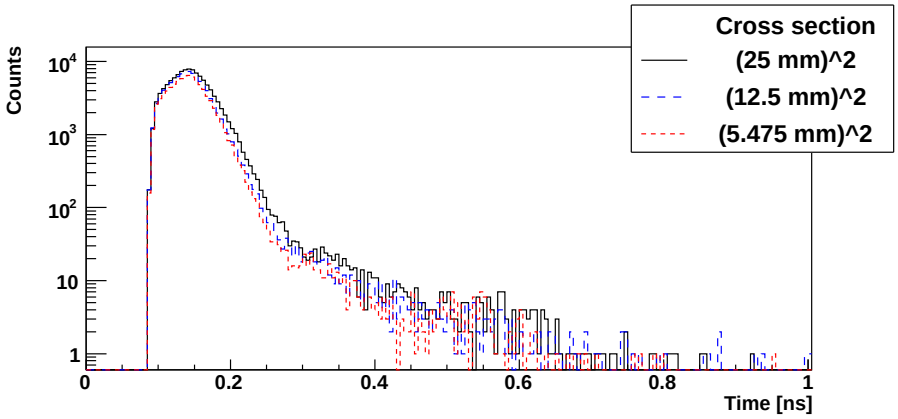

(b) Timing vs. radiator cross section

Figure 9.13: Time distributions of first photons detected per event, in case of black painted PbF_2 with different dimensions. The geometrical cross section of the radiators for the case (a) is 25×25 mm^2 while the thickness of the radiators for the case (b) is 15 mm.

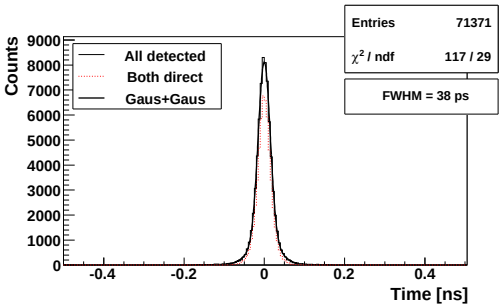

(a) 5 mm (polished, black paint)

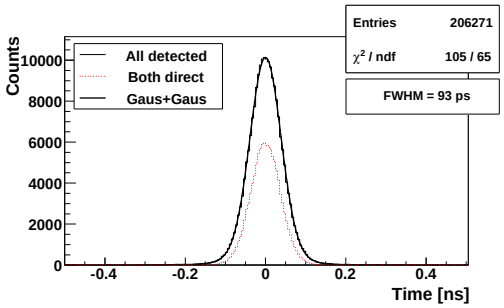

(b) 15 mm (polished, black paint)

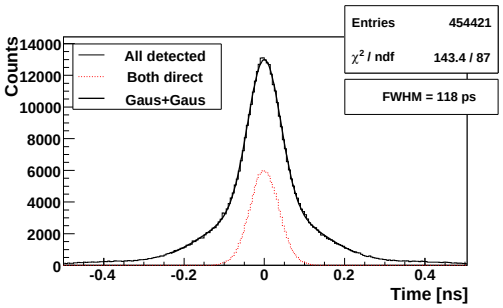

(c) 15 mm (polished, bare)

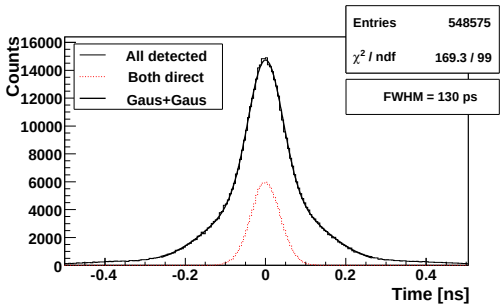

(d) 15 mm (polished, Teflon wrapping)

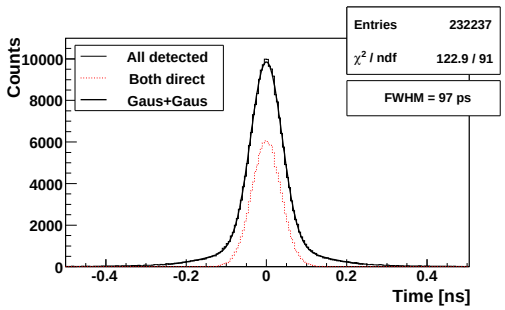

(e) 15 mm (ground, black paint)

Figure 9.14: Simulated coincidence time distributions in case of different PbF_2 Cherenkov radiators. The distributions are fitted with a sum of two Gaussian functions. The contributions from events, where the photons detected on both sides reached the photocathode without reflections on radiator surfaces, are also shown.

which in real measurements cannot be separated from Cherenkov events.

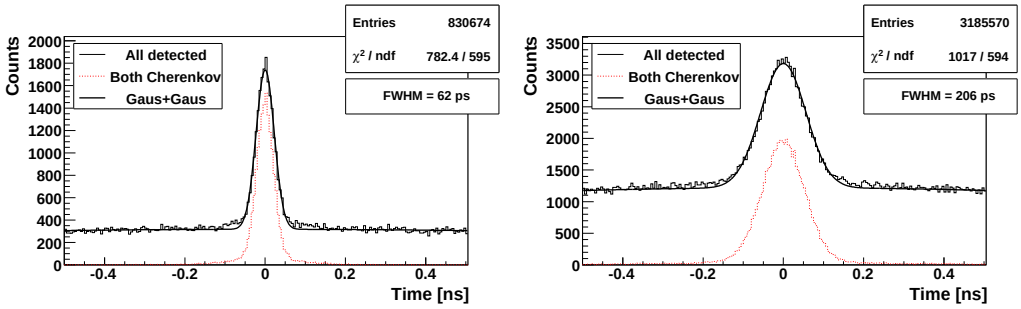

(a) 5 mm (polished, black paint) (b) 15 mm (polished, black paint)

Figure 9.15: Simulated coincidence time distributions in case of $PbWO_4$ Cherenkov radiators of two different thicknesses. The distributions are fitted with a sum of two Gaussian functions and the contributions from events, where the photons, detected on both sides were produced by the Cherenkov process, are also shown.

The effect of the photodetector time response is illustrated in Figure 9.16, where the simulation included the time response of the JY0005 MCP PMT to the red laser illumination, shown in Figure 5.5b. In this case, the distributions are wider and have about 1 ns long tails, due to electron backscattering. This makes the distribution for 15 mm thick $PbWO_4$ in better accordance with the experimental distribution (Figure 6.9b). However, it should be noted that the photodetector time response used includes the effect of laser time jitter, which means that the simulation predictions for the total time resolution are slightly too large.

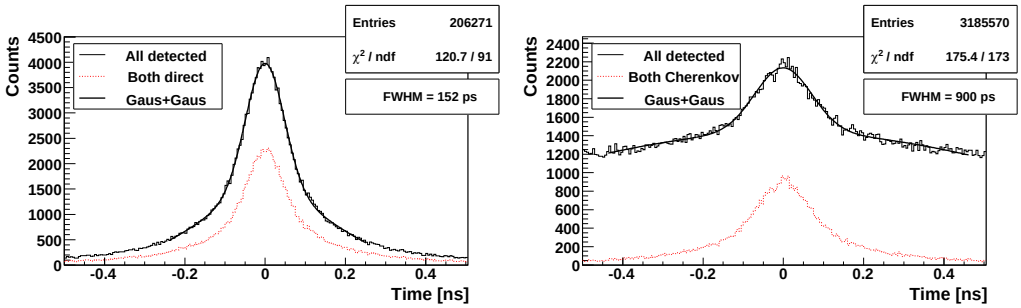

(a) PbF_2 (polished, black paint) (b) $PbWO_4$ (polished, black paint)

Figure 9.16: Simulated coincidence time distributions in case of 15 mm thick Cherenkov radiators, when the time response of the photodetector is included in the simulation.

The simulation results for 4×4 segmented PbF_2 crystal arrays with the same parameters as those used in experiments, are shown in Figure 9.17 and

Cherenkov radiator			Time resolution FWHM (σ) [ps]	
Material	Surface	Thickness	w/o photod. resp.	w/ photod. resp.
PbF_2	black painted	5 mm	37.7 (17.2)	84.4 (27.4)
PbF_2	black painted	10 mm	65.7 (29.2)	118 (37.8)
PbF_2	black painted	15 mm	92.8 (39.9)	148 (47.9)
PbF_2	bare	15 mm	118 (42.8)	215 (53.1)
PbF_2	Teflon wrapped	15 mm	130 (46.0)	241 (70.6)
$PbWO_4$	black painted	5 mm	62.2 (22.6)	399 (39.0)
$PbWO_4$	black painted	15 mm	206 (56.6)	900 (70.6)

Table 9.11: Simulated timing resolution FWHM (and narrow Gaussian sigma) of the back-to-back setup for different parameters of the Cherenkov radiator, with and without the photodetector time response included. All radiators in this table had polished surfaces.

Table 9.12. According to this results, the appearance of tails in the distributions is mostly a consequence of reflections at the crystal entry surface. Wrapping the side surfaces in Teflon only slightly reduces the time resolution compared to the black painted surfaces. This is consistent with the experimental results (Table 6.5). Not surprisingly, the best timing with FWHM of 45.9 ps is obtained when all surfaces are black painted, while the worst timing with FWHM of 63.0 ps results when all surfaces are wrapped in Teflon. This values do not include the contribution of photodetector response. Values obtained when this is included are listed in Table 9.12.

Surface treatment		Time resolution FWHM (σ) [ps]	
entry surface	side surfaces	w/o photod. resp.	w/ photod. resp.
black paint	black paint	45.7 (15.4)	92.2 (29.4)
bare surface	black paint	48.8 (18.3)	116 (29.4)
Teflon reflector	black paint	55.7 (18.1)	138 (33.5)
black paint	Teflon reflector	50.2 (20.9)	96.4 (30.4)
bare surface	Teflon reflector	54.7 (19.1)	135 (30.8)
Teflon reflector	Teflon reflector	62.5 (19.7)	154 (34.8)

Table 9.12: Simulated timing resolution of the back-to-back setup for different surface treatments of the 4×4 segmented, 7.5 mm thick PbF_2 arrays, with and without the photodetector time response included. The results are reported as the average FWHM (and narrow Gaussian sigma) of distributions, obtained between pairs of readout channels which are in geometric coincidence.

9.3 Possible improvements of the method

The simulation was also used to investigate various changes to the detector, which could lead to improvements in Cherenkov photon detection. The

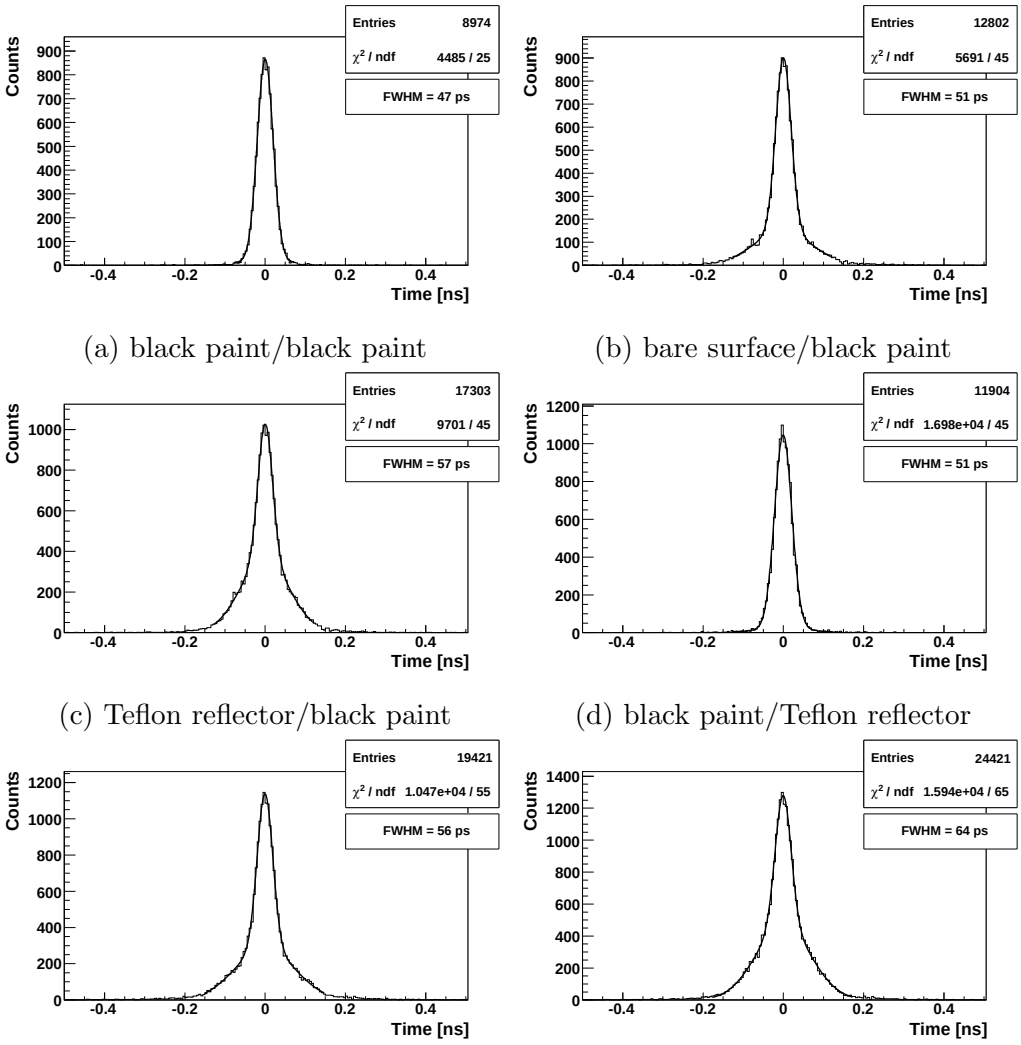

(a) black paint/black paint (b) bare surface/black paint

(c) Teflon reflector/black paint (d) black paint/Teflon reflector

(e) bare surface/Teflon reflector (f) Teflon reflector/Teflon reflector

Figure 9.17: Simulated coincidence time distributions between two channels in case of different entry/side surface treatments of the 4×4 segmented, 7.5 mm thick PbF_2 arrays. The distributions are fitted with a sum of two Gaussian functions.

biggest single limitation for detection efficiency is the photodetector, which has a PDE of a couple of % in the 200 to 800 nm range, in which the Cherenkov photons are generated and propagated to the sensitive area in numbers. Improvements with better photodetector PDE are investigated in this section. If the photodetector is sensitive in lower wavelength regions, a gain in efficiency could be obtained, if suitable Cherenkov radiators, with optical transmission also extending to lower wavelengths, would be available. Another improvement is possible, if more photons are extracted from the radiator with better optical coupling between the radiator and the photodetector.

9.3.1 Photodetector PDE

The bialkali photocathode of the JY0005 MCP PMT used in experiments features a peak QE of about 20%, and is deposited on a borosilicate glass window, which is the reason for PDE drop for wavelengths below 250 nm. In recent years, significant improvement in photocathode materials has been achieved. For example, a photocathode produced by Hamamatsu Photonics, named ultra bialkali, has a peak QE of $\approx 43\%$ [46]. Also interesting is the use of window materials, which extend the sensitivity to lower wavelengths. An example is the Hamamatsu 500S photocathode [11], which is a multialkali material deposited on fused silica (quartz) window. It has a peak QE of 25%, with sensitivity extending down to 160 nm. Figure 9.18 shows the PDE of a hypothetical photodetector, using such photocathode with a collection efficiency of 60%. A simulation of such photodetector, coupled to a 15 mm

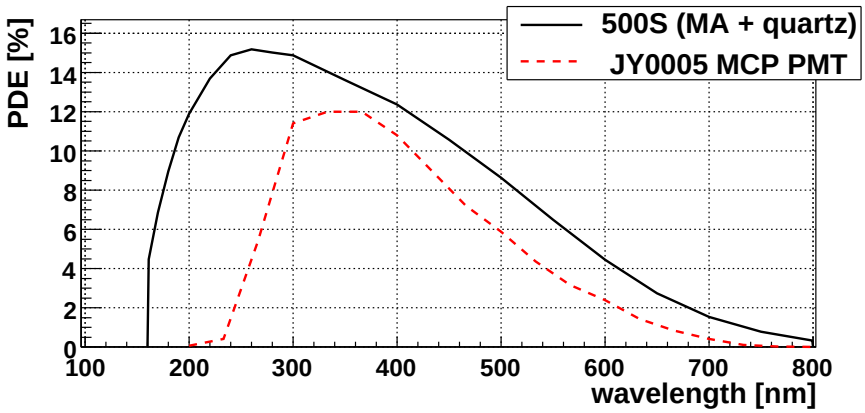

Figure 9.18: The PDE of a photodetector with Hamamatsu 500S multialkali photocathode and quartz window, compared to the PDE of JY0005 MCP PMT. A collection efficiency of 60% was presumed.

black painted PbF_2, yielded a detection efficiency of 15.6%, a factor of 1.4 improvement compared to the result obtained using the PDE of JY0005 MCP

PMT. For all simulations involving Hamamatsu 500S photocathode, the low wavelength limit for photon production and transportation was lowered from 200 nm to 160 nm.

Although such photocathode can detect photons down to 160 nm, photons below approximately 250 nm are still absorbed by the PbF_2 crystal. The improvements possible if a Cherenkov radiator with lower optical transmission cutoff wavelength were available are explored in the next section.

9.3.2 Cherenkov radiator

As has been seen, the thickness is one of the most important radiator parameters, both in terms of the timing resolution and the detection efficiency. Figures 9.19 and 9.20 show the timing resolution and efficiency for different thicknesses of a monolithic and 4×4 segmented PbF_2 crystal respectively. Here, the photodetector PDE was that of the JY0005 MCP PMT, while the detector time response was not taken into account. The efficiency was calculated as a square root of the fraction of number of detected coincidences and number of generated gamma pairs. Since annihilation gammas were generated with isotropic angular distribution, the gammas incident on the edges of radiator entry surface had less than the full thickness of the radiator to be absorbed in. The gamma absorption efficiency was thus lowered, meaning that the values for efficiency here are slightly lower than they were in Section 9.2.6. Also shown is the figure of merit (FOM) as defined in Equation (2.35), which should be the deciding factor when considering the full TOF PET performance.

As expected, the time resolution is increasing linearly with radiator thickness, while the detection efficiency first increases and then saturates, as gamma absorption efficiency reaches close to 100%. Because of this saturation effect, the FOM has a maximum at certain thickness. As can be seen, this thickness is larger for bare or Teflon wrapped than for black painted radiators and is about 10 mm for monolithic and about 8 mm for 4×4 segmented, black painted PbF_2 crystals. As a reference, in case of black painted PbF_2 crystal coupled to the JY0005 MCP PMT the maximum FOM obtainable is 0.115 ns^{-1}.

The effects of individual Cherenkov radiator parameters were explored, by constructing a hypothetical radiator with different values for refractive index and optical absorption cutoff wavelength. The material properties and composition of PbF_2 crystal was used. The refractive index was set as constant over all wavelengths, while the optical absorption was constructed as a step function, jumping from 0 to 10 m at desired cutoff wavelength. Although unrealistic, such parameters are useful to provide an insight into their contribution to Cherenkov radiator performance. The PDE of Hamamatsu 500S photocathode with sensitivity down to 160 nm was used, so that the

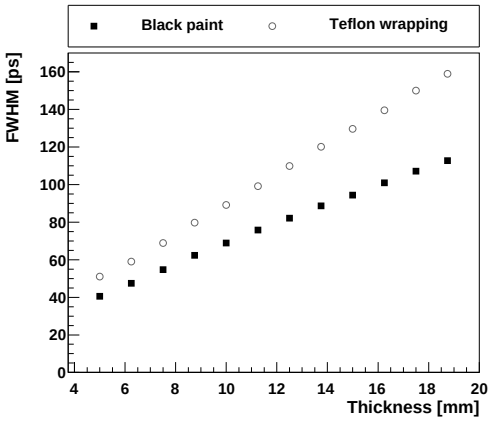

(a) Timing resolution

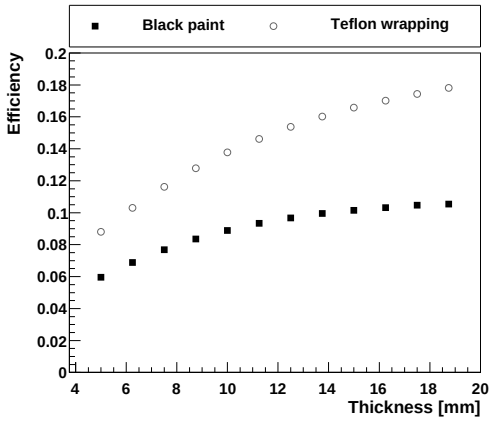

(b) Detection efficiency

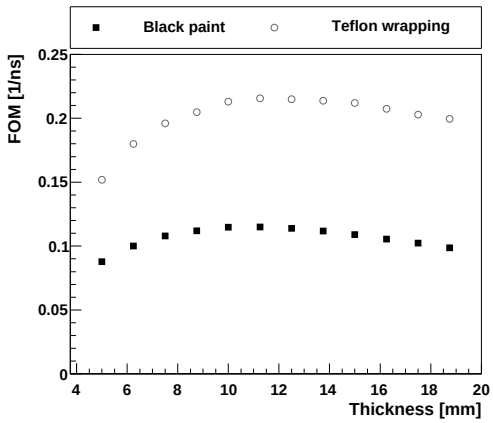

(c) Figure of merit

Figure 9.19: The performance parameters of monolithic PbF_2 crystals with 25×25 mm^2 cross section in case of different thicknesses and surface treatments. The PDE of JY0005 MCP PMT was used.

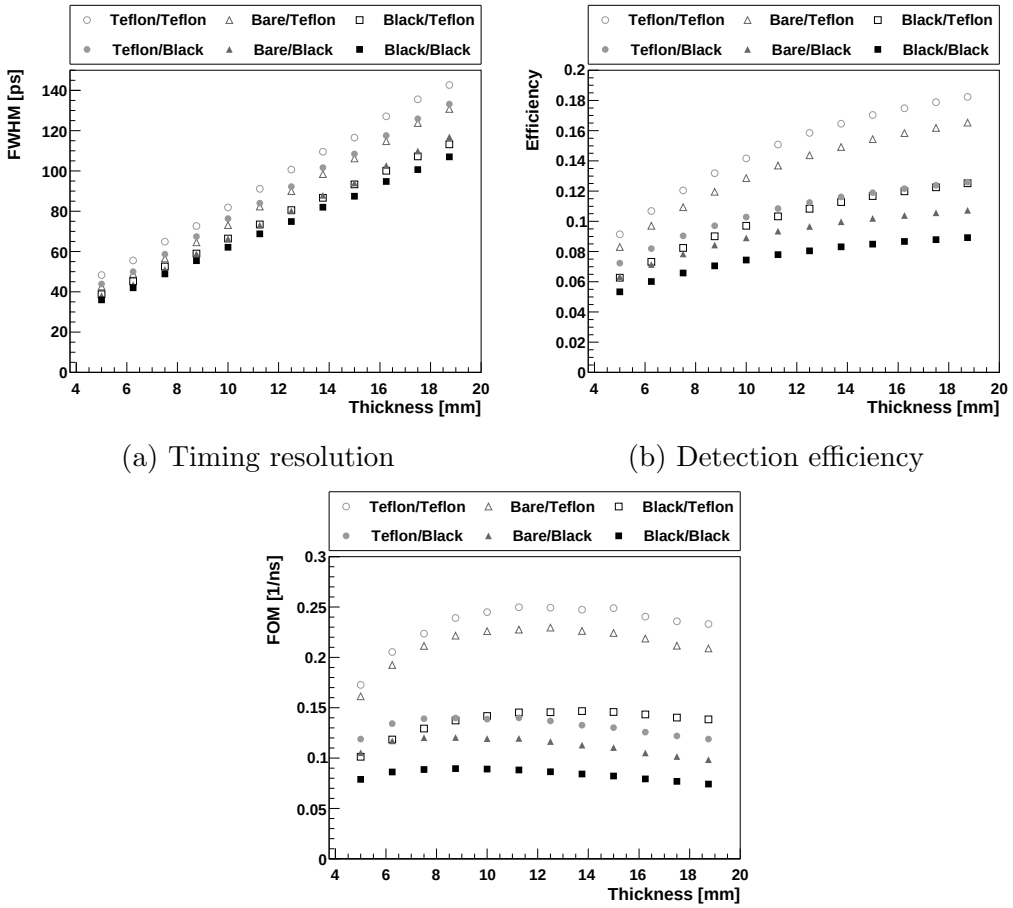

(a) Timing resolution

(b) Detection efficiency

(c) Figure of merit

Figure 9.20: The performance parameters of 4×4 segmented PbF_2 crystal arrays in case of different thicknesses and treatments of the entry/side surfaces. The PDE of JY0005 MCP PMT was used.

limitations of Cherenkov radiator were exposed.

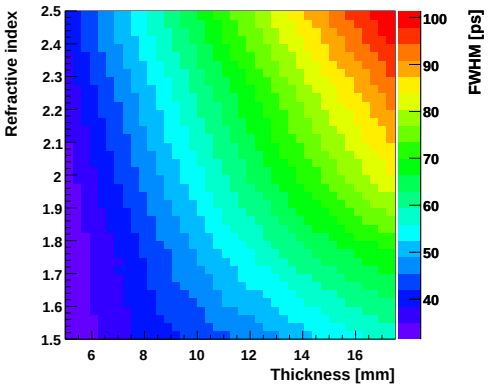

(a) Timing resolution

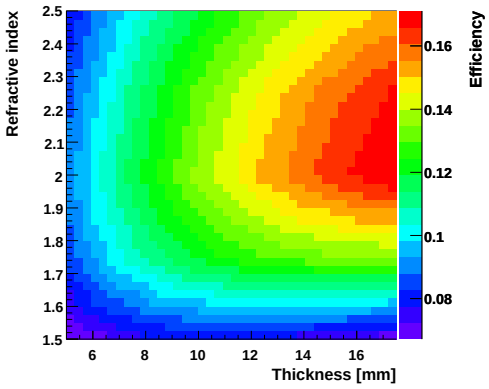

(b) Detection efficiency

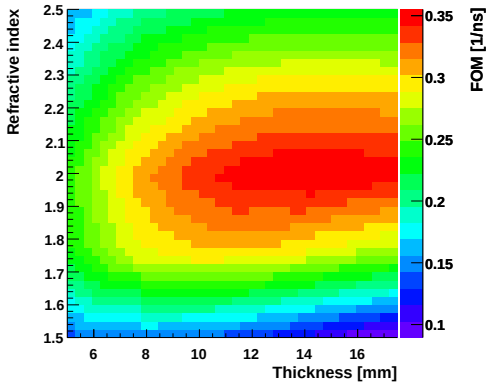

(c) Figure of merit

Figure 9.21: Thickness and refractive index dependence of performance parameters for black painted PbF_2 like crystal with 25×25 mm^2 cross section. The PDE of Hamamatsu 500S photocathode with 60% collection efficiency was used.

The timing resolution, detection efficiency and FOM for a hypothetical, PbF_2 like crystal of different thicknesses and with different refractive indices, are shown in Figure 9.21. The non realistic optical absorption with sharp cutoff at 250 nm was used to obtain this figures. Same as in Figure 9.19, the time resolution degrades with increasing radiator thickness, but now also with increasing refractive index. This is expected since the photon velocity decreases with refractive index. The detection efficiency first increases with refractive index, as the Cherenkov threshold decreases. However the efficiency starts decreasing as the refractive index reaches a value of 2.0, since the angle of total internal reflection decreases and less photons exit the radiator and reach the photodetector. This means that the refractive index can

actually be too high, which may already be the case for $PbWO_4$. The result of the combination of timing resolution and efficiency behaviors is that the FOM has a maximum in both thickness and refractive index dependence. The maximum is achieved for refractive index of about 1.95−2.05, and for thickness of about 11−16 mm. Here the FOM reaches ≈ 0.35 ns^{-1}. This factor of 3 improvement over the FOM simulated for detector used in experiments reflects both the optimization of refractive index and improvements of the photodetector PDE.

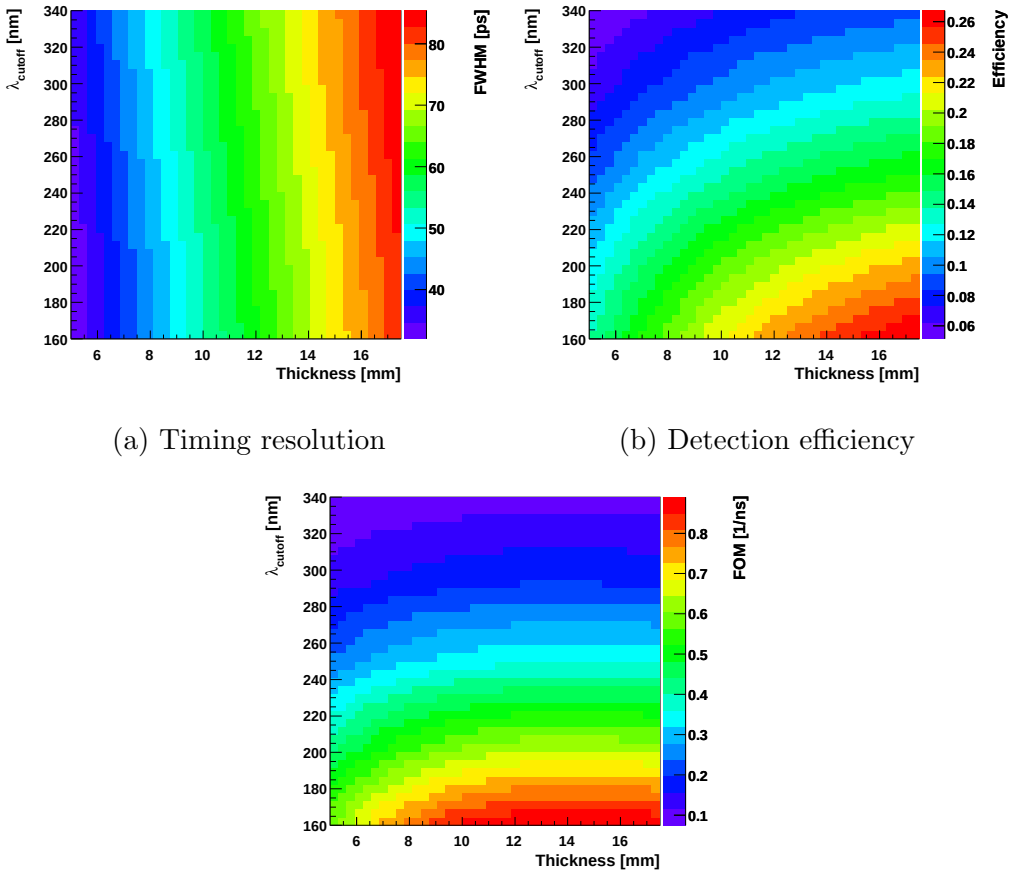

(a) Timing resolution

(b) Detection efficiency

(c) Figure of merit

Figure 9.22: Thickness and optical transmission cutoff wavelength (λ_{cutoff}) dependence of performance parameters for black painted PbF_2 like crystal with 25×25 mm^2 cross section. The PDE of Hamamatsu 500S photocathode with 60% collection efficiency was used.

Figure 9.22 shows the performance of a hypothetical PbF_2 like crystal of different thicknesses and with different optical absorption cutoff wavelengths. Here, the refractive index with constant value of 2.0, which was found to be optimal in Figure 9.21, was used. The timing resolution is slightly improving

with decreasing cutoff wavelength since more photons are available for detection. However, if a realistic dispersion of refractive index would be taken into account, the timing resolution would degrade or at least not improve that fast with decreasing absorption cutoff, due to the fact that photons extracted at lower wavelengths would travel slower. In any case, the efficiency significantly improves at lower cutoff wavelengths, leading to a clear improvement in FOM. The maximum FOM of almost 0.9 ns^{-1} is obtained at $\lambda_{cutoff} = 160$ nm and a wide range of thicknesses. Compared to the detector used in experiments, a total factor of improvement of more than 8 was achieved with ideal (if we limit ourselves to the lowest wavelength limit of 160 nm) Cherenkov radiator and much improved but still realistic photodetector. This also suggests that a factor of improvement of more than 2 in FOM is possible by extending the radiator optical transmission from 250 nm to 160 nm, providing a suitably sensitive photodetector.

9.3.3 Extraction of photons

The detection efficiency could be further increased by improving the extraction of photons. Here the goal is to reduce the fraction of photons, lost due to total internal reflection on the crystal exit surface. This can most obviously be achieved by increasing the refractive index of the photodetector window to better match the high refractive index of Cherenkov radiators and by optimizing the refractive index of optical coupling material between the radiator and the window. A 1.76 times improvement in light extraction from $PbWO_4$ has been achieved by using a YAP ($YAlO_3$) window on a Hybrid PMT photodetector, instead of a quartz window [47]. YAP has a refractive index of 1.95, which is much closer to that of $PbWO_4$ than the quartz refractive index of ≈ 1.5.

Table 9.13 lists the detection efficiencies, resulting from a simulation using PbF_2 crystal and JY0005 PDE, in case of different refractive indices of photodetector window and coupling material. The optimal coupling refractive index was calculated using the equation [48]:

$$n_{opt} = \sqrt{n_W * n_R},$$

where n_W and n_R are the refractive indices of window and radiator materials respectively. Using the window with highest simulated refractive index of 2.0 resulted in a factor of 1.4 improvement in efficiency, which means a factor of 2 improvement in FOM.

Another perspective technology that could be used to improve extraction of photons are the so called photonic crystals, which are defined as a periodic pattern of two materials with different dielectric constants, which diffracts light from a high refractive index substrate. This was demonstrated for LYSO crystals, which had a layer of silicon nitride (Si_3N_4) deposited on

n_{window}	$n_{coupling}$	Efficiency [%]
1.5	1.50	11.1
1.5	1.64	11.4
1.6	1.70	12.7
1.7	1.75	13.9
1.8	1.80	14.9
1.9	1.85	15.3
2.0	1.90	15.5

Table 9.13: The simulated annihilation gamma detection efficiencies in case of different photodetector window and coupling refractive indices. The values are obtained with a 15 mm thick, black painted PbF_2.

the exit surface and micro structured using lithographic methods [49]. An improvement for a factor of 1.5 in light extraction was achieved experimentally, while the simulation suggested that an improvement for a factor of 2 might be possible.

By combining photonic crystals with high refractive index window, a factor of improvement of 4 in FOM might be possible.

10 TOF PET Image Reconstruction

As discussed in Section 2.5, an improvement in the quality of reconstructed images is expected when a good enough TOF information is included in the reconstruction algorithm. To investigate the improvements possible with the use of Cherenkov detectors, the experiments were modified to emulate measurements with a single PET ring. Simulations of a full body PET scanner were also performed. The images of activity distributions were reconstructed using different reconstruction algorithms:

- An algorithm equivalent to **Filtered backprojection (FBP)** [50] was used as an example of non-TOF PET reconstruction algorithm.
- **TOF weighted FBP** [51] is a simple extension of FBP, where not all pixels along the LOR are incremented by the same amount. Instead, the values of pixels along the LOR are incremented by a weight, determined from the distance between the incremented pixel and the point of decay estimated from the measured TOF difference. The weight is calculated from the expected (measured or simulated) TOF distribution, as shown in Figure 10.1.
- **Most likely position (MLP) method** [51] assumes that the time information is good enough that the reconstruction is not needed. Instead, the point of decay as determined from the TOF information is presumed to be exact and its coordinates are used to directly increment the 2-D matrix of the reconstructed image. For LOR defined by endpoints (x_1, y_1, z_1) and (x_2, y_2, z_2) and a TOF information Δt, the position of event is estimated from equations:

$$x = \frac{1}{2}(x_1 + x_2) - \frac{c_0 \Delta t}{2d}(x_2 - x_1), \tag{10.1}$$

$$y = \frac{1}{2}(y_1 + y_2) - \frac{c_0 \Delta t}{2d}(y_2 - y_1), \tag{10.2}$$

$$z = \frac{1}{2}(z_1 + z_2) - \frac{c_0 \Delta t}{2d}(z_2 - z_1), \tag{10.3}$$

  where d is the length of LOR. This method is extremely fast but can only produce images with quality comparable to more advanced reconstruction algorithms if the time resolution is below 100 ps [52].
- **Filtered MLP** takes the image obtained with the MLP method and performs a 2-D deconvolution using the expected TOF distribution as the point spread function. Effectively, this method is just a sharpening of the image for a certain amount, defined by the TOF distribution.

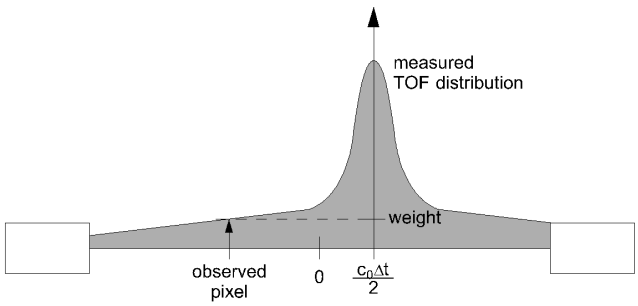

Figure 10.1: In TOF weighted FBP the value for weight is obtained by evaluating the expected TOF distribution, shifted by the measured TOF difference, at the observed pixel position.

10.1 Measurements with virtual PET ring

Since only two Cherenkov detector modules were available, construction of a full PET ring was not possible. Instead, the source was placed on a computer controlled rotational stage, and rotated to a set of discrete positions. The measurements were performed for the same amount of time at each position. Since the rotation of the source is equivalent to a rotation of the two detectors (in the opposite direction), such measurement corresponds to a measurement with a virtual PET ring, shown in Figure 10.2. Due to space constraints, the inner diameter of the ring was 185 mm. With this diameter and fixed physical dimensions of the Cherenkov detector, the best coverage of the whole ring was achieved with 22 virtual Cherenkov detectors (11 pairs). Due to gaps between the sensitive volumes in the ring, image artifacts would appear in the reconstructed image. To reduce this artifact, the measurements were performed by rotation to 44 positions inside a 360° angle, so that the data was also acquired with detectors overlapping the gaps. The Cherenkov detectors were composed of JY0002 and JY0005 MCP PMTs, coupled to 7.5 mm thick, 4×4 segmented PbF_2 crystals, that had all but the exit surface either painted black or wrapped in Teflon reflector. The expected position resolution of such PET ring is about 2.9 mm (Equation (2.9)).

To obtain the best TOF information possible, a calibration of all timing channels had to be performed. A calibration measurement was performed, with the point source stationary in the center of the system. Coincidence time distributions obtained for all combinations of channels belonging to the two MCP PMTs were shifted, so that the narrow peak was centered at $t = 0$. The same time calibration offsets were then applied for each combination of channels in measurements with the virtual ring.

The measured coincidence time distributions, shown in Figures 6.11a and 6.11f for black painted and Teflon wrapped crystals respectively, were used

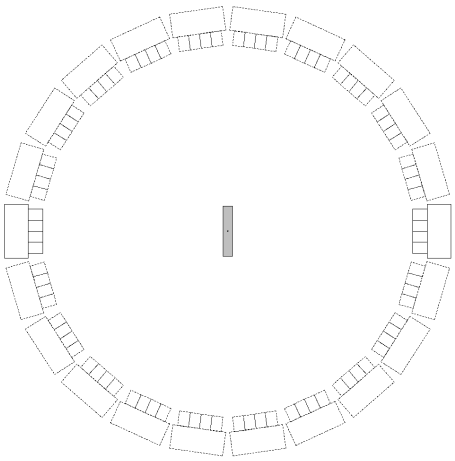

Figure 10.2: Transaxial view of the PET ring with inner diameter of 185 mm, formed by rotating one detector pair to 11 positions. In the center of the ring is the ^{22}Na point source and its plastic enclosing, shaped as a disk with a diameter of 25.4 mm and a height of 5 mm. The active volume of the source is shaped as a sphere with diameter of approximately 0.3 mm.

for the expected TOF distributions in TOF weighted FBP and filtered MLP algorithms.

Figure 10.3 shows the images reconstructed from measured data in case of black painted crystals, when the ^{22}Na point source with activity of 3200 kBq was positioned in the center of the system. The data was accumulated for 30 min in each step of rotation. To obtain the best estimate for position resolution, a very weak high frequency filter was used in the reconstruction algorithms. The position resolution was estimated as FWHM of the peak in 1-D projection histograms which are also shown in the figures.

The point source was well reconstructed with all 4 algorithms. Image artifacts are present on both images reconstructed with the FBP algorithm due to the very weak high frequency filter used. The achieved position resolution of about 3.3 mm is slightly worse than expected, which can be attributed to contributions due to the reconstruction algorithm (Section 2.4.1). The inclusion of TOF information did not improve the position resolution, however a very slight reduction in background levels was achieved with the TOF weighted FBP compared to non-TOF FBP (Figures 10.3b and 10.3a). The position resolution obtained with the MLP algorithm is significantly worse than that obtained with backprojection. However, a position resolution of 7.0 mm is not a bad result considering that it was obtained without any complex reconstruction.

Results obtained with Teflon wrapped crystals, shown in Figure 10.4, are very similar to the results obtained with black painted crystals. The slightly worse time resolution and the more pronounced long tails in coincidence

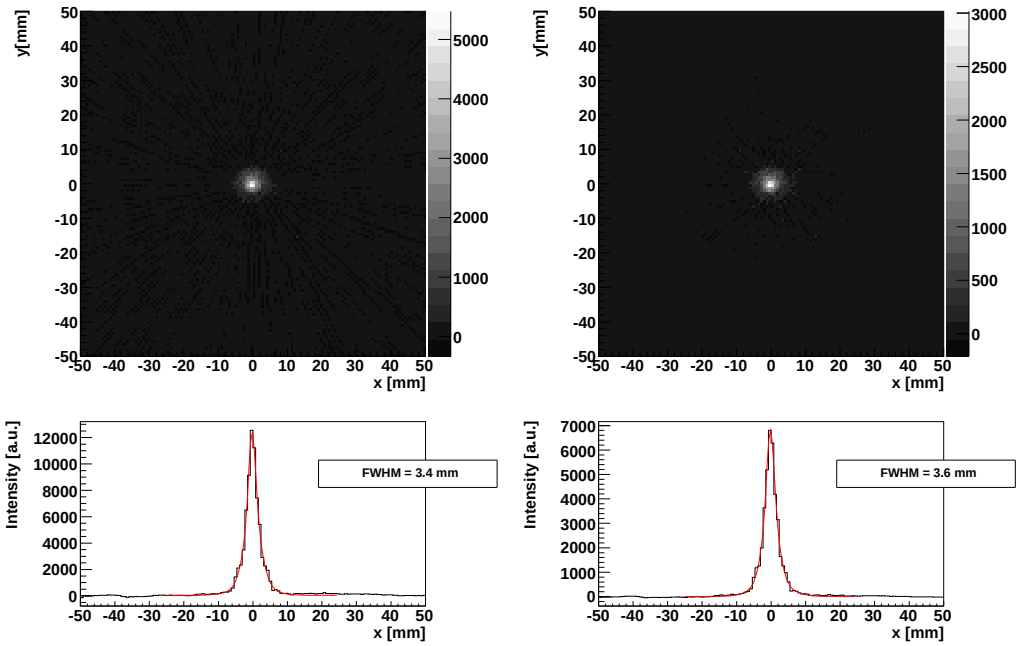

(a) FBP (non-TOF)

(b) TOF weighted FBP

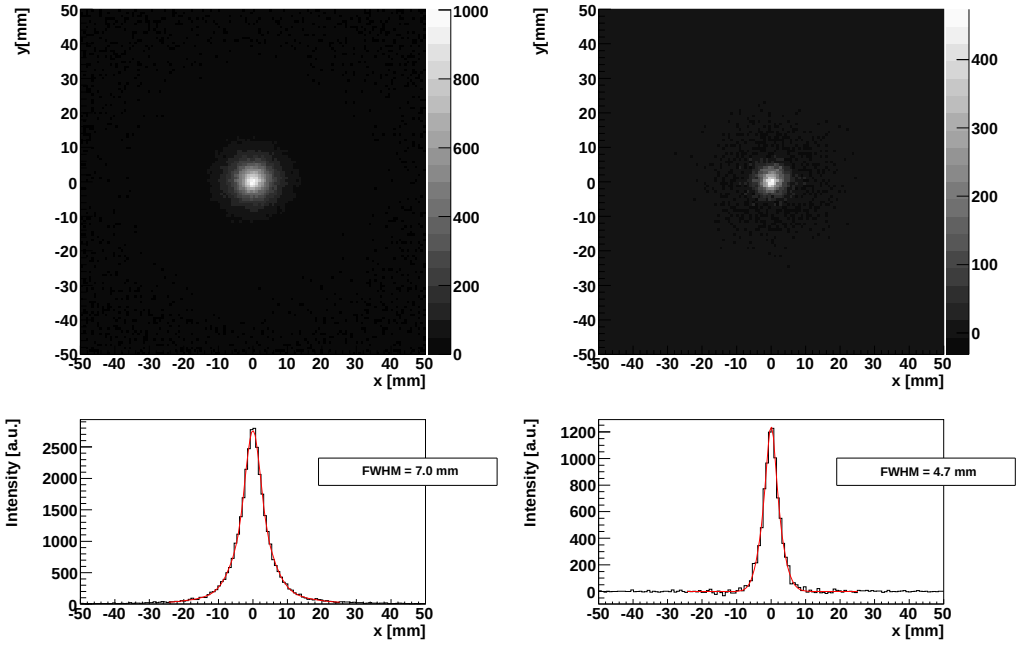

(c) MLP

(d) Filtered MLP

Figure 10.3: Reconstructed images of centered ^{22}Na point source using different reconstruction algorithms in case of black painted Cherenkov radiators. The 1D histograms are projections along 3 central bins.

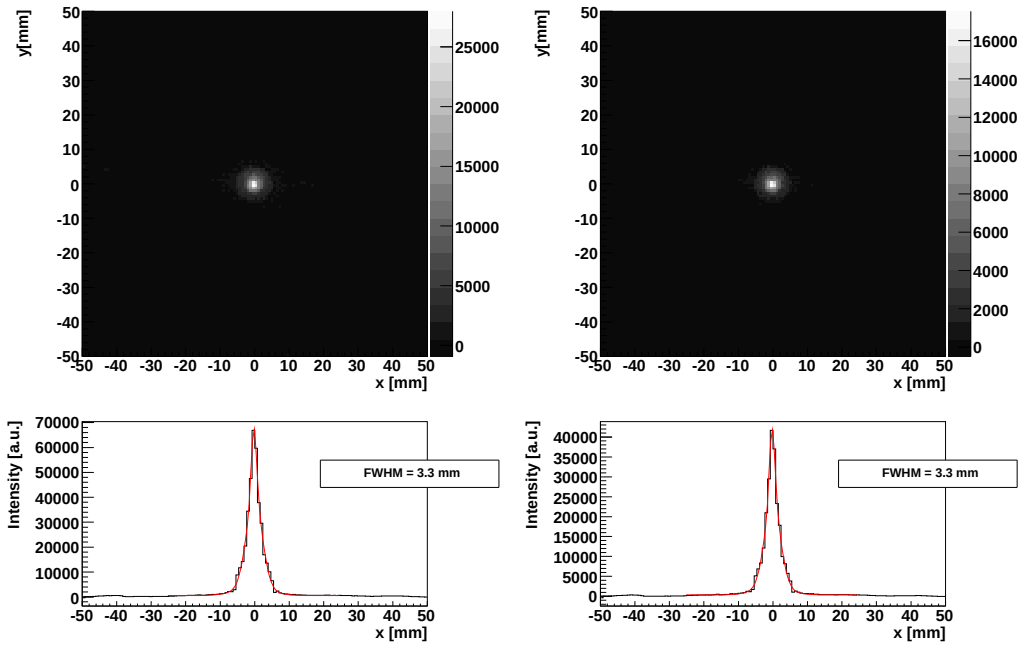

(a) FBP (non-TOF)

(b) TOF weighted FBP

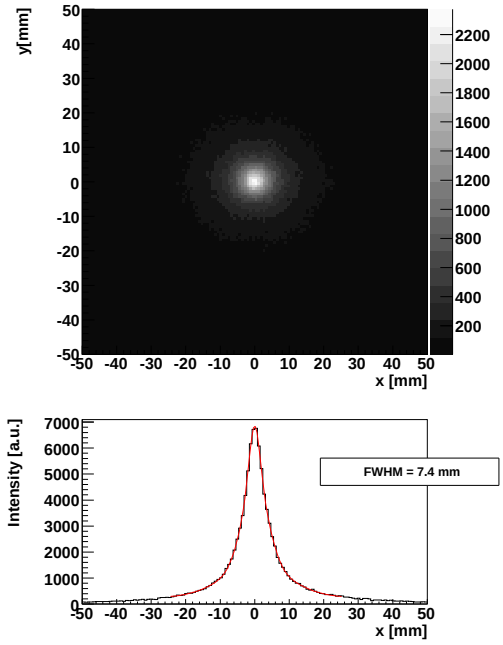

(c) MLP

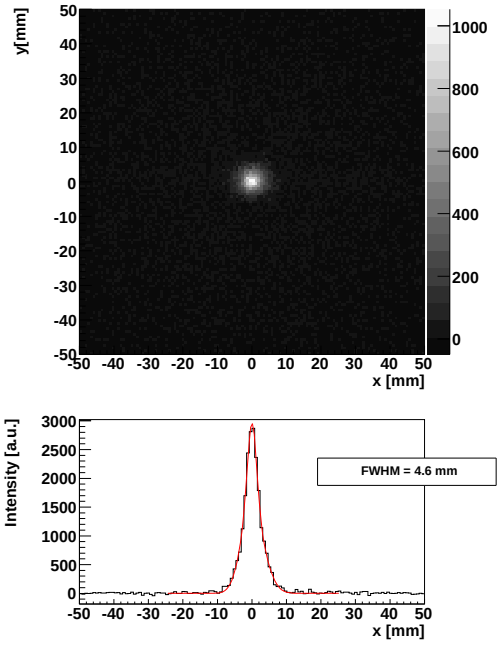

(d) Filtered MLP

Figure 10.4: Reconstructed images of centered ^{22}Na point source using different reconstruction algorithms in case of Teflon wrapped Cherenkov radiators. The 1D histograms are projections along 3 central bins.

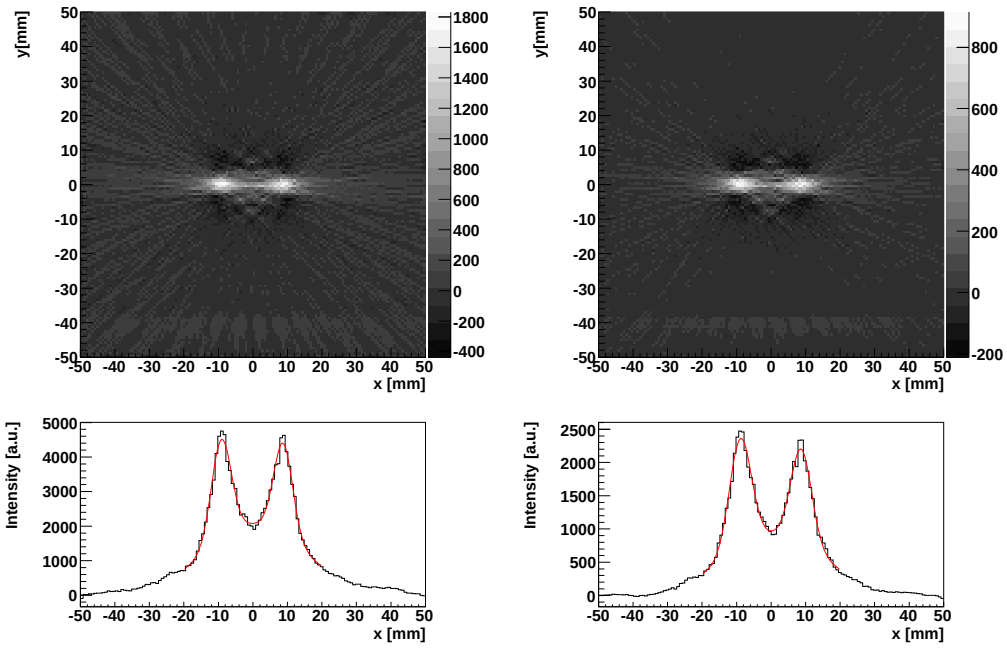

(a) FBP (non-TOF)

(b) TOF weighted FBP

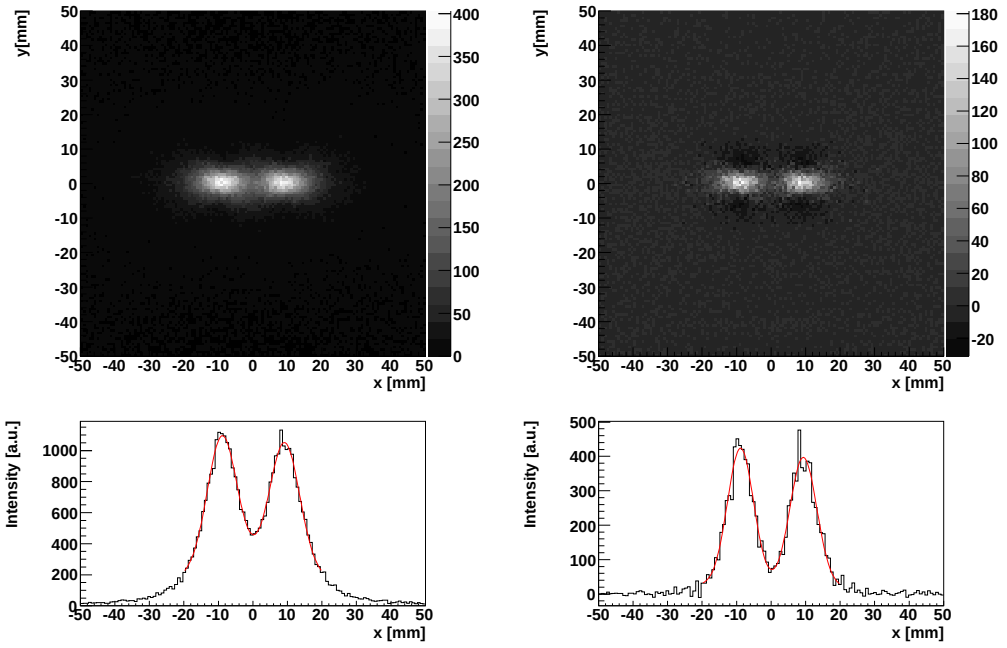

(c) MLP

(d) Filtered MLP

Figure 10.5: Reconstructed images of a simple phantom, featuring two ^{22}Na point sources positioned at ± 10 mm. The data was obtained with black painted Cherenkov radiators. The 1D histograms are projections along 3 central bins.

time distributions seem to have some effect on the results. Compared to black painted crystals, the background in TOF weighted FBP image (Figure 10.4b) is slightly more pronounced. Also, the image obtained with the MLP algorithm (Figure 10.4c) has more pronounced tails. However, the statistics collected with the same measurement time with Teflon wrapping is larger.

The data was also acquired with the source displaced from the center of the system for + 10 mm and − 10 mm. Since the source activity was relatively low, event pileup was not a problem, and the two sets of data could be combined to produce an equivalent of a very simple phantom. Images reconstructed from such data are shown in Figure 10.5. The two positions of the source are well separated and a slight reduction of background levels was again achieved in the image obtained with TOF weighted FBP (Figure 10.5b). Despite a worse position resolution, the two peaks are well separated also in the MLP image. Filtering the MLP image results in apparently the best separation. In Figure 10.5d the valley between the two peaks almost reaches the background level.

Another feature present in all of the reconstructed images in this chapter but most obvious in Figure 10.5 are the vertical "shadows" above and below the source. Most likely this feature is a result of a loss of acceptance, because only two detectors with sensitive area of about 22.5×22.5 mm^2 were used. At rotation angles close to ±90°, the point source shifted for 10 mm from the center caused coincidences only in a small fraction of available channels.

10.2 Simulated PET scanner

Results presented in the previous chapter can not fully illustrate the advantages presented by the excellent TOF resolution. The TOF information can be used to reduce contributions from activity neighboring the observed part of the image, while the measurements were only performed with activity concentrated in one or two point sources. Also the effects of the scattering could not be properly observed, due to the limited acceptance of only two detectors. To investigate this effects, simulations of a full PET scanner were performed.

The main building block of the simulated system was a Cherenkov detector, composed of 4×4 segmented, 7.5×22.5×22.5 mm^3 large PbF_2 crystals, coupled to a photodetector with JY0005 MCP PMT characteristics. The photodetector PDE and time response were included in the simulation, as described in Section 9. The surfaces of the crystals were simulated to be painted black or wrapped in a Teflon reflector. The PET scanner had an inner diameter of 800 mm and consisted of 15 rings, each featuring 112 individual Cherenkov detectors. The axial coverage of this system was 340 mm, and no collimators or absorbers were simulated between the rings. Coinci-

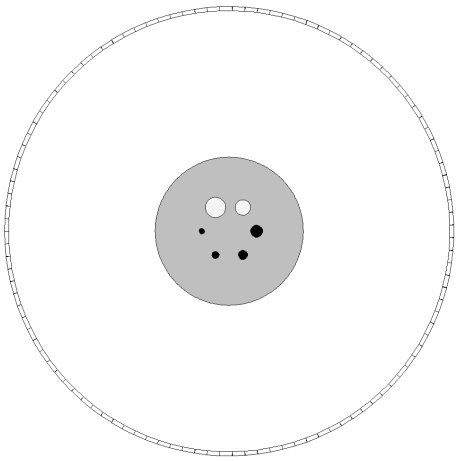

Figure 10.6: Transaxial view of the simulated ring with an inner diameter of 800 mm. Also shown is the phantom with 270 mm diameter, which includes four hot spheres (D = 10, 13, 17 an 22 mm) and two cold spheres (D = 28 and 37 mm).

dences between detectors belonging to different rings were accepted.

As a source of annihilation gammas, a phantom was simulated, featuring background radiation, attenuation and multiple spherical sources very similar to the phantom presented in [53]. The phantom was a water cylinder with a diameter of 270 mm and height of 68 mm, centered in the scanner. It was filled with an uniform distribution of activity, except for two spheres that were simulated as air "bubbles" void of activity. Additionally, four spheres with different diameters and activity concentration higher than the background were included in the phantom. The two cold and four hot spheres were centered along the height of the phantom and uniformly distributed in the transaxial direction along a circle with 50 mm diameter (Figure 10.6). The activity concentration of four hot spheres was 3 times larger than the background activity in the cylinder.

As the expected TOF distributions used for the reconstruction algorithms, coincidence time distributions obtained, when the photodetector time response was included in the simulation were used. The time resolution of this distribution is 92 ps FWHM in case of black painted and 154 ps FWHM in case of Teflon wrapped crystals (Table 9.12). The detection efficiencies are 6.7% in case of black painted and 12% in case of Teflon wrapped crystals (Table 9.9).

Figures 10.7 and 10.8 show the reconstructed images in case of black painted and Teflon wrapped crystals. Compared to reconstructed images presented in the previous chapter, some blurring (high frequency filtering) was used in the reconstruction of this images. The images represent a 20 mm thick central slice along the axial (z) direction of the scanner, where the axial po-

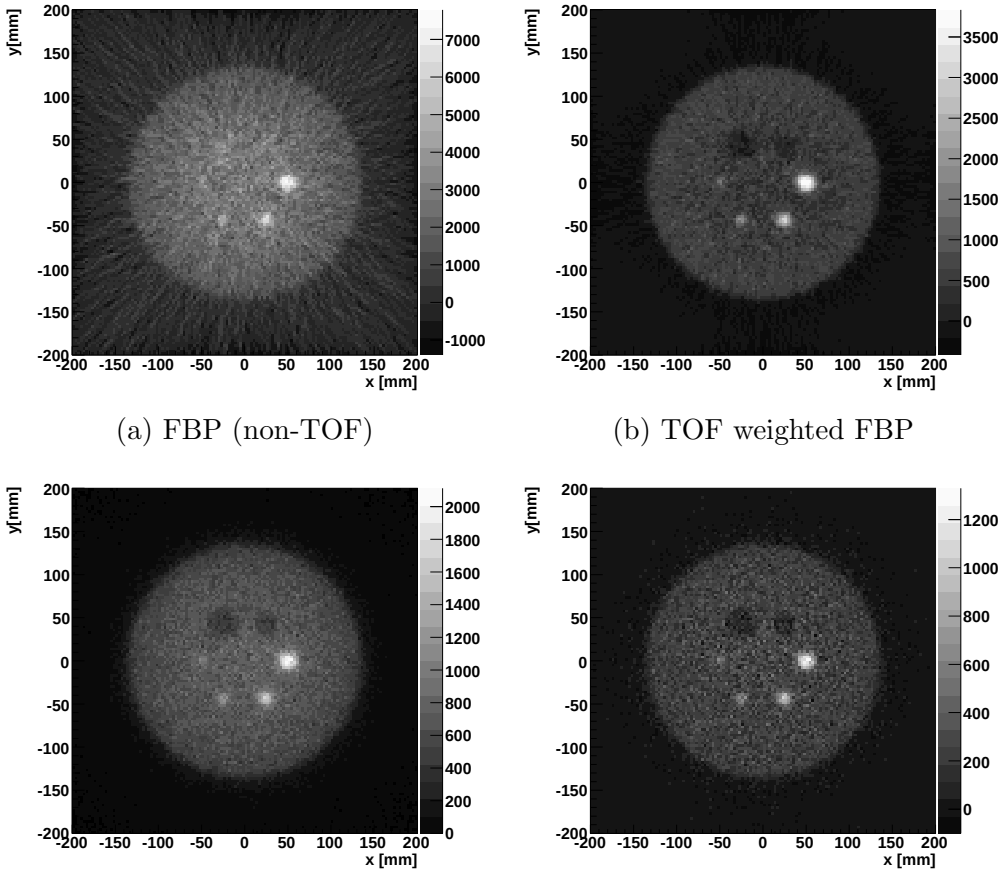

(a) FBP (non-TOF)

(b) TOF weighted FBP

(c) MLP

(d) Filtered MLP

Figure 10.7: Reconstructed images of the simulated phantom using four different reconstruction algorithms, when the Cherenkov radiators were painted with black paint.

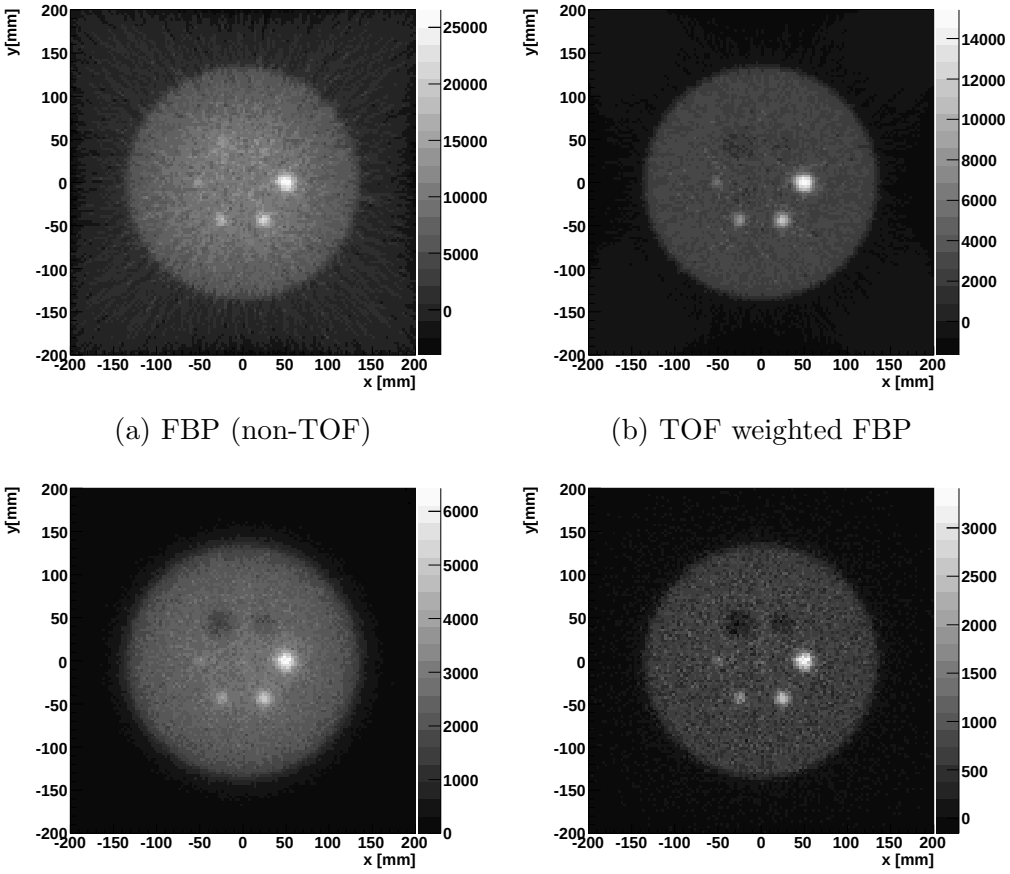

(a) FBP (non-TOF)

(b) TOF weighted FBP

(c) MLP

(d) Filtered MLP

Figure 10.8: Reconstructed images of the simulated phantom using four different reconstruction algorithms, when the Cherenkov radiators were wrapped in Teflon reflector.

sition of events was estimated from the TOF information (Equation (10.3)). The number of decays collected correspond to about 163 s of data acquisition for a background phantom activity concentrations of 8.2 kBq/ml, which is approximately equivalent to standard PET examination [13].

The volume of the phantom cylinder and the two largest hot spheres can easily be distinguished in all of the images. The two smaller hot spheres become easily distinguished only in the images, obtained with the TOF information. The two cold spheres are not visible in the non-TOF FBP image, while they are barely noticeable in the images reconstructed with the TOF information. Some of the activity reconstructed inside the cold sphere surfaces originates from the phantom background above and below the spheres, since the axial cut relies on imperfect reconstruction of the axial position of events. However, at least a part of events reconstructed inside the cold spheres results from fake coincidences, detected due to scattering. As discussed in previous chapters, no energy information can be provided by Cherenkov detectors. Rejection of scattered events has to rely on the intrinsically reduced detection efficiency for Compton scattered gammas, which only suppresses a part of the scattered events.

The reconstruction results were investigated more quantitatively by estimating the contrast and contrast-to-noise ratio (CNR) of the four hot spheres. The values of pixels in the reconstructed images were histogrammed, separately for pixels belonging to the phantom background (i.e. pixels inside the phantom radius, but not belonging to any of the spheres) and pixels, belonging to each of the hot spheres (i.e. pixels, separated from the simulated sphere position for less than the sphere radius). Mean and r.m.s. values of the obtained histograms were used as estimates of count rate and count rate fluctuations respectively. Contrast and CNR values, shown in Figure 10.9, were then calculated using Equations (2.18), (2.20) and (2.21).

When comparing results obtained with black painted and Teflon wrapped crystals, two things become apparent. The first observation is that the better timing resolution of black painted crystals (92 ps FWHM), compared to the time resolution of Teflon wrapped crystals (154 ps FWHM), results in a better contrast ratio with all three TOF algorithms. However, when comparing the CNR, the second observation is that the higher statistic gathered with more efficient Teflon wrapped Cherenkov radiators lead to lower background fluctuations and thus better detectability of the spheres. According to this simulation results, the efficiency gained by Teflon wrapping is more important than the slight loss of time resolution, as compared with black paint.

When comparing the different reconstruction algorithms, the TOF weighted FBP clearly produced the best images. Despite the very low sophistication of algorithms used, inclusion of TOF information resulted in approximately a factor of 2 improvement both in contrast and CNR, which in this case means the difference between non detectability (CNR $\lesssim 5$) and

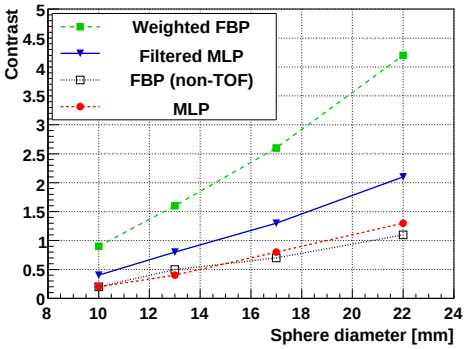

(a) Contrast, black paint

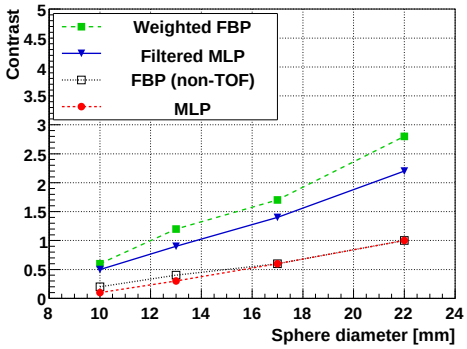

(b) Contrast, Teflon wrapping

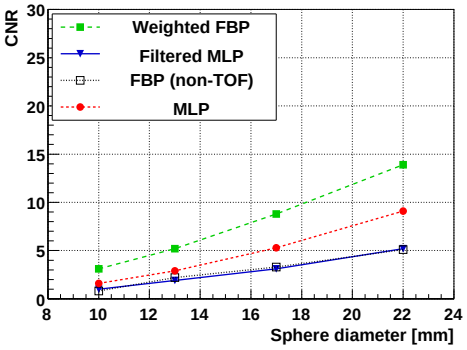

(c) CNR, black paint

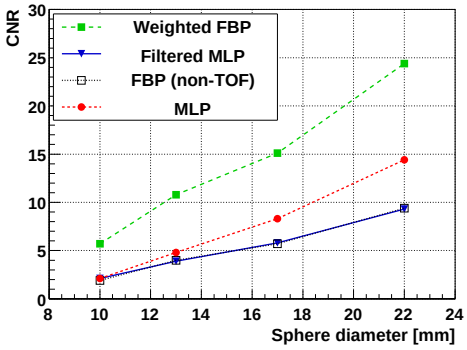

(d) CNR, Teflon wrapping

Figure 10.9: The contrast and CNR values for 4 hot spheres obtained with four different reconstruction algorithms in the case of black painted and Teflon wrapped Cherenkov radiators.

detectability ($5 < \text{CNR}$) for the smallest sphere. But it is important to remember that the non-TOF results could be obtained with traditional PET, using scintillators to detect annihilation gammas with higher efficiency. The simplest MLP method produced surprisingly good CNR values, but it clearly requires an excellent time resolution. Even in the case of Teflon wrapped crystals, which still achieved an excellent resolution of 154 ps FWHM, the CNR obtained with MLP is no longer significantly better than the CNR of non-TOF FBP (Figure 10.9d). Although filtering the MLP images resulted in improved contrast, the noise was also amplified, leading to poor CNR values.

It should be noted that in this chapter only basic reconstruction algorithms were used. Better results can be expected with the use of more sophisticated algorithms, both in the non-TOF and TOF case.

11 Conclusion

It has been demonstrated that by detecting Cherenkov photons produced in a suitable radiator material, excellent time-of-flight resolutions can be achieved. The main contribution to the time resolution comes from variation of the photon propagation time in the Cherenkov radiator. To achieve the best possible time resolution, a thinner radiator and a surface treatment, which suppresses reflections at the entry and side surfaces, are needed. Due to a high refractive index of suitable Cherenkov radiator materials, a large fraction of photons undergoes total internal reflection. Photons that are reflected can significantly decrease the time resolution and add long tails to the shape of coincidence detection time distribution. A black paint was used to stop a large fraction of photons, which are detected after one or more reflection, by effectively increasing the refractive index outside the radiator and absorbing the photons that exit it. Using black paint on the surfaces of PbF_2 crystals, a time resolution of ≈ 100 ps FWHM has been achieved, which means that a spatial resolution of about 15 mm was possible just from TOF information. Such an excellent resolution seems very promising for TOF PET application, however, a relatively low detection efficiency also needs to be considered. For example, the detector configuration which resulted in the best reported time resolution of 103 ps FWHM (the 5 mm thick, black painted PbF_2) has a detection efficiency of only 4.3%, or a coincidence detection efficiency of 0.18%. Despite the excellent time resolution, the low efficiency meant that the Cherenkov TOF PET method has a figure of merit (FOM) $2 - 20$ times worse than the traditional method using scintillation light.

However, significant improvements in detection efficiency should be possible. The photodetectors used to obtain the reported results were prototypes, designed for application other than TOF PET. Furthermore, by the time the efficiency measurements were performed, the PDE of at least one MCP PMT was most likely degraded by previous experiments. A factor of improvement of 4 in FOM might be possible just by using other samples of photodetectors, used in the presented experiments. Another factor of improvement of 2 in FOM is expected from using a more advanced photodetector, based on available technologies. Additional improvements could be achieved with improved light extraction (up to a factor of 4 improvement in FOM). If all of this improvements are considered, the FOM would improve for a factor over 30. Even further improvements would be possible if a Cherenkov radiator with light transmission properties better than PbF_2 were available. Admittedly, not all of this factors could be fully combined in a practical detector.

The majority of this work has been concentrating on achieving the best possible time resolution. To this end, most of experiments were performed with thinner, black painted Cherenkov radiators. It had been presumed that

worse time resolution and appearance of long tails in the TOF distribution in case of bare or wrapped radiators would have a very degrading effect for the final TOF PET image reconstruction. However, the images reconstructed for simulated full PET scanner suggest that the gain in efficiency is more important than the degradation of time response. Images obtained with the Teflon wrapped 4×4 segmented PbF_2 crystals had notably better diagnostic value (CNR) than those obtained with black painted crystals. The possibility of using more efficient, Teflon wrapped Cherenkov radiators significantly improves the outlooks for the presented Cherenkov TOF PET.

Although Cherenkov detectors cannot provide a measure of detected gamma energy, and with it, the rejection of scatter coincidences, the contribution from such unwanted events is reduced by the intrinsically reduced detection efficiency for scattered (lower energy) gammas. With some of the described improvements in detection efficiency, the Cherenkov method for TOF PET could reach or even surpass the performance of traditional, scintillation based methods. This depends mainly on the ability of image reconstruction algorithms to effectively use the excellent TOF information available. The extremely fast most likely position (MPL) algorithm can be used to display images of activity distribution in real time and achieved an image quality superior to that of a basic non-TOF FBP algorithm in the case of presented results. The success of Cherenkov TOF PET thus depends mainly on the availability of more sensitive photodetectors and the sophistication of TOF PET image reconstruction algorithms.

12 Povzetek doktorskega dela

12.1 Uvod

Pozitronska tomografija (angl. Positron Emission Tomography - PET) je metoda za medicinsko slikanje, ki omogoča iskanje tumorjev ter opazovanje procesov v telesu. Temelji na zaznavanju koincidenčnih žarkov γ, ki nastanejo pri razpadu sevalca, vbrizganega v telo pacienta. Meritev časovne razlike med prihodom obeh žarkov (časa preleta, angl. Time-of-Flight - TOF) lahko pomembno izboljša kvaliteto dobljenih slik. Ločljivost meritve časa preleta je odvisna od časovne ločljivosti detektorja svetlobe in relaksacijskega časa scintilatorja. Razvoj novih detektorjev svetlobe z odlično časovno ločljivostjo, kot so mikrokanalne fotopomnoževalke, pomeni, da glavno omejitev predstavljajo scintilatorji. Tej omejitvi bi se lahko izognili z zaznavanjem svetlobe Čerenkova, ki nastane v trenutku preleta nabitega delca skozi sevalec. Če želimo zaznavati svetlobo Čerenkova, potrebujemo sevalec, v katerem koincidenčni žarki γ z značilno energijo 511 keV predajo čim več energije elektronom, nadalje pa mora biti sevalec čimbolj primeren za nastanek in transport svetlobe Čerenkova. Te pogoje najbolje izpolnjujejo sevalci, sestavljeni iz elementov z visokim atomskim številom, kot sta kristala svinčev fluorid (PbF_2) in svinčev volframat ($PbWO_4$). V tem delu sta ta kristala preizkušena v preprosti napravi za pozitronsko tomografijo, v kateri sta kot detektorja svetlobe uporabljeni dve mikrokanalni fotopomnoževalki. Predstavljene so tudi računalniške simulacije, ki omogočajo boljše razumevanje rezultatov poskusov. Uporaba simulacij je omogočila tudi oceno zmogljivosti celotne narave za pozitronsko tomografijo, ki temelji na zaznavanju svetlobe Čerenkova.

12.2 Pozitronska tomografija

Ena izmed pomembnih metod nuklearne medicine je pozitronska tomografija. Metoda omogoča ne invazivno opazovanje celične aktivnosti v telesu, kar se uporablja med drugim za iskanje tumorjev in opazovanje možganske aktivnosti. PET deluje na principu zaznavanja parov koincidenčnih žarkov γ z značilno energijo 511 keV, ki nastajajo pri razpadih sevalcev β^+. Ti se nakopičijo v določenih tkivih, po tem ko pacientu vbrizgajo biološko aktivno substanco (radiofarmak), na katero predhodno vežejo β^+ sevalec. Najpogosteje uporabljen sevalac je ^{18}F z razpolovnim časom 110 min, kar je dovolj kratko da se aktivnost v pacientu po preiskavi hitro zniža na sprejemljivo nizko raven, a hkrati dovolj dolgo, da radiofarmak lahko dostavijo od mesta proizvodnje do mesta preiskave preden izgubi aktivnost.

Po razpadu β^+ koincidenčna žarka γ odletita v skoraj točno nasprotnih smereh, kar izkorišča naprava PET, ki tipično sestoji iz obročev prostorsko

občutljivih detektorjev žarkov γ, ki obdajajo pacienta. Kadar zaznamo dva žarka γ znotraj zelo kratkega časovnega okna (tipično okoli 10 ns) lahko trdimo, da se je razpad zgodil nekje na premici (angl. Line of Response - LOR) med položajema, kjer sta bila zaznana žarka γ. Tokom celotne preiskave se nabere veliko število tako zaznanih koincidenc in ustreznih premic, ki jih lahko preslikamo na 2-dimenzionalno mrežo, ki predstavlja določen presek skozi telo pacienta. Tako dobimo rekonstruirano sliko porazdelitve aktivnosti, saj se na mestu večje aktivnosti seka večje število premic (slika 12.1). V praksi se za rekonstrukcijo slik uporabljajo bolj napredni algoritmi, ki najpogosteje temeljijo na Fourierevi transformaciji preslikav premic po kotih (angl. Filtered Backprojection - FBP).

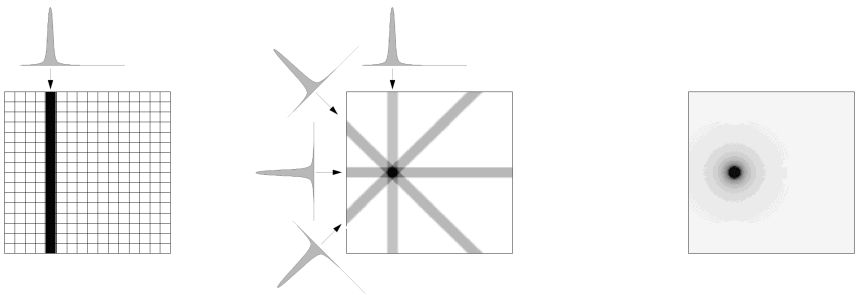

(a) 1 kot (b) 4 koti (c) 64 kotov

Slika 12.1: Princip najpreprostejše rekonstrukcije slike v primeru točkastega izvora: ko dodajamo premice, zaznane pod vedno več različnimi koti, se oblikuje vedno bolj točna slika porazdelitve aktivnosti.

Glavni sestavni del naprav PET je detektor žarkov γ, ki sestoji iz scintilacijskega kristala in detektorja svetlobe, tipično fotopomnoževalke. V scintilacijskem kristalu se del energije vpadnih žarkov γ pretvori v fotone scintilacijske svetlobe, ki jih nato zazna detektor svetlobe. Pomembna lastnost scintilacijskega kristala je njegova gostota, saj želimo čim večji delež koincidenčnih žarkov γ ustaviti v čim krajšem kristalu. Prav tako želimo da se v kristalu ustvari čim večje število scintilacijskih fotonov v čim krajšem času. V napravah PET sta najpogosteje uporabljena scintilatorja $Bi_4Ge_3O_{12}$ (BGO) in Lu_2SiO_5(Ce) (LSO). Lastnosti nekaterih najpomembnejših scintilatorjev za PET so zbrane v tabeli 12.1.

Da se doseže zadostna prostorska ločljivost, so scintilacijski kristali narezani na segmente, tipično velike okrog 6 mm v prečni dimenziji. V praksi je prostorska ločljivost dodatno omejena še z lastnostmi β^+ razpada in vplivi algoritma za rekonstrukcijo slike, zaradi česar naprave PET za slikanje celega telesa dosežejo prostorsko ločljivost okrog 5 mm. Druga pomembna lastnost naprav PET je občutljivost, ki je definirana kot delež števila parov koincidenčnih žarkov γ, nastalih v razpadih sevalca, ki se zazna kot koincidence v

	NaI(Tl)	BGO	BaF_2	LSO	$LaBr_3$(Ce)
ρ (g/cm^3)	3.7	7.1	4.9	7.4	5.1
μ_{511keV} (cm^{-1})	0.35	0.96	0.44	0.87	0.43
τ (ns)	230	300	0.6	40	17
Pridelek (fotonov/MeV)	38000	6000	2000	29000	58000
λ_{max} (nm)	415	480	220	420	356
n	1.85	2.15	1.52	1.82	1.88

Tabela 12.1: Lastnosti nekaterih scintilatorjev: gostota (ρ), atenuacijski koeficient za žarke γ z energijo 511 keV (μ_{511keV}), relaksacijski čas scintilacij (τ), pridelek scintilacijskih fotonov, valovna dolžina vrha scintilacij (λ_{max}) in lomni količnik (n) [6, 8, 9, 10].

napravi PET. Občutljivost lahko izrazimo kot:

$$\eta = \epsilon^2 g_{PET} T, \tag{12.1}$$

kjer je ϵ izkoristek posameznega detektorja žarkov γ, g_{PET} geometrijski izkoristek naprave PET in T delež aktivnosti, ki se ne absorbira v telesu pacienta. Izkoristek posameznega detektorja je odvisen predvsem od atenuacije žarkov γ:

$$\epsilon = f \cdot \left(1 - e^{-\mu_{511keV} \cdot x}\right), \tag{12.2}$$

kjer je μ_{511keV} atenuacijski koeficient za žarke γ z energijo 511 keV in x dolžina scintilacijskega kristala, faktor f pa predstavlja delež zaznanih dogodkov, ki se uporabijo v rekonstrukciji. Žarki γ se namreč lahko sipajo v telesu pacienta ali v delih detektorja in so zato zaznani na napačnem mestu, zato takšni dogodki znižajo kvaliteto rekonstruiranih slik. Iz tega razloga se v PET ne upošteva dogodkov, ki so zaznani z energijo znatno nižjo od prvotnih 511 keV, zaradi česar pa se izgubi tudi del pravih dogodkov, ki v detektorju ne pustijo celotne energije. Tipična občutljivost naprav PET je od 0.2% do 0.5% za koincidence omejene na posamezen obroč, in od 2% do 10%, če so dovoljene koincidence med več obroči.

Razvoj vedno hitrejših detektorjev svetlobe in scintilatorjev z vedno krajšim relaksacijskim časom omogoča dodatno izboljšanje meritev PET preko meritve časa preleta. Če bi čas preleta lahko izmerili poljubno natančno, rekonstrukcija slike sploh ne bi bila potrebna, saj bi bil položaj razpada določen dovolj natančno z enačbo:

$$\Delta x = \frac{c_0 \cdot \Delta t}{2}, \tag{12.3}$$

kjer vemo da razpad leži na premici med dvema detektorjema, Δx je razdalja med središčem te premice in položajem razpada, Δt pa je izmerjena razlika v času preleta. V praksi so s tradicionalnimi detektorji žarkov γ v laboratorijskih pogojih dosegli najboljšo časovno ločljivost okrog 300 ps [1, 2], kar

pomeni prostorsko ločljivost okrog 4.5 cm. To očitno ne zadošča da bi lahko določili položaj razpadov brez rekonstrukcije, vendar se ta dodatna informacija lahko uporabi za občutno izboljšanje kvalitete rekonstruiranih slik. Pri meritvi PET brez vključene meritve časa preleta namreč vsak dogodek prispeva k vsem elementom slike, ki ležijo vzdolž premice med detektorjema (slika 12.2). To pomeni, da se šum iz vsakega elementa slike razširi

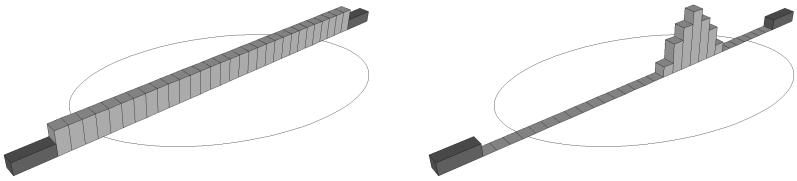

(a) Brez meritve časa preleta (b) Z meritvijo časa preleta

Slika 12.2: Prikaz vpliva meritve časa preleta na rekonstrukcijo slike: pri meritvi z časom preleta lahko omejimo prispevke posameznega dogodka le na elemente slike, ki ležijo znotraj območja, omejenega s časovno ločljivostjo meritve.

čez znaten del celotne slike. Če vključimo meritev časa preleta pa lahko prispevke posameznega dogodka omejimo na manjši del premice, katerega velikost je določena z časovno ločljivostjo. Na ta način se zmanjša nivo šuma in s tem poveča razmerje signal-šum na rekonstruirani sliki, kar lahko vodi do pomembnega izboljšanje diagnostične vrednosti slik. Izboljšanje zaradi meritve časa preleta lahko opišemo z ojačanjem občutljivosti (G_{TOF}):

$$\eta_{TOF} = G_{TOF} \cdot \eta, \tag{12.4}$$

kjer je η_{TOF} občutljivost meritve z vključenim časom preleta in η občutljivost meritve brez časa preleta (enačba (12.1)). Ojačanje občutljivosti se lahko izrazi kot:

$$G_{TOF} = \frac{2D}{c_0 \delta t}, \tag{12.5}$$

kjer je D prečna dimenzija opazovanega objekta (telesa pacienta), δt pa ločljivost meritve časa preleta. Iz enačbe (12.5) sledi, da v primeru časovne ločljivosti 300 ps in povprečnega pacienta ($D = 27$ cm [13]) lahko pričakujemo ojačanje občutljivosti za faktor 6. Ta izboljšava se lahko uporabi za skrajšanje časa preiskave, znižanje doze radioaktivnosti, ki jo je potrebno vbrizgati pacientu, ali pa za izboljšanje kvalitete preiskave pri nespremenjenih pogojih. Prav tako ob upoštevanju enačbe (12.5) vidimo, da so prednosti meritve časa preleta največje v primeru večjih (težjih) pacientov.

Časovna ločljivost meritve časa preleta je določena predvsem s časovno ločljivostjo detektorja svetlobe in relaksacijskim časom scintilatorja. Najpogosteje uporabljeni detektorji svetlobe - fotopomnoževalke - lahko dosežejo

časovno ločljivost $100 - 200$ ps [3], medtem ko novejši detektorji svetlobe, kot so mikrokanalne fotopomnoževalke, lahko dosežejo celo ločljivost z $\sigma < 30$ ps (70 ps FWHM) [4, 5]. Glavna omejitev za časovno ločljivost tako postane časovni odziv scintilatorjev.

12.3 Fotopomnoževalka

V napravah PET se kot detektor svetlobe najpogosteje uporablja fotopomnoževalka (angl. Photomultiplier Tube - PMT). Sestoji iz steklene vakuumske cevi, fotokatode, sistema pospeševanja in sistema pomnoževanja elektronov. Fotokatoda je naparjena na notranji strani vstopnega okna fotopomnoževalke. Vpadni fotoni lahko preko fotoefekta iz fotokatode izbijejo elektron. Verjetnost da vpadni foton z valovno dolžino λ izbije elektron izraža kvantni izkoristek (angl. Quantum Efficiency - QE). V PET so najpogosteje uporabljene t.i. bialkalne fotokatode, ki imajo kvantni izkoristek največ okrog 20%. Izbiti elektron se nato pospeši v močnem električnem polju znotraj fotopomnoževalke, ki elektrone tudi usmerja v sistem pomnoževanja. Tega doseže le del elektronov, ki ga izraža zbiralni izkoristek (α). Učinkovitost zaznavanja fotonov (angl. Photon Detection Efficiency - PDE) je tako $\mathrm{PDE} = \mathrm{QE} \cdot \alpha$. Sistem pomnoževanja je ponavadi zgrajen iz serije dinod, med katerimi se elektroni pospešujejo v dodatnem električnem polju. Površina dinod je prevlečena s polprevodnikom, iz katerega vpadni elektron z visoko energijo lahko izbije več sekundarnih elektronov (tipično $3 - 6$). Po tipično okoli 10 dinodah začetni elektron tako lahko ustvari plaz $10^6 - 10^7$ elektronov, ki se zbere na zadnji dinodi (anodi) in uporabi kot izhodni signal fotopomnoževalke. Kadar so fotopomnoževalke izpostavljene pulzom svetlobe, ki prihajajo npr. iz scintilatorja, je izhodni signal fotopomnoževalke sorazmeren številu fotonov v pulzu. Fotopomnoževalka tako lahko meri energijo delca, ki se je absorbiral v scintilatorju. Časovna ločljivost fotopomnoževalk je omejena predvsem z fluktuacijami v času potovanja elektrona od fotokatode do prve dinode, saj so elektroni izbiti v različnih smereh in z različnimi energijami, nakar morajo prepotovati različno dolge poti glede na to, kje na površini vstopnega okna so izbiti.

Primer novejšega tipa fotopomnoževalk so t.i. mikrokanalne fotopomnoževalke (angl. Microchannel Plate Photomultipler Tube - MCP PMT), ki za sistem pomnoževanja namesto serije dinod uporablja tanko ploščico, v kateri so zelo na gosto razporejeni $10-100$ μm široki kanali. Površina ploščice je prevlečena s kovino in služi kot elektroda za pospeševanje elektronov, medtem ko so površine kanalov prevlečene s polprevodnikom. Če vpadni elektron zadane površino kanala, sproži emisijo sekundarnih elektronov, ki se nato vzdolž kanala nadalje pospešujejo. Če se uporabi dve mikrokanalni ploščici v zaporedju (slika 12.3), lahko MCP PMT tako doseže ojačanje ki je primerljivo s klasičnimi fotopomnoževalkami. Tak sistem

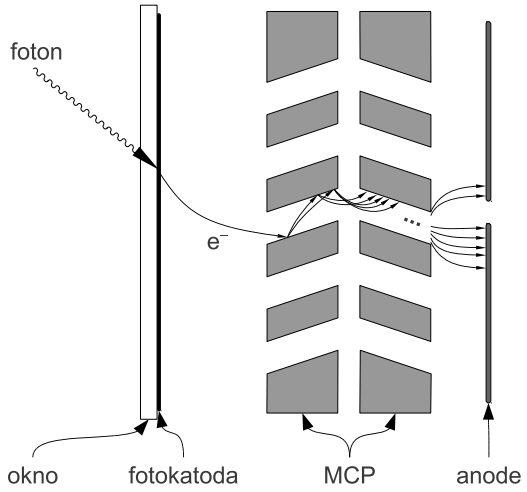

Slika 12.3: Shema delovanja mikrokanlne fotopomnoževalke, ki uporablja dve mikrokanalni ploščici.

pomnoževanja omogoča bolj kompaktne dimenzije in planarno geometrijo naprave, zaradi česar mikrokanalne fotopomnoževalke lahko dosežejo boljšo časovno ločljivost kot klasične fotopomnoževalke.

12.4 Uporaba svetlobe Čerenkova za PET

Omejitvi, ki jo za časovno ločljivost predstavljajo scintilatorji, se lahko izognemo, če namesto scintilacij uporabimo svetlobo Čerenkova. Ta nastane v trenutku preleta nabitega delca skozi snov (z lomnim količnikom n), kadar je hitrost delca večja od hitrosti svetlobe v tej snovi:

$$v > c_0/n. \tag{12.6}$$

Najprej pa morajo vpadni žarki γ predati čim večji delež svoje energije elektronom v primernem sevalcu svetlobe Čerenkova. Žarki γ z energijo 511 keV interagirajo s snovjo preko fotoefekta ali Comptonskega sipanja. V primeru fotoefekta žarek γ preda vso svojo energijo vezanemu elektronu v snovi in ga izbije iz atoma. Elektron prejme kinetično energijo, ki je enaka razliki energije žarka γ in vezavne energije elektrona. Ta je v primeru K orbitale v svincu 88.005 keV [23], kar pomeni, da po fotoefektu koincidenčnih žarkov γ elektronom ostane približno 423 keV. V primeru Comptonskega sipanja se žarek γ siplje na elektronu in mu preda le del svoje energije. Elektroni, ki nastanejo preko Comptonskega sipanja, imajo zvezno porazdelitev energije z največjo možno energijo, ki je v primeru koincidenčnih žarkov γ približno 341 keV. Zato je pomembno, da čim večji delež interakcij v sevalcu poteka preko fotoefekta. Ta pogoj izpolnijo snovi s čim večjim atomskim številom (Z),

kar je povezano tudi z večjo gostoto in s tem tudi boljšo atenuacijo žarkov γ. Nadalje mora biti sevalec prozoren za fotone Čerenkova, ki so najštevilčnejši v vidnem in UV delu spektra, ter imeti visok lomni količnik, tako da je čim večji delež elektronov nad pragom za nastanek svetlobe Čerenkova (enačba (12.6)).

	Steklo(57% Pb)	Steklo(72% Pb)	PbF_2	$PbWO_4$
n	1.7	1.8	1.8	2.3
ρ (g/cm^3)	4.07	5.2	7.77	8.28
T_{prag} (keV)	121	104	104	56
λ_{opt} (nm)	370	380	250	350
Scintilacijski pridelek (fot./MeV)	-	-	-	200
Scintilacijski τ (ns)	-	-	-	6/30
Scintilacijski λ_{max} (nm)	-	-	-	440/530

Tabela 12.2: Lastnosti kandidatov za sevalce svetlobe Čerenkova: lomni količnik (n), gostota (ρ), kinetična energija elektronov, nad katero lahko sevajo svetlobo Čerenkova (T_{prag}), spodnja meja optične prepustnosti (λ_{opt}) in lastnosti scintilacij - pridelek, relaksacijski čas (τ) in valovna dolžina vrha scintilacij (λ_{max}) [18, 24, 25, 26, 27, 28, 29].

Možni kandidati za sevalce svetlobe Čerenkova so stekla ali kristali z visokim deležem svinca. V tabeli 12.2 so zbrane lastnosti svinčevega stekla in dveh sevalcev Čerenkova, ki sta bila razvita za detektorje v fiziki osnovnih delcev: svinčev fluorid (PbF_2) in svinčev volframat ($PbWO_4$). Najprimernejša izgledata kristal $PbWO_4$, ki ima najvišjo gostoto in lomni količnik, ter PbF_2 z odlično prepustnostjo za svetlobo. Iz presekov za interakcije žarkov γ [21] lahko izračunamo atenuacijska koeficienta za interakcije žarkov γ z energijo 511 keV, ki sta 1.06 cm^{-1} za PbF_2 in 1.08 cm^{-1} za $PbWO_4$. To pomeni, da imata ta dva kristala boljšo atenuacijo kot scintilacijski kristal BGO.

Iz Frank-Tammove enačbe [19] lahko izpeljemo število fotonov Čerenkova (N), ki se izsevajo v teh kristalih v približku konstantne energije elektrona :

$$N \approx \left(\frac{370}{eVcm}\right) \Delta E L \left[1 - \left(\frac{1}{n(E)\beta}\right)^2\right], \tag{12.7}$$

kjer je ΔE interval energij fotonov Čerenkova, L dolžina poti elektrona, preden njegova energija pade pod prag produkcije svetlobe Čerenkova in $\beta = v/c_0$. V primeru največje možne energije elektronov v PbF_2 (423 keV) in če privzamemo da se lomni količnik ne spreminja z valovno dolžino sledi:

$$N \approx \frac{370}{eVcm} 3.4\ eV \cdot 0.25\ mm \left[1 - \left(\frac{1}{1.8 \cdot 0.84}\right)^2\right] = 17.7.$$

Tu energijski interval $\Delta E \approx 3.4$ eV ustreza tipičnemu območju občutljivosti detektorjev svetlobe, dolžina $L \approx 0.25$ mm pa je pot ki jo prepotuje elektron

z začetno energijo 423 keV preden mu energija pade pod prag produkcije svetlobe Čerenkova. Če upoštevamo konstantno izgube energije elektrona, ko se ta siplje in ustavlja v snovi, ter odvisnost lomnega količnika snovi od valovne dolžine fotonov, dobimo bolj točno vrednost za število izsevanih fotonov Čerenkova: N = 13.7.

Od vseh izsevanih fotonov Čerenkova lahko zaznamo le tiste, ki zapustijo kristal skozi izstopno površino, ki je sklopljena z detektorjem svetlobe. Tu se pojavi dodatna omejitev, ki je posledica popolnega odboja na površini med sevalcem Čerenkova in oknom detektorja svetlobe, ki ima tipično lomni količnik približno 1.5. Za PbF_2 (n=1.8) in $PbWO_4$ (n=2.3) sta mejni kot popolnega odboja (θ_0) in delež izsevanih fotonov ki zapustijo sevalec v smeri detektorja svetlobe ($N_{detektor}/N$):

$$\theta_0 = \begin{cases} 56.4^\circ & PbF_2 \\ 40.7^\circ & PbWO_4 \end{cases} \quad \text{and} \quad \frac{N_{detektor}}{N} = \begin{cases} 0.22 & PbF_2 \\ 0.12 & PbWO_4 \end{cases} .$$

Od $N = 13.7$ tako detektor svetlobe doseže le

$$N_{detektor} = \begin{cases} 3.1 & PbF_2 \\ 1.7 & PbWO_4 \end{cases}$$

fotonov Čerenkova. Za fotopomnoževalke je tipična učinkovitost zaznavanja fotonov, povprečena med valovnimi dolžinami med 250 in 800 nm, le okrog 5%. To pomeni, da je učinkovitost zaznavanja koincidenčnih žarkov γ veliko nižja, če se jih zaznava preko sevanja Čerenkova, kot v primeru tradicionalnih scintilatorjev. Prav tako ni možna meritev energije žarkov γ in s tem izločanje dogodkov, zaznanih po sipanju.

Čeprav svetloba Čerenkova nastane brez znatnega časovnega zamika v trenutku interakcije žarka γ, sevalec Čerenkova vseeno prispeva k časovni ločljivosti, saj mora svetloba še vedno potovati od mesta interakcije do detektorja svetlobe. V primeru 15 mm dolgega kristala PbF_2 je razlika v času potovanja med fotoni, izsevanimi na samem začetku in samem koncu kristala 40 ps, če v obeh primerih foton potuje po najkrajši možni poti do detektorja svetlobe. Fluktuacije v času potovanja se še povečajo, če upoštevamo vse možne poti fotonov, ki lahko vključujejo tudi večkratne odboje od stranskih ploskev kristala. Fluktuacije v času potovanja fotonov tako postanejo glavni prispevek k časovni ločljivosti meritev.

Uporaba svetlobe Čerenkova za PET je bila že predlagana v [17], kjer so kot sevalec uporabili aerogel z lomnim količnikom do $n = 1.2$. Prednost takšnega sevalca je neobčutljivost za žarke z energijo pod polno energijo koincidenčnih žarkov γ, vendar je občutljivost takšnega detektorja prenizka. Z uporabo gostejših sevalcev so v [18] s preprostim poskusom dosegli časovno ločljivost 170 ps, v [16] pa so z zelo majhnimi nedopiranimi scintilacijskimi kristali dosegli ločljivost 250 ps.

12.5 Meritve

12.5.1 Postavitev poskusa

Meritev časa preleta preko zaznavanja svetlobe Čerenkova je bila preizkušena v poskusu z dvema detektorjema žarkov γ, ki sta bila sestavljena iz mikrokanalnih fotopomnoževalk in različnih sevalcev. Lastnosti takšnega osnovnega gradnika naprave PET so bile preizkušene s točkastim sevalcem ^{22}Na, ki je bil postavljen med oba detektorja (slika 12.4). Razdalja med

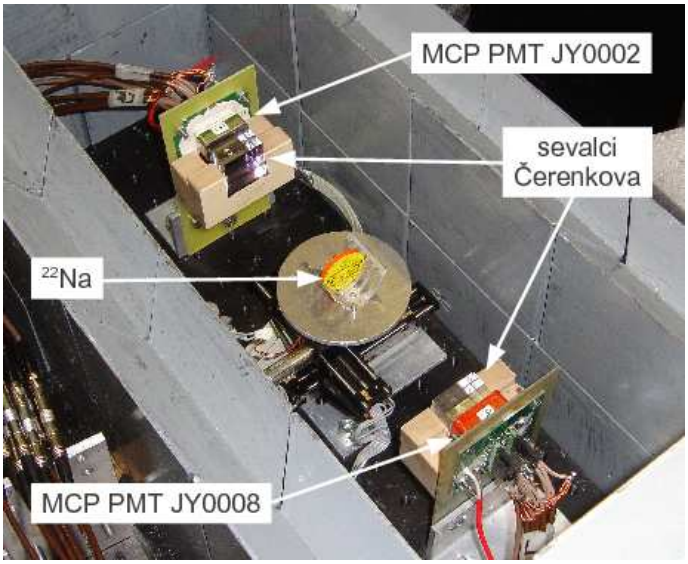

Slika 12.4: Postavitev poskusa z dvema detektorjema. Sevalca svetlobe Čerenkove na sliki sta gola, 15 mm dolga kristala PbF_2.

detektorjema je bila 200 mm, merjeno med oknoma obeh fotopomnoževalk.

Za meritve so bile na volje tri mikrokanalne fotopomnoževalke proizvajalca Hamamatsu Photonics, zasnovane na podlagi prototipov ki so bili razviti za števec časa preleta v načrtovanem spektrometru Belle II [34]. Lastnosti teh fotopomnoževalk, ki bodo označene kot JY0002, JY0005 in JY0008, so zbrane v tabeli 12.3, slika 12.5 pa prikazuje njihov kvantni izkoristek.

Meritve so bile opravljene s sevalci svetlobe Čerenkova z različnimi lastnostmi: dolžino, obdelavo površin in prevleko površin. Preizkušeni so bili kristali PbF_2 in $PbWO_4$ s presekom 25×25 mm^2 in z dolžinami 5 in 15 mm, ter sevalci PbF_2 v obliki 4×4 segmentiranih kristalov z dolžino 7.5 mm in presekom posameznih kosov 5.575×5.575 mm^2. Površina kristala, ki je bila sklopljena s fotopomnoževalko (izstopna površina) je bila v vseh primerih gladka, ostalih pet površin pa je bilo lahko gladkih ali grobo obdelanih. Površine so bile lahko zavite v bel Teflonski trak, pobarvane s črno barvo ali neprevlečene. Trije tipi prevlek površin sevalca so prikazani na sliki 12.6. S segmentiranimi kristali so bile meritve opravljene tudi v primeru različnih

	Vse tri		
Dimenzije	$27.5\times27.5\times15$ mm^3		
Občutljiva površina	22.5×22.5 mm^2		
Vstopno okno	1.5 mm debelo borosilikatno steklo		
Fotokatoda	bialkalij		
Premer kanalov MCP	10 μm		
Število MCPjev	2		
Anoda	4×4 segmentirana		
Velikost anode	5.575 mm		
	JY0002	JY0005	JY0008
Napetost za ojačanje 10^6	2400 V	2600 V	3400 V
Zaščitna plast Al	Ne	Ne	Da
Zbiralni izkoristek	≈60%	≈60%	≈30%
Največji QE	6.4%	20%	24%
Integral PDE (250−800nm)	1.6%	5.9%	4.1%

Tabela 12.3: Lastnosti treh mikrokanalnih fotopomnoževalk, uporabljenih v poskusih.

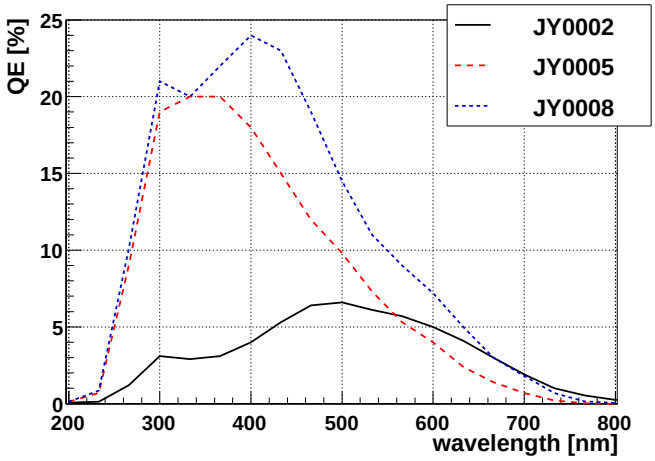

Slika 12.5: Kvantni izkoristki uporabljenih mikrokanalnih fotopomnoževalk, po specifikacijah proizvajalca.

Slika 12.6: Kristali PbF_2 dimenzij $25\times25\times15$ mm^3, katerih površine so: pobarvane s črno barvo, zavite v Teflonski trak in gole.

prevlek vstopne in stranskih površin kristala. Segmentirani kristali z nekaj različnimi kombinacijami prevlek so prikazani na sliki 12.7.

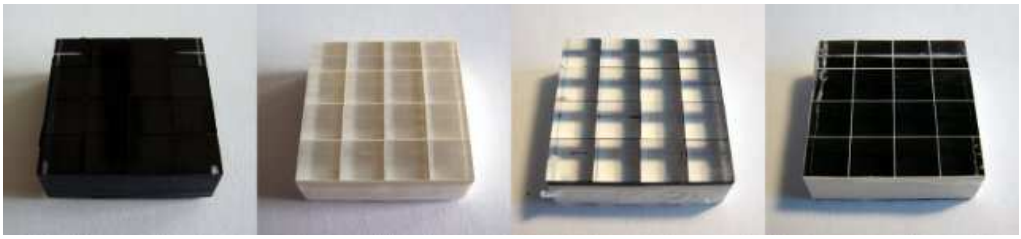

Slika 12.7: 4×4 segmentirani kristali PbF_2, ki imajo vstopno in stranske ploskve pobarvane s črno barvo ali pa zavite v bel Teflonski trak.

Delovno napetost sta mikrokanalnim fotopomnoževalkam zagotavljali napajalni vezji, ki sta služili tudi kot vmesnika za priklop signalov iz vseh 16 anod posamezne fotopomnoževalke. Signali iz anod so bili speljani preko ojačevalnika na analogno digitalni pretvornik naboja (angl. Charge to Digital Converter - QDC) in na diskriminator. Logični signali iz diskriminatorja so za merilnik časa (angl. Time to Digital Converter - TDC) definirali čas dogodkov. Meritev je bila sprožena, kadar je bila na vsaki fotopomnoževalki zadeta vsaj ena anoda. Na voljo je bilo 32 kanalov za meritev naboja a le 16 kanalov za meritev časa. To pomeni, da niso bile možne meritve na vseh 32 anodah obeh fotopomnoževalk hkrati. Zato so bile meritve opravljene z le nekaj posamično povezanimi anodami na fotopomnoževalko, pri čemer so bili ostali anodni signali lahko sešteti v 2 do 4 kanale. Natančne meritve časa preleta so bile opravljene le na posamično povezanih anodah, medtem ko so sešteti kanali zagotavljali informacijo o naboju, izmerjenem po ostalih kanalih fotopomnoževalke.

12.5.2 Lastnosti mikrokanalnih fotopomnoževalk

Delovanje mikrokanalnih fotopomnoževalk je bilo preizkušeno v poskusu, v katerem so bile izpostavljene zelo kratkim pulzom svetlobe iz laserja, ki je bil lahko rdeče (636 nm) ali modre (404 nm) barve. Intenziteta laserskih pulzov je bila s pomočjo nevtralnih filtrov nastavljena na zelo nizko raven, tako da so fotopomnoževalke redko zaznale več kot en foton na pulz. Od laserja do fotopomnoževalke so pulzi svetlobe potovali preko optičnih vlaken, sistem leč pa je zagotavljal, da so imeli laserski pulzi na površini fotopomnoževalke širino manj kot 1 mm. S pomočjo računalniško vodene mizice je bila laserska svetloba natančno usmerjena nad posamezne anode fotopomnoževalk. Za te poskuse je bilo posamično povezanih 8 anod vsake fotopomnoževalke, ostalih 8 anod na fotopomnoževalko pa je bilo združenih v 2 kanala. Meritev je bila prožena s signalom iz laserke enote, ki je označeval začetek laserskega pulza.

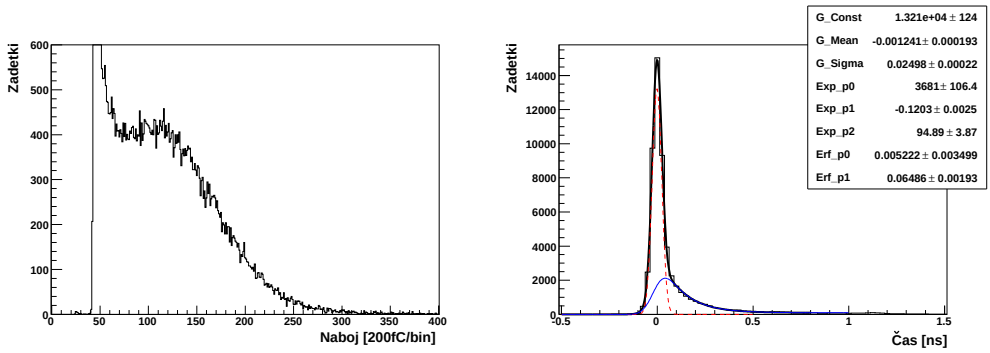

(a) (b)

Slika 12.8: Porazdelitev naboja (a) in časa (b) za fotopomnoževalko JY0005 v primeru osvetlitve z rdečim laserjem.

Tipični porazdelitvi naboja in časa signalov iz posamično povezane anode sta prikazani na sliki 12.8. Porazdelitve časa vsebujejo le dogodke, kjer je imel opazovani kanal izmerjen največji naboj na svoji fotopomnoževalki, in so bile popravljene za fluktuacije, ki so posledica delovanja diskriminatorja (angl. Time-Walk).

Časovna porazdelitev je sestavljena iz ozkega vrha, ki je posledica običajnih dogodkov v mikrokanalni fotopomnoževalki, in manjšega deleža dogodkov, ki so zaznani z zakasnitvami do približno 1.5 ns. Ti dogodki nastanejo zaradi povratnega sipanja elektronov na mikrokanalni ploščici [4] in poslabšajo sicer odličen časovni odziv mikrokanalnih fotopomnoževalk.

Na porazdelitve časa je bila prilagojena funkcija, sestavljena iz Gaussove funkcije in eksponentne funkcije, ki je pomnožena s Gaussovo funkcijo napake (angl. Error function). Časovna ločljivost je bila ocenjena kot širina prilagojene funkcije na polovici višine porazdelitve (angl. Full-Width Half-Maximum - FWHM). Časovna ločljivost, povprečena po osmih posamično povezanih anodah, je v primeru osvetlitve z rdečo svetlobo 63.4 ps za fotopomnoževalko JY0002, 63.2 ps za JY0005 in 58.7 ps za JY0008. Za fotopomnoževalki JY0002 in JY0005 sta bili časovni ločljivosti izmerjeni tudi z osvetlitvijo z modro svetlobo, rezultata sta 74.8 ps in 83.4 ps. Vrednosti časovnih ločljivosti vsebujejo fluktuacije, ki so posledica delovanja laserja (prispevek s standardno deviacijo $\sigma \approx 15$ ps) in elektronike (prispevek s standardno deviacijo $\sigma \approx 11$ ps).

12.5.3 Meritev časa preleta

Prve meritve časa preleta so bile opravljene s fotopomnoževalkama JY0005 in JY0008. Individualno povezani sta bili le dve anodi na fotopomnoževalko, locirani blizu centra občutljive površine. Ostalih 14 anodnih izhodov na fo-

topomnoževalko je bilo združenih v dva kanala. Meritev časa preleta je bila tako na voljo za 4 kombinacije posamično povezanih anod. Čas koincidenc je bil izračunan kot razlika časov, izmerjenih na kanalih ki sta pripadala različni fotopomnoževalki, popravljenih za efekt diskriminatorja (Time-Walk). Nadalje so bili uporabljeni le dogodki, kjer sta imela opazovana kanala izmerjena največja naboja na svojih fotopomnoževalkah. Na sliki 12.9 so zbrane

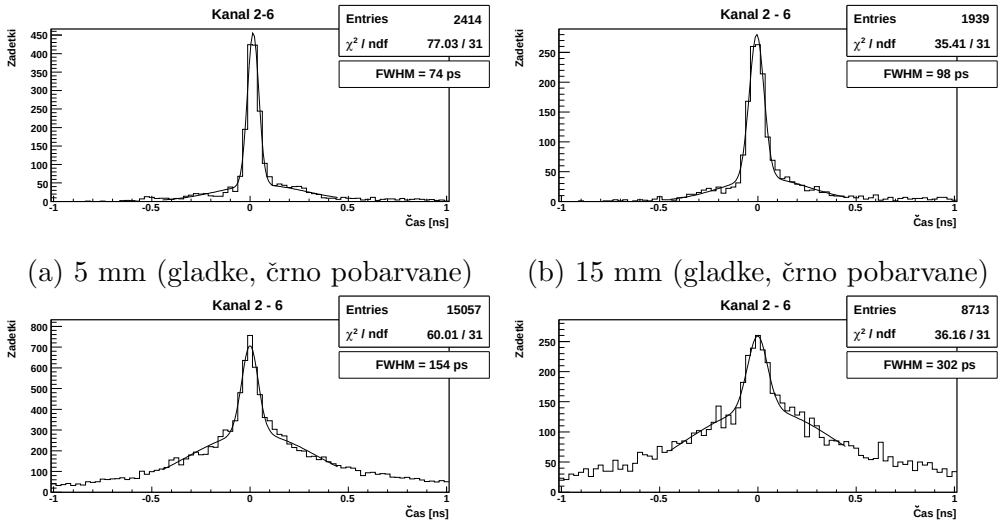

(a) 5 mm (gladke, črno pobarvane) (b) 15 mm (gladke, črno pobarvane)

(c) 15 mm (gladke, gole) (d) 15 mm (gladke, zavite v Teflon)

Slika 12.9: Porazdelitve časa koincidenc v primeru različno obdelanih površin in dolžin kristalov PbF_2.

porazdelitve časa koincidenc za eno od štirih kombinacij kanalov v primeru različnih sevalcev svetlobe Čerenkova. Porazdelitve imajo ozek centralni vrh in širšo porazdelitev, kot je za pričakovati za konvolucijo odzivov dveh mikrokanalnih fotopomnoževalk. Porazdelitvam so bile prilagojene funkcije, sestavljene kot vsota dveh Gaussovih funkcij, ločljivost meritve časa preleta pa je bila ocenjena kot širina prilagojene funkcije na polovici višine porazdelitve. Časovne ločljivosti v primeru različnih sevalcev, izmerjene za eno kombinacijo kanalov, so navedene v tabeli 12.4.

Bolj natančne meritve so bile opravljene s fotopomnoževalkama JY0002 in JY0005, vključenimi v izboljšani čitalni vezji. Nova verzija vezij je omogočala lažjo povezavo velikega števila anodnih izhodov z merilno elektroniko in lažje združevanje signalov anod, ki niso bile individualno povezane. Za sledeče meritve je bilo individualno povezanih 8 anod na fotopomnoževalko, ki so ležali na zgornji polovici naprave. Ostalih 8 anodnih signalov na fotopomnoževalko je bilo združenih v dva kanala. Meritev časa preleta je bila tako na voljo za 64 kombinacij posamično povezanih anod. Porazdelitve časa koincidenc za eno od teh kombinacij so prikazane na sliki 12.10 v primeru PbF_2 in na sliki 12.11 v primeru $PbWO_4$. V primerjavi s prvotnimi merit-

	Sevalec			Časovna ločljivost [ps]	
Material	Površine	Prevleka	Dolžina	FWHM	σ
PbF_2	gladke	črna barva	5 mm	74.2	29.3
PbF_2	gladke	črna barva	15 mm	98.0	37.5
PbF_2	grobe	črna barva	5 mm	76.1	30.2
PbF_2	grobe	črna barva	15 mm	104	39.0
PbF_2	gladke	brez	5 mm	90.1	31.7
PbF_2	gladke	brez	15 mm	154	41.9
PbF_2	grobe	brez	15 mm	156	42.5
PbF_2	gladke	Teflon	15 mm	302	50.4

Tabela 12.4: Ločljivost meritve časa preleta za različne sevalce svetlobe Čerenkova. Ločljivost je podana tudi kot standardna deviacija ožje Gaussove funkcije (σ).

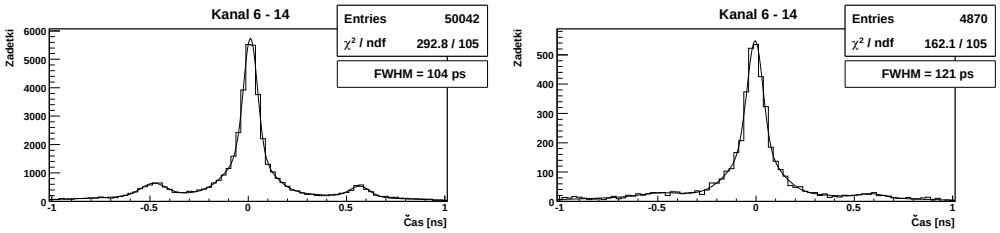

(a) 5 mm (gladke, črno pobarvane) (b) 15 mm (gladke, črno pobarvane)

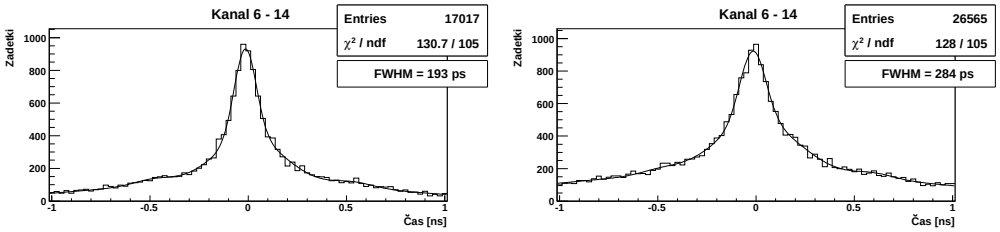

(c) 15 mm (gladke, gole) (d) 15 mm (gladke, zavite v Teflon)

Slika 12.10: Porazdelitve časa koincidenc v primeru različno obdelanih površin in dolžin kristalov PbF_2, v primeru osmih posamično povezanih anod na fotopomnoževalko.

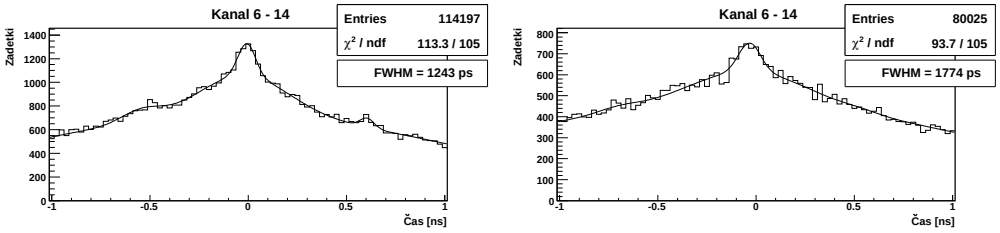

(a) 5 mm (grobe, črno pobarvane) (b) 15 mm (grobe, črno pobarvane)

Slika 12.11: Porazdelitve časa koincidenc v primeru različnih dolžin kristalov $PbWO_4$, v primeru osmih posamično povezanih anod na fotopomnoževalko.

vami sta se na porazdelitvah pojavila manjša vrhova, ki sta od centralnega vrha oddaljena približno 0.6 ns. Ta vrhova sta najverjetneje posledica presluha med kanali ali odbojev signalov v povezavah med fotopomnoževalko in merilno elektroniko. Porazdelitvam časa koincidenc so bile prilagojene funkcije, sestavljene kot vsota petih Gaussovih funkcij, od česar sta dve kot prej opisali ozek centralni vrh in del širše porazdelitve, dve sta opisali dodatna manjša vrhova, še zadnja pa je pomagala opisati širše prispevke ki so posledica močno zakasnjenih fotonov v primeru površin zavitih v Teflon ali scintilacijskih fotonov v primeru kristala $PbWO_4$. V tabeli 12.5 so zbrane časovne ločljivosti v primeru različnih sevalcev, povprečene po osmih kombinacijah kanalov, ki so iz geometrijskih razlogov zbrale najvišje število dogodkov. Časovne ločljivosti izmerjene v primeru osmih so slabše kot v primeru dveh

Sevalec				Časovna ločljivost [ps]	
Material	Površine	Prevleka	Dolžina	FWHM	σ
PbF_2	gladke	črna barva	5 mm	103	35.1
PbF_2	gladke	črna barva	15 mm	132	45.4
PbF_2	grobe	črna barva	5 mm	106	35.9
PbF_2	grobe	črna barva	15 mm	132	44.0
PbF_2	gladke	brez	5 mm	125	38.1
PbF_2	gladke	brez	15 mm	186	53.3
PbF_2	gladke	Teflon	5 mm	162	46.2
PbF_2	gladke	Teflon	15 mm	271	66.2
$PbWO_4$	grobe	črna barva	5 mm	1402	47.2
$PbWO_4$	grobe	črna barva	15 mm	2067	72.0

Tabela 12.5: Ločljivost meritve časa preleta za različne sevalce svetlobe Čerenkova, v primeru osmih posamično povezanih anod na fotopomnoževalko. Vrednosti predstavljajo povprečje po osmih kombinacijah kanalov z največ dogodki in so podane tudi kot standardna deviacija ožje Gaussove funkcije (σ).

posamično povezanih anod na fotopomnoževalko. To je deloma posledica dejstva, da so vrednosti v tabeli 12.5 izražene kot povprečje po osmih kombinacijah kanalov, medtem ko so vrednosti v tabeli 12.4 podane za kombinacijo kanalov, ki je konsistentno merila z najboljšo ločljivostjo. Drug razlog za poslabšanje ločljivosti je geometrijski, saj so bile v prvem primeru v meritev časovne informacije vključene le anode, blizu centra naprave. Ko je bilo individualno povezanih 8 anod na fotopomnoževalko, so se povečale možne fluktuacije v poti fotonov Čerenkova, ki so prispevali k meritvi. Verjetno največji prispevek k poslabšanju pa predstavlja dodatno ozadje, povezano z dvema manjšima vrhovoma.

V tabeli 12.6 so zbrani še rezultati, dobljeni za različne prevleke površin 4×4 segmentiranih, 7.5 mm dolgih kristalov PbF_2.

Najboljša ločljivost meritve časa preleta, 74.2 ps FWHM v primeru 5 mm dolgih, črno pobarvanih kristalov PbF_2, se dobro sklada s pričakovanju, če

Prevleka površin		Časovna ločljivost [ps]	
vstopna površina	stranske površine	FWHM	σ
črna barva	črna barva	116	39.3
brez	črna barva	133	41.0
Teflon	črna barva	178	49.4
črna barva	Teflon	172	44.5
brez	Teflon	245	50.9
Teflon	Teflon	301	63.5

Tabela 12.6: Ločljivost meritve časa preleta za različne prevleke površin 4×4 segmentiranih, kristalov PbF_2, v primeru osmih posamično povezanih anod na fotopomnoževalko. Vrednosti predstavljajo povprečje po osmih kombinacijah kanalov z največ dogodki in so podane tudi kot standardna deviacija ožje Gaussove funkcije (σ).

upoštevamo, da vključuje prispevka detektorjev svetlobe in elektronike. Najboljše ločljivosti so bile dobljene s kristali, katerih površine so bile pobarvane s črno barvo. V primeru kristalov z neobdelanimi površinami k rezultatom prispevajo tako fotoni, ki dosežejo detektor svetlobe neposredno brez odbojev, kot fotoni, ki se pred detekcijo lahko tudi večkrat odbijejo od vstopne in stranskih površin kristala. Časovne fluktuacije, s katerimi so zaznani slednji so lahko zelo velike, kar razširi centralni vrh in prispeva k širokemu delu porazdelitev časa koincidenc. V primeru površin, zavitih v Teflonski trak, k rezultatom prispevajo tudi fotoni, ki so zaznani šele po tem ko zapustijo kristal in se od prevleke odbijejo nazaj v kristal. Takšni dogodki še dodatno prispevajo k široki porazdelitvi. Če pa je kristal prevlečen s črno barvo, ta ne samo da ustavi fotone ki zapustijo kristal, temveč tudi zmanjša delež fotonov, ki se odbijejo od pobarvanih površin kristala. Med barvo in površino kristala namreč ne ostane tanke plasti zraka z lomnim količnikom $n = 1$. Barva spremeni lomni količnik zunaj kristala v $n > 1$, kar poveča mejni kot popolnega odboja in s tem zmanjša delež odbitih fotonov. V primeru črno pobarvanih kristalov tako k porazdelitvam časa koincidenc prispevajo predvsem fotoni ki so zaznani brez odbojev in imajo zato najmanjše fluktuacije v času potovanja.

V nasprotju s pričakovanji so bili rezultati, dobljeni z grobo obdelanimi skoraj povsem enaki rezultatom z gladko obdelanimi stranskimi površinami. V rezultatih dobljenih s kristali $PbWO_4$ pa prevladujejo prispevki scintilacij, ki predstavljajo zelo široko ozadje. Na porazdelitvah časa koincidenc sta prisotna ozka vrhova, ki najverjetneje pripadata dogodkom, ko sta oba detektorja zaznala foton Čerenkova, a nista zelo izrazita.

12.5.4 Meritev učinkovitosti detektorja

Za meritev učinkovitosti detektorjev Čerenkova je bil eden od dveh detektorjev z mikrokanalnima fotopomnoževalkama zamenjan z referenčnim detektor-

jem žarkov γ. Ta je bil sestavljen iz klasične fotopomnoževalke in scintilatorja BGO s presekom 4.2×4.2 mm^2 in dolžino 20 mm. Referenčni detektor je bil od izvora oddaljen 200 mm, kar je v kombinaciji z majhnim presekom scintilatorja zagotavljalo, da so žarki γ v koincidenci vpadali le na ozek centralni del detektorja Čerenkova. Anodni signali mikrokanalne fotopomnoževalke so bili združeni v 4 kanale. Časovna ločljivost izmerjena z združenimi kanali je bila slabša kot v primeru posamično povezanih anod, vendar zadostna za meritev učinkovitosti.

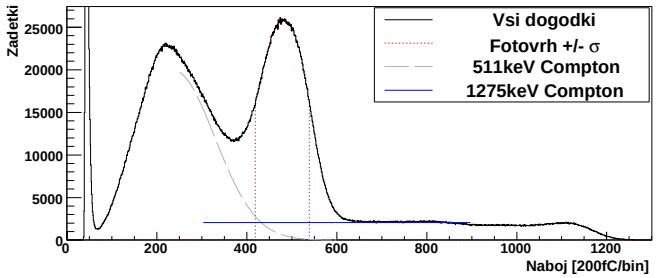

Slika 12.12: Porazdelitev naboja na referenčnem detektorju (črna barva). Z rdečo barvo je označen 2 σ širok interval okrog središča fotovrha, ki je bil uporabljen za izbiro koincidenčnih dogodkov. Siva in modra barva pa predstavljata prispevke Comptonskega kontinuuma za žarke γ z energijama 511 keV in 1275 keV.

Slika 12.12 prikazuje porazdelitev naboja, izmerjenega na referenčnem detektorju. Porazdelitev je sestavljena iz zvezne porazdelitve Comptonsko sipanih žarkov γ (Comptonov kontinuum) z začetno energijo 511 keV in ozkega vrha, ki ustreza fotoefektu žarkov z energijo 511 keV (fotovrh). Dodatno sta v porazdelitvi vidna še fotovrh in Comptonov kontinuum, ki ustrezata žarkom γ z začetno energijo 1275 keV. Ti so tako kot koincidenčni žarki γ posledica razpadov ^{22}Na. V primeru dogodka, ki je na referenčnem detektorju zaznan v fotovrhu (ima energijo blizu 511 keV), lahko z veliko gotovostjo trdimo, da ga je povzročil koincidenčni žarek γ. To pomeni, da je bil v tem dogodku detektor Čerenkova skoraj zagotovo zadet z drugim koincidenčnim žarkom γ. Učinkovitost detekcije se tako lahko oceni kot razmerje dogodkov, zaznanih na Čerenkovem detektorju, in dogodkov, ki jih referenčni detektor zazna v fotovrhu.

Slika 12.13 prikazuje časovne porazdelitve dogodkov, zaznanih z detektorjem Čerenkova. Za oceno učinkovitosti so bili izbrani dogodki, ki so bili na referenčnem detektorju zaznani znotraj intervala dveh standardnih deviacij okrog središča fotovrha. Dodatno so k oceni prispevali le dogodki, ko je imel opazovani kanal izmerjen največji naboj na mikrokanalni fotopomnoževalki. Učinkovitost je bila ocenjena iz števila dogodkov, ki v porazdelitvi naboja ref-

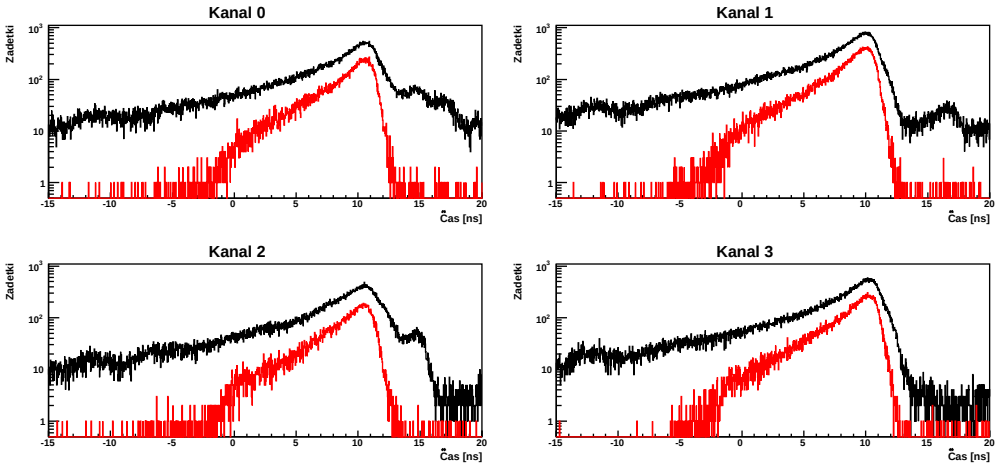

Slika 12.13: Časovna porazdelitev dogodkov za 4 združene kanale mikrokanalne fotopomnoževalke. S črno so označeni vsi zaznani dogodki, z rdečo pa dogodki, ko je referenčni detektor zaznal dogodek v fotovrhu.

erenčnega detektorja (slika 12.12) ležijo znotraj 2σ širokega intervala okrog središča fotovrha ($N_{2\sigma}$) in vsote dogodkov, ki v štirih porazdelitvah časa preživijo izbiro dogodkov ($N_{MCPPMT/fotovrh}$, rdeči histogrami na sliki 12.13):

$$\epsilon = \frac{N_{MCPPMT/fotovrh}}{N_{2\sigma} - N_{Compton}}. \tag{12.8}$$

Tu je $N_{Compton}$ ocenjeno število dogodkov, ki ležijo znotraj 2σ širokega intervala okrog središča fotovrh in izvirajo iz Comptonovega kontinuuma žarkov γ z začetno energijo 1275 keV.

Material	Površine	Prevleka	Segmentacija	Dolžina	ϵ [%]
PbF_2	gladke	črna barva	brez	5 mm	4.3
PbF_2	gladke	črna barva	brez	10 mm	5.7
PbF_2	gladke	črna barva	brez	15 mm	5.9
PbF_2	gladke	brez	brez	15 mm	12
PbF_2	gladke	Teflon	brez	15 mm	18
PbF_2	grobe	črna barva	brez	15 mm	6.2
PbF_2	gladke	črna barva	4×4	7.5 mm	4.3
PbF_2	gladke	Teflon	4×4	7.5 mm	8.6
$PbWO_4$	grobe	črna barva	brez	5 mm	16
$PbWO_4$	grobe	črna barva	brez	15 mm	29

Tabela 12.7: Izmerjene učinkovitosti različnih sevalcev Čerenkova. Za detektor svetlobe je bila uporabljena mikrokanalna fotopomnoževalka JY0005. V primeru 4×4 segmentiranih kristalov je bila za vstopno in stranske površine uporabljena enaka prevleka. Vrednosti za sevalec $PbWO_4$ vključujejo prispevek scintilacij.

V tabeli 12.7 so zbrane tako izračunane vrednosti za učinkovitost detektorja Čerenkova. Najslabšo učinkovitost imajo sevalci pobarvani s črno barvo, ki so dosegali najboljše časovne ločljivosti. Črna barva namreč poveča delež fotonov, ki se na vstopni in stranskih površinah lomijo iz kristala in so izgubljeni za meritev. Učinkovitost je znatno višja v primeru golih ali v Teflon zavitih površin, ko preko popolnega odboja ali odboja od Teflona detektor svetlobe doseže več fotonov. Vendar so ti fotoni zaznani s slabšo časovno ločljivostjo, zato je njihova uporabnost vprašljiva. S kristali $PbWO_4$ je bila izmerjena največja učinkovitost, vendar je treba upoštevati, da so v tem primeru k rezultatom prispevali predvsem scintilacijski fotoni, ki so zaznani z zelo slabo časovno ločljivostjo.

Fotopomnoževalka	Učinkovitost [%]
JY0002	3.9
JY0005	5.9

Tabela 12.8: Izmerjene učinkovitosti detektorjev s 15 mm dolgim, črno pobarvanim sevalcem PbF_2, v primeru dveh mikrokanalnih fotopomnoževalk.

Meritev s 15 mm dolgim, črno pobarvanim sevalcem PbF_2 je bila ponovljena še z mikrokanalno fotopomnoževalko JY0002. V primerjavi s fotopomnoževalko JY0005 (tabela 12.8) je JY0002 dosegla večjo učinkovitost, kot je bilo pričakovano. Glede na učinkovitost zaznavanja fotonov (tabela 12.3) bi morala JY0005 zaznati za faktor 3.6-krat več fotonov, kot JY0002, medtem ko je izmerjen faktor je 1.5. Možna razlaga je dejstvo, da je bila fotopomnoževalka JY0005 pred meritvijo učinkovitosti dolgo izpostavljena svetlobi v različnih meritvah, kar bi lahko izrabilo fotokatodo, medtem ko JY0002 večino časa ni bila v uporabi.

12.5.5 Primerjava sevalcev

Uporabnost sevalcev za detekcijo žarkov γ v TOF PET je odvisna tako od učinkovitosti zaznavanja koincidenc (ϵ^2) kot od časovne ločljivosti (δt). Sevalce lahko primerjamo, če obe količini združimo v merilo kvalitete (angl. Figure of Merit - FOM):

$$\mathrm{FOM} = \frac{\epsilon^2}{\delta t}. \tag{12.9}$$

V tabeli 12.9 so zbrane vrednosti FOM, izračunane iz izmerjenih vrednosti učinkovitosti in časovne ločljivosti. Za primerjavo so navedene tudi vrednosti, ki jih lahko dosežejo tradicionalni detektorji s scintilatorji. Časovna ločljivost 300 ps je bila s scintilatorji dosežena le v laboratorijskih pogojih, kar pa je ustrezna primerjava za vrednosti, dobljene s predstavljenimi poskusi.

Kljub odlični časovni ločljivosti, doseženi z nekaterimi sevalci, ima celo detektor z najboljšim sevalcem Čerenkova za faktor 2 slabši FOM kot scintilacijski detektor. Prav tako vrednosti za časovno ločljivost ne vsebujejo

Sevalec	ϵ^2 [%]	FWHM [ps]	FOM [%/ns]
5 mm, črna barva	0.18	103	1.8
15 mm, črna barva	0.37	132	2.8
5 mm, goli	0.49	125	3.9
15 mm, goli	1.44	186	7.7
5 mm, Teflon	1.21	162	7.5
15 mm, Teflon	3.24	271	12.0
4×4 črna barva	0.18	116	1.6
4×4 Teflon	0.74	301	2.5
PET s scintilatorji	10	300	33.3

Tabela 12.9: Izmerjene vrednosti za učinkovitost zaznavanja koincidenc (ϵ^2) in časovno ločljivost (FWHM) ter iz njih izračunano merilo kvalitete sevalcev (FOM). Za primerjavo so navedene tudi približne vrednosti za detektor, ki temelji na scintilatorjih.

vpliva, ki bi ga široki deli časovnih porazdelitev lahko imeli na končno rekonstrukcijo slike. Glavno omejitev za učinkovitost zaznavanja predstavljajo razpoložljivi detektorji svetlobe, ki imajo v območju razpoložljivih fotonov Čerenkova le nekaj % učinkovitost zaznavanja fotonov. Bolj občutljivi detektorji svetlobe bi učinkovitost zaznavanja in s tem FOM izboljšali, morda celo do stopnje, ko bi detektorji Čerenkova postali primerljivi s scintilacijskimi detektorji.

12.6 Simulacije

Da bi podrobneje preučili procese, ki vplivajo na lastnosti detektorjev Čerenkova, je bila v okolju GEANT4 [40] razvita simulacija. Ta je upoštevala vse pomembne parametre, ki so bili prisotni v poskusih: geometrijo, obdelavo in prevleko površin sevalca, sklopitev sevalca z detektorjem svetlobe ter njegovo učinkovitost zaznavanja fotonov. Simulacije so lahko vključevale tudi časovni odziv detektorja svetlobe. Tega večina predstavljenih rezultatov ne upošteva, da so tako vplivi sevalca bolj očitni.

12.6.1 Parametri

Simulacija je generirala fotone Čerenkova v območju valovnih dolžin med 200 in 800 nm. Simulacija je uporabljala podatke za lomni količnik in absorpcijsko dolžino optičnih fotonov v sevalcih PbF_2 in $PbWO_4$, ki so prikazani na sliki 12.14. Sevalec je bil sklopljen z 1.5 mm debelim oknom detektorja svetlobe preko 0.2 mm debele plasti optične masti, oba sta imela v simulaciji lomni količnik $n = 1.5$. Absorpcija v oknu je vključena v učinkovitost zaznavanja fotonov, za katero so bile v simulaciji uporabljene vrednosti za mikrokanalno fotopomnoževalko JY0005. Teflonska prevleka sevalcev je bil simuliran kot zelo tanka plast zraka ($n = 1.0$), ki ji je sledil Teflon, simuli-

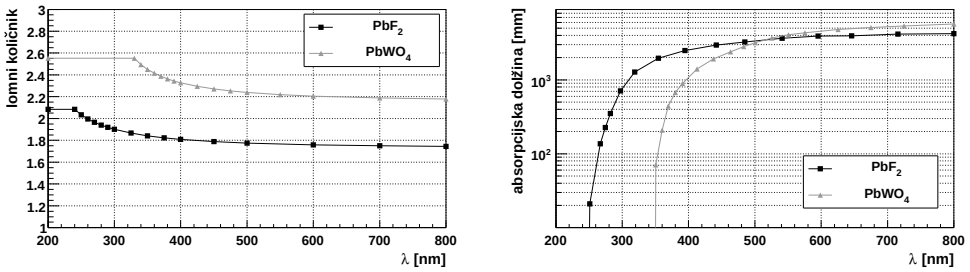

(a) (b)

Slika 12.14: Vrednosti lomnega količnika (a) in absorpcijske dolžine (b) sevalcev PbF_2 in $PbWO_4$, ki so bile uporabljene v simulaciji.

ran s 100% odbojnostjo. Črna barva pa je bila simulirana kot tanka plast brez odbojnosti in z lomnim količnikom $n = 1.5$, ki je bila v neposrednem stiku s površinami sevalca. Simulacije kristalov $PbWO_4$ so vključevale tudi scintilacije, katerih lastnosti so podane v tabeli 12.2.

12.6.2 Rezultati

V tabeli 12.10 so zbrani rezultati simulacij, povezani s številom izsevanih fotonov Čerenkova za primer 15 mm dolgih, črno pobarvanih sevalcev. V prvem koraku je simulacija sledila koincidenčnim žarkom γ in njihovim interakcijam v sevalcu. V 15 mm dolgih sevalcih je interagiralo približno 80% žarkov. V povprečju je za vsak žarek γ, ki je interagiral s sevalcem, nastal vsaj 1 elektron. Ta je, preden se je ustavil, izseval v povprečju 15.1 in 22.2 fotonov Čerenkova v sevalcu PbF_2 in $PbWO_4$. Čeprav je v sevalcu $PbWO_4$ nastalo več fotonov Čerenkova, kot v PbF_2, jih je fotokatodo detektorja svetlobe doseglo manj. Razlog je boljša optična prepustnost sevalca PbF_2. Ko je bila v zadnjem koraku upoštevana še učinkovitost zaznavanja fotonov detektorja svetlobe, je v bilo dobljeno povprečno število zaznanih fotonov, ki je le 0.14 za PbF2 in 0.072 za $PbWO_4$. Porazdelitve zaznanih fotonov po valovni dolžini so prikazane na sliki 12.15. Pri nižjih valovnih dolžinah se porazdelitvi končata zaradi spodnje meja optične prepustnosti in zaradi učinkovitost zaznavanja fotonov fotopomnoževalke. Očitno je, kako pomembno za število zaznanih fotonov je območje nižjih valovnih dolžin.

Če normiramo povprečno število zaznanih fotonov glede na delež vpadnih žarkov γ, ki interagirajo, lahko ocenimo učinkovitost detektorja Čerenkova. V tabeli 12.11 so zbrane učinkovitosti za različne sevalce, v tabeli 12.12 pa za učinkovitosti zaznavanja fotonov različnih fotopomnoževalk. Rezultati simulacij se najbolje ujemajo z meritvami v primeru sevalcev, zavitih v Teflon ali z golimi površinami, medtem ko so v primeru črno pobarvanih sevalcev simulirane vrednosti do približno 2-krat večje od izmerjenih. Odstopanja so

	PbF_2	$PbWO_4$
Delež γ interakcij	79.7%	80.1%
e^-/γ	1.53	1.57
Izsevanih fotonov Čerenkova/γ	15.1	22.2
Fotonov Čerenkova na fotokatodi/γ	2.11	1.27
Zaznanih fotonov Čerenkova/γ	0.14	0.072
Zaznanih scintilacijskih fotonov/γ	-	0.47

Tabela 12.10: Rezultati simulacij 15 mm dolgega, črno pobarvanega sevalca: delež vpadnih žarkov γ z začetno energijo 511 keV, ki so interagirali s sevalcem; povprečno število elektronov, ki nastanejo v interakcijah; povprečno število izsevanih fotonov Čerenkova; povprečno število fotonov Čerenkova, ki dosežejo fotokatodo; povprečno število fotonov, zaznanih z detektorjem svetlobe. Povprečja so izračunana glede na žarke γ ki interagirajo s sevalcem. Za učinkovitost zaznavanja fotonov so bile uporabljene vrednosti fotopomnoževalke JY0005.

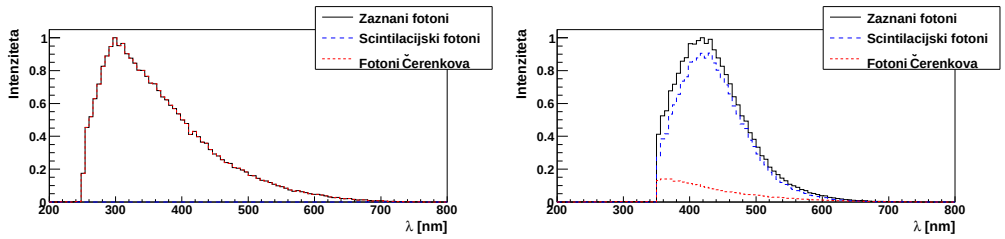

(a) PbF_2 (b) $PbWO_4$

Slika 12.15: Porazdelitve zaznanih fotonov po valovni dolžini, v primeru 15 mm dolgih sevalcev PbF_2 in $PbWO_4$ ter fotopomnoževalke JY0005. Prikazani so tudi prispevki scintilacij in fotonov Čerenkova.

največja v primeru fotopomnoževalke JY0005, medtem ko je ujemanje za JY0002 veliko boljše.

Sevalec				ϵ [%]	FWHM [ps]	
Material	Prevleka	Segmentacija	Dolžina		brez odziva	z odzivom det.
PbF_2	črna barva	brez	5 mm	6.2	37.7	84.4
PbF_2	črna barva	brez	10 mm	9.5	65.7	118
PbF_2	črna barva	brez	15 mm	11	92.8	148
PbF_2	brez	brez	15 mm	16	118	215
PbF_2	Teflon	brez	15 mm	18	130	241
PbF_2	črna barva	4×4	7.5 mm	6.7	45.7	92.2
PbF_2	Teflon	4×4	7.5 mm	12	62.5	154
$PbWO_4$	črna barva	brez	5 mm	21	62.2	399
$PbWO_4$	črna barva	brez	15 mm	43	206	900

Tabela 12.11: Rezultati simulacij za učinkovitost (ϵ) in časovno ločljivost (FWHM) brez in z upoštevanim časovnim odzivom detektorja svetlobe. Za učinkovitost zaznavanja fotonov so bile uporabljene vrednosti fotopomnoževalke JY0005. V primeru 4×4 segmentiranih kristalov je bila za vstopno in stranske površine uporabljena enaka prevleka. Vrednosti za sevalec $PbWO_4$ vključujejo prispevek scintilacij.

MCP PMT	ϵ [%]
JY0002	3.3
JY0005	11
JY0008	7.1

Tabela 12.12: Učinkovitosti, ki so rezultat simulacij s 15 mm dolgim, črno pobarvanim sevalcem PbF_2, v primeru različnih učinkovitosti zaznavanja fotonov mikrokanalnih fotopomnoževalk.

Tabela 12.11 vsebuje tudi rezultate za ločljivosti meritve časa preleta za različne sevalce. Slika 12.16 prikazuje porazdelitve časa koincidenc za nekaj primerov sevalca. V primeru sevalca $PbWO_4$ dogodki, ki so posledica scintilacijskih fotonov, predstavljajo zelo široko ozadje, medtem ko dogodki, ki jih na obeh straneh sprožijo fotoni Čerenkova tvorijo relativno ozek vrh. Ko je v simulacijo vključen časovni odziv detektorja, se porazdelitve znatno razširijo in dobijo širok prispevek, ki je posledica oblike časovnega odziva mikrokanalnih fotopomnoževalk. Porazdelitev v primeru $PbWO_4$ je tako veliko bolj podobna rezultatom poskusov.

Ker detektor Čerenkova zazna le en ali največ nekaj fotonov na dogodek, ni možna meritev energije vpadnih žarkov γ. Zato ni možna diskriminacija dogodkov, ko se je žarek sipal v telesu pacienta ali v delih naprave PET, ki predstavljajo neželeno ozadje. V napravi PET, ki bi delovala na principu zaznavanja fotonov Čerenkova, je prispevek sipanih dogodkov vseeno

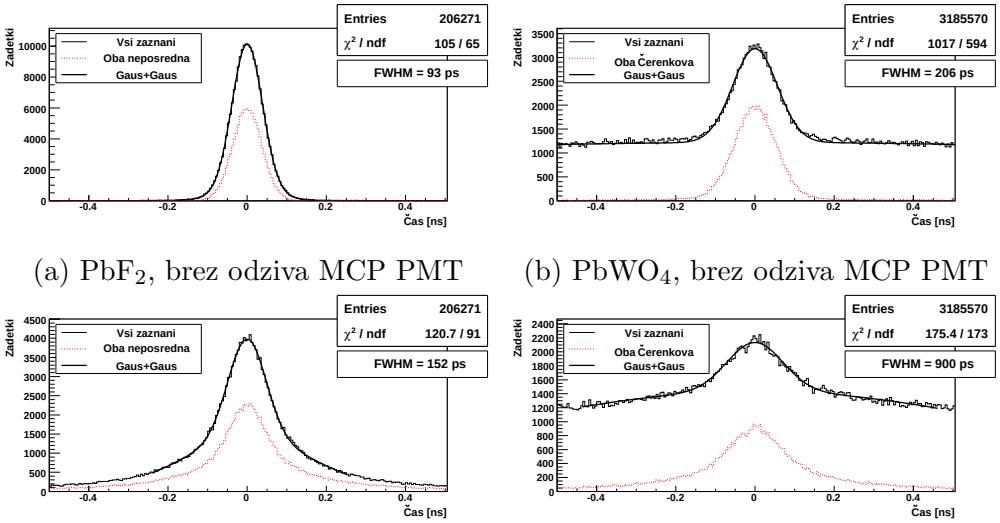

(a) PbF_2, brez odziva MCP PMT (b) $PbWO_4$, brez odziva MCP PMT

(c) PbF_2, z odzivom MCP PMT (d) $PbWO_4$, z odzivom MCP PMT

Slika 12.16: Rezultati simulacij za porazdelitve časa koincidenc v primeru 15 mm dolgih, črno pobarvanih sevalcev. Prikazani so rezultati, ko v simulaciji ni bil ali je bil vključen časovni odziv detektorja svetlobe, ter prispevek dogodkov, ko sta oba detektorja zaznala foton brez odbojev od stranic sevalca (za sevalec PbF_2) oz. ko sta oba detektorja zaznala foton Čerenkova (za sevalec $PbWO_4$).

omejen zaradi padca učinkovitosti detekcije za žarke z nižjo energijo. Ko se žarki γ Comptonsko sipljejo, izgubijo del energije. To pomeni, da v detektorju Čerenkova povzročijo izsevanje manjšega števila fotonov, s tem pa pade tudi verjetnost, da bo dogodek zaznan. Slika 12.17 prikazuje odvisnost učinkovitosti od energije vpadnih žarkov γ ter od kota Comptonskega sipanja.

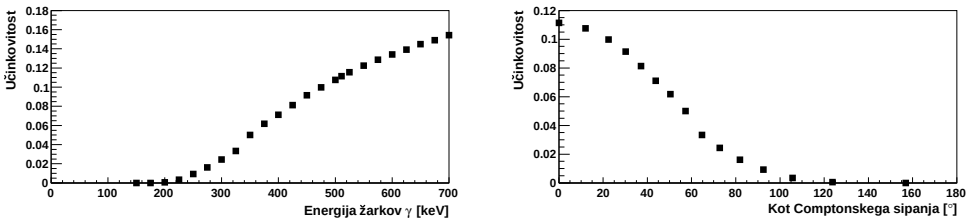

(a) (b)

Slika 12.17: Rezultati simulacij za učinkovitost detektorja Čerenkova v odvisnosti od energije vpadnih žarkov γ (a) in od kota Comptonskega sipanja žarkov z začetno energijo 511 keV (b).

12.6.3 Izboljšave detektorja

S pomočjo simulacije se je lahko raziskalo vplive parametrov detektorja, ki jih v poskusih ni bilo mogoče spreminjati. Največjo omejitev za učinkovitost detektorja predstavlja učinkovitost zaznavanja fotonov uporabljenih mikrokanalnih fotopomnoževalk, še posebej v področju nizkih valovnih dolžin. Fotokatoda, uporabljena za meritve učinkovitosti, je imela kvantni izkoristek največ okrog 20%. Novejše fotokatode imajo lahko občutno višji kvantni izkoristek, do približno 43% (t.i. ultra bialkalna fotokatoda proizvajalca Hamamatsu Photonics [46]). Zanimiva možnost je tudi uporaba okna fotopomnoževalke z nižjo mejo optične prepustnosti. Uporabljene fotopomnoževalke imajo okno iz borosilikatnega stekla, ki prepušča svetlobo nad približno 250 nm, medtem ko nekatere fotopomnoževalke uporabljajo okna z boljšimi lastnostmi, npr. kvarčno okno, ki prepušča svetlobo od spodnje meje 160 nm navzgor. S simulacijami je bila preverjena učinkovitost v primeru detektorja 500S, proizvajalca Hamamatsu Photonics [11], ki uporablja izboljšano fotokatodo na kvarčnem steklu. Slika 12.18 prikazuje učinkovitost zaznavanja fotonov detektorja s takšno fotokatodo in zbiralnim izkoristkom $\alpha = 60\%$, v primerjavi z fotopomnoževalko JY0005. Detektor s takšno fotokatodo je v simulacijah dosegel 1.4-krat večjo učinkovitost, kot fotopomnoževalka JY0005.

Učinkovitost zaznavanja bi se lahko povečalo tudi z izboljšanjem transporta fotonov iz sevalca v detektor svetlobe. Zaradi visokega lomnega

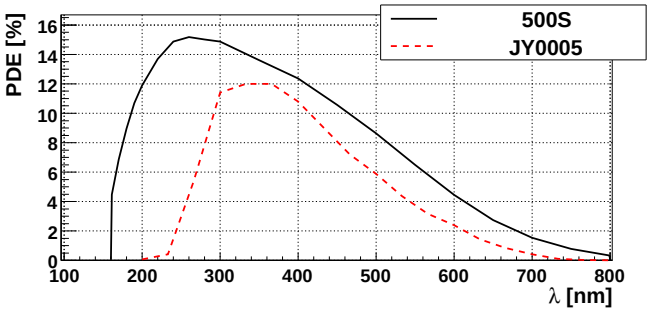

Slika 12.18: Učinkovitost zaznavanja fotonov detektorja s fotokatodo 500S in zbiralnim izkoristkom $\alpha = 60\%$, ter fotopomnoževalke JY0005.

količnika sevalcev Čerenkova se znaten del fotonov popolno odbije na izstopni površini sevalca. Če bi uporabili okno detektorja svetlobe in optično sklopitev z višjim lomni količnikom, bi se tako povečalo število fotonov, ki se lomijo iz sevalca v okno detektorja svetlobe. V primeru sevalca PbF_2 in okna z lomnim količnikov $n = 2.0$, ki bi bila sklopljena z optično mastjo z $n = 1.9$, je bila simulirana učinkovitost detektorja za približno 1.4-krat večja glede na parametre detektorja iz poskusov. Transport fotonov iz sevalca bi lahko povečali tudi s tehnologijo t.i. fotonskih kristalov (angl. photonic crystals), kjer na površini kristala ustvarijo mikrostrukture z različnimi lomnimi količniki. Te lahko usmerijo skozi površino fotone, ki bi se sicer popolno odbili in tako povečajo število izhodnih fotonov. V [49] so v poskusih tako dosegli 1.5-kratno povečanje števila izhodnih fotonov.

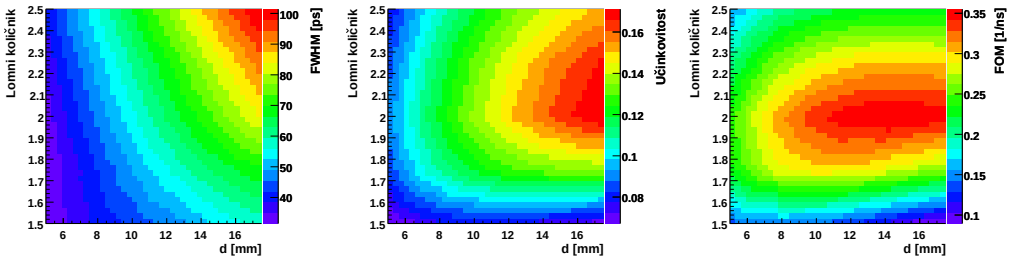

(a) (b) (c)

Slika 12.19: Odvisnost ločljivosti meritve časa preleta (a), učinkovitosti detekcije (b) in merila kvalitete (c) od dolžine in lomnega količnika črno pobarvanega sevalca s presekom 25×25 mm^2 in lastnostmi kristalov PbF_2. Uporabljena je bila učinkovitost zaznavanja fotonov detektorja s fotokatodo 500S.

Simulacije so omogočile tudi spreminjanje parametrov sevalcev Čerenkova. Slika 12.19 prikazuje rezultate za ločljivost meritve časa preleta, učinkovitost detektorja in iz njih izračunane vrednosti FOM za sevalec, ki

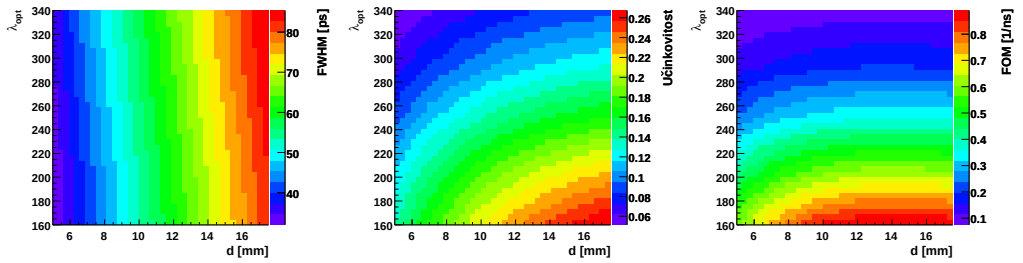

(a) (b) (c)

Slika 12.20: Odvisnost ločljivosti meritve časa preleta (a), učinkovitosti detekcije (b) in merila kvalitete (c) od dolžine in spodnje meje optične prepustnosti (λ_{opt}) črno pobarvanega sevalca s presekom 25×25 mm^2 in lastnostmi kristalov PbF_2. Uporabljena je bila učinkovitost zaznavanja fotonov detektorja s fotokatodo 500S.

ima lastnosti kristalov PbF_2 a spremenljiv lomni količnik. Da bi se bolj izpostavilo vpliv sevalca, je bila uporabljena učinkovitost zaznavanja fotonov detektorja s fotokatodo 500S prikazana na sliki 12.18. Iz teh rezultatov sledi, da ima najboljši sevalec lomni količnik okrog $n = 2.0$ in dolžino približno 11−16 mm. Za takšno kombinacijo sevalca in detektorja svetlobe je vrednost FOM približno 3-krat večja kot za detektorje uporabljene v poskusih. Na sliki 12.20 so prikazani rezultati simulacij za primer sevalca, podobnega kristalom PbF_2, a s spremenljivo spodnjo mejo optične prepustnosti in lomnim količnikom $n = 2.0$. Takšen idealen sevalec, s spodnjo mejo prepustnosti λ_{opt} =160 nm, v kombinaciji s še vedno realističnim detektorjem svetlobe, doseže vrednosti FOM ki so približno 8-krat večje od detektorjev v poskusih.

V tabeli 12.13 so povzeti faktorji izboljšanja za detektorje Čerenkova z opisanimi izboljšavami. Seveda v praksi ne bi mogli v enem detektorju združiti vseh naštetih izboljšav, vendar lahko upamo na izboljšanje FOM za faktor 16 z razpoložljivimi tehnologijami (boljša fotokatoda in transport fotonov). Razvoj boljših sevalcev Čerenkova pa bi lahko prinesel še dodaten faktor 8.

	f_ϵ	f_{FOM}
detektor svetlobe	1.4	2
transport fotonov	≈2	≈4
detektor svetlobe + optimalni n	1.5	3
detektor svetlobe + optimalni n + optimalni λ_{opt}	2.4	8

Tabela 12.13: Rezultati simulacij za možne faktorje izboljšanja v učinkovitosti detekcije (f_ϵ) in merilu kvalitete sevalca (f_{FOM}). Faktor izboljšanja f_{FOM} vključuje tudi prispevke časovne ločljivosti.

12.7 Rekonstrukcija

Čeprav sta bila za poskuse na voljo le dva detektorja, je bilo možno opraviti meritev, ekvivalentno meritvi s celotnim obročem PET. Opravljenih je bilo več zaporednih meritev, pri katerih je bil izvor zavrten v enakomernih intervalih okrog središča naprave. Tako dobljene koincidence, združene v eno meritev, so dober približek za meritev, kjer bi izvor obkrožal obroč detektorjev. V postavitvi poskusa je bil ta obroč sestavljen iz 22 detektorjev in imel notranji premer 185 mm. Uporabljeni so bili 4×4 segmentirani kristali PbF_2 s površinami pobarvanimi s črno barvo ali zavitimi v Teflon. Pričakovana prostorska ločljivost takšnega obroča je 2.9 mm.

Za rekonstrukcijo slik so bili uporabljeni štirje algoritmi. Za primerjavo je služil standardni algoritem FBP, ki ne vključuje informacije o času preleta. Ta je bila vključena v uteženem algoritmu FBP, kjer je bil prispevek koincidence upoštevan le v elementih slike, ležečih znotraj območja ki ga definira pričakovan časovni odziv naprave. Druga vrsta rekonstrukcije pa je temeljila na principu najverjetnejšega položaja (angl. Most Likely Position - MLP), določenega iz meritve časa preleta (enačba 12.3). Rekonstrukcija tu ni bila potrebna, posamezna koincidenca je prispevala le k elementu slike, ki je ustrezal izračunanemu položaju. Zadnji algoritem je na rezultatu MLP algoritma izvedel 2-dimenzionalno dekonvolucijo za pričakovan časovni odziv detektorja.

Ko je bil točkast izvor ^{22}Na postavljen v središče naprave, so imele rekonstruirane slike prostorsko ločljivost 3.3 mm. V primerjavi s kristali, zavitimi v Teflon, boljša časovna ločljivost črno pobarvanih kristalov ni izboljšala prostorske ločljivosti, je pa prispevala k rahlemu znižanju nivoja ozadja. Slika 12.21 prikazuje rezultate rekonstrukcije, za primer dveh združenih meritev, kjer je bil izvor iz središča naprave oddaljen enkrat za +10 mm in drugič za −10 mm. Položaja izvora sta ločena v primeru vseh štirih algoritmov, pri čemer je opazno rahlo znižanje ozadja, ko je v algoritem FBP vključena časovna informacija. Algoritem MLP ima slabšo prostorsko ločljivost, vendar še vedno dobro loči vrhova. Dekonvolucija MLP slike izostri sliko, vendar hkrati izpostavi statistične fluktuacije meritev.

Meritve z le dvema detektorjema hkrati ter s točkastim izvorom ne morejo v celoti raziskati vpliva časovne ločljivosti na rekonstruirane slike, saj ne vključujejo prispevkov sipanih žarkov γ in ozadja enakomerne porazdelitve aktivnosti. Za to so bile opravljene simulacije celotne naprave PET, ki je sestojala iz 15 obročev premera 800 mm. Vsak obroč je sestavljajo 112 detektorjev Čerenkova, ki so bili kar se da podobni detektorjem, uporabljenim v meritvah. Za sevalec so uporabljali 7.5 mm dolge 4×4 segmentirane kristale PbF_2, ki so bili zaviti v Teflon ali črno pobarvani. V simulaciji sta bila upoštevana učinkovitost zaznavanja fotonov in časovni odziv mikrokanalne fotopomnoževalke JY0005. Kot izvor koincidenčnih žarkov γ je bil simuliran

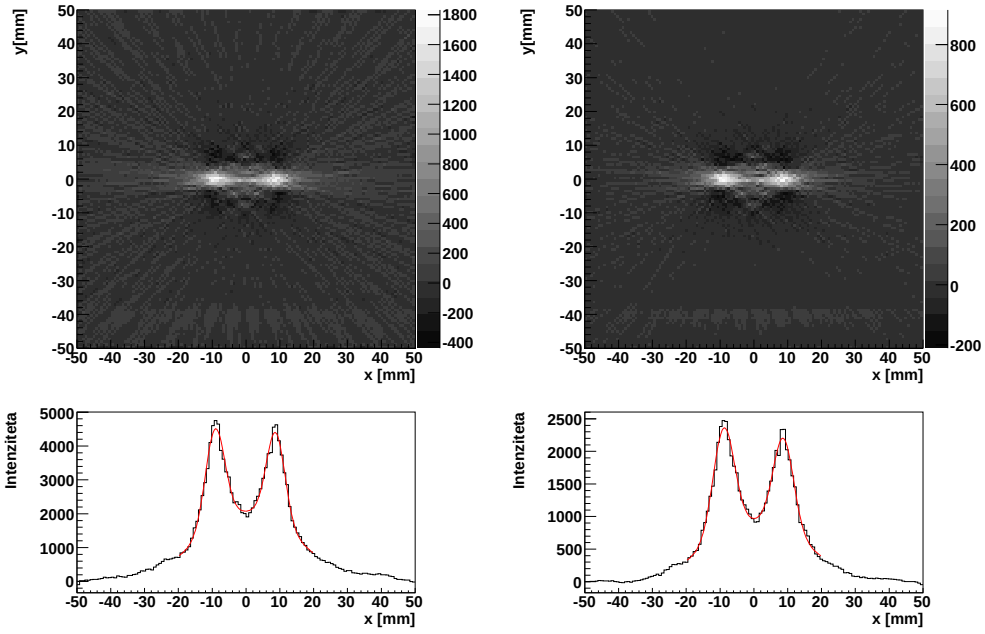

(a) FBP

(b) FBP utežen z TOF

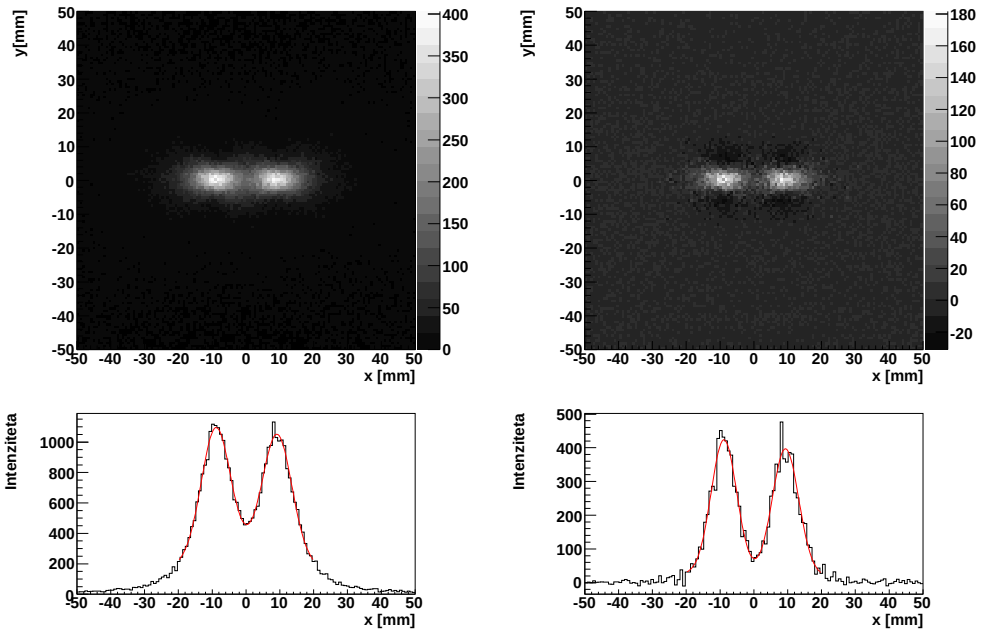

(c) MLP

(d) Dekonvolucija MLP

Slika 12.21: Rekonstruirane slike za izvor ^{22}Na v dveh položajih, od središča zamaknjenih za ±10 mm. Slike predstavljajo 30 min meritev s črno pobarvanimi kristali.

fantom, ki je sestojal iz cilindra s premerom 270 mm, napolnjenega z vodo in enakomerno razporejeno aktivnostjo. V središču cilindra so bili razporejeni štirje sferični sevalci, različnih velikosti in z 3-krat višjo gostoto aktivnosti. V cilindru sta bili še dve sferični praznini, napolnjeni z zrakom.

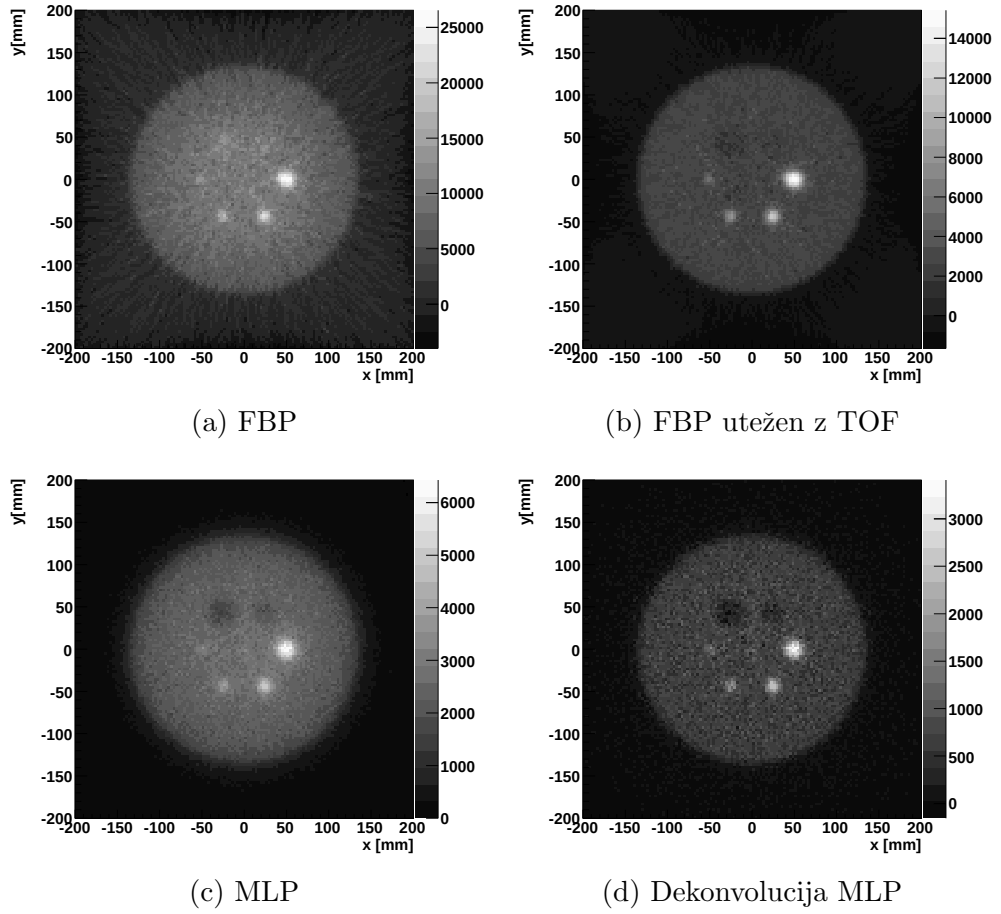

(a) FBP

(b) FBP utežen z TOF

(c) MLP

(d) Dekonvolucija MLP

Slika 12.22: Rekonstruirane slike za simulacijo celotne naprave PET in fantoma, v primeru v Teflon zavitih sevalcev.

Slika 12.22 prikazuje rekonstruirane slike v primeru v Teflon zavitih sevalcev, za statistiko ki ustreza približno 163 s standardne PET preiskave [13]. Na slikah so dobro vidni cilinder fantoma in dva večja sevalca. Dva manjša sevalca postaneta očitna šele na slikah z vključeno informacijo o času preleta. Praznini na sliki brez časovne informacije nista vidni. Tudi na slikah z vključenim časom preleta sta komaj opazni, zaradi sipanih dogodkov in omejene natančnosti rekonstrukcije.

Na sliki 12.23 je vidna primerjava kontrasta (razmerja nivoja signala in nivoja ozadja) in razmerja kontrasta proti šumu (angl. Contrast to Noise Ratio - CNR) črno pobarvanih in v Teflon zavitih. Razmerje CNR je glavno

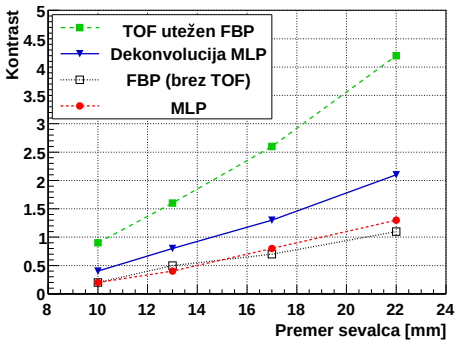

(a) Kontrast, črna barva

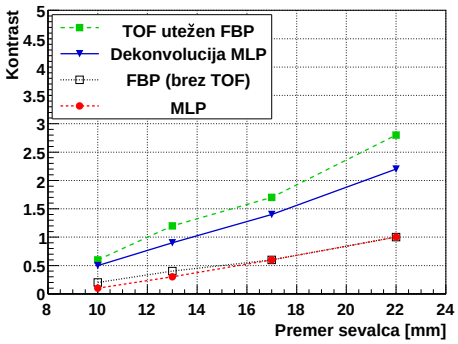

(b) Kontrast, Teflon

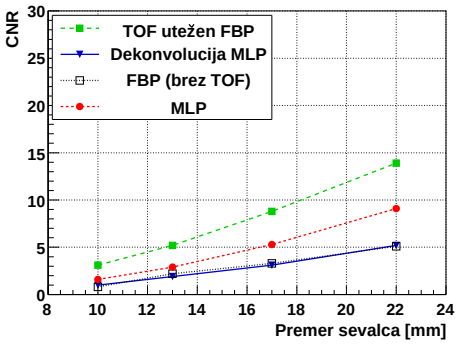

(c) CNR, črna barva

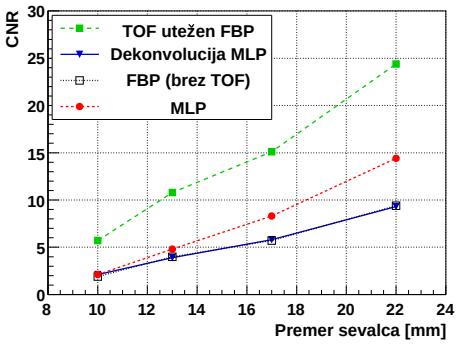

(d) CNR, Teflon

Slika 12.23: Kontrast in razmerje CNR za sevalce različnih velikosti, ocenjene za različne algoritme rekonstrukcije slik.

merilo za kakovost rekonstruiranih slik in mora biti za nepravilnost na sliki večji od približno 3−5, da se ta lahko zazna [7]. Vrednosti kontrasta so boljše, ko so dobljene z boljšo časovno ločljivostjo črno pobarvanih sevalcev, vendar boljši izkoristek v Teflon zavitih sevalcev vodi do boljših vrednosti CNR in s tem bolj očitnemu najmanjšemu sevalcu. Meritev časa preleta vodi k očitnemu izboljšanju razmerja CNR za faktor približno 2, če primerjamo algoritma FBP in uteženi FBP, in v tem primeru pomeni ključno razliko za zaznavnost najmanjšega sevalca. Preprost algoritem MLP je dosegel rezultate, ki so boljši od računsko mnogo bolj zahtevnega algoritma FBP. Dekonvolucija je sicer izboljšala kontrast, vendar je z njim tudi ojačala šum do stopnje, ko dosežena razmerja CNR niso boljša od rekonstrukcije brez informacije o času preleta.

12.8 Zaključek

V poskusih z detektorji Čerenkova, ki so kot detektor svetlobe uporabljali mikrokanalne fotopomnoževalke, so bili koincidenčni dogodki zaznani z odlično ločljivostjo meritve časa preleta $\approx$ 100 ps. Najboljša časovna ločljivost 74 ps je bila dosežena s 5 mm dolgimi, črno pobarvanimi kristali PbF_2, ki pa sta v kombinaciji z uporabljenimi detektorji svetlobe dosegla učinkovitost detekcije koincidenc le 0.18%. Kljub odlični časovni ločljivosti ima takšen detektor približno 20-krat slabše merilo kvalitete (FOM) kot bolj tradicionalen scintilacijski detektor. Razlike je manjša za daljše in v Teflon zavite kristale, ki pa imajo še vedno vsaj 2-krat nižjo vrednost FOM kot scintilacijski detektor.

Iz rezultatov simulacij sledi, da imajo zaradi boljše učinkovitosti detekcije višjo kvaliteto rekonstruiranih slik sevalci, ki so zaviti v Teflon. Učinkovitost detekcije bi lahko občutno povišali, če bi sevalce združili z bolj občutljivimi detektorji svetlobe. Tako bi lahko dosegli vrednosti FOM scintilacijskih detektorjev, če pa bi našli tudi boljši sevalec Čerenkova, bi le to lahko celo občutno presegli.

Čeprav z detektorji Čerenkova ni možna diskriminacija Comptonsko sipanih dogodkov na podlagi meritve energije, k rezultatom prispeva le del sipanih dogodkov, saj žarki γ pri sipanju izgubijo del energije, s tam pa se zniža tudi verjetnost za detekcijo. Ali naprava TOF PET, ki temelji na zaznavanju fotonov Čerenkova, lahko preseže zmogljivosti tradicionalnih naprav s scintilacijskimi detektorji pa je v veliki meri odvisno tudi od algoritmov za rekonstrukcijo slike. Izredno hiter algoritem najverjetnejšega položaja (MLP), ki se lahko uporablja za prikaz slike v realnem času, je za predstavljene rezultate celo presegel kvaliteto slik, dobljeno s preprostim algoritmom FBP, ki ne vključuje meritve časa preleta. Razvoj naprednih algoritmov, ki bi v celoti upoštevali odlično časovno ločljivost, bi lahko predstavljal odločilno prednost za meritve s svetlobo Čerenkova.

13 Bibliography

[1] T.F. Budinger, *Time-of-flight positron emission tomography: Status relative to conventional PET*, J. Nucl. Medicine, **24** (1983) 73.

[2] W.W. Moses, *Time of Flight in PET Revisited*, IEEE Trans. Nucl. Sci. **50** (2003) 1325.

[3] T.Szczesniak et al., *Fast Photomultipliers for TOF PET*, IEEE Trans. Nucl. Sci., **56**,(2009), 173.

[4] S. Korpar et al., *Timing and cross-talk properties of BURLE multichannel MCP PMTs*, Nucl. Instrum. Meth. A **595** (2008) 169.

[5] M. Akatsu et al., *MCP-PMT timing property for single photons*, Nucl. Instrum. Meth. A **528** (2004) 763.

[6] Gobal B.Saha, *Basics of PET Imaging*, Springer(2005).

[7] S.R. Cherry, J.A. Sorenson, M.E. Phelps, *Physics in Nuclear Medicine*, Saunders (2003).

[8] C.M. Pepin et al., *Properties of LYSO and Recent LSO scintillators for Phoswich PET Detectors*, IEEE Trans. Nucl. Sci., **51**,(2004), 789.

[9] M. Conti et al., *Comparison of Fast Scintillators With TOF PET Potential*, IEEE Trans. Nucl. Sci., **56**,(2009), 926.

[10] Soint-Gobain Crystals, http://www.detectors.saint-gobain.com (Retrieved on February 27, 2012).

[11] Hamamatsu Photonics catalogue, *Photomultiplier Tubes and Related Products*, (2010).

[12] Hamamatsu Photonics catalogue, *Photomultiplier Tubes and Assemblies for Scintillation Counting & High Energy Physics*, (2009).

[13] J.S. Karp et al., *Benefit of Time-of-Flight in PET: Experimental and Clinical Results*, J. Nucl. Medicine, **49** (2008) 462.

[14] Y. Shao, *A new timing model for calculating the intrinsic timing resolution of a scintillator detector*, Phys. Med. Biol., **52** (2007) 1103.

[15] P. Lecoq, *Progress on Photonic Crystals*, 2010 IEEE Nuclear Science Symposium Conference Record.

[16] P. Lecoq, *Factors Influencing Time Resolution of Scintillators and Ways to Improve Them*, IEEE Trans. Nucl. Sci. **57** (2010) 2411.

[17] T. Ooba et al., *Proposal of Cherenkov TOFPET with Silica Aerogel*, 2004 IEEE Nuclear Science Symposium Conference Record.

[18] M. Miyata et al., *Development of TOF-PET using Cherenkov Radiation*, J. Nucl. Sci. Technol. **43** (2006) 339.

[19] J.V. Jelley, *Cherenkov Radiation*, Pergamom Press, New York (1958).

[20] F.L. Roder, A.K. Richard, *Theory and application of X-ray and gamma-ray backscatter to landmine detection*, Technical Report 2134, US Army Mobility Equipment Research and Development Center(1975).

[21] NIST Standard Reference Database 8, *XCOM: Photon Cross Sections Database*, http://www.nist.gov/pml/data/xcom/index.cfm (Retrieved on January 24, 2012).

[22] W.R. Leo, *Techniques for Nuclear and Particle Physics Experiments*, Springer-Verlag, Berlin (1987).

[23] J.A. Bearden, A.F. Burr, *Reevaluation of X-Ray Atomic Energy Levels*, Rev. Mod. Phys., **39** (1967) 125.

[24] The Shanghai Institute of Ceramics and Chinese Academy of Sciences (SICCAS), http://www.siccas.com/.

[25] P. Achenbach, *Observation of Scattering and Absorption Centers in Lead Fluoride Crystals*, IEEE Trans. Nucl. Sci. **48** (2001) 144.

[26] D.F. Anderson et al., *Lead fluoride: An ultra-compact Cherenkov radiator for em calorimetry*, Nucl. Instrum. Meth. A **290** (1990) 385.

[27] A.A. Annenkov et al., *Lead tungstate scintillation material*, Nucl. Instrum. Meth. A **490** (2002) 30.

[28] P. Yang et al., *Growth of large-size crystal of $PbWO_4$ by vertical Bridgman method with multi-crucibles*, Journal of Crystal Growth **236** (2002) 589.

[29] S. Baccaro et al., *Ordinary and extraordinary complex refractive index of the lead tungstate ($PbWO_4$) crystal*, Nucl. Instrum. Meth. A **385** (1997) 209.

[30] Refractive index database, http://refractiveindex.info (Retrieved on January 26, 2012).

[31] R. Chipaux, M. Géléoc, *Optical anisotropy effects in lead tungstate crystals*, CMS NOTE 1998/090 (1998).

[32] NIST Standard Reference Database 124, *Stopping-Power and Range Tables for Electrons, Protons, and Helium Ions*, http://www.nist.gov/pml/data/star/index.cfm (Retrieved on January 24, 2012).

[33] Tectra Microchannel Plate Detectors, http://www.tectra.de/MCP.htm (Retrieved on May 31, 2012).

[34] K. Inami et al., *Cross-talk suppressed multi-anode MCP-PMT*, Nucl. Instrum. Meth. A **592** (2008) 247.

[35] R. Brun, F. Rademakers, *ROOT - An object oriented data analysis framework*, Nucl. Instrum. Meth. A **389** (1997) 81.

[36] LNE - LNHB/CEA, *Table de Radionucleides*, http://www.nucleide.org/NucData.htm (Retrieved on January 3, 2012).

[37] PiLas, the picosecond diode laser system, http://www.alsgmbh.com/pilas.htm (Retrieved on October 23, 2011).

[38] Producers specifications (Advanced Laser Diode Systems GmbH).

[39] Hamamatsu Photonics, R5900-00-M16 Specification Sheet.

[40] S. Agostinelli et al., *Geant4-a simulation toolkit*, Nucl. Instrum. Meth. A **506** (2003) 250.

[41] *Re: Strange total internal reflection when using polishedbackpainted*, http://hypernews.slac.stanford.edu/HyperNews/geant4/get /opticalphotons/313/1/1.html (Retrieved on November 29, 2011).

[42] A. Levin, C. Moisan, *A More Physical Approach to Model the Surface Treatment of Scintillation Counters and its Implementation into DETECT*, TRIUMF Preprint TRI-PP-96-64, October 1996.

[43] D.V. Aleksandrov et al., *A high resolution electromagnetic calorimeter based on lead-tungstate crystals*, Nucl. Instrum. Meth. A **550** (2005) 169.

[44] The CMS Electromagnetic Calorimeter Group et al., *Radiation hardness qualification of PbWO4 scintillation crystals for the CMS Electromagnetic Calorimeter*, Journal of Instrumentation **5** (2010) P03010.

[45] C. Ye et al., *Growth and uniformity improvement of large-size PbWO4 crystal with PbF2 doping*, Nucl. Instrum. Meth. A **592** (2008) 472.

[46] Hamamatsu Photonics catalogue, *UBA (Ultra Bialkali), SBA (Super Bialkali) Photomultiplier Tube Series*, (2007).

[47] C. D'Ambrosio et al., *Improved light transitions from scintillators to new photocathode windows*, Nucl. Instrum. Meth. A **431** (1999) 455.

[48] K. Deiters et al., *Comparison of photomultiplier and avalanche photodiode readout of $PbWO_4$*, Nucl. Instrum. Meth. A **387** (1997) 211.

[49] A. Knapizsch et al., *Photonic crystals: A novel approach to enhance the light output of scintillation based detectors*, Nucl. Instrum. Meth. A **628** (2011) 385.

[50] A.C. Kak, *Computerized Tomography with X-Ray, Emission, and Ultrasound Sources*, Proceedings of the IEEE, **67** (1979) 1245.

[51] D.L. Snyder et al., *A Mathematical Model for Positron-emission Tomography Systems having Time-of-flight measurements*, IEEE Trans. Nucl. Sci. **28** (1981) 3575.

[52] S. Vandenberghe, J. Karp, *Rebinning and reconstruction techniques for 3D TOF-PET*, Nucl. Instrum. Meth. A **569** (2006) 421.

[53] M.E. Daube-Witherspoon, *PET Performance Measurements Using the NEMA NU 2-2001 Standard*, J. Nucl. Medicine, **43** (2002) 1398.

Appendices

A Time-walk correction with coincidence data

The method for obtaining the time-walk correction parameters, described in Section 4.3.3, relies on the fact that the measurements start time is defined by an external source, e.g. the start of laser pulse as provided by the laser control unit. In coincidence measurements, the start time is defined by nearly simultaneous arrival of pulses from two MCP PMTs. This means that the time-walk effect of both detectors influences the start time of the measurement and with it, the measured time of each event.

It was convenient for the measurements presented in this work to have one of the two detectors to always define the start time. Logic signals belonging to second MCP PMT were delayed compared to the signals of the first MCP PMT, which meant that the trigger signal started only after the second MCP PMT signal arrived. Due to the excellent time resolution of the system, a delay of only a few ns was required. Figure A.1 shows the time vs. charge distributions for two channels belonging to different MCP PMT, obtained with the coincidence trigger. It can be seen that the time response for channels belonging to the delayed MCP PMT are essentially a delta function, while the time response for channels belonging to the first MCP PMT is widened by the time-walk effect. Actually, the time-walk on the first channel is a convolution of time-walk effects of this channel and all channels of the second MCP PMT, which contribute to the trigger logic.

The time-walk contributions of individual channels and the corresponding time-walk correction parameters can still be extracted from the data obtained with the coincidence trigger. Lets say that we are observing two channels: channel 1 belonging to one MCP PMT and channel 2, belonging to the other MCP PMT. The difference in detection time between channels 1 and 2 ($\mathrm{TDC}_1 - \mathrm{TDC}_2$) vs. the charge registered on channel 1 (QDC_1) can be plotted. This distribution is still distorted by the time-walk effect of both channels. However, if only events where channel 2 signal was registered with a large charge ($\mathrm{QDC}_2 > \mathrm{QDC}_{Thr}$) are plotted, the coincidence time vs. channel 1 charge distribution will be dominated by channel 1 time-walk contribution at lower charge values, exactly where the time-walk effect is most prominent. This distribution can be used to obtain approximate values for channel 1 time-walk correction parameters. This is than repeated for channel 2: channel 2 time-walk correction parameters are obtained from plot of $\mathrm{TDC}_2 - \mathrm{TDC}_1$ vs. QDC_2, when $\mathrm{QDC}_1 > \mathrm{QDC}_{Thr}$. In this way, approximate correction parameters are obtained for all individual channels.

The whole procedure is than repeated for plots, using time-walk corrected

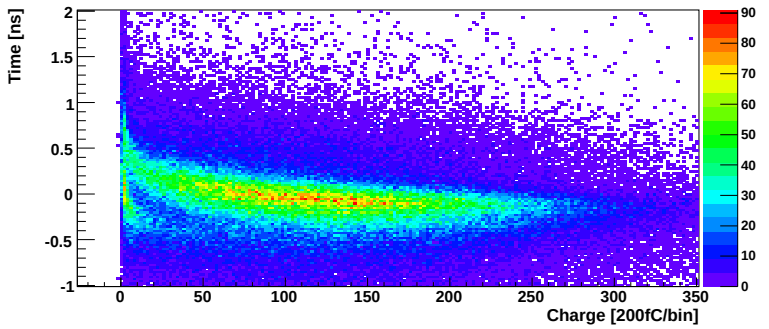

(a) MCP PMT 1

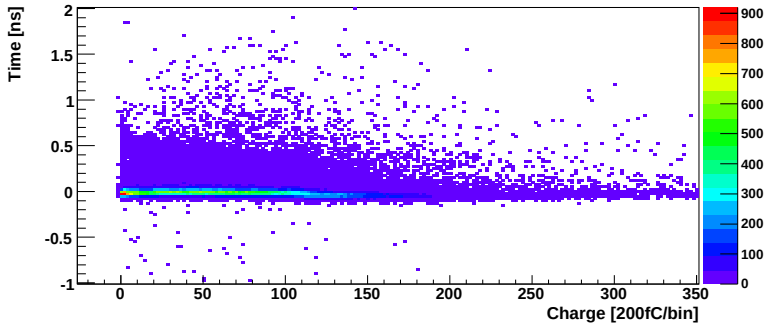

(b) MCP PMT 2

Figure A.1: Time vs. charge plots for two channels belonging to different MCP PMTs. Logic signals belonging to MCP PMT 2 were delayed compared to MCP PMT 1.

information (cTDC) for one of the channels, i.e. using plots of $TDC_1 - cTDC_2$ vs. QDC_1, when $QDC_2 > QDC_{Thr}$. This way the correction parameters for channel 1 become less dependent on the time-walk effect of channel 2. By repeating this procedure for a certain number of iterations, the exact time-walk correction parameters for individual channels can be obtained.

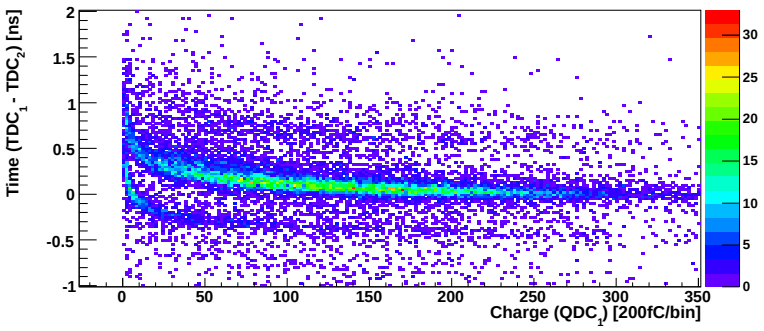

(a) Raw TDCs

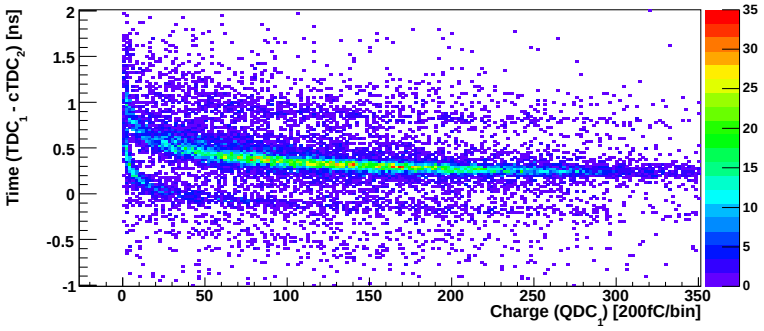

(b) Raw and corrected TDC

Figure A.2: The difference in detection time between two channels vs. charge plots, calculated with raw (uncorrected) time information on both channels (a) and with time-walk corrected information for the second channel (b).

Figure A.2a shows the first step of the described procedure: $TDC_1 - TDC_2$ vs. QDC_1, when $QDC_2 > QDC_{Thr}$. The value of QDC_{Thr} used here was 150. After the first iteration, correction parameters are obtained and applied for all channels. The time-walk corrected information is included in Figure A.2b, which shows the $TDC_1 - cTDC_2$ vs. QDC_1, when $QDC_2 > QDC_{Thr}$ plot. The time-walk contribution from the second channel is almost gone from this plot, which now provides a much better way to determine the correction parameters for channel 1. Although this difference is almost unobservable in time vs. charge plots, when time-walk corrected time information is used for both channels to calculate the coincidence time (TOF information), a significant improvement in time resolution is achieved. This

is demonstrated in Figure A.3.

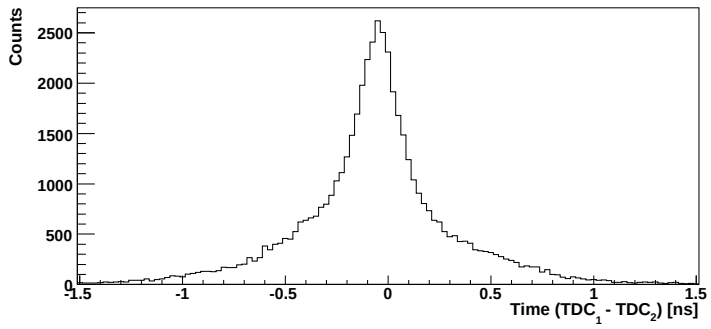

(a) Raw TDCs

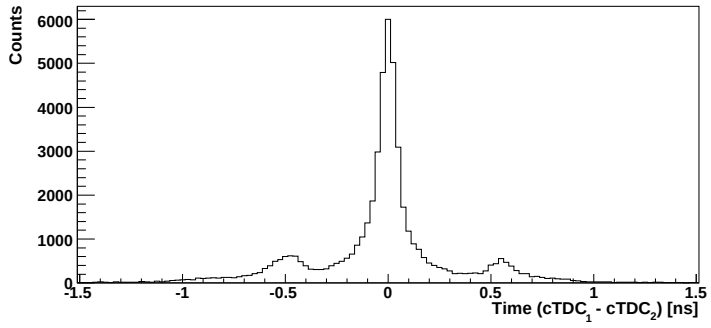

(b) Corrected TDCs

Figure A.3: The coincidence time distribution between the two channels, calculated with raw (a) and time-walk corrected information (b).

The method for obtaining the time-walk correction parameters described here, produced time resolutions comparable to results of time-walk correction with laser obtained parameters. The results did not improve if more than two steps of iteration were performed.

B Detection of gammas with the MCP PMT

The 511 keV annihilation gammas can be detected with some efficiency by the MCP PMT itself. Incident gammas can cause emission of Cherenkov photons in the photodetector window. They can also interact with the material of the microchannel plate. An electron produced in such way has a chance to enter a microchannel and cause a charge multiplication event, very similar to a normal photo detection event.

The efficiency with which the MCP PMT can detect annihilation gammas was measured using the setup presented in Section 7. Table B.1 lists the measured efficiency, obtained with just the MCP PMT and when the gammas are first absorbed in the Cherenkov radiator. In the latter case a 15 mm thick black painted PbF_2 crystal was placed just before the MCP PMT window. The unpainted surface, which was usually coupled to the photodetector, was facing the source, while the surface closest to the photodetector was painted black (Figure B.1). In this way the gamma intensity was attenuated as it would be in a PET application. The detection efficiency of the MCP PMT is small compared to the efficiency of 6% measured with the full gamma detector, composed of a 15 mm thick, black painted PbF_2 Cherenkov radiator coupled to the MCP PMT.

	Efficiency [%]
MCP PMT	0.51
15 mm thick absorber & MCP PMT	0.15

Table B.1: The gamma detection efficiencies with just the MCP PMT and the MCP PMT, after the incident gamma intensity is attenuated by the PbF_2 crystal. Here, JY0005 MCP PMT was used.

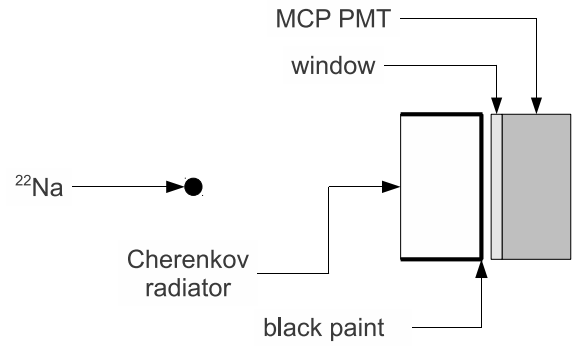

Figure B.1: The configuration of the setup used to estimate the gamma detection efficiency of MCP PMT, when the absorber (Cherenkov radiator) was present.

B.1 Effects of the window

The MCP PMTs used in experiments have a 1.5 mm thick borosilicate glass windows, which have a density of about 2.2 g/cm^3. This is much lower than the density of proposed Cherenkov radiators and scintillators typically used for PET. However some Cherenkov photons are still produced from gamma interactions with the window material and can be detected after reaching the photocathode. In any case, events detected by the MCP PMT window are registered with an excellent timing due to small thickness and refractive index of the window and contribute to the results in a desired way.

B.2 Effects of the MCP

The gammas that survive the passage trough the Cherenkov radiator and the window can interact with the microchannel plate. The MCP material can be approximated with silicon dioxide (SiO_2), which has a density of about 2.2 g/cm^3 and a 511 keV gamma attenuation coefficient of about 0.2 cm^{-1} [21]. In the photodetectors used in experiments the total thickness of the two cascaded MCPs is about 0.8 mm, which means that 1.5% of incident gammas interact with the MCP material. However, some of the material is missing due to microchannels, so the total interaction probability is roughly about 1%.

Almost all 511 kev gamma interactions in SiO_2 occur through the Compton scattering [21], meaning electrons with energies on the order of $10-100$ keV will be produced. The probability that gamma interaction will result in a charge multiplication event, similar to a normal photo detection, is hard to estimate. In normal events the photoelectrons impact the microchannels with energy of about 200 eV. Considering the estimates in Section 3.5.3 and the lower density of SiO_2, compared to PbF_2, the range of electrons in the MCP, produced in Compton scattering of gammas, is about 50 times larger than the 10 μm diameter of the microchannels. All this suggests that some charge amplification is very likely after 511 keV gamma interaction in the MCP.

Events detected directly by the MCP are registered sooner than normal photo detection event, due to the photoelectron travel time from the photocathode to the MCP in the latter case. This time delay can be estimated as one half of the longest delay due to photoelectron backscattering, which according to measurements (long tails in Figure 5.5) is about 1 ns.

The difference in detection time between normal photo detection and MCP gamma detection is the cause of ± 0.6 ns delayed peaks in coincidence time distributions (Section 6). The delayed peaks are barely noticeable in the initial measurements (Figure 6.3) but are very prominent in the later results (Figures 6.8, 6.9 and 6.11). The reason for this difference is that

JY0008 MCP PMT, used in the initial measurements, had a different time response characteristics and a much higher QE than JY0002 MCP PMT, which replaced it. Also, the QE of JY0005 MCP PMT, which was used for all measurements, most likely degraded with time. Lower QE of photodetectors meant that less events were detected trough detection of Cherenkov photons. The efficiency of gamma detection in MCP stayed the same, leading to an increase of the fraction events in delayed peaks relative to the central peak. If photodetectors with improved QE were be used, the fraction of events in delayed peaks could become negligibly small.

The fraction of events in delayed peaks is also reduced when a Cherenkov radiator wtih larger thickness is used, since a larger fraction of incident gammas is stopped in the radiator and is no longer available for detection in the MCP. This can be seen when comparing results obtained with 5 mm (Figure 6.8a) and 15 mm (Figure 6.8b) thick PbF_2 crystals. Table B.2 lists the fraction of events in delayed peaks, compared to the number of events in the central peak. Effects of gamma detection in MCP were already very small when a 15 mm thick radiator was used, even in the case of photodetectors with very low QE.

	Fraction [%]	
	5 mm	15 mm
Left peak	11	3
Right peak	9	3

Table B.2: The fraction of events in delayed peaks, compared to the central peak in case of 5 mm and 15 mm thick, black painted, monolithic PbF_2 radiators.

The fraction of events in delayed peaks could also be reduced by increasing the threshold for the charge of events. When a normal photo detection event takes place, the charge multiplication starts almost at the beginning of the microchannel. The detected charge has a statistical distribution with a peak (Figure 5.2). In the case of detection in the MCP, the charge multiplication starts at different depths along the microchannels. This means that most of the events are detected with a charge smaller than the average charge generated in a full amplification event. Therefore a small increase in threshold will remove a large part of events, where gamma was detected in the MCP, but only a small part of Cherenkov photon detection events. Figure B.2 shows the fraction of delayed peaks compared to the central peak and the relative reduction of events in central peak, as an additional charge threshold was applied in analysis. As can be seen, if a small reduction in efficiency is acceptable, a significant reduction in delayed peaks is possible with a small increase in threshold.

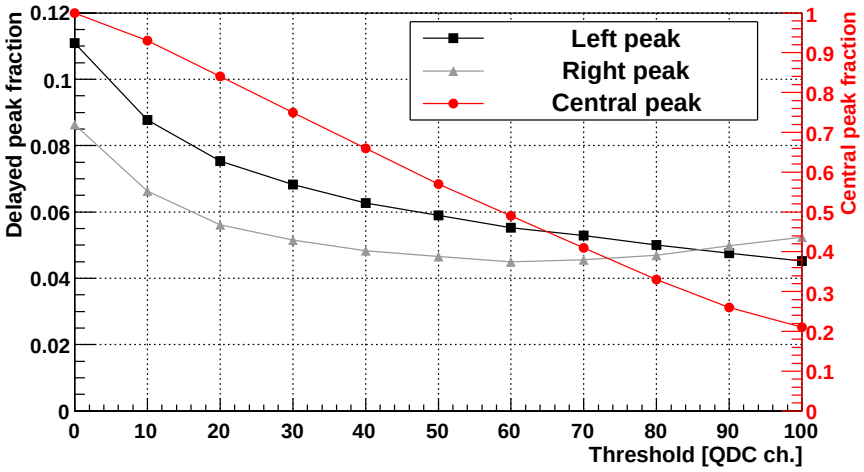

Figure B.2: Threshold dependence of the fraction of events in delayed peaks compared to the central peak (left y-axis) and the fraction of the central peak compared to the central peak, when no additional threshold was applied (right y-axis). This are results obtained with a 5 mm thick, black painted PbF_2 radiators, coupled to JY0002 and JY0005 MCP PMTs.

Izjavljam, da je disertacija rezultat samostojnega raziskovalnega dela.

Ljubljana, oktober 2012 Rok Dolenec, univ. dipl. fiz.